UNIVERSITÉ DE SHERBROOKE
Faculté de génie
Département de génie civil

BEHAVIOR OF SLENDER CONCRETE COLUMNS REINFORCED WITH GFRP-BARS AND SPIRALS UNDER CONCENTRIC AND ECCENTRIC LOADS

ÉTUDE DU COMPORTEMENT DE COLONNES ÉLANCÉES EN BÉTON ARMÉ DE BARRES ET DE SPIRALES DE PRFV SOUS CHARGES AXIALES ET EXCENTRIQUES

Thèse de doctorat
Spécialité : génie civil

WASEEM MOHAMMED ABDELRAHMAN ABDELAZIM
(WASEEM ABDELAZIM)

A dissertation submitted in partial fulfilment
of the requirements for the degree of
Doctor of Philosophy
(Civil Engineering)

Sherbrooke (Québec) Canada
March 2020

MEMBRES DU JURY

Prof. Brahim Benmokrane

Directeur

Prof. Adel ElSafty

Évaluateur

Prof. Emmanuel Ferrier

Évaluateur

Prof. Sebastien Langlois

Évaluateur

Prof. Nathalie Roy

Rapporteur

ABSTRACT

Rapid innovations in the concrete industry and high-strength materials have allowed for the design of more slender members more than the past, such as slender reinforced concrete (RC) columns. Such members suffer several corrosion problems if traditional steel is used as an internal reinforcement material. Consequently, reinforcing slender RC columns with the non-corrosive fiber-reinforced polymers (FRP) reinforcement extends the structure's lifetime span and can eliminate the high repair and rehabilitation expenditures due to the inevitable corrosion of conventional steel. This undoubtedly satisfies the designers' needs and successfully introduces FRP-reinforcements in the construction market. However, limited endeavors have been driven to investigate the structural performance of slender RC columns entirely reinforced with FRP-bars. Moreover, current design recommendations proposed for slender FRP-RC columns have many discrepancies attributed to the slenderness limit and the effective flexural stiffness.

The research program herein has been directed to experimentally and theoretically assess the structural behavior of GFRP-RC columns. Therefore, thirty-four GFRP-RC columns with various slenderness ratios were prepared and tested at four different initially applied eccentricity ratios (0, 16 %, 33 %, and 66 %). In addition, four steel-RC slender columns were conducted and observed at the same conditions of GFRP-RC ones to serve as benchmarks. Besides the reinforcement type, the slenderness, and the eccentricity ratios, test variables were also included the longitudinal and transverse reinforcement ratios and the concrete compressive strength. Based on the test results, the GFRP longitudinal-bar contribution to the column capacity and its provision of adequate stability can be described as "significant" over the wide range of parameters tested. Then, the research was extended, developing a second-order model for slender FRP-reinforced concrete columns accounted for materials and geometrical nonlinearities. A good correlation was observed between the generated analytical model and the experimental results of the current study and more than 120 FRP-RC columns were assembled from the literature. The developed model was therefore employed to provide design provisions for slenderness lower and upper limits and to refine the moment magnifier approach

addressed in North American codes and guidelines to accommodate GFRP-RC columns. This included proposing simple and practical design equations for the effective flexural stiffness of GFRP-RC columns based on a multiple linear regression analysis of more than 9,500 slender GFRP-RC columns.

Finally, the experimental and analytical evidence from this study provide valuable data and design provisions that encourage implementation of GFRP reinforcement in slender RC compression members. These provisions, therefore, support including sections dealing with the design and use of non-prestressed slender compression members (columns, piles, and piers) entirely reinforced with GFRP bars into the future editions of the AASHTO LRFD *Bridge Design Guide Specifications for GFRP-Reinforced Concrete* (AASHTO 2018a), CAN/CSA S6-19 (CSA 2019), ACI 440.1R-15 (ACI 2015), and CSA S806-12 (CSA 2012).

Keywords: Concrete, FRP bars, columns, axial, eccentricity, stress, strain, model, failure, second-order analysis, stability, curvature, stiffness, design, codes.

RÉSUMÉ

Les innovations rapides dans l'industrie du béton et les matériaux à haute résistance ont permis de concevoir des éléments plus élancés que le passé, tels que des colonnes élancées en béton armé (BA). Ces éléments structuraux montrent des problèmes de corrosion si l'acier traditionnel est utilisé comme matériau de renforcement interne. Par conséquent, le renforcement des colonnes élancées en BA avec l'armature en polymères renforcés de fibres (PRF) non corrosives prolonge la durée de vie de la structure et peut éliminer les coûts de réparation et de réhabilitation élevées dues à la corrosion inévitable de l'acier conventionnel. Cela répond sans aucun doute aux besoins des concepteurs et introduit avec succès des renforts en PRF sur le marché de la construction. Cependant, des efforts limités ont été menés pour étudier la performance de colonnes élancées en BA entièrement renforcées de barres en PRF. De plus, les recommandations de conception actuelles proposées pour les colonnes élancées en PRF-BA présentent de nombreuses différences attribuées à la limite d'élancement et à la rigidité à la flexion effective.

Ce programme de recherche a été effectué pour évaluer expérimentalement et théoriquement le comportement des colonnes en BA renforcées de PRFV. Par conséquent, trente-quatre colonnes en BA-PRFV avec divers élancements ont été préparées et testées à quatre différents rapports d'excentricité initialement appliqués (0, 16%, 33% et 66%). De plus, quatre colonnes élancées en BA d'acier ont été réalisées et observées dans les mêmes conditions que celles en BA-PRFV pour servir de référence. Outre le type d'armature, l'élancement et les rapports d'excentricité, les variables d'essai comprenaient également les rapports d'armature longitudinale et transversale et la résistance à la compression du béton. Sur la base des résultats d'essais, la contribution des PRFV comme barres longitudinales à la capacité de la colonne et son apport d'une stabilité adéquate peuvent être décrites comme « significatives » sur la large gamme de paramètres testés. Ensuite, la recherche a été étendue, en développant un modèle de second ordre pour les colonnes élancées en béton armé de PRFV prises en compte pour les matériaux et les non-linéarités géométriques. Une bonne corrélation a été observée entre le modèle analytique généré et les résultats expérimentaux de la présente étude et plus de 120

colonnes en BA-PRFV ont été assemblées à partir de la littérature. Le modèle développé a donc été utilisé pour fournir des dispositions de conception pour les limites inférieures et supérieures d'élancement et pour affiner l'approche d'amplification du moment abordée dans les codes et lignes directrices Nord-Américains pour tenir compte des colonnes en BA-PRFV. Cela comprenait la proposition d'une équation de conception simple et pratique pour la rigidité à la flexion efficace des colonnes en BA-PRFV basée sur une analyse de régression linéaire multiple de plus de 9 500 colonnes élancées en BA-PRFV.

Enfin, les preuves expérimentales et analytiques de cette étude fournissent des données précieuses et des dispositions de conception qui encouragent la mise en œuvre de l'armature de PRFV dans les éléments élancés en BA soumis aux efforts en compression. Par conséquent, ces dispositions soutiennent l'inclusion de sections traitant de la conception et de l'utilisation d'éléments élancés en compression non précontraints (colonnes, pieux et piliers) entièrement renforcés avec des barres en PRFV dans les futures éditions du guide de conception de pont AASHTO LRFD *Spécifications du guide de conception des ponts pour le béton armé de PRFV* (AASHTO 2018 a), CAN / CSA S6-19 (CSA 2019), ACI 440.1R-15 (ACI 2015) et CSA S806-12 (CSA 2012).

Mots clés : Béton, barres d'armature de PRF, poteaux, axial, excentricité, contraintes, déformations, modèle, rupture, analyse du second ordre, stabilité, courbure, rigidité, conception, normes.

BIBLIOGRAPHY

During the research work at the University of Sherbrooke, the candidate has participated in the following publications:

Journal Papers:

- Abdelazim, W.; Mohamed, H. M.; Afifi, M. Z.; and Benmokrane, B. (2020a). "Proposed Slenderness Limit for GFRP-RC Columns Based on Experiments and Buckling Analysis." ACI Structural Journal. V. 117. No. 1. January 2020.
- Abdelazim, W.; Mohamed, H. M.; and Benmokrane, B. (2020b). "Inelastic Second-Order Analysis for Slender GFRP-Reinforced Concrete Columns: Experimental Investigations and Theoretical Study." *Journal of Composites for Construction*. ASCE. V. 24. No. 3. April 2020.
- Abdelazim, W.; Mohamed, H. M.; Afifi, M. Z.; and Benmokrane, B. (2020c). "Effect of Critical Test Parameters on the Behavior of GFRPRC Slender Columns under Eccentric Load." ACI Structural Journal. accepted.
- Abdelazim, W.; Mohamed, H. M.; and Benmokrane, B. (2020d). "Strength of High-Strength Concrete Bridge Slender Compression Members Reinforced with GFRP Bars and Spirals Based on Experimental and Second-Order Analysis." *Journal of Bridge Engineering*. ASCE. (accepted).
- Abdelazim, W.; Mohamed, H. M.; and Benmokrane, B. (2020e). "Proposed Flexural Stiffness of Slender Concrete Columns Reinforced with GFRP-Bars." (under review).

Refereed Conferences Publications:

1. Abdelazim, W.; Mohamed, H. M.; and Benmokrane, B. (2019). "Effect of slenderness ratio on the performance of concrete columns reinforced with GFRP bars and spirals." *CSCE Annual Conference*. Proceedings. 12-15 June 2019, Laval, QC, Canada, 10p.
2. Abdelazim, W.; Mohamed, H. M.; and Benmokrane, B. (2020f). "Second-Order Response of Glass Fiber-Reinforced Polymer -Reinforced Concrete Slender Columns," *8th*

International Conference on Advanced Composite Materials in Bridges and Structures (ACMBS-VIII), proceedings, Aug. 18-20, Sherbrooke, QC, Canada, 6p.

3. Abdelazim, W.; Mohamed, H. M.; and Benmokrane, B. (2020g). "Assessment of The Flexure Stiffness of Slender Concrete Columns Reinforced with Glass Fiber-Reinforced Polymers," *8th International Conference on Advanced Composite Materials in Bridges and Structures* (ACMBS-VIII), proceedings, Aug. 18-20, Sherbrooke, QC, Canada, 6p.

Technical Presentations:

4. **Abdelazim, W.** "Behavior of Slender Circular Concrete Columns Reinforced with GFRP Bars and Spirals under Eccentric Loads." *Technical report for project definition*, University of Sherbrooke, QC, Canada, April 2018; 161p.
5. **Abdelazim, W.** "Performance of Slender Circular Concrete Columns Reinforced with GFRP Bars and Spirals." *Presentation in the 2017 Annual Meeting of the 4th Five-Year Term of the NSERC Research Chair*, June 2017, University of Sherbrooke, QC, Canada.

To my beloved family ……,

CONTENTS

List of Figures

List of Tables

CHAPTER 1

INTRODUCTION

1.1 General Background

Reinforced concrete (RC) columns can be classified into two broad categories: short columns and slender columns. Slender columns experience considerable reduction in the column capacity due to the induced column buckling compared to the capacity of short or stocky columns that fail without undergoing any noticeable lateral deformations. Most of columns are preferred to be short to eliminate any losses due to lateral deformations and to achieve the maximum loading resistance. However, slender columns are common nowadays because of rapid development of the high strength materials and improved methods of erection which enabled for design some much smaller sections than in the past. Figure 1.1 shows some examples of slender columns in various applications.

(a) (b) (c)

Figure 1.1– (a) Viaduct St. Kilian, Germany (structurae.net); (b) University of Magdeburg Library, Germany (designbuild-network.com); (c) Estádio Nacional Mané Garrincha, Brazil (structurae.net).

To overcome the tensile stresses caused by the existing loads, misalignments, and/or lateral buckling and second-order effects, such columns are usually reinforced with conventional steel bars and spirals or ties. Steel reinforcement has a limited service life and entails high maintenance costs because of corrosion when used in aggressive and/or harsh marine environments. Therefore, reinforcing slender RC columns with FRP reinforcement extends the structure's lifetime span and can eliminate the high repair and rehabilitation expenditures due to the inevitable corrosion of conventional steel. For example, the US Federal Highway Administration (FHWA) reported that, in 2018, the estimated rehabilitation costs of structurally deficient (SD) national and nonnational highway system bridges due to steel corrosion exceeded $32.8 billion. Furthermore, the Canadian Construction Association (CCA) estimated that the investment required to rehabilitate public infrastructure overall hovers around C$900 billion (ISIS Canada 2007).

Current editions of North American design codes include comprehensive sections dealing with the design of slabs and beam members reinforced with GFRP-bars. Yet, current standards either do not recommend integrating FRP bars into compression members (ACI 440.1R-15) or conservatively ignore their contribution to the capacity of such members (AASHTO 2018; CSA S806-12). Furthermore, CSA S806-12 stipulates that slender columns shall not be permitted to have FRP longitudinal reinforcement. Consequently, enormous efforts are being deployed to provide detailed sections dealing with the design of GFRP-RC columns in upcoming editions of FRP design codes. This, in turn, requires a large experimental database to assess the behavior of short and long GFRP-RC columns and to propose rational design limits to the code technical committees. Consequently, this research intended to assess the performance of FRP reinforcement in slender columns, accounting for the induced second-order effects. Furthermore, the moment magnifier approach permitted in ACI 318-19 and CSA A23.3-14 for the design of steel-RC slender columns, was re-examined to accommodate FRP reinforcement through proposing design limits, equations, and general recommendations.

1.2 Objectives and Scopes

This research program attempted to provide comprehensive tests and analytical investigations of slender GFRP-RC columns in order to support the work of the relevant technical committees.

The performance of GFRP bars and spirals were observed through strain measurements at different locations including the most stressed zones. Moreover, the impact of various slenderness ratios on the failure envelope and second-order responses were clearly highlighted and well-presented. Further, the test results of GFRP-RC slender columns were compared with steel-RC counterparts prepared and tested in the same testing conditions as GFRP-RC ones. Therefore, the main and general objective of this study can be drawn as:

Addressing the feasibility of integrating GFRP bars as an internal reinforcement of RC slender columns, proposing design provisions for the relevant North-American codes and guidelines.

Besides, the following points summarize the specific objectives:

1. To assess the general behavior of slender GFRP-reinforced concrete columns with critical slenderness ratios ranging from $\lambda = 14$ to $\lambda = 33$ under concentric and different levels of eccentric loading.

2. To quantify the capacity of slender GFRP-reinforced concrete columns, identifying the strength reduction owing to initiated second-order effects.

3. To develop a P–M failure surface of slender GFRP-reinforced concrete columns reflecting the influence of second-order effects on the failure paths.

4. To propose recommendations for slenderness lower and upper limits for GFRP-reinforced concrete columns that could support the work of the North American technical committees engaged in developing standards and design provisions for GFRP-reinforced concrete columns.

5. To experimentally assess the moment-curvature relationship of GFRP-RC slender columns, identifying the influence of the different test parameters on the column flexural stiffness.

6. To develop EI design equations for GFRP-RC slender columns that could generalize the moment magnification approach to accommodate GFRP-RC slender columns.

1.3 Methodology

The above objectives were gained through conducting a large-scale research plan including experimental program and theoretical studies. The experimental plan was consisted of 34 RC columns entirely reinforced with GFRP bars and spirals. All columns are 305-mm in diameter with various heights (1000-mm, 1250-mm, 1750-mm, 2000-mm, and 2500-mm). In addition to the slenderness ratio as a studied parameter, a further set of variables will be investigated such as longitudinal reinforcement ratio, confinement level, and the load eccentricity ratio. Two batches of ready-mixed, normal-weight concrete were used to cast the column specimens: one was for normal-strength concrete; the other was high-strength concrete. As designers are more familiar with the behavior of steel-RC columns, a total of 4 RC columns reinforced with steel reinforcements were prepared and tested at the same testing conditions of GFRP-RC ones to be served as a benchmark.

Any experimental work is going to be of limited usefulness unless it is utilized to develop some simplified design equations. Consequently, a detailed theoretical analysis was carried out in conjunction with the experimental findings to develop models capable to clearly define the behavior of the slender columns reinforced with GFRP. Developed models considered both material and geometrical nonlinearities of GFRP-RC columns. Therefore, these models were capable to predict and simulate the second-order effects attributed to slender columns. Thereafter, the analytical models were verified with the experimental results of the current study and with the experimental database from literature. The analytical models were then employed to extend the research program over a wide range of parametric values including the elastic modulus of GFRP-bars, the column cross-section geometry, and GFRP-bars arrangement in addition to the above-mentioned variables in the experimental program. At last, a multiple linear regression analysis was conducted of the simulated theoretical data in order to propose a simple and practical design equation of the effective flexural stiffness of GFRP-RC slender columns.

1.4 Thesis organization

The thesis is organized into eight chapters including the introduction. As usual, the thesis begins commonly with an introduction defining the research objectives and methodology as described earlier. Thereafter, A short review is presented in Chapter 2 to provide the reader with most research studies related to the aimed objectives. The next chapters are arranged as follows:

Chapter 3 (1st article) presents an experimental and theoretical investigation of GFRP-RC columns with various slenderness ratios under concentric axial loads with a focus on stability problems. An estimation of the axial capacity of slender FRP-RC columns along with a new slenderness limit are also proposed based on the experimental results and the buckling analysis.

Chapter 4 (2nd article) presents test results of an experimental program to investigate the structural performance of slender columns loaded at different eccentricities. Based on the test results, a detailed second-order analysis were then conducted. Furthermore, a comprehensive parametric investigation was performed using interaction diagrams and stability curves.

Chapter 5 (3rd article) presents a detailed experimental study to discuss the effect of different test parameters on the second-order response of GFRP-RC slender columns. In addition, based on the stability index specified in ACI 318-19, the maximum permissible tensile design strain of the GFRP-bars was proposed to eliminate the probability of the undesired stability failure of such columns.

Chapter 6 (4th article) investigated experimentally and analytically the feasibility of high-strength concrete (HSC) in circular GFRP-RC columns under concentric and eccentric loading. The proposed slenderness limit was verified and required modifications have been applied to account for the effect of using HSC on the slenderness lower limit.

Chapter 7 (5th article) introduces a 2nd-order analytical model was derived to assess the structural performance of more than 9,500 GFRP-RC slender columns includng a wide range of design parameters. The model was used to re-examine the moment magnifier approach

specified in ACI 318 for the structural analysis of steel-reinforced concrete (RC) slender columns to accommodate glass fiber-reinforced polymer (GFRP)-RC columns.

The last Chapter of the thesis, **Chapter 8**, presents some detailed conclusions of the results obtained from the experiments and analyses with respect to observations and highlights discussed throughout the thesis in addition to recommendations for future work.

CHAPTER 2

LITERATURE REVIEW

2.1 General

RC columns are considered as the most substantial element in any RC structure and failure of one column may be an adequate reason for the whole building collapse. Consequently, extensive studies have been carried out in order to assessing the behavior of steel-RC columns. However, limited research was directed to investigate the behavior of fiber-reinforced polymers (FRP)-RC columns, especially slender ones. In addition to the literature review provided in each chapter, the following sections provide a short review of the relevant studies in literature, emphasizing the general behavior and design aspects.

2.2 Performance of FRP-RC Columns

In general, the behavior of FRP-RC columns was found to be similar to those columns that are reinforced with traditional steel bars (De Luca et al. 2010; Tobbi et al. 2012; Afifi et al. 2014; Mohamed et al. 2014; Hadhood et al. 2017a, b, c, and d). For example, Fig. (2.1) is adopted from Hadhood et al. (2017a) and presents the load-axial deformation relationship of two groups of columns. One group was reinforced with CFRP-bars and the other one was reinforced using traditional steel-bars. This plot illustrates the very close performance of both CFRP- and steel-RC tested columns where no major discrepancies were observed. Moreover, the failure of the tested FRP-RC short columns in literature was typically dominated by a material-type failure in terms of gradual concrete cover spalling at the peak load (Hadi et al. 2016; Hassan et al. 2017) as shown in Fig. (2.2). Prior to the point of peak load, the initial applied eccentricity controlled the elastic portion of the ascending loading branch. The more the applied

eccentricity is, the less of the elastic loading path occur. Finally, FRP-bars were found to have a significant contribution to the column axial and flexural capacities of such FRP-RC columns (Tobbi et al. 2012; Tobbi et al. 2014; Afifi et al. 2014).

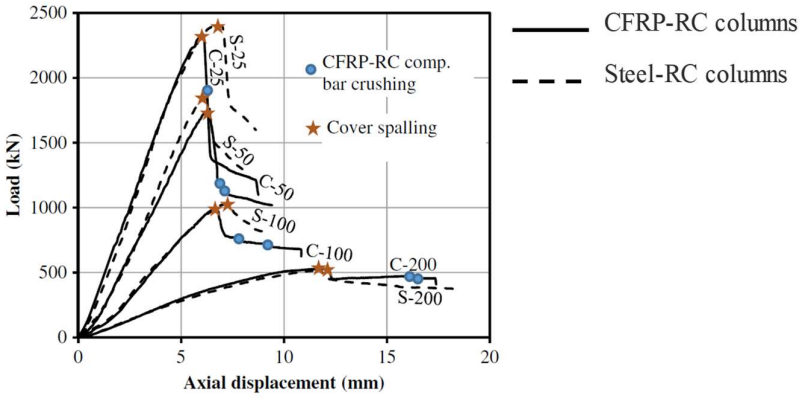

Figure 2.1– Load versus axial displacement at specimen centerline (Hadhood et al. 2017a).

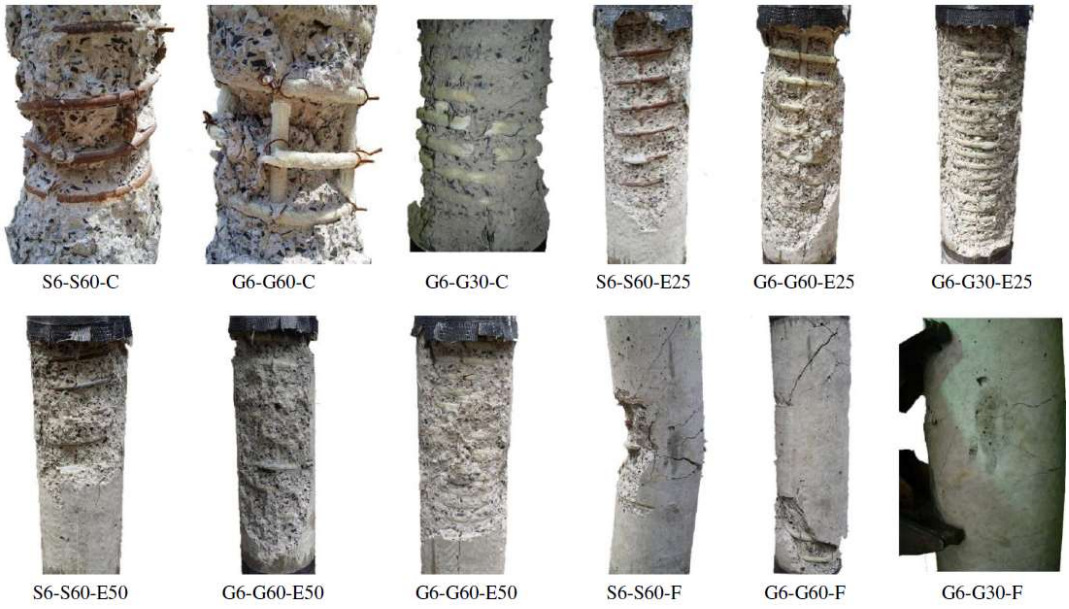

Figure 2.2– Failure modes of the tested specimens (Hadi et al. 2016).

In most cases, FRP-bars behave elastically up-to failure at large tensile strains exceeds 0.02 compared to a steel yield-strain equals 0.002. These large tensile strains related to FRP-bars (which is approximately 10 times of yielding strain of steel bars) causes that most of the tested

specimens in labs fails in compression before reaching the FRP-failure tensile strains. However, some researchers (Hadhood et al. 2017a; Guérin et al. 2018a, b) reported that the tested high-eccentrically loaded columns suffered exaggerated tensile cracks accompanied with large deformations before concrete cover spalling occurred. Fig. (2.3) shows the cracking pattern and failure mode of the GFRP-RC columns tested by Guérin et al. (2018a). The shown test specimen was loaded at an eccentricity-to-depth ratio of 0.80. As ACI 318-14 defines the tension failure as that failure at which a sufficient warning is achieved in terms of excessive tensile cracks and large curvature. Similarly, failure of FRP-RC columns loaded at large eccentricities can be defined as a tension-based failure.

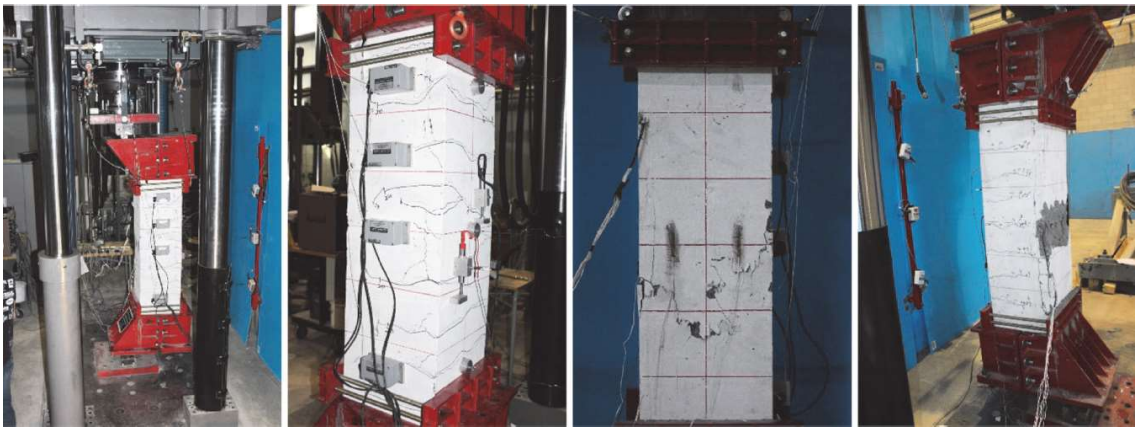

Figure 2.3– Crack appearance and failure mode of columns tested under large eccentricity (e/ho = 80%; G2) (Guérin et al. 2018a).

As mentioned earlier, FRP-bars do not yield and have an elastic behavior up-to failure (ACI 440.1R-15). This affected the achieved ductility of FRP-reinforced columns compared to steel counterparts. However, studies in literature showed that such FRP-RC columns still have the ability to attain adequate deformations even after achieving the peak loads or spalling of the concrete cover at compression side (Pantelides et al. 2013; Afifi et al. 2014; Mohamed et al. 2014). Therefore, the term of "deformability factor" was introduced to define the latter behavior of FRP-RC after failure (ISIS 2007). The ductility and confinement efficiency of the concrete core can be effectively improved using smaller FRP-spirals with closer spacing. Such confinement configuration causes the FRP-RC columns to fail in more gradual manner,

enhancing the ductile behavior in the post-peak stage as concluded by Afifi et al. (2014) and Mohamed et al. (2014). Afifi et al. (2014) defined the ductility of the tested GFRP-RC columns as the ratio $\varepsilon_{c85}/\varepsilon_{c1}$, where ε_{c85} is the axial strain defined at an axial load corresponding to 85% of the maximum loading capacity in the descending part of the load–strain curve (see Fig. 2.4), and ε_{c1} is defined at a strain corresponding to the limit of elastic behavior on the ascending part.

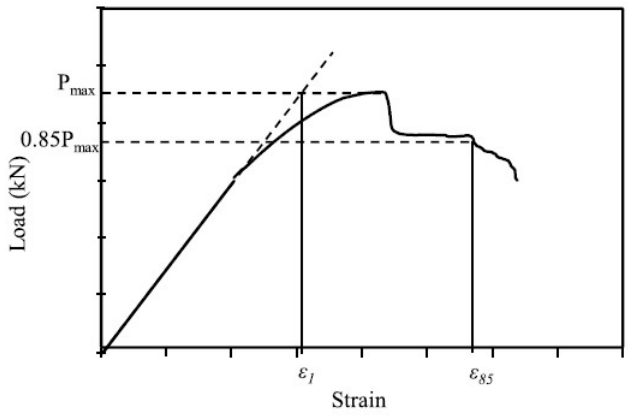

Figure 2.4– Ductility of the GFRP RC columns on the basis of strain measurements (Afifi et al. 2014).

Several studies have been published recently by a research group in University of Wollongong on the behavior of GFRP-RC columns under axial and/or eccentric loading (Hadi and Youssef 2016; Hadi et al. 2016 and 2017; Karim et al. 2016). These studies include experimental and analytical investigations of various parameters. The experimental program used square cross section of 210 mm sides and 800 mm height and/or circular sections of diameter 205 mm and height 800 mm. The specimens tested under concentric loading; eccentric loading of 25 mm and 50 mm; and/or two-point loading flexure. The test variables were the type of reinforcement (steel vs. GFRP); external confinement or none; internal reinforcement or none; normal concrete or fiber-reinforced concrete. The analytical program included developing interaction diagrams; parametric studies; estimation of ductility.

Their concentric GFRP-RC specimens exhibited second peak points indicating proper confinement, provided by helices spaced each 30 mm or 60 mm. The closely spaced specimen exhibited, however, higher second peak than the other (Hadi et al. 2016). They reported that

reducing the GFRP helices pitch from 60 to 30 mm led to an improvement in the performance of the GFRP-RC specimens in terms of load-carrying capacity, bending moment, and ductility. They also reported that the contribution of the longitudinal steel bars in the load carrying capacity of the concentric column specimens was about twice the contribution of the longitudinal GFRP bars, whereas the ductility of the GFRP-RC column specimens was slightly greater than the ductility of the reference steel-RC column specimens under different loading conditions.

Limited available experimental results discussed the behavior of FRP-RC slender columns. Tikka et al. (2010) conducted an experimental program to investigate the behavior of eccentrically loaded slender columns reinforced longitudinally by GFRP bars and laterally tied by Carbon Fiber spirals. Eight square columns 150 mm width with 1800 mm total height were tested. The test variables are the reinforcement ratio and the supplier. Two reinforcement ratios are studied 2.3%, and 3.4%. Also, two sets based on the suppliers were arranged. Figure (2.5) shows the specimens and testing details. The results from this study showed that using GFRP bars from two different manufacturers provided very similar strengths. The plotted load-deflection curves of the tested specimens revealed that GFRP-RC columns had a reasonable amount of ductility and would provide adequate warning perior to failure.

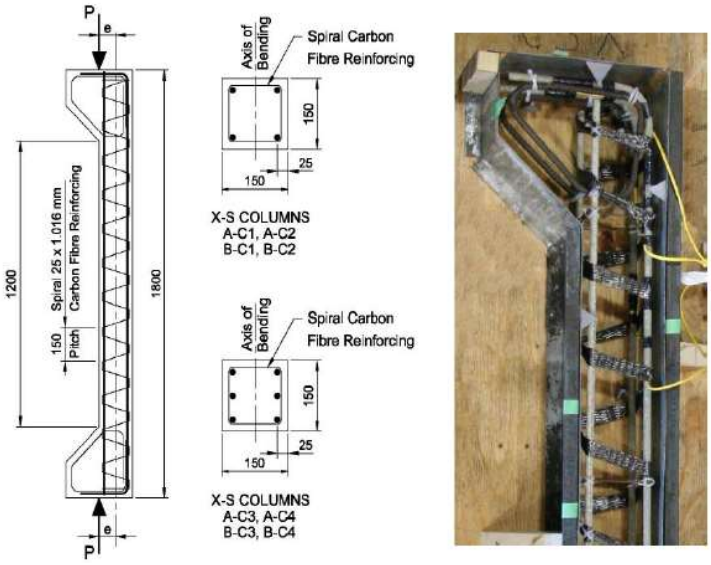

Figure 2.5– Specimen and Testing Details (Tikka et al. 2010).

Hales et al. (2016) tested nine high-strength concrete (90 MPa) columns reinforced using either GFRP-bars or steel-bars or a combination of both. The tested columns had slenderness ratios (heights) equalled to 10 (760-mm) and 49 (3730-mm). The reduction in the loading capacity due to slenderness variations could not be observed as the short and long columns had different loading conditions. It was reported that the strength of slender columns with small eccentricity (8.3% of the column size) was governed by material-type failure, while that of slender columns with large eccentricity (33% of column size) was governed by a stability-type buckling failure. Also, GFRP longitudinal reinforcement can provide larger deflection capacity compared to steel bars due to their higher tensile strength; in addition, they retrieved its original shape once the load is removed, which can be beneficial in case of earthquakes. Fig. 2.6 shows the failure mode of the slender column due to 102 mm eccentric load.

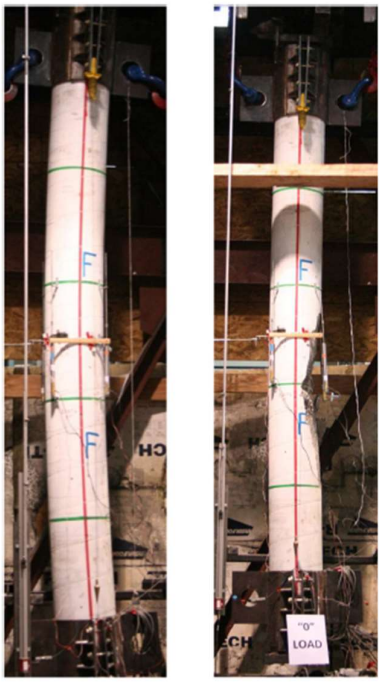

(a) (b)

Figure 2.6– Slender Columns Tested to Failure (102-mm eccentricity): (a) Before Failure; (b) After Failure.

Recently, Xue et al. (2018) conducted concentric and eccentric loading tests on slender rectangular GFRP-RC columns. Columns were tested under a wide range of the applied eccentricity-to-depth ratios varied from 0 to 1.0. The slenderness ratio of the tested columns

ranged from 20.8 to 41.6. The test results from Xue et al. (2018) indicated that All columns failed by concrete crushing followed by spalling of the concrete and eventually buckling of the GFRP bars on the compression bars near the mid-height, as shown in Fig. (2.7). The exhibited concrete crushing was in a brittle manner, even for the column with low longitudinal FRP reinforcement ratio (1.34%), large eccentricity ratio (1.0), and high slenderness ratio (41.6). Furthermore, very little post-peak deformation was observed. All GFRP-bars remained intact up-to concrete crushing and the failure load was achieved. As expected, columns with large load eccentricity cracked and deformed significantly prior to failure.

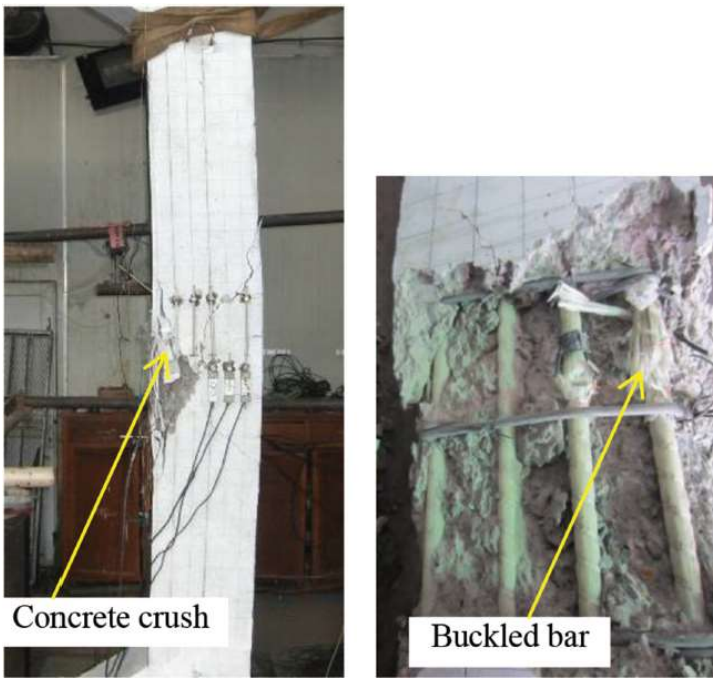

Figure 2.7– Typical failure mode of columns (Xue et al. 2018).

2.3 Design for FRP-RC Columns

Design of any FRP-RC column can be generally divided into two main stages. Stage one defines the exact analysis of the structure considering the applied loads and the induced deformations of the structure due to sidesway and/or slenderness effects. This (stage one) is called as a second-order analysis. The next stage is to find an adequate section to resist the

applied loads and the loads from the second-order effects. The latter stage is established and well-addressed by many codes and guidelines. Regarding stage one, it is beneficial to point out that integrating the structure into a rigorous second-order analysis is a time-consuming process and not suitable for repetitive designs. Therefore, MacGregor et al. (1970) stated that 5% reduction in the column capacity due to second-order effects was acceptable and additional moments from second-order effects may be neglected. For such cases, columns may be designed as short columns satisfying the first-order analysis.

ACI 318-19 and CSA A23.3-14 applied the latter definition originally defined by MacGregor et al. (1970) to set a slenderness limit below which second-order effects on steel-RC columns can be safely ignored. ACI and CSA guidelines express the mechanical slenderness ratio ($\lambda = kl_u / r$) in terms of the unsupported length of the column (l_u); the effective length factor, k; and the radius of gyration of its cross section, $r = \sqrt{I_g / A_g}$, where I_g and A_g are the gross second moment of inertia and the gross cross-sectional area of the column, respectively. Regarding steel-RC columns, the earlier mentioned codes stated that a slender lower limit of 22 is a safe limit for short columns bent in a symmetrical single curvature. Table 2.1 compares the different slenderness limits stipulated in the North American codes and standards. The upper limit for the slenderness ratio provided by ACI is to eliminate the probability of any undesired stability failure. Limited efforts have been directed to define similar slenderness limit dealing with columns entirely reinforced with FRP-bars. The following section summarizes these attempts.

2.3.1 Slenderness Limits of FRP-RC columns

As mentioned before, two slenderness limits govern the design of FRP-RC columns: lower and upper slenderness limits. So far, there is not any attempt to define an upper slenderness limit for FRP-RC columns. Regarding the lower slenderness limit, CSA S806-12 classifies GFRP-RC columns as short or long, relying on the ACI slenderness limit of 22 for steel-RC columns, disregarding that FRP-reinforced concrete members might resist buckling instability differently than steel-reinforced ones. Moreover, CSA S806-12 allows for using FRP-bar as an internal reinforcement for short columns only and explicitly prohibited using it for slender columns. This undoubtedly is due to the lack of the experimental results.

Table 2.1 – Slenderness limits in North American Codes

Margins	Member and condition	ACI 318-14	CSA A23.3-04 (2010)
Lower limit	Columns not braced against sidesway and individual compression members.	$\frac{k\,l_u}{r} \leq 22$	$\frac{k\,l_u}{r} \leq \frac{35}{\sqrt{P_u/(f_c' A_g)}}$
	Columns braced against sidesway.	$\frac{k\,l_u}{r} \leq 34 - 12(M_1/M_2)$ and $\frac{k\,l_u}{r} \leq 40$	$\frac{k\,l_u}{r} \leq \frac{25 - 10(M_1/M_2)}{\sqrt{P_u/(f_c' A_g)}}$
Upper limit	All compression members	$M_{secondary} \geq 1.4\,M_{primary}$	$\frac{k\,l_u}{r} \geq 100$
		Beyond this limit the structural system should be revised.	Beyond this limit, more accurate analysis should be performed.

Mirmiran (1998) developed an analytical model to investigate the slenderness effect on FRP-RC concrete columns. The developed model accounted for the constitutive properties of materials including concrete, steel and FRP rebar. The studied parameters considered the compressive-to-tensile strength ratio of FRP rebar. The second-order effect was also implemented in the model by integrating deflections over the length of the column. The model was validated with 4 square CFRP-RC columns with 152 mm sides. He reported that slenderness limits shall be reduced by 5%, 15% and 22% for aramid, carbon and glass rebar, respectively, if the minimum reinforcement ratio is held at 1%. Later, Mirmiran et al. (2001) carried out an analytical study by making 11,000 columns to investigate the effect of internally reinforced FRP bars on the slenderness limits and to examine the applicability of ACI moment magnification to FRP-RC columns. A 254 x 254 mm^2 section with 27.6 MPa concrete was considered for the parametric study. The chosen parameters were reinforcement ratios, modular ratios, strength ratios, compressive to tensile strength ratios, yielding response of reinforcing bars, slenderness ratios, end eccentricities, and eccentricity ratios to investigate the effect of

internally reinforced FRP bars on the slenderness concrete column. Figure 2.8 to Figure 2.10 show the effect of strength ratio, compressive/tensile strength ratio, and reinforcement yielding on the columns' slenderness limit. The following conclusions were made:

1. Variation in tensile strength of typical FRP bars does not affect the slenderness limit of RC columns;

2. Except for aramid bars that have very low compressive strength, variation in compressive strength of FRP bars does not affect the slenderness limit of RC columns. Lower compressive strengths result in more stable columns; and

3. The yielding phenomenon of reinforcing bars does not affect the slenderness limit of RC columns.

4. Based on the parametric studies, it is recommended that the current slenderness limit of 22 for steel-RC columns bent in single curvature be reduced to 17 for FRP-RC columns.

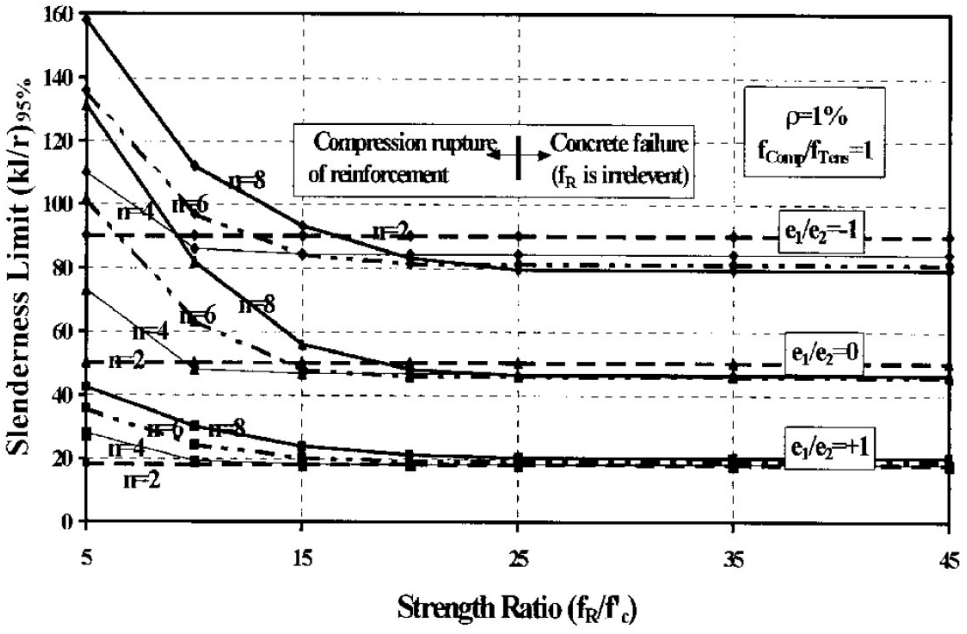

Figure 2.8– Slenderness Limit Versus Strength Ratio (Mirmiran et al., 2001).

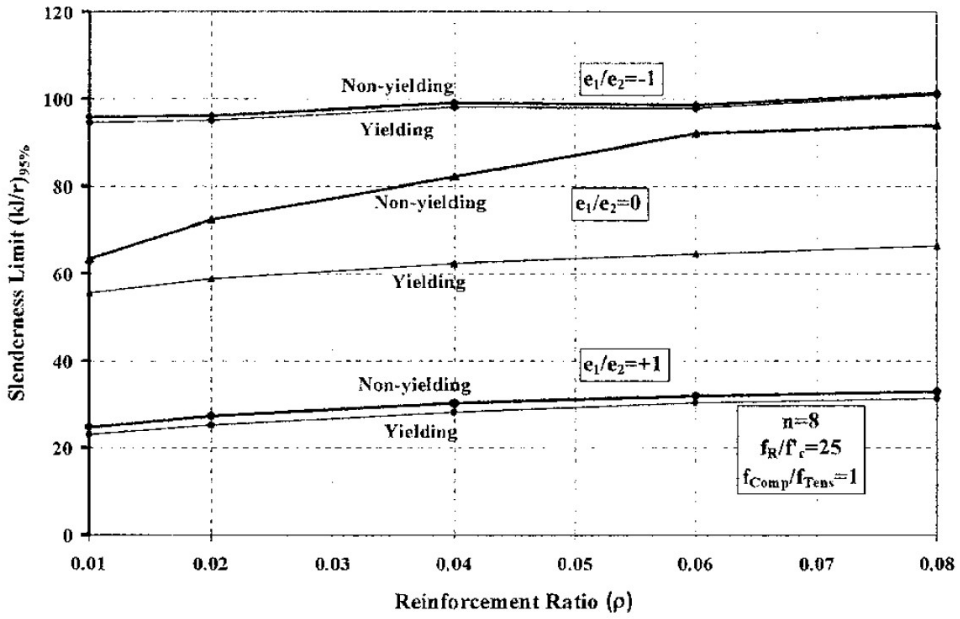

Figure 2.9– Effect of Reinforcement Yielding on Slenderness Limit (Mirmiran et al., 2001).

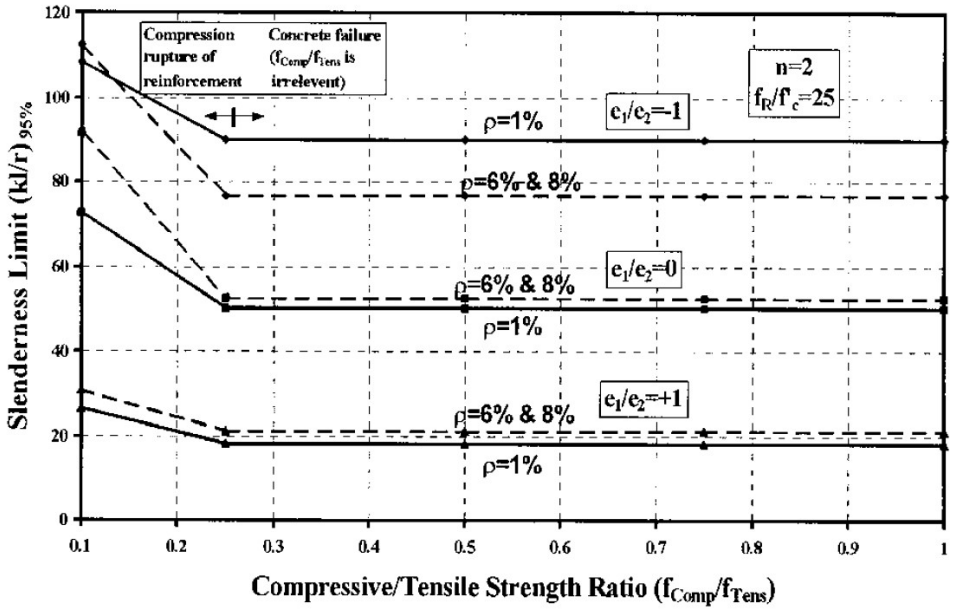

Figure 2.10– Slenderness Limit Versus Compressive/Tensile Strength Ratio, (Mirmiran et al., 2001).

Jawahery Zadeh and Nanni (2017) applied a theoretical derivation for the slenderness limits of FRP-RC columns with a rectangular cross section. The contribution of FRP bars in compression was limited to the concrete compressive strength. This means that the area of FRP-bars in compression was replaced by concrete. This was considered as a safe and justifiable hypothesis between two extremes of either subtracting the area of FRP-bars from the gross cross-sectional area or consider the full contribution of the FRP-bars in compression based on equivalent tensile and compressive moduli of elasticity. Finally, they proposed a slenderness limits of 14 and 19 for GFRP-RC and CFRP-RC columns bent in a symmetrical single curvature, respectively. These slenderness limits are considered as more conservative compared to those proposed by Mirmiran et al. (2001)

Karim et al. (2017) conducted a numerical integration to determine the compression force of the concrete in the compression zone of GFRP-RC cross-sections. The results were verified with 12 circular GFRP-RC specimens. All test specimens had a slenderness ratio of 15.6. however, they extended the research program to investigate the influence of column slenderness ratio on the behavior of GFRP-RC columns. At 5% strength reduction, Karim et al. (2017) proposed a slenderness limit of 18.7 below which GFRP-RC columns may be designed as short. The authors explained the higher proposed value of the slenderness limit compared to that reported by Mirmiran et al. (2001) as the latter used GFRP-bars had a relatively low elastic modulus. Recalling Fig. 2.8, the strength ratio on horizontal axis was defined as the ratio of tensile strength of FRP bars (or yield strength of steel bars) and compressive strength of concrete. Based on the current available GFRP-bars on markets, this strength ratio varies between 18 to 27 and 33 to 50 considering a concrete compressive strength of 55 MPa and 30 MPa, respectively. According to Mirmiran's analytical study, it could be noticed that beyond a strength ratio of 20 both the modular and strength ratios have a trivial effect on the slenderness limit particularly for columns bent in a symmetrical single curvature. The modular ratio is defined as the ratio of moduli of elasticity of the reinforcement and concrete, and ranges (considering GFRP-bars on market) between 1.55 to 2.33 and 1.15 to 1.72 for 30 MPa and 55 MPa normal-strength concrete, respectively. Finally, the scattering in the proposed values of the slenderness limit of FRP-RC columns in literature accentuates the need for more experimental and analytical studies to be conducted.

To sum up, the design of FRP-RC columns starts with checking the column as being whether short or long. Once the column category is defined, one of the following design approaches can be established.

2.3.2 Short FRP-RC Columns

As mentioned earlier, FRP-RC columns have slenderness ratio less than the slenderness lower limits can be designed as being short, satisfying the 1st-order analysis. Strength of such columns is governed by the strength of the used materials and the column cross-section geometry. Several studies proved the significant contribution of FRP-bars in compression. The compression contribution of the GFRP-bars to the column axial capacity prior to concrete spalling was reported to be ranged from 2.9% to 4.5% (De Luca et al. 2010), with 5% to 10% (Afifi et al. 2014), and 6.6% to 10.5% (Maranan et al. 2016) for reinforcement ratios of 1%, 2.2%, and 2.4%, respectively. However, CSA S806-12 offers a conservative expression to determine the axial capacity of FRP-RC columns. The offered formula not only ignores the contribution of FRP-bars in compression but also subtract the area of FRP-bars from the total gross concrete area of the column's cross-section. Afifi et al. (2014) reported that ignoring the contribution of FRP longitudinal bars in the CSA S806-12 design equation underestimated the maximum capacity of the tested specimens on average by 35%.

Tobbi et al. (2012) reported that setting the FRP compressive strength at 35% of the FRP maximum tensile strength yielded a reasonable estimate of the ultimate compressive capacity of FRP-RC short columns compared to the experimental results. Afifi et al. (2014) described the latter recommendations as an accurate and a conservative prediction of the nominal capacity of the tested GFRP-RC columns. Jawahery Zadeh and Nanni (2013) showed that it is possible to develop a methodology for the design of concrete columns with rectangular or circular cross section using GFRP bars and ties. This can be achieved by discussing the theoretical approach at the basis of the behavior of GFRP-RC members subject to simultaneous flexural and axial loads. It was concluded that:

1. The authors developed Interaction diagrams assuming that GFRP longitudinal bars are only effective in tension. It's suggested to limit the maximum design strain of GFRP longitudinal bars to be 0.01 to avoid exaggerated deflections.

2. They proposed modification factors for the flexural stiffness of GFRP-RC members which are based on the modulus of elasticity of GFRP bars. The proposed design provisions in this paper are not applicable to structures in seismic zones and may be applicable only to buildings of limited size and height.

The authors proposed stiffness modifications to the values presented in ACI 318-19 for steel-reinforced columns to represent the behavior of the same columns if the latter were reinforced with FRP. These values were slightly modified by the same authors in 2017 (Jawahery Zadeh and Nanni 2017). Table 2-2 shows a summary of these modifications.

Table 2.2 – Comparison of Stiffness Modifications in Steel-RC and FRP-RC.

Steel-RC (ACI 318-19)	Proposed for FRP-RC (2013)	Proposed for FRP-RC (2017)
$I_{beam} = 0.35\ I_g$	$I_{beam} = [0.075 + 0.275(E_f/E_s)]\ I_g \leq 0.35 I_g$	$I_{beam} = [0.10 + 0.25(E_f/E_s)]\ I_g \leq 0.35 I_g$
$I_{slab} = 0.25\ I_g$	$I_{slab} = [0.10 + 0.15(E_f/E_s)]\ I_g \leq 0.25 I_g$	$I_{slab} = [0.10 + 0.15(E_f/E_s)]\ I_g \leq 0.25 I_g$
$I_{column} = 0.70\ I_g$	$I_{column} = [0.40 + 0.30(E_f/E_s)]\ I_g \leq 0.70 I_g$	$I_{column} = [0.40 + 0.15(E_f/E_s)]\ I_g \leq 0.55 I_g$

2.3.3 Slender FRP-RC Columns

As the building deflects laterally, gravity loads acting on the building produce additional moments and forces in the structure. When these effects are considered in the structural analysis of the building, the analysis is referred to as "second-order analysis". If the second-order analysis uses nodes along compression members, the analysis accounts for slenderness effects due to lateral deformations along individual members, as well as sidesway of the overall structure. If the second-order analysis uses nodes at the member intersections only, the analysis

captures the sidesway effects for the overall structure but neglects individual member slenderness effects (ACI 318-19). In this case, individual member slenderness effects should be calculated and added to the analysis results. Again, applying a second-order analysis is a time-consuming process and is not preferred from designers in repetitive office work. Therefore, many codes and guidelines offer simpler approaches for the design of slender columns.

ACI 318-19 and CSA A23.3-14 permit considering a first‑order analysis results for design, while the impact of member slenderness (i.e., effect of lateral deformations of an individual member) and sidesway effects for the overall structure should be calculated and added to the analysis results. In the literature, two approaches have been considered to include slenderness effects in column design; applying a reduction factor to the load carrying capacity of a short column or the moment magnifying approach. The latter approach is recommended by the recent codes and guidelines for the design of steel-RC slender columns. In order to account for reflecting the degree of cracking, creep due to sustained loads, and inelastic actions that have occurred along each member, effective member stiffness should be used in such analysis. Limited attempts have been exerted to accommodate the moment magnifier approach addressed in ACI 318-19 and CSA A23.3-14 to the FRP-RC columns (Mirmiran et al. 2001; Jawahery Zadeh and Nanni 2017; Xue et al. 2018). A comprehensive review of the moment magnifier approach and the previous attempts conducted to propose an effective lateral flexural stiffness of steel- and FRP-RC slender columns, is presented in Chapter 7.

CHAPTER 3

Proposed Slenderness Limit for GFRP-RC Columns Based on Experiments and Buckling Analysis

Proposition de l'élancement limite pour les poteaux en béton armé de prfv basée sur des essais expérimentaux et l'analyse du flambement

Foreword

Authors and Affiliation:

- **Waseem Abdelazim** is a doctoral candidate in the Department of Civil Engineering at the University of Sherbrooke, Sherbrooke, QC, Canada, J1K 2R1.
- **Hamdy M. Mohamed** is a research associate and lecturer in the Department of Civil Engineering at the University of Sherbrooke, Sherbrooke, QC, Canada, J1K 2R1.
- **Mohammad Z. Afifi** is a postdoctoral fellow in the Department of Civil Engineering at the University of Sherbrooke, Sherbrooke, QC, Canada, J1K 2R1.
- **Brahim Benmokrane**, **FACI**, is a Professor in the Department of Civil Engineering, Université de Sherbrooke, Sherbrooke, Quebec, Canada, J1K 2R1

Journal Title and Paper Status:

Published in *ACI Structural Journal*, V. 117, No. 1, January 2020. *DOI: 10.14359/51718073*

Contribution to the Thesis:

The study presented in the manuscript aims to establish for the first time a rational slenderness limit for design of concrete columns reinforced with GFRP bars and spirals based on experimental and theoretical results. This research study developed an experimental and theoretical investigation of GFRP-reinforced concrete columns with slenderness ratios of 14, 17, 23, 26, and 33 under concentric axial loads with a focus on stability problems. An

estimation of the axial capacity of slender GFRP- reinforced concrete columns along with a new slenderness limit are proposed based on the experimental results and the buckling analysis, that could support the work of the North American technical committees engaged in developing standards and design provisions for GFRP- reinforced concrete columns.

Abstract

In order to develop design provisions for concrete columns reinforced with fiber-reinforced polymer (FRP) bar for North American codes and guidelines (ACI 440.1R; CSA S806), a slenderness limit below which it is acceptable to ignore the induced second-order effects must be determined. Nevertheless, limited attempts have been made to define a safe slenderness limit for such columns. Therefore, this study aimed at experimentally and analytically investigating the buckling behavior of 12 full-scale concrete columns reinforced with glass FRP (GFRP) with slenderness ratios of 14, 17, 23, 26, and 33 under concentric loading. The impact of longitudinal reinforcement ratios and confining levels on the performance of slender glass-fiber-reinforced-polymer-reinforced concrete (GFRP-RC) columns is, also, presented. Test results indicate that the GFRP reinforcement contributed significantly to resisting the applied compression loads and resulted in failure modes similar to that of the counterpart steel-reinforced-concrete columns at different slenderness ratios. In addition, a theoretical buckling analysis considering a total of 50 test specimens, assembled from the current study and the literature, was developed to verify the applicability of Euler–Johnson's stability envelope as well as the reduced and incremental modulus theories to FRP-RC columns. Good correlation was observed between the experimental results and the models developed analytically. Based on the experimental data and the developed buckling analysis, the safe limit of the slenderness ratio for FRP-RC columns bent in single curvature of 18 is proposed.

3.1 Introduction

Design Codes have not yet addressed stability and buckling issues related to slender concrete columns reinforced with fiber-reinforced polymer (FRP) bars owing to a lack of experimental data. Columns are defined as slender if they experience considerable reduction in the column

capacity due to the induced column buckling compared to the capacity of short or stocky columns that fail without undergoing any noticeable lateral deformations. The reduction in the buckling load of slender columns is closely related to the maximum column failure load and can be significant, particularly for materials with a relatively low elastic modulus (E). The design of slender columns requires that the deformed geometry of the structure be included in the equilibrium equations, that is, a second-order analysis. Second-order analysis is complicated and not practical for repetitive office design. Hence, MacGregor et al. (1970) stated that for steel-RC columns bent in a symmetrical single curvature, reduction in the column capacity due to second-order effects may be ignored if the column slenderness ratio $(\lambda = L_e / r)$ is less than 22, where L_e is the column effective buckling length and r is the radius of gyration of the column cross section. This slenderness limit corresponds to a 5% reduction in the column cross-section axial capacity. For such cases, the column could be safely designed as a short column satisfying the first-order analysis. ACI 318 and CSA A23.3 applied the latter definition along with an effective column lateral stiffness to set a slenderness limit λ, below which steel-RC columns may be treated as being short. Regarding FRP-RC columns, CSA S806-12 allows the use of FRP reinforcement in short columns and conservatively ignores the contribution of FRP bars in compression. Moreover, CSA S806-12 classifies GFRP-RC columns as short or long, relying on the ACI 318 slenderness limit for steel-RC columns, disregarding that FRP-reinforced concrete members might resist buckling instability differently than steel-reinforced ones.

Over the last two decades, valuable extensive experimental and analytical research have been conducted to establish the behavior of concrete columns internally reinforced with FRP bars considering a wide range of parameters such as column cross section (square or circular), reinforcement type (glass or carbon), reinforcing bars from different suppliers (different batch effect), longitudinal-reinforcement ratios, confinement levels and configurations (spirals or ties), concrete compressive strength (normal- or high-strength concrete), loading type (concentric or eccentric), and so on (De Luca et al. 2010; Tobbi et al. 2012; Pantalides et al. 2013; Afifi et al. 2014; Mohamed et al. 2014; Hadi et al. 2016; Youssef and Hadi 2017; Hadhood et al. 2017a, b, c, and d; Guérin et al. 2018; Sheikh and Kharal 2018; Hadhood et al. 2019). Most of the experimental programs found in literature were performed for short columns

and, therefore, the second-order effects due to buckling problems were excluded. In general, it was found that ignoring the FRP-bar contribution in compression underestimates the load-carrying capacity of short FRP-RC columns. The compression contribution of the GFRP bars to column axial capacity prior to concrete spalling was reported as an average value of 3.7% (De Luca et al. 2010), with 7.4% (Afifi et al. 2014), and 7.6% (Maranan et al. 2016) for reinforcement ratios of 1%, 2.2%, and 2.4%, respectively. Moreover, none of the FRP bars, spirals, or ties evidenced any compressive failure until the peak loads were reached. Two approaches were used to define the contribution of FRP bars to column compression capacity: (1) the compressive strength of the FRP bars was limited to 25% and 35% of tensile bar strength for CFRP and GFRP bars, respectively, or (2) applying limited FRP-bar compression strains (0.002 ~ 0.0035), considering equal elastic moduli for FRP bars in tension and compression.

Few studies have investigated the stability of slender FRP-RC compression members. Mirmiran et al. (2001a) developed an analytical model to study the behavior of slender FRP-RC columns. The model was verified with steel-RC columns from the literature. Mirmiran et al. (2001a) recommended reducing the slenderness limit of 22 for steel-RC columns to 17 for FRP-RC columns with a reinforcement ratio of 1%. Zadeh and Nanni (2017) applied a theoretical derivation for the slenderness limits of FRP-RC columns with a rectangular cross section. The contribution of FRP bars in compression was limited to the concrete compressive strength. The suggested slenderness limits were 14 and 19 for GFRP-RC and CFRP-RC columns bent in a single curvature, respectively. Maranan et al. (2016) tested eight circular GFRP-RC columns under concentric loading with two different slenderness ratios: $\lambda = 8$ (six columns) and $\lambda = 16$ (two columns). They found that the columns with $\lambda = 16$ failed at loads of 66% and 82% of the strength of their short-column counterparts with $\lambda = 8$. Hales et al. (2016) evaluated the behavior of slender $(\lambda = 49)$ high-strength-concrete columns (concrete compressive strength of 90 MPa) reinforced with GFRP bars under eccentric and concentric loading. The short and slender columns had various loading conditions, so that the reduction in loading capacity due to slenderness variations could not be observed. They concluded that the failure mode for low-eccentricity $(e = 0.08D)$ slender columns was a material-type failure, consisting of compressive failure of the concrete, tensile rupture of the GFRP spirals, and compressive rupture of the longitudinal GFRP bars. Recently, Xue et al. (2018) conducted concentric and eccentric loading tests on slender (λ varied from 20.8 to 41.6) rectangular

GFRP-RC columns. They concluded that all tested columns exhibited concrete-crushing failure with no rupture of the FRP bars. the experimental research on slender FRP-RC columns is very limited, which accentuates the need for more experimental studies that investigate the performance of slender FRP-RC columns. Therefore, this paper aimed at experimentally and analytically assessing the general behavior of slender GFRP-reinforced concrete columns with slenderness ratios ranging from $\lambda = 14$ to $\lambda = 33$ under concentric loading. Moreover, buckling-load analyses was conducted to predict the axial capacity of FRP-RC columns considering second-order effects.

3.2 Research Significance

North American technical committees are currently deploying enormous efforts to include sections dealing with the design of FRP-RC columns in the upcoming editions of FRP design codes. This requires an explicit definition of the slenderness limits for such columns with a better knowledge of their performance before and after failure occurs. This study, therefore, developed an experimental and theoretical investigation of GFRP-RC columns with slenderness ratios of 14, 17, 23, 26, and 33 under concentric axial loads with a focus on stability problems. An estimation of the axial capacity of slender FRP-RC columns along with a new slenderness limit are also proposed based on the experimental results and the buckling analysis. The design recommendations herein could support the work of the North American technical committees engaged in developing standards and design provisions for GFRP-RC columns.

3.3 Experimental Program

This section summarizes the characteristics of the materials used, investigated test parameters, specimen organization and classification, instrumentation, preparation, and casting. A description of the test setup, including the definition of the boundary conditions and applied loading rates, is presented.

3.3.1 Test Parameters and Column Design

A total of 12 full-scale circular concrete columns (10 with GFRP reinforcement and 2 with steel reinforcement as reference specimens) were prepared and tested under monotonic static concentrically axial loading. All of the columns were 305 mm (12 in.) in diameter. The experimental program investigated the behavior of slender GFRP-RC columns with the slenderness ratio and the longitudinal- and transverse-reinforcement ratios as test parameters. Herein, the slenderness ratio, $\lambda = kL / r$, is expressed in terms of the unsupported length of the column (L); the effective length factor, k; and the radius of gyration of its cross section, $r = \sqrt{I_g / A_g}$, where I_g and A_g are the gross second moment of inertia and the gross cross-sectional area of the column, respectively. The test setup was designed to achieve an effective length factor k equal to unity, as explained below. Five different heights were selected to cover a wide range of column slenderness ratios. One column each had heights of 1000 mm (39.4 in.) $(\lambda = 14)$ and 1250 mm (49.25 in.) $(\lambda = 17)$ to give an indication of the behavior of short columns and to verify the proposed slenderness limits of GFRP-RC columns found in the literature (Mirmiran et al. 2001a; Zadeh and Nanni 2017). Four columns were 1750 mm (68.95 in.) in height $(\lambda = 23)$, approximately the threshold of the slenderness limits recommended in ACI 318-14 and CSA A23.3-14 for steel-reinforced concrete columns. One column was 2000 mm (78.8 in.) in height $(\lambda = 26)$ and five 2500 mm (98.5 in.) in height $(\lambda = 33)$ to represent the zone of slender columns.

Two main design parameters determine the design of longitudinal reinforcement: the total number of bars and bar diameter. If the number of longitudinal bars in any circular column is less than eight, bar orientation may significantly affect the bending strength of the loaded column and should be considered in the column analysis (ACI 318-14). Although all test specimens are loaded concentrically, there are second-order bending moments due to the expected lateral buckling. Hence, and to eliminate the test complexity, a minimum of eight equally spaced bars were used for each column. On the other hand, CSA S806-12 stipulates that the minimum bar diameter for longitudinal FRP bars shall not be less than 15 mm (0.59 in.). Therefore, consistent with code recommendations and to mirror practical applications,

three configurations of longitudinal reinforcement were used: 8 No. 5, 12 No. 5, and 12 No. 6 bars (2.19%, 3.28%, and 4.66%, respectively).

All GFRP spirals were designed according to CSA S806-12 to provide thorough confinement so as to avoid buckling of the GFRP longitudinal bars. All columns were reinforced in the transverse direction with No. 3 continuous spirals without any lapped splices. The significance of the spiral volumetric ratio, ρ_T , was quantified in terms of the spiral pitch distance. Two columns were fabricated with 40 mm (1.58 in.) center-to-center spacing along the whole height. Each of the remaining 10 columns was divided into two regions: a middle region with a spiral pitch of 80 mm (3.15 in.), and top- and bottom-end regions 250 mm (9.85 in.) in length each with a tighter spiral pitch of 50 mm (1.97 in.) to prevent any premature failure near the zones of stress concentration, as shown in Fig. 3.1. The 12 specimens were divided into four groups as indicated in Table 3.1. Group 1 consists of two steel-reinforced concrete columns as reference specimens, while Groups 2, 3, and 4 were designed to reflect the impact of slenderness ratio as well as longitudinal- and transverse-reinforcement ratios, respectively, on the performance of GFRP-RC columns.

3.3.2 Materials and Specimen Production

All reinforcing cages were assembled and fabricated in the laboratory of materials and structures of the University of Sherbrooke (Sherbrooke, Quebec, Canada). The GFRP bars and spirals used were sand coated and manufactured by a pultrusion process using continuous glass fibers impregnated in a thermosetting vinyl-ester resin (see Fig. 3.1). Two sizes of GFRP bars with an average fiber content of 83.8% were used as longitudinal reinforcement (No. 5 and No. 6), while all the GFRP-RC columns were transversally reinforced with No. 3 GFRP spirals. Normal-strength deformed steel bars (M15) and spirals (M10) were used, respectively, to reinforce the two reference columns in both the longitudinal and transverse directions. The average ultimate longitudinal tensile properties of the GFRP materials were provided by the manufacturer and were determined according to CSA S806-12 (Annex C), as reported in Table 3.2. The bars and spirals were tightly connected with cable ties to avoid self-twisting and to ensure cage verticality.

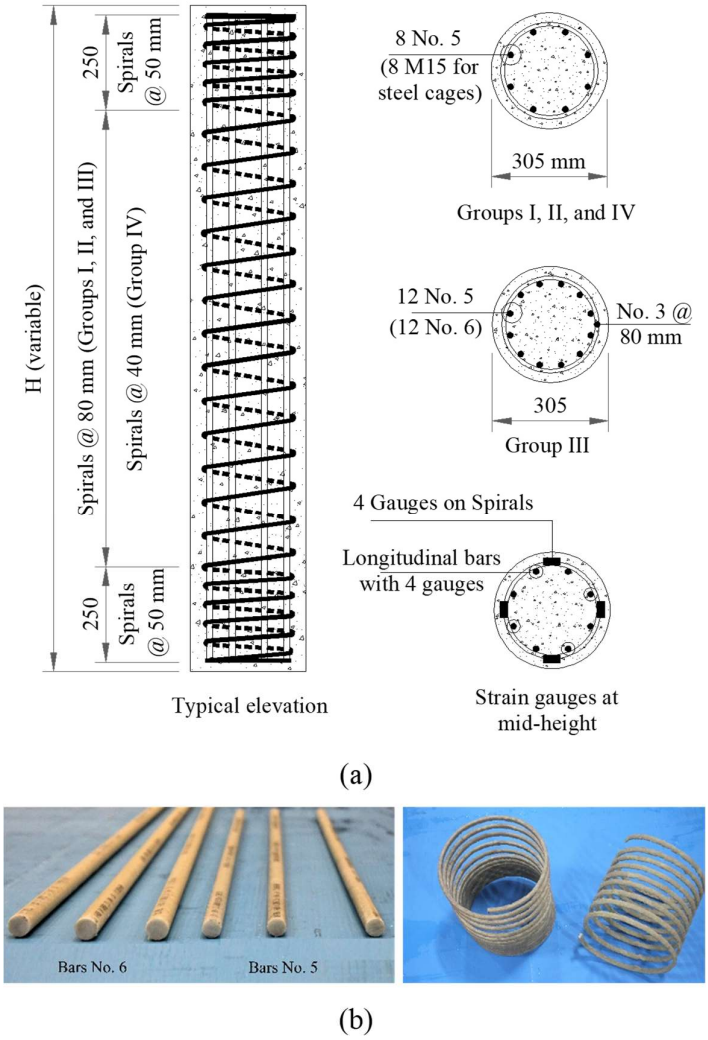

Figure 3.1– (a) Typical layout, reinforcement details, and internal instrumentation; (b) samples of the GFRP bars and spirals. (Note: Dimensions in mm; 1 mm = 0.0394 in.)

A single batch of ready-mixed normal-strength, normal-weight concrete with a maximum aggregate size of 10 mm (0.394 in.) was used to cast all the columns in an upright position. In compliance with ASTM C39, the average concrete compressive strength was determined based on testing nine 100 mm x 200 mm (3.94 in. x 7.88 in.) standard concrete cylinders cured under the same conditions as the column specimens. Concrete cylinders were tested on the same day as the start of testing of the column specimens (153 days after concrete casting). The measured average concrete compressive strength used in the analysis was 46.6 MPa (6764 psi); the target 28-day compressive strength of the concrete was 40 MPa (5800 psi).

Table 3.1 – Test matrix, specimens' details, and test results

Group	Specimen ID	Geometry*		Longitudinal Reinforcement		Transverse Reinforcement			P_{peak} (*kN*)	P_{peak} / $f'_c A_g$
		L (mm)	λ	ρ_L (%)	Number of bars	ρ_T (%)	Bar size	Pitch *(mm)*		
I	S-23	1750	23	2.19	8 M 15	0.93	M 10	80	3,866	1.13
	S-33	2500	33						3,627	1.06
II	G1-14	1000	14	2.19	8 No. 5	1.17	No. 3	80	3,535	1.04
	G2-17	1250	17						3,490	1.02
	G3-23	1750	23						3,453	1.01
	G4-26	2000	26						3,359	0.99
	G5-33	2500	33						3,331	0.98
III	G6-23	1750	23	3.28	12 No. 5	1.17	No. 3	80	3,463	1.02
	G7-33	2500	33	3.28	12 No. 5				3,360	0.99
	G8-33	2500	33	4.66	12 No. 6				3,588	1.05
IV	G9-23	1750	23	2.19	8 No. 5	2.34	No. 3	40	3,417	1.00
	G10-33	2500	33						3,460	1.02

* All columns are 305 mm in diameter.
Notes: 1 mm = 0.0394 in.; 1 kN = 0.225 kpi

Table 3.2 – Mechanical and physical properties of the GFRP and steel reinforcement

Bar Size	Diameter (mm)	Area [1] (mm^2)	Fiber Content [2] (%)	Elastic Tensile Modulus [3] (GPa)	Nominal Tensile Strength [4] (MPa)	Tensile Strain (%)
GFRP reinforcement						
# 3	9.5	71	78.9	51.1	1281	2.51
# 5	15.9	200	83.6	61.8	1449	2.35
# 6	19	284	84	61.7	1411	2.29
Steel reinforcement						
M10	9.5	71	-	200	400	0.2
M15	15.9	200	-	200	400	0.2

[1] Nominal area.
[2] According to the test method described in ASTM D2584 (temp 650°C, sand coating discarded from results).
[3] Average ultimate longitudinal tensile properties as provided by the manufacturer; test method CSA S806 Annex C.
[4] Yield stress of steel bars.
Notes: 1 mm = 0.0394 in.; 1 MPa = 145.04 psi; 1 GPa = 145.04 ksi.

3.3.3 Instrumentation

All of the specimens were instrumented to measure the axial and lateral deformations as well as the local strains in the longitudinal bars, spirals, and concrete surface. All of the strain gauges were located at the mid-height of the columns, where the maximum strain values are expected. Strain gauges on concrete face, bars, and spirals were installed on the outermost locations on opposite sides defining the expected concave and convex faces of the columns as they deform. Readings of concrete strain gauges after concrete-cover spalling cannot be relied upon. Therefore, two linear potentiometers (LPOTs) were mounted vertically on two steel rods (300 mm or 11.82 in. apart) at the concrete strain-gauge locations and embedded in the columns before casting the concrete to monitor the strains after spalling of the concrete cover. The column's horizontal deflection was gauged with three LPOTs mounted horizontally at column mid- and quarter-heights.

3.3.4 Test Setup and Loading Protocol

Prior to testing, both ends of each column were capped with a thin self-leveling layer of high-strength cementitious grout to achieve uniform distribution of the applied loads. Two identical rigid steel collars were designed to confine the top and bottom zones of the tested specimens to prevent any premature local failure. The test specimen was then placed in the testing machine and column verticality verified with a laser level. Then, the axial load was applied with a knife-edge pattern using a rounded steel bar attached to the center of the top rigid plate welded to the steel collars. These rounded steel top and bottom bars replicate the case of a perfect pin-ended column, $k = 1$ (see Fig. 3.2). The column specimens were tested with an 11400 kN (2565 kip) MTS testing machine. All columns were loaded up-to a level of 75% of the estimated capacity under loading control at a constantly increasing rate of 2.5 kN/s (562.5 lb/s). Testing continued under displacement control at a displacement rate of 0.002 mm/s (7.87×10^{-5} in./s) until the specimens could not withstand any additional increase in the applied axial force or the longitudinal GFRP bars ruptured. Strain gauges and LPOTs were connected to an automatic data-acquisition system to record all measured strains and deflections during testing, respectively. The axial applied load and the machine-head axial displacement were measured with the machine's internal sensitive load cell and LVDTs, respectively.

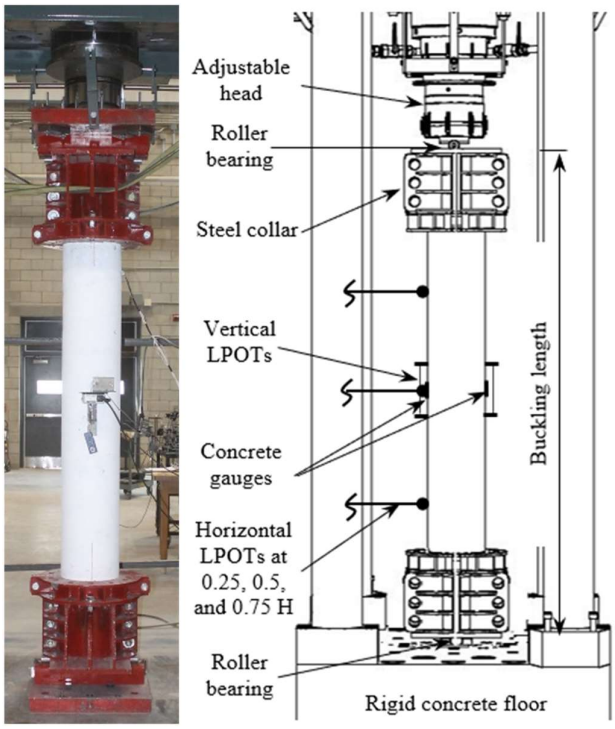

Figure 3.2– Test setup.

3.4 Test Observations and Analysis of Results

3.4.1 Axial Capacity and Failure Modes

The failure modes of all the columns could be broken down into two main stages. Stage one is represented by concrete rupture initiated by gradual cover spalling accompanied with a significant reduction in the load-carrying capacity of the tested column. Prior to cover spalling, vertical cracks started to initiate at an average load level of approximately 90% of the achieved maximum load. These cracks rapidly widened and propagated, causing the concrete cover to spall off the concrete core. At this stage, the GFRP bars were contributing to the axial capacity. In general, the slender GFRP-RC columns with the same reinforcement ratio lost more load-carrying capacity after the initial spalling of the concrete cover. For example, GFRP-RC columns G1-14 (considered a short column) and G5-33 (considered a long column) lost around 20% and 40%, respectively, of their maximum bearing capacity after the concrete cover had

completely spalled off. This could be because the stress distribution over the column cross section was not perfectly uniform on all sides. In such cases, the cover spalling often occurred on one side, resulting in load eccentricity. This eccentricity suddenly increased the column's lateral deformation, which, in turn, increased the second-order moment at the column mid-height for the slender columns. These additional moments require a corresponding decrease in the axial load to maintain the same level of resultant stresses. As the lateral deformation (additional second-order moments) was higher for the slender columns than the short ones, the relative axial-load drop after peak was more pronounced in the slender columns.

The second failure stage of the column corresponds to the rupture of the core components (transversal spirals, longitudinal bars, and concrete core). In addition to separation of the concrete cover, the concrete core started to dilate, causing a passive confining pressure of the spirals. The recorded tensile strains of the GFRP spirals at the peak loads ranged from 700 to 1,600 $\mu\varepsilon$ (3% to 6.4% of the ultimate spiral tensile strains). After the peak load, the GFRP spirals confined the concrete core of the column to recover the load drop due to the concrete cover spalling and to enhance the column's ability to experience higher lateral deformations. The test results indicated that all the tested columns experienced no second-peak load. On the other hand, depending on the type of internal reinforcement (GFRP or steel), stage two was dominated by either a tensile rupture of the GFRP spirals with or without a compressive rupture of GFRP longitudinal bars or buckling of the steel bars. Finally, it was observed that the well-confined columns with tight spiral spacing (G9-23 and G10-33) or narrow bar spacing (G8-33) did not exhibit any crushing of the concrete-core components until testing ended (the test was halted for safety precautions). Figure 3.3 shows the predominant material failure modes of the steel- and GFRP-reinforced columns, as outlined above.

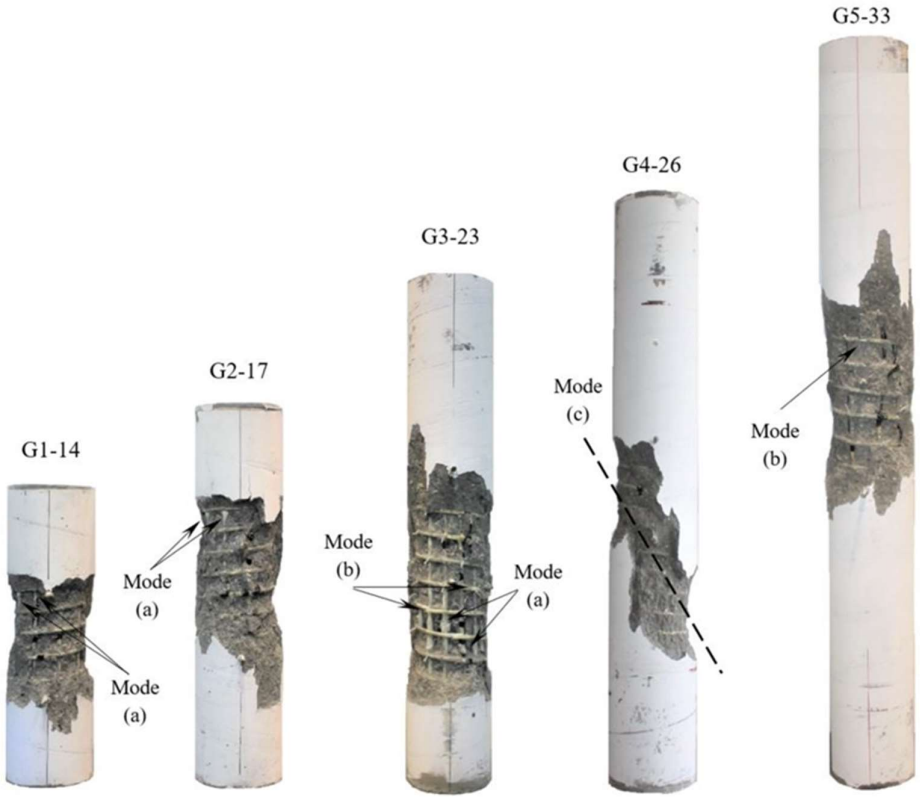

Figure 3.3– Typical failure modes: (a) Compressive rupture of GFRP bars; (b) tensile rupture of GFRP spirals; and (c) failure shear plan..

Figure 3.4 depicts the axial stress–axial strain relationship of the tested columns. The vertical axis displays the cross-sectional axial stresses calculated considering the column gross and core cross-section areas for pre- and beyond peak zones, respectively. As expected, the elastic stress–strain diagram was linear during the initial loading state and up-to around 85% of the maximum peak load. Furthermore, all measured concrete strains at the peak loads exceeded the theoretical values of ε_o, where ε_o is the concrete strain corresponding to the maximum concrete compressive strength and ranges from 1,900 to 2,500 $\mu\varepsilon$ for normal-strength concrete (Popovics 1973). Overall, the effect of column slenderness on the concrete strains at peak was very limited and not observed. The GFRP-reinforced columns in Group No. 2 recorded an average concrete strain at peak load approximately equal to 3,200 $\mu\varepsilon$ (~1.45 ε_o). Regardless of the specimen's slenderness ratio, the GFRP-RC columns averaged 6% lower strain levels than the control specimens (steel-reinforced columns).

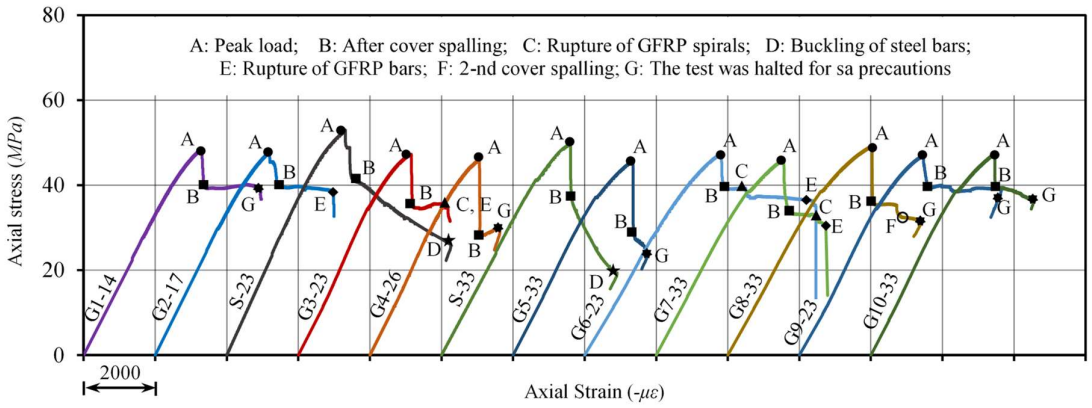

Figure 3.4– Axial stress-axial strain response (Note: 1 MPa = 145.04 psi).

As for the internal reinforcement, strain compatibility between GFRP longitudinal reinforcement and the surrounding concrete was experimentally proven during testing. At the maximum compressive stresses (peak load), the measured bar and concrete strains were alike, so no slippage occurred. This reflects the compression contribution of the FRP bars to the ultimate bearing capacity of the tested columns. The average recorded compressive bar strain at the maximum load-bearing capacity was 3,240 $\mu\varepsilon$ (14% of the ultimate tensile GFRP-bar strain). The compression contribution of the GFRP bars was around 11% of the column ultimate bearing capacity. Herein, bar contribution to the compressive capacity of the GFRP-RC columns was calculated deeming an average strain values measured on four GFRP longitudinal bars at mid-height. This, in general, was 50% of the contribution of the steel bars to the columns. In general, FRP reinforcing bars did not exhibit any compression failure up-to peak load.

Both the steel- and GFRP-reinforced columns experienced similar behavior until the peak load was reached. Table 3.1 summarizes the experimental ultimate axial bearing capacity of all tested columns. Columns S-23 and S-33 respectively reached axial compression loads of 3,866 kN (869 kips) and 3,627 kN (815 kips), which are, on average, 9.5% higher than their counterpart columns G3-23 and G5-33. Column G1-14 sustained a maximum compressive load of 3,535 kN (795 kips) which is 1.3%, 2.3%, 5.2%, and 5.8% higher than columns G2-17, G3-23, G4-26, and G5-33, respectively. In general, based on the gross cross-sectional area of the columns, at peak load level, all steel- and GFRP-RC columns reached experimental concrete compressive-failure stresses close to the average compressive strength of the standard concrete

cylinders tested: $(f_c')_{column} \cong 0.98 \sim 1.13(f_c')_{cylinder}$. The column-to-cylinder compressive-strength ratio (0.98 ~ 1.13) exceeds 0.85, which is commonly used in theoretical predictions of cross-section nominal axial strength at zero eccentricity. This obviously reflects the significant contribution of GFRP reinforcement to the ultimate compressive strength of the tested columns. To sum up, the slender GFRP-RC columns under concentric loads experienced a material-type failure similar to that of the short ones with insignificant effect on column stability up-to ultimate load. The material-failure mode consisted of compressive failure of the concrete, tensile rupture of the GFRP spirals, compressive rupture of the longitudinal GFRP bars, and compressive buckling of the longitudinal steel bars. In addition, using GFRP bars as internal reinforcement in short and slender RC columns significantly contributed to the column bearing capacity

3.4.2 Second-Order Response

Perfectly axially-loaded columns that have no initial imperfections with zero-eccentricity loading tend to deflect laterally under a specific load levels called instability buckling loads. Instability buckling could be defined as the deviation of the perfect column's centerline from the loading line. The induced second-order deformations or load-delta $(P-\delta)$ effects create additional nonlinear second-order moments reaching their maximum values at the mid-height of the loaded column. The additional moments, in turn, produce additional stresses on the column cross section, which inevitably reduces the column's compressive strength.

Experimentally, $P-\delta$ effects could be observed in terms of the lateral displacement response of the column to the peak and post-peak loads (Fig. 3.5-a). During the test, the steel-reinforced control specimens had load–lateral-displacement responses similar to that of the corresponding GFRP-RC columns until peak load was reached. After that, the steel-reinforced columns exhibited higher ductility (in terms of lateral-deformation capacity). Overall, none of the columns experienced any instability deformations near to 75% of the ultimate capacity $P_{\max}$. After that limit, and since the stress distribution was not perfectly uniform due to initial imperfections or unsymmetrical initiation of internal cracks, the irregular stress distribution over the column cross section induced column buckling. Once buckling started, column

slenderness controlled the maximum lateral buckling response to peak and post-peak loads. All columns buckled into a single-curvature deformed shape with concave and convex faces. At the start of buckling at 75% of P_{max}, the compressive strains on the concave (loading) face of the columns further increased, and the compressive strains on the convex (unloading) face decreased within a value of $\Delta\varepsilon$ (Fig. 3.5-b). The loading and unloading responses of the buckled columns are comprehensively discussed below in the theoretical-analysis sections.

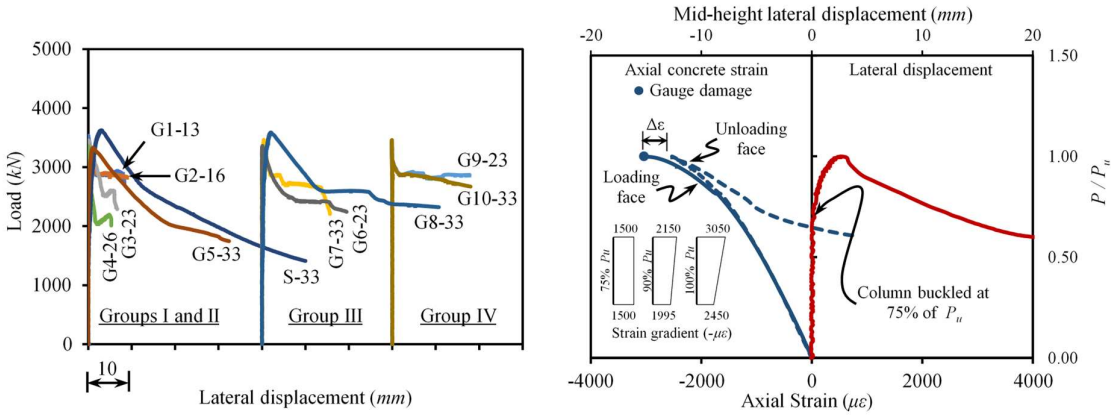

Figure 3.5– −(a) Mid-height lateral displacement; (b) Axial strain gradient at loading and unloading faces and mid-height lateral displacement of specimen G5-33. (Note: 1 mm = 0.0394 in.; 1 kN = 0.225 kpi).

The maximum mid-height lateral displacement at peak (δ) or the induced load eccentricity due to the column instability was measured for all tested columns. Columns G5-33 and S-33 recorded the most visually noticed lateral displacements at peak with an average approximate value of 3 mm (0.118 in.) ($\delta/D = 0.01$; where D is the column diameter in mm). Regardless of column slenderness, ACI 318-14 requires a minimum eccentricity $(e_{\min-ACI})$ equal to $15+0.03D$ for the analysis of concentrically loaded columns. Using the column geometry yields $e_{\min-ACI}/D=0.08$, which is eight times more than the maximum measured lateral displacement at $\lambda = 33$. After peak and until the end of the test, the GFRP-RC columns with higher reinforcement ratios (Group 3) or tighter spirals (Group 4) evidenced greater buckling resistance than the GFRP-RC columns in Group 1. Once the applied loads had been removed

at the end of testing, all the GFRP-RC columns returned to a shape similar to that prior to loading state. This confirms the fact that FRP exhibits linear elastic behavior up-to failure.

Degradation of the peak load could also be used as an index for the impact of additional second-order induced stresses on column-bearing capacity. Both the steel- and GFRP-reinforced columns exhibited gradual degradation of the maximum concentric loads as slenderness increased. For example, the ultimate capacity of specimens G2-17, G3-23, G4-26, and G5-33 was 1.3%, 2.3%, 5.2%, and 5.8%, respectively, lower than that of specimen G1-14. A similar decrease was observed in the ultimate capacity of the steel-reinforced specimen S-33 with respect to specimen S-23. This confirms an inverse relationship between the ultimate strength of the GFRP-RC columns and column slenderness. In the case of concentrically loaded GFRP-RC columns, however, the effect of slenderness on column axial-bearing capacity could be experimentally concluded as limited and not significant over the studied range of slenderness ratios ranges from $\lambda = 14$ to $\lambda = 23$.

3.4.3 Effect of Test Parameters

Reinforcement Type — The GFRP- and steel-reinforced columns were designed with the same reinforcement ratios $\left(A_s = A_{FRP}\right)$ with eight No. 5 longitudinal bars, where A_{FRP} and A_s are the areas of the GFRP and steel longitudinal reinforcement, respectively. The GFRP-RC columns achieved a loading capacity of 89% at $\lambda = 23$ and 92% at $\lambda = 33$, compared to the corresponding reference columns reinforced with steel. Moreover, the GFRP bars developed higher average compressive strains at peak, where the average recorded compressive strains of GFRP and steel bars were, respectively, $\varepsilon_f = 3,200\mu\varepsilon$ (13.6% of the ultimate tensile strain of the GFRP bars; see Table 3.2) and $\varepsilon_s = 2,350\mu\varepsilon$, $\left(\varepsilon_s = \varepsilon_{yield}\right)$. This could be explained by the GFRP bars having a lower modulus of elasticity, around one-third that of the steel bars $\left(E_f = 61 \text{ GPa } (8,845 \text{ ksi}) \text{ and } E_s = 200 \text{ GPa } (29,000 \text{ ksi})\right)$. Reinforcement type had an insignificant effect on the column failure mechanism. The failure of the GFRP-RC and steel-reinforced columns were governed by the compressive failure of the concrete. As loading continued, the GFRP bars ruptured and steel bars buckled. The conclusion can be drawn that

the GFRP reinforcement significantly contributed to the resistance of applied loads and failed similarly to the tested steel-reinforced columns at different slenderness ratios.

Longitudinal-Reinforcement Ratio **—** This study investigated the effect of three reinforcement ratios: low (2.19%), moderate (3.28%), and high (4.66%). Figure 3.6 shows the applied axial load versus the bar-strain gradient measured at mid-height of the tested specimens. All the GFRP and steel longitudinal bars exhibited similar axial stiffness with a linear stress–strain distribution up-to around 80% of the peak. Afterwards, the performance became plastic up-to and after the peak. The expression "plastic", herein, describes the overall behavior of the column and is not limited to the longitudinal bars. Any GFRP-bar failure occurred in a brittle explosive manner. The difference between the lower and higher reinforcement ratios was that the bars with the low reinforcement ratio failed after reaching or near the peak, while the bars in the specimens with higher reinforcement ratios produced a longer descending loading branch. The GFRP reinforcing bars in the slender well-confined specimens (G8-33, G9-33, and G10-33) did not exhibit any failure up-to a compressive bar strain of 11,060, 12,980, and 10,700 $\mu\varepsilon$, respectively (48.3%, 55.2%, and 45.7% of the ultimate tensile strain). Strain gauges attached to GFRP bars in specimens G1-13 and G2-16 recorded compressive-strain failures of 13,660 $\mu\varepsilon$ and 15,350 $\mu\varepsilon$, representing 58.1% and 65.3% of the ultimate tensile strain, respectively. These values of strain readings imply that GFRP bars efficiently resist applied compressive loads if used as internal reinforcement in short or long columns. On the other hand, the impact of reinforcement ratio on the ultimate bearing capacity was more pronounced for slender columns with relatively high reinforcement ratios. Indeed, increasing the reinforcement ratio of specimens G3-23 and G5-33 from 2.2% to 3.3% (G6-23 and G7-33) increased specimen strength by less than 1%. In contrast, increasing the reinforcement ratio of specimen G5-33 from 2.2% to 4.7% (G8-33) enhanced the column axial capacity by 7.7%. Clearly, the carrying capacity of GFRP-RC columns is enhanced by increasing the GFRP-reinforcement ratio.

Spiral Volumetric Ratio **—** The confinement effect was discussed above in terms of pitch distance of GFRP spirals. All the GFRP spiral pitches were designed according to CSA S806-12 to provide sufficient confinement and to prevent premature buckling of the GFRP longitudinal bars between any two consecutive turns. In other words, this study looked at the behavior of two well-confined GFRP-RC columns with different transverse-reinforcement ratios. No. 3 GFRP spirals with two various center-to-center spacings were tested: 80 mm (3.15

in.) and 40 mm (1.58 in.). In general, confinement had a limited effect during the ascending part of loading and could be described as insignificant (verified with more than one index).

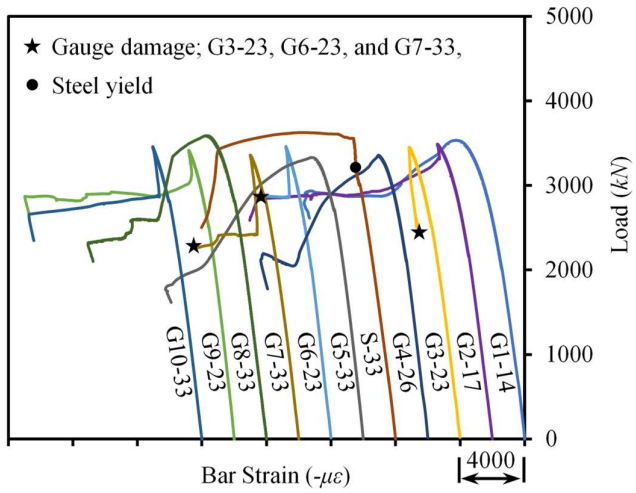

Figure 3.6– Loads versus longitudinal-bar strain curves. (Note: 1 kN = 0.225 kpi).

First, the average measured tensile strains at peak were 1,400 $\mu\varepsilon$ (5.6% ε_{su}) and 850 $\mu\varepsilon$ (3.4% ε_{su}) for light and dense spiral-reinforcement ratios, respectively, (where ε_{su} is the ultimate tensile strain of the GFRP spirals). Second, around 50% of the abovementioned spiral strains at peak were achieved after 90% of the maximum loading capacity had been reached, which made the spirals less effective along most of the pre-peak loading path. In addition, the gain in peak-load capacity as a result of doubling the spiral volumetric ratio ranged from 0% to less than 4% for the columns with $\lambda = 23$ and λ=33, respectively. In the post-peak branch of the well-confined columns (G9-23 and G10-33), the ultimate-to-peak concrete axial strains were higher than in the less-confined columns (G3-23 and G5-33). Furthermore, the closer spiral spacing laterally constrained the concrete core and delayed any crack propagation until the end of the test. Lastly, it is important to highlight that using a spiral spacing of 40 mm render the column failure in more ductile manner than those reinforced with larger spacing spirals. These dense spirals comply with the limitations of CSA S806-12 for the design of FRP spirals as it states that the pitch or distance between two successive turns of the spirals shall not exceed 1/6 of the core diameter (42.5 mm in our case).

3.5 Slenderness-Limit Analysis for FRP-RC Columns

Stability or strength curves are a convenient way to define the reduction in the ultimate capacity of slender RC columns in terms of unit load (or unit stress) and slenderness ratio. In addition, column-strength curves can be used to define the safe slenderness limit of compression members (Mirmiran et al. 2001b; Mohamed et al. 2010). A slenderness limit for short columns is defined as a 5% reduction in the maximum column capacity based on cross-section analysis. This condition complies with the provisions in ACI 318-14 and CSA A23.14 for the slenderness limit of steel-reinforced-concrete columns, which was primarily developed by MacGregor et al. (1970). Therefore, this study used Euler's and Johnson's formulas to produce normalized column-strength curves for FRP-RC columns over a wide range of slenderness ratios to locate the slenderness limit at which the column capacity was reduced by 5% due to second-order effects. The results of the analytical model developed were compared to the test results for 50 specimens in the current study and from the literature with different types of internal reinforcement (GFRP and CFRP), cross section (rectangular and circular), concrete compressive strength (ranging from 32 to 50 MPa (4,640 to 7,250 psi)), and slenderness ratios (from 6 to 42).

3.5.1 Euler–Johnson's Failure Envelope

The proposed column-stability curve is composed of two zones based on a column's tendency to buckle under compression. The first zone considers the FRP-RC columns with low to intermediate slenderness ratios and governed by Johnson's formula (Eq. 3.1), which gives admissible values under low levels of slenderness-ratio conditions. The other zone follows Euler's formula (Eq. 3.2), which is valid for cross-section stresses that do not exceed the proportionality limit of the column stress–strain diagram, which could be attributed to high slenderness ratios

$$P_J = P_o - \frac{L_e^2}{(EI)_{eff.}}\left(\frac{P_o}{2\pi}\right)^2 \tag{3.1}$$

$$P_E = \frac{\pi^2}{L_e^2}(EI)_{eff.} \tag{3.2}$$

$$P_o = 0.85 f_c' A_g \tag{3.3}$$

where P_o is the cross-sectional strength based on plane analysis; $L_e = kL$ is the effective column length; L is the column height; k is the effective length factor taken as 1.0 and 0.5 for pin-ended and fixed-fixed columns, respectively; $(EI)_{eff.}$ is the effective flexural stiffness of FRP-RC columns; and P_o is the cross-sectional capacity of FRP-RC columns (Eq. 3.3).

Further development of the Euler–Johnson failure envelope requires that two major parameters be defined: (1) the effective lateral stiffness, which reasonably reflects the variation in column stiffness due to cracking and inelastic characteristics of the concrete columns; and (2) the cross-sectional strength of the FRP-RC columns. Table 3.3 compares the proposed effective flexural stiffnesses found in literature to the ACI 318-14 equations. Equation (b) in Table 3.3 was derived for small eccentricity ratios and high levels of axial loads, while Eq. (a) is a simplified approximation of Eq. (b) and less accurate (see ACI 318-14 commentary). Based on a theoretical parametric study, Mirmiran et al. (2001a) modified Eq. (a) for ACI effective flexural stiffness and retained Eq. (b) without any modifications in the proposed flexural-stiffness equations for FRP-RC columns. Zadeh and Nanni (2017) reduced the contribution of the FRP reinforcement to the effective flexural stiffness of FRP-RC columns. The second parameter required for establishing the Euler–Johnson's curve is to define the ultimate cross-sectional capacity of the FRP-RC column. Based on a comprehensive experimental and analytical study presented below, it is assumed replacing the compressive FRP bars with concrete in the cross-sectional analysis of the FRP-RC column (Eq. 3.3). This also complies with the recommendations of Zadeh and Nanni (2017); Hadhood et al. (2017a and b).

Figure 3.7 shows the strength curves for the GFRP-RC columns considering two values of longitudinal-reinforcement ratios (ρ_L): 1% and 8% of the gross area of the section as per CSA S806-12 provisions for the lower and upper limits of longitudinal-reinforcement ratios of FRP-RC columns, respectively. The strength of slender columns on the vertical axis has been normalized to the ultimate capacity of the column deeming gross cross-section analysis of the short columns. In general, the proposed strength curves demonstrate conservative values of the

column's ultimate capacity against the test results over the selected range of slenderness ratios. The limit of applicability of Euler's and Johnson's formula to plot the failure curve is defined in Fig. 3.7 as the tangent point at $\lambda = 60$ for the lower limit of ρ_L and $\lambda = 70$ and $\lambda = 75$ for the upper limit of ρ_L with respect to the lateral stiffness provisions given by Zadeh and Nanni (2017) and Mirmiran et al. (2001a), respectively. The effective flexural stiffness provided by ACI 318-14 Eq. (b) for steel-reinforced-concrete columns can be used for FRP-RC columns with all ranges of ρ_L up-to a slenderness ratio of less than 40. As expected, at lower limits of λ , the longitudinal reinforcement has a limited effect on column strength.

Table 3.3 – Proposed effective flexural stiffness from literature[1]

Steel-reinforced columns (ACI 318-14)		FRP-reinforced columns	
		Mirmiran et al. (2001a)	Zadeh and Nanni (2017)
a)	$0.4E_cI_g$	$0.25E_cI_g$ for (e/D ≤ 0.4)	$0.23E_cI_g\,(GFRP)$ $0.29E_cI_g\,(CFRP)$
b)	$0.2E_cI_g + E_sI_s$	Retained as ACI	$0.2E_cI_g + 0.75E_fI_f$

[1] Effect of sustained loads is omitted from all equations.
Subscripts c, s, f, and g stand for concrete, steel, FRP, and gross cross section, respectively. E and I are the modulus of elasticity and the moment of inertia about the centroidal axis, respectively.

ACI 318-14 defines slenderness limit as the slenderness ratio at which the column capacity is reduced by 5% due to second-order effects according to MacGregor et al. (1970). Herein, ACI philosophy was respected to provide the slenderness limit of FRP-RC columns. Therefore, Figure 3.7 is plotted to define the reduction in the column axial capacity at different slenderness ratios. Then, a horizontal line was drawn at 95% of the column cross-section capacity. This line defines the 5% acceptable reduction as per ACI limits. The intersection between the strength curve (at a reinforcement ratio 1%) and the horizontal dashed line locates the corresponding slenderness limits for FRP-RC columns at $\lambda = 18.5$ and $\lambda = 22.4$ for reinforcement ratios of 1% and 8%, respectively. This way to define slenderness limits has been previously adopted by Mirmiran et al. (2001b). Note that the axially loaded test specimens showed a 5% reduction in axial strength at $\lambda \cong 23$ for a reinforcement ratio of 2.19%. Consequently, a value of 18 is proposed as the reasonable conservative limit for the slenderness

ratio of FRP-RC columns bent in a single curvature. The proposed slenderness limit can be reformulated in a form similar to that of the limit set in ACI 318-14 as:

$$\frac{kl_u}{r} \le 30 + 12\left(M_1/M_2\right) \le 36 \tag{3.4}$$

where M_1 is the smaller end moment; and M_2 is the larger end moment; M_1 and M_2 are factored end moments obtained by an elastic frame analysis, and M_1/M_2 is negative if the column is bent in a single curvature and positive if bent in a double curvature.

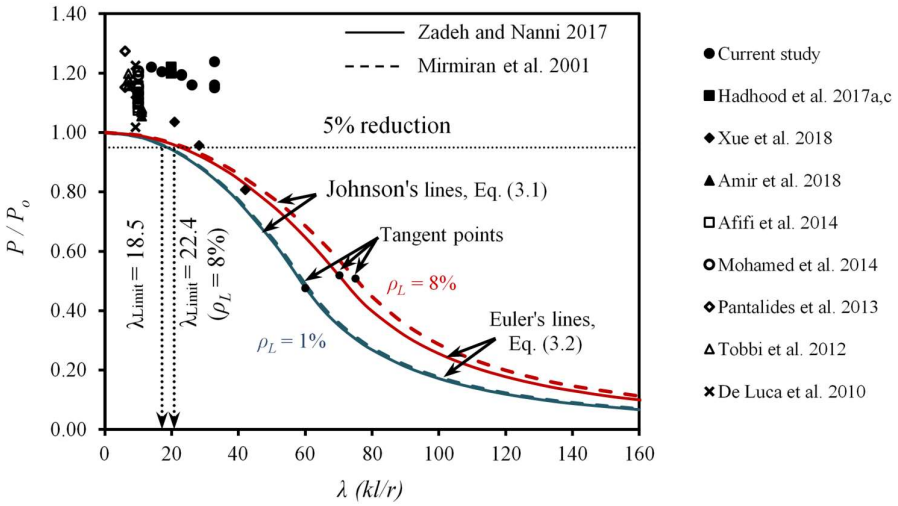

Figure 3.7– Euler-Johnson's failure envelope.

3.6 Buckling-Load Analysis

Concrete columns may fail as a result of material failure, instability failure, or a combination of both. Material failure of stocky or short concrete columns is governed by the material strength and column cross section. Instability failure is governed by the column geometry at which the column starts buckling and its ultimate carrying capacity is significantly reduced. Two theories are used herein to explain the reduction in the limit load at which a perfect column can start to deflect: (1) the tangent (or incremental) modulus theory; and (2) the reduced (or double) modulus theory. Both theories, under different conditions, require that when a column starts to buckle, the buckling load must be equal to the axial-force resultant relative to the

stress–strain curve of the materials used. In the following sections, the buckling load for an FRP-RC column is calculated and verified against test results.

3.6.1 Incremental Modulus Theory

Engesser's first theory for incremental (or tangent) modulus, which was subsequently generalized by Shanley (1947), assumes that a perfectly undeformed column ($e = 0$) starts to buckle under increasing incremental axial loading. This could be developed by incorporating the tangent moduli of concrete and FRP materials at different strain increments into Euler's buckling load $\left(P_{t(E)}\right)$ and comparing it with the cross-sectional material strength $\left(P_{t(M)}\right)$ at the same strain increment.

$$P_{t(E)} = \frac{\pi^2}{L_e^2}\left(E_c^t I_c + E_f^t I_f\right) \tag{3.5}$$

$$P_{t(M)} = f_c\left(A_g - A_{FRP}\right) \tag{3.6a}$$

$$P_{t(M)} = f_c A_g \tag{3.6b}$$

$$P_{t(M)} = f_c\left(A_g - A_{FRP}\right) + \varepsilon_f E_f A_{FRP} \tag{3.6c}$$

where E_c^t and E_f^t are the tangential moduli of concrete and FRP, respectively; I_c and I_f are the second moment of area of the concrete cross section and FRP bars about the centroidal axis, respectively; f_c and f_f are the compressive stresses of concrete and FRP bars, respectively. The concrete compressive stress–strain distribution could be accurately established by the unconfined three-parameter model proposed by Popovics (1973). The compressive stress $\left(f_c\right)$ at the corresponding strain $\left(\varepsilon_c\right)$ is expressed as:

$$f_c = f_c'\left(\frac{n\left(\varepsilon_c/\varepsilon_o\right)}{n-1+\left(\varepsilon_c/\varepsilon_o\right)^n}\right) \tag{3.7}$$

where $\varepsilon_o = 0.002$ is the concrete strain at the compressive strength of concrete f_c' and n is a curve-fitting factor equals to $0.8+f_c'/17$ in MPa. The tangent modulus of elasticity of concrete $\left(E_c^t\right)$ is defined as the first derivative of the stress–strain model at each strain increment and could be calculated as follows:

$$E_c^t = \frac{nf_c'}{\varepsilon_o}\left(\frac{(n-1)-(n-1)(\varepsilon_c/\varepsilon_o)^n}{\left((n-1)+(\varepsilon_c/\varepsilon_o)^n\right)^2} \right) \tag{3.8}$$

In contrast to steel bars, FRP bars exhibit a linear elastic stress–strain relationship up-to failure; i.e., $E_f^t = E_f$. Using the results from compression analytical and experimental studies, Afifi et al. (2014), and Hadhood et al. (2017a, b) deduced that taking the compressive and tensile moduli of elasticity as being equal yielded a predicted capacity of FRP-RC columns similar to the results from experimental tests. Accordingly, the modulus of elasticity of the FRP bars in compression is assumed to be the same as their tensile modulus (see Table 3.2).

Three approaches were used in determining the cross-sectional strength of FRP-RC columns (see Eq. (3.6)). The first approach—Eq. (3.6-a)—follows CSA S806-12 provisions, which neglect the contribution of FRP bars in compression and deduce the cross-sectional area of FRP bars from the gross area of the concrete column. The second approach—Eq. (3.6-b)—was recommended by Zadeh and Nanni (2017) and replaces the FRP bars under compression with concrete. The third approach—Eq. (3.6-c)—preserves the strain compatibility in the column cross section considering the contribution of FRP bars in compression and limiting the compressive strain of FRP bars to concrete compression strains, i.e., $\varepsilon_c = \varepsilon_f = \varepsilon$. Equations 3.5 and 3.6 are two nonlinear equations with one unknown (ε), which can be solved using an iterative analysis. For a given column geometry, incremental strain is assumed and the convergence of the buckling load (Eq. 3.5) and the cross-sectional strength (Eq. 3.6) is checked. If that holds true, then another value for column height is selected and the steps are repeated to develop the column's strength curve over a wide range of column heights that cover the regions of short and long columns.

3.6.2 Incremental Modulus Theory

The reduced (or double) modulus theory implies that, at the start of buckling, the column cross section of a perfect pin-ended column undergoes a shortening (loading) on one side and an extension (unloading) on the other side with incremental force resultants having opposite signs and equal magnitudes; that is, a constant load. To develop the buckling load based on the double

modulus theory, tangent (E_c^t) and initial (E_c^o) column moduli are incorporated into the stiffness calculations for both portions of the section that undergoes loading and unloading, respectively. Note that before column failure occurs, the initial and unloading moduli of elasticity could be assumed as equal. This explains why the initial modulus substitutes for the unloading one in the context above. Similar to what Bažant et al. (1991) presented, the reduced buckling load of FRP-RC columns $(P_{r(E)})$ can be expressed as the Euler's load of a perfect column (e = 0) as:

$$P_{r(E)} = \frac{\pi^2}{L^2}\left(\left(EI\right)_c^r + E_f I_f\right) \tag{3.9}$$

$$\left(EI\right)_c^r = E_c^t I_L + E_c^o I_U \tag{3.10}$$

where $\left(EI\right)_c^r$ is the reduced effective lateral stiffness of the column; I_L and I_U are the moment of inertia of the loaded and unloaded portions of the cross section about the gross cross-section centroidal axis. To define I_L and I_U considering a circular cross section of a perfect pin-ended column, Figure 3.8 shows the cross-sectional uniform and bilinear stress distributions before and during column buckling, respectively. Consequently, the loading (F_L) and unloading (F_U) resultant forces are computed as:

$$F_U = \left(\psi E_c^o D_U\right)\frac{y_U}{D_U} A_U \tag{3.11}$$

$$F_L = \left(\psi E_c^t D_L\right)\frac{y_L}{D_L} A_L \tag{3.12}$$

where ψ is the column curvature due to buckling; A_L and A_U are the area of loading and unloading segments, respectively; y_L and y_U are the distance from the center of the loading and unloading segments to the neutral axis, respectively (refer to Fig. 3.8 for the definitions of other symbols). Applying the condition of constant load, which requires the loading and unloading resultant forces to be equal (i.e., $F_L = F_U$) and substituting $D_U = D - D_L$ yields the

following expression that defines the unloading length in terms of initial and incremental moduli.

$$\frac{E_c^t}{E_c^o} = \frac{D_U}{D - D_U}\left(\frac{\omega}{2\pi - \omega}\right) \tag{3.13}$$

$$\omega = \theta_U - \sin\theta_U \tag{3.14}$$

Then, I_L and I_U can be easily calculated. The moment of inertia of the FRP bars in loading and unloading zones were subtracted from I_L and I_U to avoid any duplication in Eq. (3.6). Again, the reduced buckling load—Eq. (3.9)—should be equal to the axial-load resultant of the column cross section in the undeflected state (see Eq. (3.6)). This could be iteratively solved by assuming a strain value in the cross section and calculating the corresponding moduli and stresses from the previously discussed stress–strain curves. Afterwards, I_L and I_U were calculated, and the reduced effective lateral stiffness of the column could be found from Eq. (3.10). If Eq. (3.6) and (3.9) are not satisfied, another strain value must be selected, and the process repeated until a reasonable accuracy is achieved.

3.6.3 Verification of Models

Figure 3.9 compares the tangent and reduced modulus loads obtained with the test results. In general, both proposed models for the buckling load showed a reduction less than 2% in the load-carrying capacity of FRP-RC columns at low slenderness ratios up to 40. In addition, all the failure loads of the tested columns lie between the tangent modulus load (the lower bound) and the reduced modulus load (the upper bound). At low slenderness ratios (G1-14 and G2-17), the theoretical failure loads based on the reduced modulus theory are more accurate for predicting the column's experimental ultimate capacity. The tangent modulus buckling loads represent the buckling loads reached with more slender columns (G4-26 and G5-33) that failed at a lateral displacement of 1% of the column diameter. This matches the case observed by Bažant et al. (1991) for steel-reinforced-concrete columns for which the theoretical tangent loads were equal to the peak load of a column with a load eccentricity equals 0.01 of the column

size. In the following theoretical investigations, the tangent modulus load is used as a low limit for column ultimate capacity.

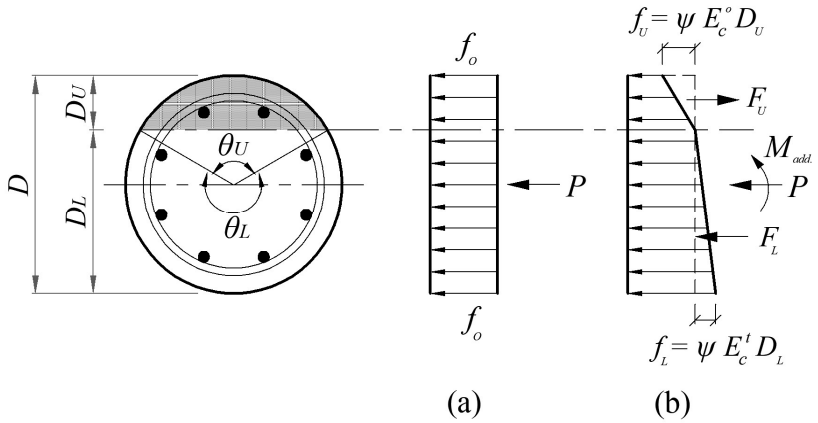

Figure 3.8– Cross-section stress distribution: (a) Before and (b) during column buckling.

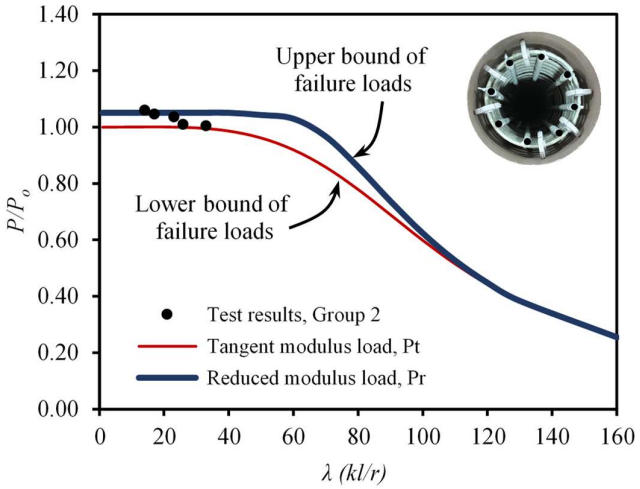

Figure 3.9– Verification of the theoretical buckling loads against test results.

3.6.4 Additional Investigations

The analytical model based on the tangential (incremental) modulus was verified with the test results for 50 specimens (from the current study and the literature) with different reinforcement types (GFRP and CFRP), cross-section shapes (rectangular and circular), concrete compressive strengths (ranging from 32 to 50 MPa (4,640 to 7,250 psi)), and slenderness ratios (from 6 to 42). Figure 3.10 shows the experimental versus the theoretical column failure loads considering the three design approaches discussed above. The dashed lines show ±5% permissible discrepancies between theoretical and test results. All the verified approaches agree well with

the test results with a standard deviation from unity ranging from 5.1% to 6.7%. Approach 1, which neglects the FRP-bar contribution to the column's carrying capacity, exhibits a high level of conservatism and underpredicts column capacity. In contrast, Approach 3 considers the contribution of FRP bars to column capacity by taking the compressive elastic modulus of the FRP bars as equal to their tensile modulus, resulting in around 26% of the tested columns achieving less than 95% of their theoretical capacity. By restricting the FRP compressive strength to the concrete compressive strength, Approach 2 provides an acceptable hypothesis between two extremes and is, therefore, recommended for defining the load-bearing capacity of FRP-RC columns.

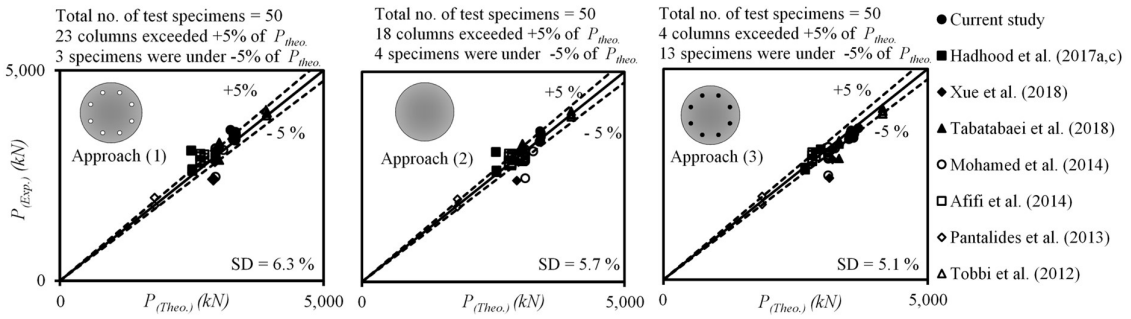

Figure 3.10– Effect of considering FRP-bar contribution on the tangent modulus loads.

Figure 3.11 illustrates the three anticipated modes of failure of FRP-RC columns $(\rho_L = 1\%)$ by plotting the normalized column ultimate load with the column geometry in terms of slenderness ratio. The ultimate column load was defined with the tangent modulus theory considering the three abovementioned approaches for the FRP contribution to column axial capacity. At $\lambda = 18$, which is the proposed limit for short FRP-RC columns, column resistance is governed by the cross-section strength, while column slenderness has no considerable effect on column-carrying capacity; this is material failure. Between $\lambda = 18$ and $\lambda = 85$ is the transition zone, in which column cross-section strength begins to be affected by column slenderness and the column loses more than 25% of its loading capacity. All the GFRP-RC columns tested experienced material failure. The effect on column capacity was experimentally determined for GFRP-RC columns with $\lambda \cong 23$. The stability failure of the FRP-RC columns occurred at $\lambda = 85$, at which point the column cross-section strength is significantly reduced, and the

column capacity is limited to Euler's critical load, where the three approaches coincide at $\lambda = 85$.

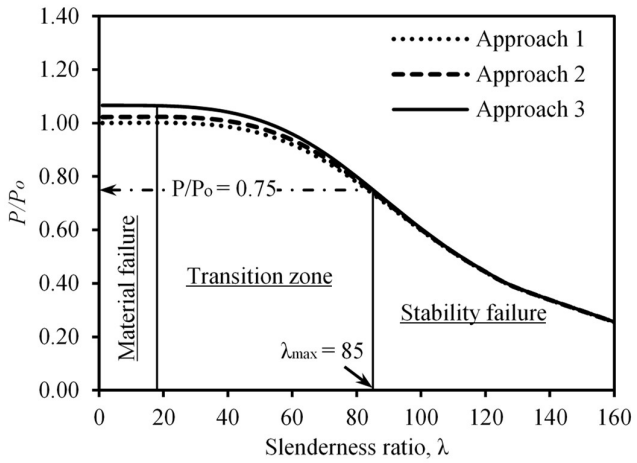

Figure 3.11– Maximum slenderness limit of material failure.

Finally, deeming the experimental tests conducted and the developed buckling analysis, the GFRP-RC columns behaved similarly as steel-RC ones. In addition, GFRP longitudinal reinforcement significantly contributed to the axial capacity of slender as well as short columns as discussed earlier. Therefore, the authors recommend that GFRP reinforcement can safely replace traditional steel bars in both short and long columns provided the proposed limitations herein are complied with.

3.7 Conclusions

The effect of slenderness on GFRP-RC columns subjected to uniaxial compression loads was investigated using 12 full-scale pin-ended columns with slenderness ratios of 14, 17, 23, 26, and 33. An experimental database composed of 50 test specimens studied by the authors and others were incorporated into buckling analysis to provide the limit of slenderness ratios and conduct critical buckling-load analysis for FRP-RC columns. The main concluding remarks are as follows:

1. The failure of both the short and slender GFRP-RC columns was dominated by a material-type failure in terms of gradual concrete cover spalling at the peak load. Beyond peak, tensile rupture of GFRP spirals, compression rupture of GFRP bars, and buckling of steel bars were observed at ultimate stages.
2. The GFRP reinforcement significantly contributed to resisting the applied compression loads and yielded failure modes similar to the steel-reinforced-concrete columns at all slenderness ratios tested from $\lambda = 14$ to $\lambda = 33$. In comparison to the short-column control specimens $(\lambda=14)$, the more slender columns lost 1.3%, 2.3%, 5.2%, and 5.8% of their strength at slenderness ratios of $\lambda = 17$, $\lambda = 23$, $\lambda = 26$, and $\lambda = 33$, respectively.
3. The instability of FRP-RC columns was experimentally investigated in terms of column lateral displacement and was observed at 75% of the column capacity with an ultimate lateral response measured 1% of the column size. The experimental second-order moments were limited and not significant over the range of slenderness ratios studied ($\lambda = 14$ to $\lambda = 23$).
4. The design provisions for FRP spirals in CSA S806-12 for short FRP-RC columns provided sufficient confining levels for the slender GFRP-RC columns tested with slenderness ratios up-to 33. Therefore, these design provisions for FRP spirals are recommended for slender FRP-RC columns.
5. Euler–Johnson's proposed stability envelope yielded conservative values of column ultimate capacity against the test results over the range of the slenderness ratios tested. The method developed revealed the applicability limit of Euler's and Johnson's formulas for FRP-RC columns at $\lambda = 60$ for $\rho_L = 1\%$ and at $\lambda = 70$ and $\lambda = 75$ for $\rho_L = 8\%$, using

the lateral stiffness provisions of Zadeh and Nanni (2017) and Mirmiran et al. (2001a), respectively.

6. When the test results were verified, the proposed tangent modulus model yielded a lower and acceptable limit for the buckling load of FRP-RC columns for the range of the slenderness ratios investigated. The double (reduced) modulus theory provided rational limits for FRP-RC-column strength with slenderness ratios less than or equal 14.
7. Based on the experimental database and the suggested buckling analysis, a reasonable limit of 18 is proposed for the slenderness ratio for FRP-RC columns bent in single curvature. This limit can be reformulated in a form similar to the limit in ACI 318-14 as $kl_u/r \le 30+12\left(M_1/M_2\right) \le 36$.

CHAPTER 4

Inelastic Second-Order Analysis for Slender GFRP-Reinforced Concrete Columns: Experimental Investigations and Theoretical Study

Analyse inélastique de second ordre de poteaux élancés en béton armé de prfv: étude expérimentale et théorique

Foreword

Authors and Affiliation:

- **Waseem Abdelazim** is a doctoral candidate in the Department of Civil Engineering at the University of Sherbrooke, Sherbrooke, QC, Canada, J1K 2R1.
- **Hamdy M. Mohamed** is a research associate and lecturer in the Department of Civil Engineering at the University of Sherbrooke, Sherbrooke, QC, Canada, J1K 2R1.
- **Brahim Benmokrane**, **FACI**, is a Professor in the Department of Civil Engineering, Université de Sherbrooke, Sherbrooke, Quebec, Canada, J1K 2R1

Journal Title and Paper Status:

Published in *Journal of Composites for Construction, ASCE*, V. 24, No. 3, April 2020. *DOI: 10.1061/(ASCE)CC.1943-5614.0001019*

Contribution to the Thesis:

Over the last two decades, substantial number of experimental research studies and discussions have been published related to the compression behavior of GFRP-RC short columns. So far, this study is the one of the limited testing programs aimed at investigating the slender behavior of full-scale concrete columns reinforced with GFRP bars and ties. The results will contribute

to implementing the use of GFRP bars and ties in concrete piles and piers, which can be an innovative solution to the corrosion problem in bridge foundations. This study also provides new insights into the slenderness limit of GFRP RC columns reinforced with GFRP with an extensive theoretical study.

Abstract

Designing reinforced concrete (RC) columns reinforced entirely with fiber-reinforced polymer (FRP) bars requires an explicit definition of the slenderness upper and lower limits for use in code provisions. To date, limited research has focused on experimentally assessing the behavior of slender FRP-reinforced concrete columns. As a result, North American codes and guidelines lack design provisions. This study was conducted to enrich the research database with a total of 20 full-scale columns reinforced with steel or glass FRP (GFRP) bars. The columns were 305 mm in diameter and had slenderness ratios of 14, 19, 23, 26, and 33, and were tested under concentric and eccentric loading. The steel-reinforced columns were tested to serve as benchmark for their GFRP-reinforced concrete counterparts. The interrelated effects between the slenderness ratio and the load eccentricity level were investigated with four different eccentricity-to-diameter ratios of 0%, 16%, 33%, and 66%. Test results proved the efficiency of GFRP bars as internal reinforcement for slender RC columns. The research program was then extended, developing a second-order model for slender FRP-reinforced concrete columns. Good correlation was observed between the experimental results and the model developed analytically. In addition, based on the stability analysis, it was found that the ACI 318-19 (ACI 2019) margin for stability failure of steel-reinforced concrete columns was appropriate and can be applied to GFRP-reinforced concrete columns, as well. Lastly, the experimental results and the analytical model indicated that a maximum slenderness limit of 18 was appropriate for short GFRP-reinforced concrete columns bent in a single curve.

4.1 Introduction

The inevitable lateral deformations associated with eccentrically loaded columns increase the susceptibility to second-order effects compared to perfectly axially loaded columns that have no initial imperfections. This induced lateral buckling accompanied by the existing axial loads magnifies the initial column moments, thereby reducing overall column capacity. In general, the strength reduction follows the formation of secondary moments and is a function of many factors, such as the initial applied eccentricity (e), column slenderness ratio $(\lambda = L_e / r)$, and the stress–strain relationship of the reinforcing material, where L_e is the column effective buckling length and r is the radius of gyration of the column cross section. In order to reflect such secondary responses in column analysis, the structure's deformed geometry must be incorporated into the equilibrium equations for second-order analysis. Rigorous nonlinear second-order analysis is, however, impractical for frequent engineering office design methods. Consequently, ACI 318-19 (ACI 2019) and CSA A23.3-14 (CSA 2014) offer a moment-magnifier approach to analyze slender steel-reinforced concrete columns that accounts for the secondary effects owing to column slenderness. This method uses a simple estimate of the flexural stiffness that can be included in a first-order analysis using the original undeformed geometry of the structure. This approximate design procedure for slender columns is acceptable up to an ultimate limit called the "slenderness upper limit." ACI 2019 defines the slenderness upper limit at a secondary-to-primary moment ratio equal to 1.4 to eliminate any probabilities of stability failure. CSA, however, limits the implementation of the moment-magnifier approach to slender columns with $\lambda < 100$; otherwise, more accurate analysis must be performed. The CSA 2014 upper limit for slenderness is based on the maximum slenderness ratio of experimentally tested concrete columns. Moreover, ACI 2019 and CSA 2014 allow that a 5% reduction in column axial capacity due to second-order effects is acceptable, and the column could be safely designed as a short column satisfying first-order analysis. This corresponds to a slenderness ratio of 22 for steel-reinforced concrete columns not braced against sideway or those bent in a single curvature: this is called the slenderness lower limit.

As for columns entirely reinforced with FRP bars, ACI 440.1R-15 (ACI 2015) provisions do not recommend designs using FRP bars to resist compressive stresses. On the other hand, in the case of GFRP-reinforced concrete members, CSA S806-12 (CSA 2012) and AASHTO LRFD 2018a used the vast database dedicated to investigating FRP-reinforced concrete short columns with a wide range of tested parameters (De Luca et al. 2010; Tobbi et al. 2012; Pantelides et al. 2013; Afifi et al. 2014; Mohamed et al. 2014; Hadi et al. 2016; Hassan et al. 2017; Youssef and Hadi 2017; Hadhood et al. 2017a, b, c, d, and e; Guérin et al. 2018a, and b; Sheikh and Kharal 2018). They also allow the use of FRP reinforcement in short columns and conservatively ignore the contribution of FRP bars in the compression zone. Moreover, CSA S806-12 (CSA 2012) classifies GFRP-reinforced concrete columns as short or long, relying on the ACI 2019 slenderness limit for steel-reinforced concrete columns and disregarding that FRP-reinforced members might resist secondary effects differently than steel-reinforced ones. Nevertheless, limited experimental and analytical work has been conducted to define a slenderness limit for slender columns reinforced with FRP bars. So far, the literature contains no experimentally or analytically based recommendations for the upper limit of the slenderness ratio of FRP-reinforced concrete columns similar to those for steel-reinforced concrete columns.

In general, analytical modelling provides for investigating an enormous range of different design parameters, including different loading and boundary conditions. Designers, however, place greater trust in experimental observations and consider them to be more reliable. Therefore, analytical investigations validated with an adequate number of experimental tests are more mature and functional. Tikka et al. (2010) tested eight 150×150×1800 mm columns reinforced with GFRP bars and laterally tied with a carbon-fiber spiral wrap under eccentric loading. They concluded that the GFRP-reinforced concrete columns provided a reasonable amount of ductility and would provide adequate warning prior to failure. Hales et al. (2016) conducted an experimental study on the behavior of slender and short high-strength-concrete columns under eccentric and concentric loading. The reduction in loading capacity due to slenderness variations could not be observed as the short and long columns had different loading conditions. They observed a stability-type buckling failure with concrete-cover spalling in the compression zone for slender columns $(\lambda = 49)$ loaded at large eccentricity $(e/D = 33\%)$. Recently, Xue et al. (2018) conducted concentric and eccentric loading tests on

slender rectangular GFRP-reinforced concrete columns (λ varied from 20.8 to 41.6). They concluded that all tested columns exhibited concrete-crushing failure with no rupture of the FRP bars.

Mirmiran (1998) and Mirmiran et al. (2001a) developed valuable analytical models to study the behavior of slender FRP-reinforced concrete columns. The models were verified with CFRP- and steel-reinforced concrete columns from the literature, respectively. Mirmiran concluded that FRP-reinforced concrete columns were more susceptible to slenderness effects than steel-reinforced concrete columns, and therefore recommended reducing the current slenderness limit of 22 for steel-reinforced concrete columns to 17 for FRP-reinforced concrete columns. Since FRP bars do not yield, interaction diagrams of FRP-reinforced concrete columns analytically plotted by Choo et al. (2006) did not show any balanced points like those of steel-reinforced concrete columns. Jawaheri Zadeh and Nanni (2017) applied a theoretical derivation for the slenderness limits of FRP-reinforced concrete columns with a rectangular cross section. The contribution of FRP bars in compression was limited to the concrete compressive strength. The suggested slenderness limits were 14 and 19 for GFRP-reinforced and CFRP-reinforced concrete columns bent in a single curvature, respectively.

4.2 Objectives

The differences in the proposed slenderness limits found in the literature and the obvious scarcity of experimental data accentuate the need for more experimental studies that investigate the performance of slender FRP-reinforced concrete columns. Therefore, the main objectives of our experimental and analytical study can be summarized as follows:

7. To assess the general behavior of slender GFRP-reinforced concrete columns with critical slenderness ratios ranging from $\lambda = 14$ to $\lambda = 33$ under concentric and different levels of eccentric loading.
8. To quantify the capacity of slender GFRP-reinforced concrete columns, identifying the strength reduction owing to initiated second-order effects.

9. To develop a P–M failure surface of slender GFRP-reinforced concrete columns reflecting the influence of second-order effects on the failure paths.
10. To propose recommendations for slenderness lower and upper limits for GFRP-reinforced concrete columns that could support the work of the North American technical committees engaged in developing standards and design provisions for GFRP-reinforced concrete columns.

4.3 Experimental Program

This experimental investigation aimed at assessing the feasibility of GFRP reinforcement in slender RC columns. The testing plan, therefore, consisted of 20 full-scale circular concrete columns: 16 were reinforced with GFRP bars and spirals; four with traditional steel reinforcement. The following sections outline the investigated test parameters and the test matrix, characteristics of the materials used, instrumentation, and test setup.

4.3.1 Design of the Test Specimens

The structural behavior of the slender GFRP-reinforced concrete columns was observed by testing the 16 full-scale GFRP-reinforced concrete columns considering two test parameters: slenderness ratio and load eccentricity level. In addition, 4 steel-reinforced concrete columns were tested for comparison with the GFRP-reinforced specimens under similar testing conditions. Five different slenderness ratios $(\lambda = kL/r)$ were used (14, 19, 23, 26, and 33), where k is the effective length factor equal to unity (case of ideal pin-ended column); L is the unsupported length of the column; and r is the radius of gyration of its cross section. All tested columns measured 305 mm in diameter (D). The second observed test parameter was the applied eccentricity level. Four eccentricities were selected and considered to cover a wide range of loading zones: $e = 0.0$ (concentric loading), $e(e/D) = 50\ \text{mm}(16\%)$ (low eccentricity), $e(e/D) = 100\ \text{mm}(33\%)$ (moderate eccentricity), and $e(e/D) = 200\ \text{mm}(66\%)$ (high eccentricity). In addition, the eccentricities selected provide for defining and providing an experimental interaction diagram for the tested slender GFRP-reinforced concrete columns considering the second-order effects.

The design of internal reinforcement in all the column specimens complied with ACI 318-19 (ACI 2019) and CSA S806-12 (CSA 2012) provisions to achieve the minimum longitudinal and transversal reinforcement ratios with less test complexity. Therefore, all of the GFRP- and steel-reinforced columns were reinforced vertically with 8 equally spaced bars 15.9 mm in diameter—No. 5 GFRP bars and M15 steel bars $\left(\rho_L = 2.19\%\right)$—where ρ_L is the longitudinal-reinforcement ratio. As for the horizontal reinforcement, GFRP and steel spirals were designed to provide thorough confinement so as to avoid buckling of the longitudinal reinforcing bars. All the GFRP-reinforced columns were reinforced in the transverse direction with No. 3 (M10 for the steel specimens) continuous spirals without any lapped splices. Each column was divided into two regions: a middle region with a spiral pitch of 80 mm and top and bottom end regions 250 mm in length. A tighter spiral pitch of 50 mm was used in the latter regions to prevent any premature failure near the zones of stress concentration, as shown in Fig. 4.1. The test specimens were divided into five series, as indicated in Table 4.1. Series I consists of four steel-reinforced concrete columns as control specimens tested under two different eccentricities $(e/D = 0, \text{ and } 66\%)$, while series II to V reflect the impact of slenderness ratio and eccentricity-to-diameter ratio on the performance of GFRP-reinforced concrete columns. Each specimen was identified with three characters. The first letter indicates the type of internal reinforcement: S for steel and G for GFRP. The next two numbers stand for slenderness ratio and applied load eccentricity-to-diameter ratio, respectively.

4.3.2 Material Properties

Number 5 Grade III sand-coated GFRP bars with an average fiber content of 83.8% and No. 3 Grade II sand-coated GFRP spirals with an average fiber content of 78.9% were used to fully reinforce all of the GFRP-reinforced specimens. Both the GFRP bars and spirals were manufactured using a pultrusion process with continuous glass fibers impregnated in a thermosetting vinyl-ester resin (see Fig. 4.1). Normal-strength deformed steel bars (M15) and spirals (M10) were used to reinforce the steel-reinforced control specimens in the longitudinal and transverse directions. Table 4.2 reports the average ultimate longitudinal tensile properties of the GFRP and steel materials, as provided by the manufacturers.

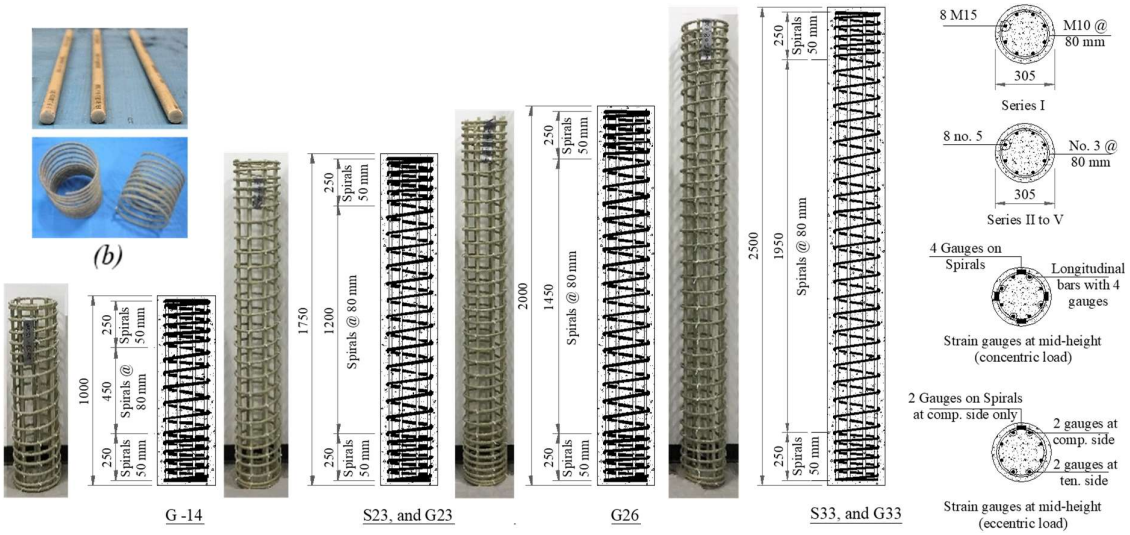

(*a*)

Figure 4.1– (a) Reinforcement details, GFRP cages, and internal instrumentation, (b) Sand-coated GFRP bars and spirals.

All columns were cast in an upright position from a single batch of ready-mixed normal-strength, normal-weight concrete with a maximum aggregate size of 10 mm. During casting, the concrete was compacted with an electrical needle vibrator inserted to the lowest point of the column to ensure adequate consistency of the concrete paste. The average concrete compressive strength was 46.6 MPa and determined based on testing nine 100 mm×200 mm standard concrete cylinders cured under the same conditions as the column specimens. The concrete cylinders were tested on the same day as the start of testing of the column specimens.

4.3.3 Instrumentation and Testing Procedure

Several responses were targeted and monitored during the testing. First, the applied axial load and the machine-head axial displacement were measured, respectively, with the machine's sensitive internal load cells and linear variable differential transformers (LVDTs). Second, the load–lateral-displacement response was defined using the column's horizontal deflection, which was gauged with three linear potentiometers (LPOTs) mounted horizontally at column mid- and quarter-heights.

Table 4.1 – Test specimens and results

S	Specimen ID	Geometry [1]		e (mm); e/D (%)	ε_b ($\mu\varepsilon$) [2]		ε_c ($-\mu\varepsilon$)	δ (mm)	P_n (kN)	M_{1st}. P_n . e ($kN.m$)	M_{2nd}. P_n . δ ($kN.m$)	M_n. $M_{1st}+M_{2nd}$ ($kN.m$)	M_{2nd} / M_{1st} (%)
		L (mm)	λ		Ten.	Comp.							
I	S-23-C	1750	23	—	—	2,310	2,350	1.1	3,866	—	4.3	4.3	—
	S-23-66			200; 66	3,015	2,580	3,875	12.9	504	100.8	6.5	107.3	6.4
	S-33-C	2500	33	—	—	2,420	2,330	3.2	3,627	—	11.6	11.6	—
	S-33-66			200; 66	2,480	2,210	3,750	26.4	477	95.4	12.6	108.0	13.2
II	G-14-C	1000	14	—	—	3,420	3,230	0	3,535	—	—	—	—
	G-19-C [3]	1500	19		—	3,500	3,500	—	3,472	—	—	—	—
	G-23-C	1750	23		—	3,370	3,130	0.8	3,453	—	2.8	2.8	—
	G-26-C	2000	26		—	3,370	2,930	1.9	3,359	—	6.4	6.4	—
	G-33-C	2500	33		—	3,150	3,170	2.9	3,331	—	9.7	9.7	—
III	G-19-16 [3]	1500	19	50; 16	640	3,360	4,850	5.5	1,910	95.5	10.5	106.0	11.0
	G-23-16	1750	23		420	3,170	4,100	6.3	1,807	90.3	11.3	101.6	12.5
	G-33-16	2500	33		740	3,270	3,790	13.7	1,725	86.3	23.6	109.9	27.3
IV	G-19-33 [3]	1500	19	100; 33	3,500	3,335	3,830	9	972	97.2	8.7	105.9	9.0
	G-23-33	1750	23		3,810	3,190	4,440	12.2	891	89.1	10.9	100.0	12.2
	G-33-33	2500	33		4,200	3,490	3,920	22.2	786	78.6	17.4	96.0	22.2
V	G-14-66	1000	14	200; 66	6,610	3,050	3,530	9.1	417	83.4	3.8	87.2	4.6
	G-19-66 [3]	1500	19		5,620	2,410	3,840	10.5	416	83.2	4.4	87.6	5.3
	G-23-66	1750	23		6,690	3,100	3,425	15.4	388	77.6	6.0	83.6	7.7
	G-26-66	2000	26		8,280	3,070	3,990	26.3	381	76.2	10.0	86.2	13.2
	G-33-66	2500	33		8,750	3,020	4,100	32.7	371	74.2	12.1	86.3	16.4

[1] All columns were 305 mm in diameter (D). [2] All listed test results are at the first peak loads. [3] Adapted from Hadhood et al. 2017a.
Notes: L is the column height; λ is the slenderness ratio; e is the initial load eccentricity; ε_b and ε_c are the bar and concrete strains. respectively; δ is the mid-height lateral displacement; P_n and M_n are the ultimate load and the corresponding secondary moment. respectively; M_{1st} and M_{2nd} are the first- and second-order moments. respectively; 1 mm = 0.0394 in.; 1 kN = 0.225 kpi.

Table 4.2 – Mechanical and physical properties of the GFRP and steel reinforcement

Bar Size	D (mm)	Nominal area[1] (mm^2)	Immersion area (mm^2)	Fiber Content [2] (%)	E [3] (GPa)	f [4] (MPa)	ε (%)
GFRP Reinforcement							
# 3 (Spiral)	9.5	71	89	78.9	51.1	1281	2.51
# 5	15.9	200	225	83.6	61.8	1449	2.35
Steel Reinforcement							
M10 (Spiral)	9.5	71	-	-	200	400	0.2
M15	15.9	200	-	-	200	400	0.2

Note: D = the nominal diameter; E = the elastic tensile modulus; f = the nominal tensile strength; and ε = the tensile (yield) strain.
[1] The strength and modulus were calculated based on this area.
[2] ASTM D2584 (ASTM 2008) (temp 650°C. sand coating discarded from results).
[3] Average mechanical properties as provided by the manufacturer; CSA S806-12 (CSA 12) Annex C test method.
[4] Yield stress of steel bars as provided by the manufacturer.

Furthermore, both the tensile or compressive bar strains and the tensile strains induced in the confining spirals were recorded with strain gauges with a 6 mm gauge length located at column mid-height in one of two configurations depending on the loading type (concentric or eccentric); see Fig. 4.1. Moreover, the compressive concrete strain was observed up to concrete-cover spalling with strain gauges with a 60 mm gauge length. The concrete strain gauges were fixed at mid-height on the expected concave face (compression side) of the column as it deformed. Readings of concrete strain gauges taken after concrete-cover spalling cannot be relied upon. Therefore, two LPOTs were mounted vertically on two steel rods (300 mm apart) at the locations of the concrete strain gauges and embedded in the columns before casting the concrete to monitor the strains after spalling of the concrete cover.

All the test specimens were tested at the Canada Foundation for Innovation (CFI) structural laboratory of the University of Sherbrooke (Sherbrooke, Quebec, Canada). Prior to testing, a thin perfectly self-leveling grout was used to level the top and bottom ends of each column to allow for uniform distribution of the applied loads. All columns were prevented from experiencing any undesired local failure with the installation of top and bottom rigid steel caps to enhance the confinement level at these stress-concentration zones. Each test specimen was then placed in an 11,400 kN capacity MTS testing machine and precisely aligned with the machine's central axis using a laser level. Afterwards, the strain gauges and LPOTs were connected to an automatic data-acquisition system to record all measured strains and deflections during testing. Top and bottom adjustable steel roller bearings bolted to the top rigid plate of the steel end caps were used to attain the predesignated eccentricity as well as to replicate the case of a perfect pin-ended column: $k = 1$ (see Fig. 4.2). For the portion of the expected linear stress–strain response (up to 75% of the estimated specimen capacity), the test was conducted with a load-controlled technique at a rate of 2.5 kN/s. Then, the testing continued under displacement control at a displacement rate of 0.002 mm/s up to failure.

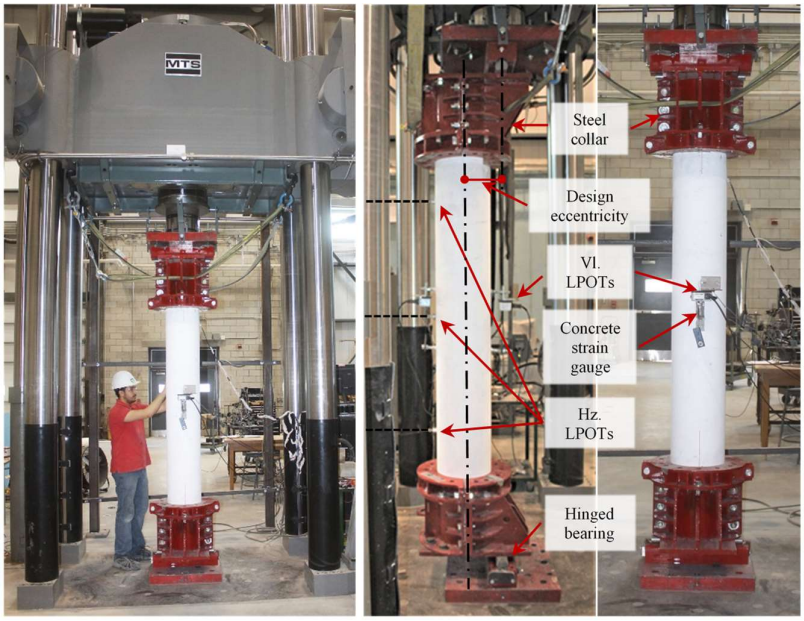

(a) (b)

Figure 4.2– Testing plan: (a) Connecting the external instrumentation, (b) Test-setup components.

4.4 Test Results and Discussion

4.4.1 General Behavior and Failure Modes

Initiation of tensile cracks at tension side, concrete-cover spalling at compression side, state of the ascending loading branch, and post-peak performance are main characteristics upon which column failure mechanisms can be identified. Accordingly, the test specimens exhibited three distinct failure patterns: compression-based, tension-based, and transition failure (zone). The compression-based failure mode is defined as concrete rupture initiated by gradual cover spalling accompanied by a significant sudden reduction in the load-carrying capacity of the tested column. This was quite evident with the columns tested with pure axial loads and those tested under low eccentricity, $e/D = 0$ and 16%, respectively. As the load was applied to the series II $(e/D=0)$ and series III $(e/D=16\%)$ specimens, the columns behaved elastically up to 90% and 75% of the peak load when the slenderness ratio varied from 14 to 33, respectively. Then, nonlinear behavior dominated column performance up to and after peak. Prior to cover spalling

in the concentrically loaded specimens, vertical cracks started to initiate at an average load level of approximately 90% of the achieved maximum load. These cracks rapidly widened and propagated, causing the concrete cover to spall off the concrete core. While no tensile cracks were observed in the concentrically loaded columns in the pre-peak stage, the columns tested under $e/D = 16\%$ evidenced limited mid-height visual tensile cracks near 95%, on average, of the gained ultimate strength before developing the ultimate column capacity and splitting the concrete cover in the compression zone. After the peak point, the slenderness ratio controlled the strength degradation for both of series II and series III specimens. The average recorded drop in column capacity was 25% and 37% for the columns with slenderness ratios of $\lambda = 23$ and $\lambda = 33$, respectively. Lastly, the tested specimens experienced either tensile rupture of the GFRP spirals with or without compressive rupture of GFRP longitudinal bars or buckling of the steel bars.

The series V GFRP-reinforced concrete columns were tested under high eccentricity $(e/D=66\%)$. This high eccentricity loading resulted in the early formation of tensile cracks at a load level approximately equal to 24% of the column strength for all the tested slenderness ratios from $\lambda = 14$ to $\lambda = 33$. Soon after, the cracks propagated along the column height and widened increasingly. These tensile cracks migrated within the concrete core towards the compression side, eliminating the concrete block under compression. Consequently, the column axial and lateral resistance noticeably declined. Meanwhile, the properties of the cracked section governed overall specimen behavior, and the columns acted as flexural members. On the other hand, the compression side was free of any visual cracks up to 92% of the first peak load. Limited decay (7%, on average) in column strength was observed after concrete-cover spalling. The concrete compression failure did not control the specimens' capacity and the GFRP bars in the compression zone maintained the columns' ability to recover the strength loss and achieve a second peak load with a slight average increase of 2% over the first peak. At the same time, the tested specimens sustained exaggerated tensile cracks, accompanied by excessive lateral deformations triggered by large support rotation. The test was terminated for reasons of safety without any rupture of the GFRP reinforcement. Given this situation, the failure mode of the specimens tested under high eccentricity $(e/D=66\%)$ was dominated by the initiation of large tensile cracks and considerable lateral deformations,

which can be referred to as tension-based failure. It is important to note that Jawaheri Zadeh and Nanni (2013) related the design of GFRP-reinforced concrete columns to the unacceptably large deformations achieved if the full tensile rupture strain (more than 0.02) is incorporated in the design and therefore would limit the FRP tensile-rupture design strain to 0.01. Moreover, Bazant (1991) showed that this cannot be a failure state—even if the maximum strain of the concrete or internal reinforcement reaches the specified ultimate limit—if the column had another increase in load. In contrast, the column would be considered in a failure state without achieving the ultimate strain limits if it exhibited decreasing load. In addition, these observations and conclusions closely agree with the experimental investigations conducted by Guérin et al. (2018a).

Series IV $(e/D=33\%)$ specimens exhibited a transition failure mechanism between two extremes—compression-based failure and tension-based failure—governed by the formation of excessive tensile cracks and large lateral deformations. Columns tested under moderate eccentricity-to-diameter ratios revealed inelastic behavior beyond 75% of the applied load, initiation of tensile cracks at 40% of the ultimate sustained load, and a 12% approximate load drop preceded by compression vertical cracks at the compression face. In contrast to the specimens tested under high eccentricity $(e/D=66\%)$, the GFRP bars on the compression face could not maintain column capacity, and the columns suffered successive concrete-cover spalling as the load increased. The descending loading branches were governed by the failure of the concrete compression block along with widening of pre-formed tensile cracks causing degradation of the axial- and lateral-stiffness capacities. Compared to the columns tested under concentric and low eccentric loading, those tested under moderate and high eccentricities experienced smooth failure and gradual concrete-cover spalling with GFRP reinforcement, bars, and spirals remaining intact until the test was halted for reasons of safety. Lastly, both the steel- and GFRP-reinforced columns showed similar behavior until the peak load was reached. Nevertheless, the tension-based failure of the steel-reinforced concrete columns with initial high eccentric loading was more explicit and included the steel yielding. Regarding spiral configuration, the spiral spacing prevented the steel and GFRP bars on the compression side from developing any undesirable bar buckling up to failure. Figure 4.3 clarifies the

predominant material failure modes of the steel- and GFRP-reinforced columns, as outlined above.

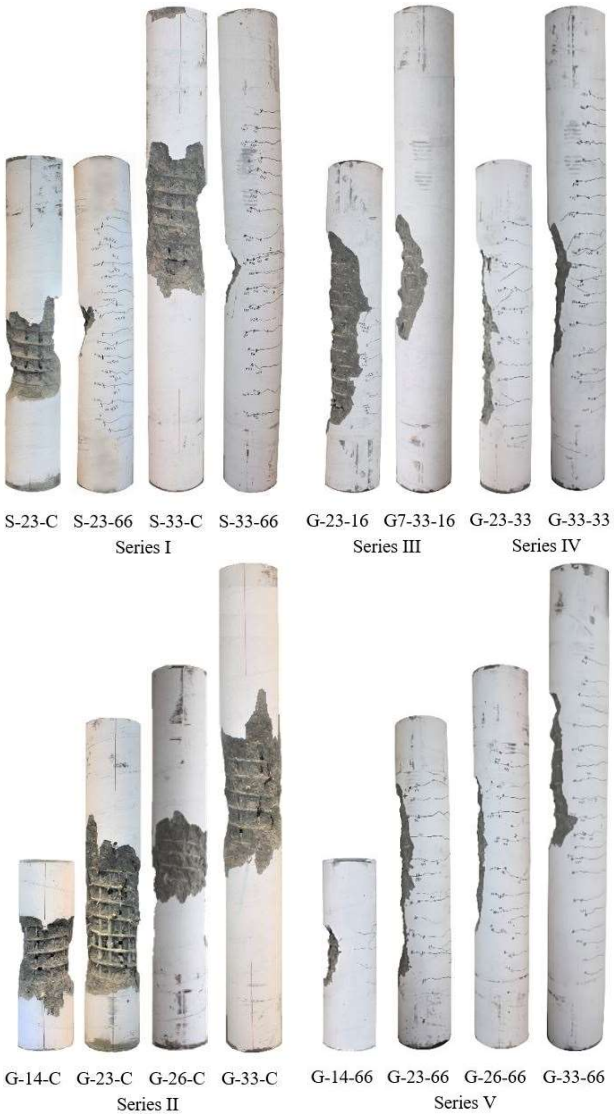

Figure 4.3– Failure modes.

4.4.2 Reinforcement and Concrete Strains

Figure 4.4(a) depicts the normalized applied load to the concrete compression strain relationship of the tested specimens, defined at mid-height where the critical strain values were expected. All measured concrete strains at the peak load exceeded the theoretical values of ε_o

and ε_{cu} for the concentrically and eccentrically loaded specimens, respectively, where ε_o is the concrete strain corresponding to the maximum concrete compressive strength and ranges from 1,900 to 2,500 $\mu\varepsilon$ for normal-strength concrete (Popovics 1973), and ε_{cu} is the ultimate strain in concrete in compression, specified as 3,000 or 3,500 $\mu\varepsilon$ in ACI 2019, CSA 2014, and CSA 2012 guidelines, respectively. Overall, the effect of column slenderness on the concrete strains at peak was insignificant and not observed. Although the increase in the eccentricity level from low to high did not affect the observed ultimate compression strains, it decreased the ascending elastic portion from 90% of the peak load for concentrically loaded columns to 75%, 43%, and 18% for the specimens with low, moderate, and large eccentricity, respectively.

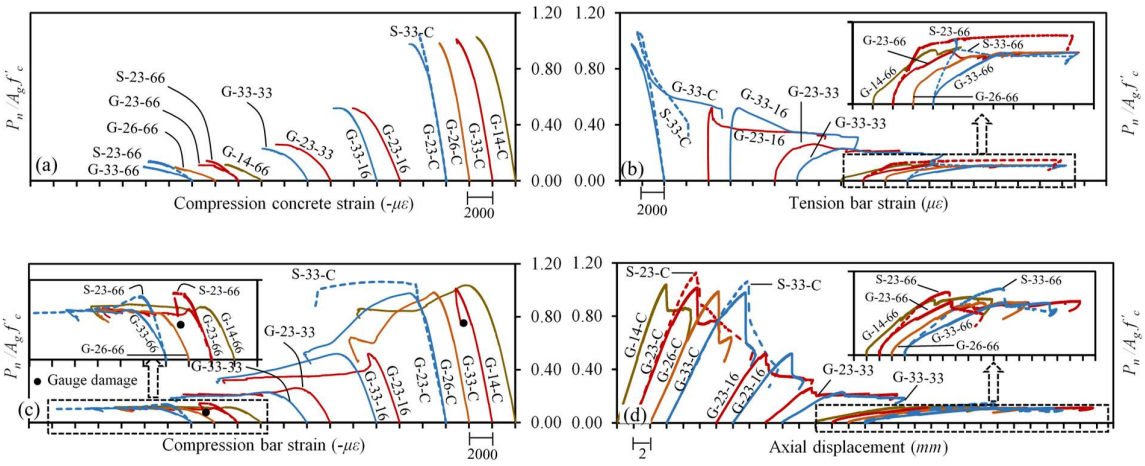

Figure 4.4– Normalized applied load: (a) Concrete compression strain. (b) Tension-bar strain. (c) Compression-bar strain, (d) Axial-displacement response at mid-height.

As for the internal reinforcement, Figs. 4.4(b) and 4.4(c) describe the growth of tension- and compression-bar strains with the applied axial loads, respectively. In general, all measured GFRP-bar and concrete compressive strains were almost equal, so no slippage occurred. This emphasized the contribution of the GFRP bars in the compression block to the overall strength of the tested columns for the full range of the levels of load eccentricity and slenderness ratios. With respect to the tensile strains in the GFRP bars on the convex face of the column, as expected, applying an initial eccentricity located outside of the cross-section kernel transformed the strain distribution over the column cross section from a pure compression state

(Series II) to a combined distribution of compression and tension strains (Series III, IV, and V). The tensile strains in the specimens with the initial eccentricity near to the kernel (G-23-16 and G-33-16) approached 50% of the ultimate load with values of 420 and 740 $\mu\varepsilon$ at peak, respectively. It was also observed that the second-order effects owing to higher slenderness ratios magnified the tensile GFRP-bar strains gained at the same eccentricity levels. For example, columns G-23-33 and G-33-33—with the same eccentricity (33%) but different slenderness ratios (23 and 33, respectively)—recorded tensile strains of 3,810 and 4,200 $\mu\varepsilon$, respectively, (see Table 4.1). Lastly, the average tensile and compressive strains measured at the peak load were, respectively, 38% ε_{frpu} and 15% ε_{frpu}, while the ultimate recorded tensile and compressive strains were 77% ε_{frpu} and 64% ε_{frpu}, respectively, where ε_{frpu} is the ultimate tensile strain in the GFRP bars as provided by the manufacturer (see Table 4.2).

4.4.3 Axial Stiffness

The effect of the test parameter on the axial stiffness of the GFRP-reinforced concrete columns, in terms of the applied load and the corresponding machine-head axial displacement, is illustrated in Fig. 4.4(d). In short columns, axial stiffness was influenced substantially more by the change in applied eccentricity than column slenderness. Comparing the steel- and GFRP-reinforced concrete specimens revealed that they had similar levels of initial axial stiffness when concentrically loaded (G-23-C, G-33-C, S-23-C, and S-33-C). In the case of the specimens tested under high eccentricity $(e/D = 66\%)$, the steel- and GFRP-reinforced concrete columns developed similar levels of axial stiffness up to an average applied load of 43% and 24% of the ultimate carrying capacity for columns with $\lambda = 23$ and $\lambda = 33$, respectively. These limits defined when the tensile cracks occurred. Once tensile cracks had initiated, the ratio of the stiffness achieved by the uncracked concrete to the whole column stiffness started to decline. In addition, the reinforcement type controlled overall column stiffness. This explains why the specimens reinforced with steel bars achieved greater axial stiffness than those with GFRP. The experimental axial stiffness of the GFRP-reinforced concrete columns was, on average, 37% lower than their corresponding steel-reinforced concrete counterparts. As a result, this led to a decay of the column ultimate capacity within 23% compared to the steel-reinforced concrete columns. Axial stiffness is of less importance

for columns loaded under high initially applied eccentricities as this type of loading corresponds to low levels of applied axial loads accompanied by large moments. In such cases, a more rational approach would be treating the element according to beam theories (Jawaheri Zadeh and Nanni 2017; Guérin et al. 2018a).

4.4.4 Lateral-Displacement Response

Figure (4.5) plots the buckling profile of the tested GFRP-reinforced concrete columns for various loading intervals: 25%, 50%, and 100% of the first and second peak loads, if any. Three LPOTs were mounted horizontally at 0.25, 0.50, and 0.75 of the column free buckling length to record the change in the achieved lateral displacement during the test period. All the tested columns were restrained against in- and out-of-plane displacements with a rigid concrete base and the machine head at the top and bottom ends, respectively. The earlier the tension cracks initiated, where the stress distribution over the column cross section changed from pure compression to a tension–compression stress state, the more the column abruptly lost its lateral stiffness. Consequently, for such cases, exposure to higher lateral deformations was expected to occur in the early ages of loading. This is clearly evident in the columns tested under higher eccentricity. In the case of the GFRP-reinforced concrete columns that experienced compression-based $\left(e/D=16\%\right)$ or tension–compression-based $\left(e/D=33\%\right)$ failure, the induced buckling was more obvious beyond 50% of the peak, while those tested under $e/D=66\%$ (tension-based failure) reached high levels of lateral buckling at earlier stages of loading, especially the more slender columns G-26-66 and G-33-66. Furthermore, column lateral responses were more sensitive to changes in applied eccentricity at low levels of eccentricity than at higher ones. For example, testing the columns under an $e/D=33\%$ enlarged the lateral deformations at peak, on average, by around 80% compared to specimens tested under $e/D=16\%$. Increasing the e/D from 33% to 66% increased the lateral displacement by only 30%, on average. Moreover, at same eccentricity level, increasing the slenderness ratio from 23 to 33 approximately doubled the lateral deformations at peak load. Lastly, unlike the steel-reinforced concrete columns, all the GFRP-reinforced concrete columns dissipated all the energy gained during testing and returned to their pre-loading initial states

after releasing the applied loads, thereby confirming the fact that GFRP bars behave elastically up to failure.

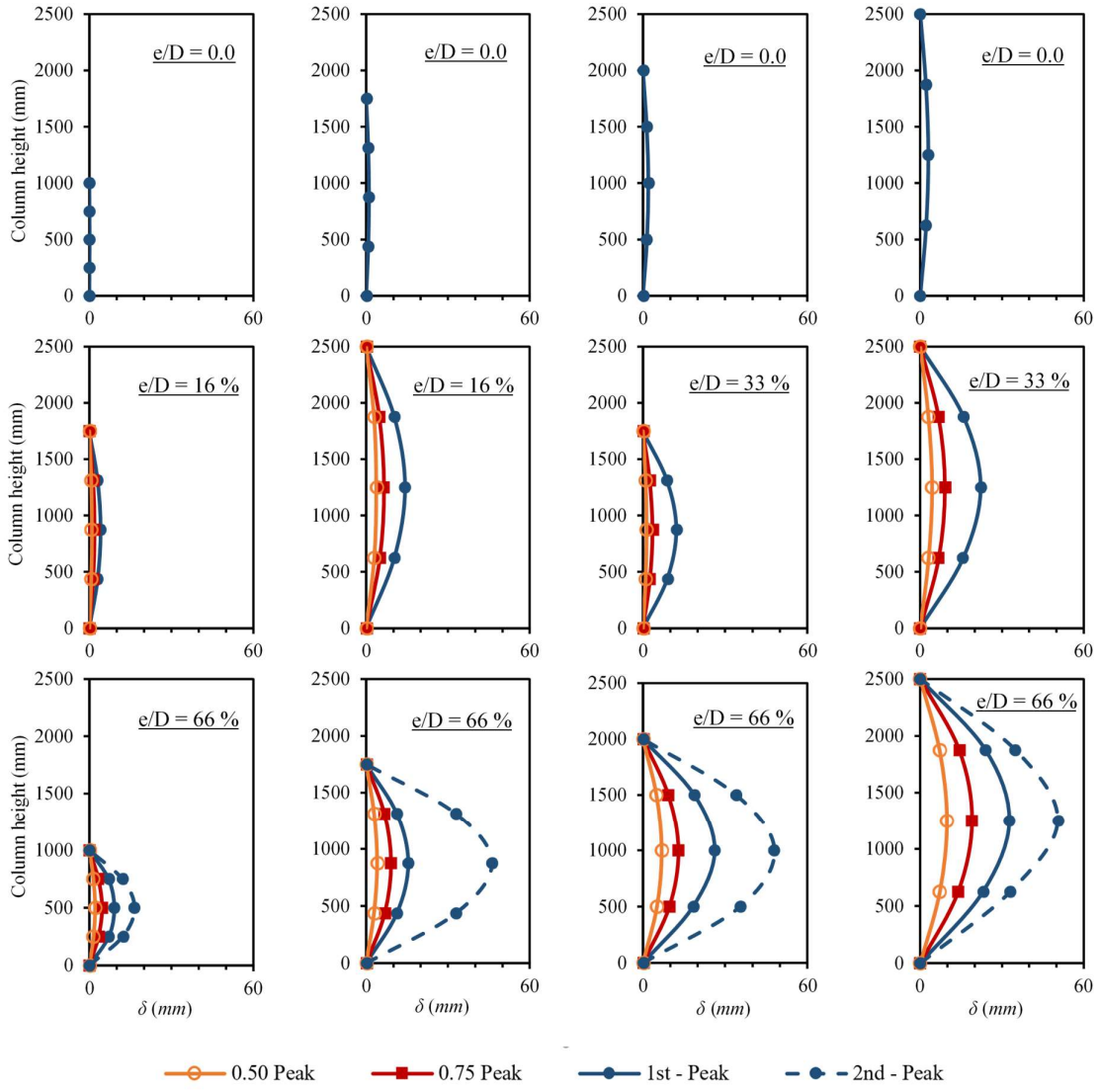

Figure 4.5– Experimental buckling profile for the GFRP-reinforced concrete columns.

4.4.5 Load-Carrying Capacity

In general, column ultimate strength decreased as the applied eccentricity and slenderness ratio increased, although the influence of the applied eccentricity was more pronounced. Columns tested under low (series III), moderate (series IV), and high levels of eccentricity (series V)

lost, on average, 47%, 77%, and 88% of their peak strength, respectively, compared to the columns tested under pure axial loading. This degradation in load-bearing capacity was found to be quite consistent with the test observations of Hadhood et al. (2017a). The impact of the column slenderness on axial capacity was limited when the ultimate capacity of specimens G-19-C, G-23-C, G-26-C, and G-33-C was 1.8%, 2.3%, 5.2%, and 5.8%, respectively, which was lower than that of specimen G-14-C. In contrast, the specimens tested under initial low and moderate eccentricities showed higher sensitivity to slenderness variations. For example, specimens G-23-16 and G-33-16, respectively, had ultimate axial loads 5.4% and 9.7% lower than specimen G-19-16, while specimens G-23-33 and G-33-33 had peaks loads 8.3% and 19.1% lower, respectively, than specimen G-19-33. Further, the axial loading capacity of columns tested under high eccentricity $\left(e/D=66\%\right)$ was less influenced by slenderness effects than those loaded under $e/D=33\%$, since the former tended to behave as flexural members for which the effect of slenderness is negligible. This confirms the theoretical findings of Mirmiran et al. (2001a) in which the lowest slenderness limit (i.e., the farthermost effect of slenderness) was defined at an eccentricity-to-depth ratio $\left(e/h\right)$ of 40%.

4.4.6 Second-Order Effects

Nonlinear second-order responses can be represented as the additional moments induced by the curvature of compression members. Generally, the total column curvature comprises both the curvature owing to the initial eccentricity (first-order moments) and the curvature due to the additional applied moments resulting from multiplying the first-order curvature by the axial loads. The latter is governed by column slenderness, lateral stiffness, and initial moments. Thus, multiplying the overall curvature (lateral deformations) by the applied load produces the experimental ultimate secondary moments, as calculated in Table (4.1). It should be emphasized that applying an initial eccentricity catalyzes the column to buckle, promising second-order effects. This applied initial eccentricity, however, reduces the increased load-carrying capacity, which may end with smaller secondary moments. In other words, employing a higher initial eccentricity does not necessarily magnify the second-order moments. In addition, there is an inflection point at which the largest second-order effects occur. Table 4.1

shows that the ratio of the experimental second- to first-order moments, $M_{2^{nd}-order}/M_{1^{st}-order}$, was at its highest when e/D ranged from 16% to 33%. In addition, column slenderness significantly controlled the value of $M_{2^{nd}-order}/M_{1^{st}-order}$ at the same eccentricity level. Furthermore, the $M_{2^{nd}-order}/M_{1^{st}-order}$ was amplified by more than twice when the slenderness ratio increased by less than 50%. With respect to code limitations, ACI 318-19 (ACI 2019) requires revising the structural system when the secondary-to-primary moment ratio's upper limit of 1.4 is reached. At that level, the probability of stability failure increases rapidly and the structure (column) tends to lose strength due to instability buckling. This corresponds to a $M_{2^{nd}-order}/M_{1^{st}-order}$ of 40%. Subsequently, all the tested GFRP-reinforced concrete columns experienced material failure; instability failure was not experimentally observed.

Figure (4.6) compares the experimental failure envelopes (interaction diagrams) for the GFRP-reinforced concrete columns with slenderness ratios of 23 and 33. The developed interaction diagrams normalize the axial-load response to $A_g f_c'$ and the corresponding bending moments to $A_g f_c' D$. Second-order effects were incorporated in the interaction curve by subtracting the second-order moments from the nominal sustained moments at failure. In addition, two loading paths were presented in the interaction diagram: one with a straight dashed line depicting the behavior of short columns and a solid line displaying the actual performance of the test specimens. As expected, the deviation from the initial straight loading path was greater with the columns with higher slenderness ratios for all eccentricity ranges. Thus, the dotted line $OABC$ expresses the interaction diagram for the slender columns considering the secondary effects due to column slenderness. The earlier remarks regarding the second-order responses can be demonstrated and concluded from the constructed experimental interaction diagrams.

4.5 Model for Slender GFRP-RC Columns

Precise analysis for a structure requires that the deformed geometry of the structural elements and the initial applied forces be integrated into the equilibrium equations; this is called second-order analysis. The main challenge in second-order analysis is that the structure deformations

and the applied external loads are reciprocal, interdependent parameters that necessitate a convergence iterative process. An iterative inelastic second-order analysis model, therefore, was developed considering material nonlinearity and member curvature. The proposed simple theoretical slender-column model for standard hinged steel-reinforced concrete columns externally confined with FRP developed by Jiang and Teng (2013) was adapted to RC columns internally reinforced with FRP bars. The model was previously adopted by Bažant et al. (1991) for pin-ended steel-reinforced concrete columns. This model for slender FRP-reinforced concrete columns follows the compatibility of the internal resultant forces and the external applied loads and deformations, as explained below.

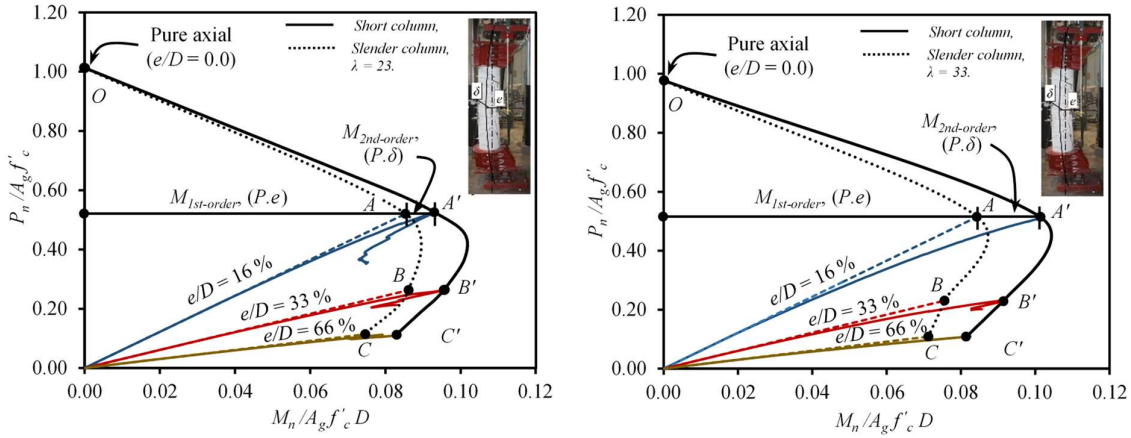

Figure 4.6– Experimental normalized load–normalized bending envelopes for slender GFRP-RC columns.

Given the fundamental assumptions of reinforced-concrete mechanics, five additional assumptions were applied: (1) A column's deflected shape can be approximately defined using a half-sine wave; (2) FRP bars have a linear elastic stress–strain response up to failure; (3) The contribution of FRP bars in compression is limited to the concrete's compressive strength. This assumption has been adopted by many other researchers and proved its applicability to predict the compressive capacity of FRP-RC members (Zadeh and Nanni 2017; Hadhood et al. 2017a, b, c, d, e; Guérin et al. 2018a, b); (4) The confinement effect is limited by the strength of eccentric slender columns (Martin et al. 1966) and is therefore neglected in the analysis; and

(5) The ACI 440.1R15 (ACI 2015) provisions for the ultimate concrete strain ε_{cu} are met (i.e., $\varepsilon_{cu}=0.003$). In addition, the concrete compressive stress–strain distribution could be accurately established by the unconfined three-parameter model proposed by Popovics (1973). The compressive stress (f_c) at the corresponding strain (ε_c) is expressed as

$$f_c = f_c'\left(\frac{n(\varepsilon_c/\varepsilon_o)}{n-1+(\varepsilon_c/\varepsilon_o)^n}\right) \tag{4.1}$$

where $\varepsilon_o=0.002$ is the concrete strain at the compressive strength of concrete f_c' and n is a curve-fitting factor equal to $0.8+f_c'/17$ in MPa.

In constructing a model for slender GFRP-RC columns, first suppose a pin-ended FRP-RC column with a circular cross section exposed to an eccentric axial load and bent in a single curvature, as shown in Figure (4.7). Based on the first assumption, the lateral deflection (y) can therefore be defined as

$$y = -y_{mid}\sin\left(\frac{\pi}{L}x\right) \tag{4.2}$$

where y_{mid} is the mid-height lateral deflection and x is the distance from the column base to the point at which the lateral deflection is calculated. Hence, the expression for the column curvature can be expressed by applying the second differentiation of the deflection as

$$y'' = y_{mid}\frac{\pi^2}{L^2}\sin\left(\frac{\pi}{L}x\right) \tag{4.3}$$

Substituting $x=l/2$ in Eq. (4.3) and solving for y_{mid} yields

$$y_{mid} = \frac{L^2}{\pi^2}y''_{mid} \tag{4.4}$$

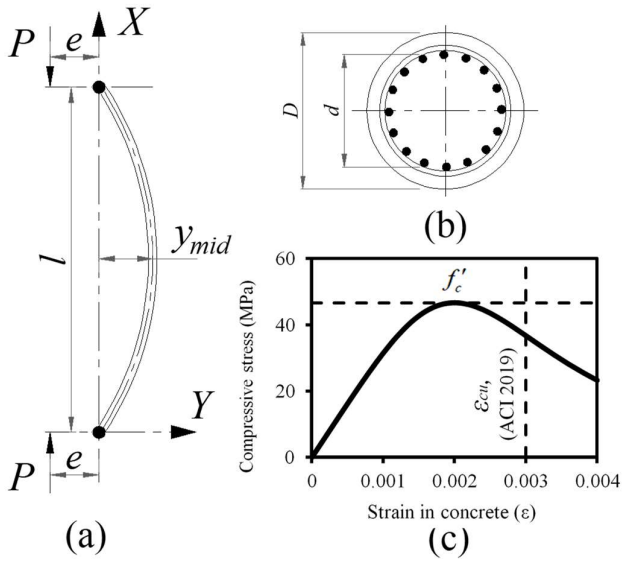

Figure 4.7– (a) Pin-ended column bent in a single curvature, (b) Column cross-section, (c) Concrete stress–strain model.

Equation (4) expresses the induced mid-height lateral deformation in terms of the corresponding column curvature and column overall height. Consequently, the mid-height bending moment (maximum expected value) considers the column's lateral deformation (i.e., the second-order effect) can be determined based on Eq. (4.5) as

$$M_n = M_{1^{st}-order} + M_{2^{nd}-order} = P\left(e + y_{mid}\right) \tag{4.5}$$

The analysis starts by assuming a lateral-displacement increment, so the corresponding curvature could be determined with Eq. (4.3) for $x = L/2$. Subsequently, a common strip-by-strip section analysis can be iteratively applied by assuming a strain value in the cross section and calculate the corresponding concrete and FRP internal forces using the stress–strain curves discussed above. The iterative process terminates when the ultimate moment calculated from the section analysis converges with the secondary moments of Eq. (4.5) with reasonable accuracy. Afterwards, another increment for the lateral displacement is set, and the process is repeated until plotting the whole loading path up to failure. Failure is defined either as the ultimate concrete predefined strain or when the FRP rupture tensile strain is achieved. Figure (4.8) shows a schematic flowchart of the analysis process.

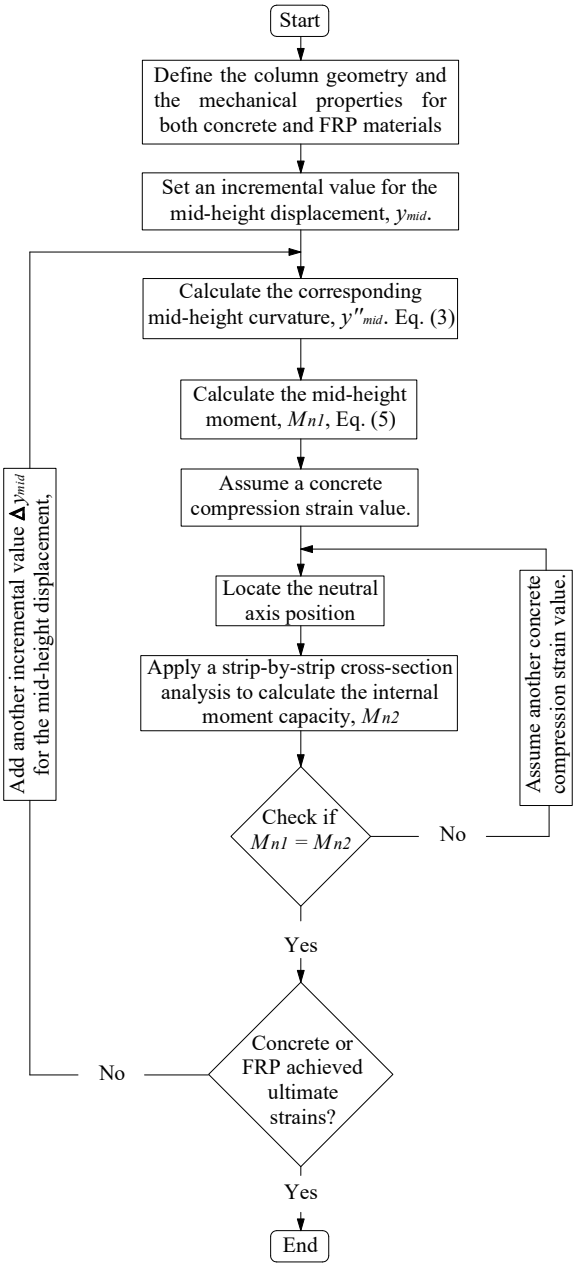

Figure 4.8– Schematic flowchart for the analysis process.

Figure (4.9) verifies the theoretically developed interaction diagram against test data. These data were obtained from the current study and the literature. The column specimens were used in the analytical model validation, covering various slenderness ratios, reinforcement ratios, concrete compressive strengths, shapes, and sizes of the column cross section. The proposed model for FRP-reinforced concrete columns substantially correlated with the selected

comprehensive experimental data. Then, the analytical model was employed to extend the experimental observations and thoroughly investigate the behavior of the comprehensive FRP-reinforced concrete columns as well as define slenderness lower and upper limits for design purposes.

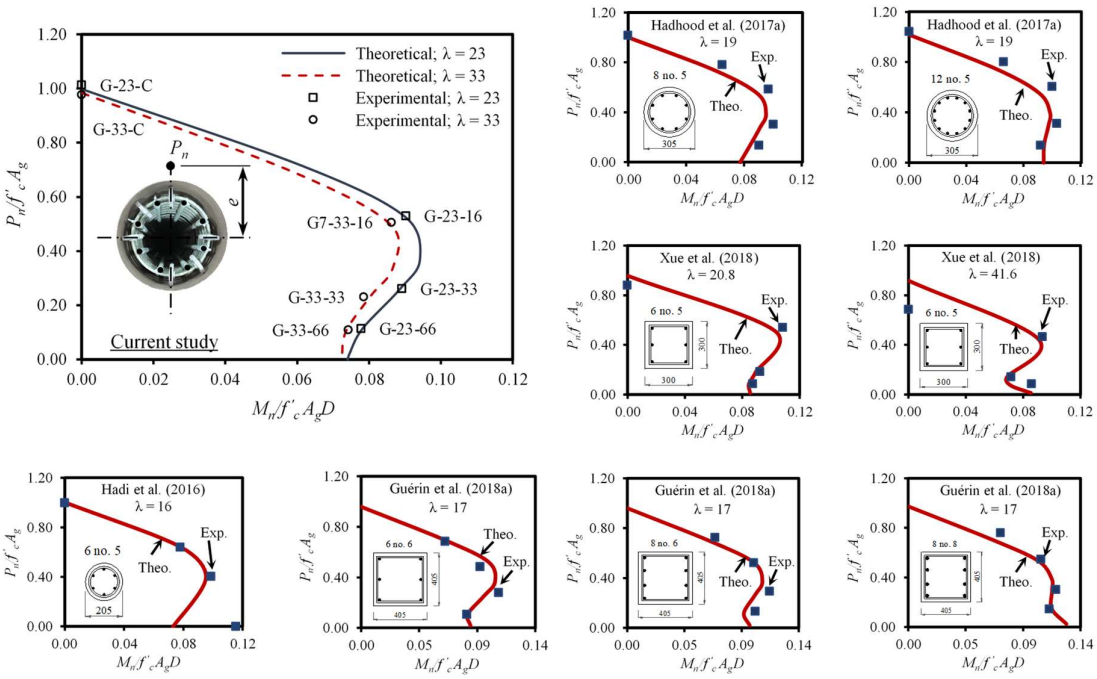

Figure 4.9– Verification of the theoretical interaction diagram with test results considering 2nd-order effects.

4.6 Proposed Slenderness Lower and Upper Limits

Lower and upper limits for slenderness ratios are required to eliminate insignificant second-order rigorous analysis and to prevent any undesired stability failures at excessive slenderness ratios, respectively. The stability or strength curves in Fig. (4.10) define the reduction in the ultimate capacity of slender RC columns (reinforcement ratio of 1%) in terms of normalized axial load and the slenderness ratio for a wide range of load eccentricity ratios. In the literature, these curves were commonly used to determine the slenderness lower limits below the induced

second-order effects can be ignored (Mirmiran 1998; Mirmiran et al. 2001b; Mohamed et al. 2010). ACI 318-19 (ACI 2019) and CSA A23.14 (CSA 2014) set the slenderness lower limit for short columns as a 5% reduction in the maximum column capacity based on cross-section analysis, which was primarily developed by MacGregor et al. (1970). Alternatively, Eurocode 2 applies a 10% strength reduction to define the slenderness lower limit. Hence, the dashed and dotted lines in Fig. (4.10) define the boundary for the slenderness lower limit based on 5% and 10% strength reductions as specified in these guidelines and standards. The slenderness lower limits reach their lowest when the applied eccentricity ranges from 25% to 33%, which satisfies the experimental investigation outcomes. Moreover, the effect of changing the column slenderness ratio on the maximum axial column capacity vanishes at $e/D \geq 66\%$ which, also confirms the test results. The 5% dashed line defining the slenderness limit intersects the strength curves of $e/D = 25\%$ and $e/D = 33\%$ at a lowest slenderness value equal to 18.7. Therefore, and based on the developed strength curves in Fig. (4.10) confirming the observed experimental results, a value of 18 was conservatively proposed considering the ACI 2019 provisions for the slenderness lower limit of GFRP-reinforced concrete columns bent in a single curvature.

Manuel and MacGregor (1967) performed a numerical integration to define steel-RC column behavior under sustained loads. They concluded that, for a geometrical slenderness ratio of $L/t = 10$ ($kL/r = 29$), sustained loading had little effect on the failure loads compared to the corresponding values under short-time loading. Moreover, Chovichien et al. (1973) conducted an analytical study to investigate the effect of the level of sustained load on short and slender steel-RC columns. Chovichien concluded that, in a braced frame, there is no strength reduction due to sustained loads for a geometrical slenderness ratio of $L/t = 10$ ($kL/r = 29$). Therefore, the effect of sustained loads in terms of creep parameter was ignored for the current study. Further research is needed to provide a slenderness value at which the effect of sustained loads on FRP-RC columns is pronounced, such as those for steel-RC columns (Manuel and Macgregor 1967; Chovichien et al. 1973).

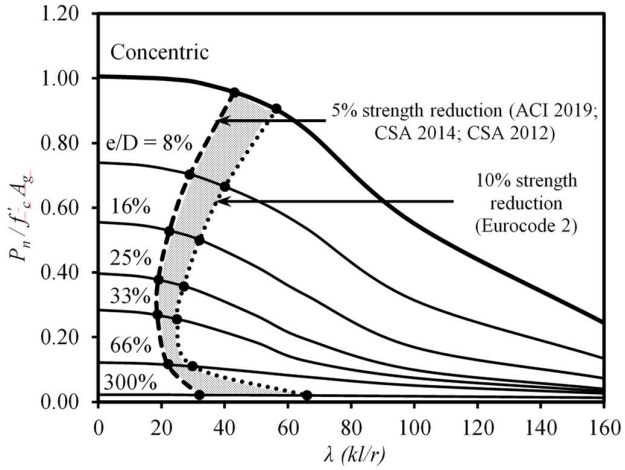

Figure 4.10– Effect of load eccentricity ratio on the strength curves of GFRP-reinforced concrete columns.

On the other hand, the upper limit for the column slenderness ratio specifies when RC columns need accurate analysis and the approximate analysis methods in guidelines—such as the moment-magnifier method in ACI 2019—are far from accurate. MacGregor et al. (1970) proposed a constant slenderness upper limit for steel-reinforced concrete columns of 100, regardless of loading type or column boundary conditions. This limit corresponds to the upper range of slenderness ratios for the columns tested in frames. CSA A23.3-14 (CSA 2014) applies the slenderness upper limit of 100, primarily proposed by MacGregor et al. (1970), to the design limitations of steel-reinforced concrete columns exposed to second-order effects. Conservatively, MacGregor and Hage (1977) conducted a stability analysis on concrete frames and showed that the probability of stability failure increases when the stability index approaches 0.2. That correlates with a secondary-to-primary moment ratio of 1.25. Alternatively, ACI 318-19 (ACI 2019) defines a stability index of 0.25 at which the probability of stability failure increases rapidly. This stability index corresponds to a secondary-to-primary moment ratio of 1.33. Thus, ACI 2019 attributed the upper limit for the slenderness ratio of steel-reinforced concrete members to a secondary-to-primary moment ratio of 1.4.

Figure (4.11) defines the stability and material failure modes of the GFRP-reinforced concrete columns at a constant eccentricity and various slenderness ratios. In the case of the not overly slender columns $(\lambda < 50)$, all reached their maximum axial capacity (failed) at a point tangent

to the envelope of the cross-section strength. This defines the case of material failure. On the other hand, the failure (peak) for overly slender columns $(\lambda > 50)$ occurred early before the ultimate cross-section strength was achieved due to the significant second-order effects. This is called stability failure. Now, it is clear that column stability failure initiates at a slenderness ratio close to but less than 50. To precisely define the upper limit for the slenderness of GFRP-reinforced concrete columns at which stability failure initiates, Fig. (4.12) provides the $M_{2^{nd}-order}/M_{1^{st}-order}$ and slenderness-ratio relationship at different eccentricities. Then, ACI 2019 provisions were followed and the slenderness upper limit was located at $M_{2^{nd}-order}/M_{1^{st}-order}$ being equal to 40%. Consequently, the proposed upper limit for the slenderness ratio ranges from 42 to 60 for e/D ranging from 8% to 66%, respectively.

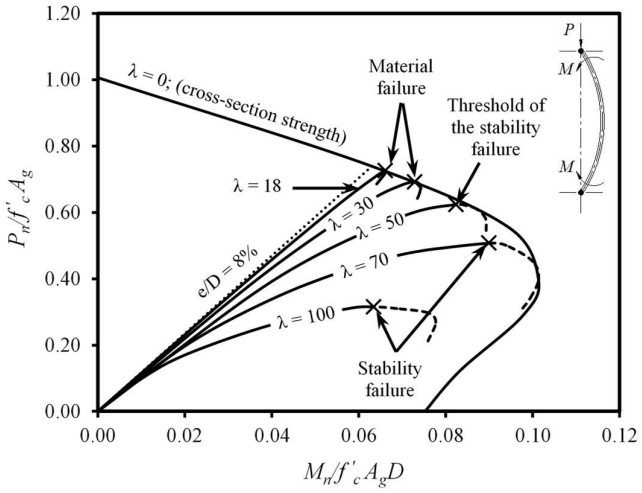

Figure 4.11– Definition of material and stability failures.

4.7 Theoretical Investigations

Figure (4.13) plots a family of theoretically developed interaction diagrams for GFRP-reinforced concrete columns depicting the influence of various slenderness ratios on the ultimate load-to-moment relationship. The axial applied load and the corresponding moment are normalized to f'_cA_g and f'_cA_gD, respectively. The plotted interaction diagrams were found to agree well with those based on the fiber-element model developed by Mirmiran (1998). The

predicted interaction diagrams also compare the current lower slenderness limit of CSA S806-12 (CSA 2012) and the proposed one to the full cross-section strength. The hatched area defines the beam region where the member behavior is more consistent with beam-analysis theories.

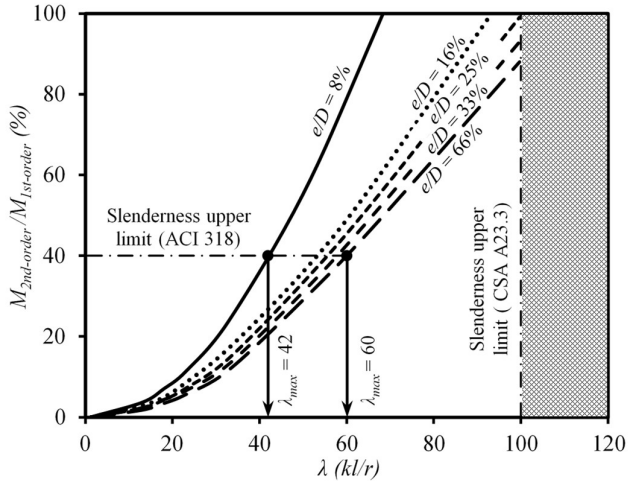

Figure 4.12– Proposed slenderness upper limit for GFRP-reinforced concrete columns on the basis of ACI 2019 provisions.

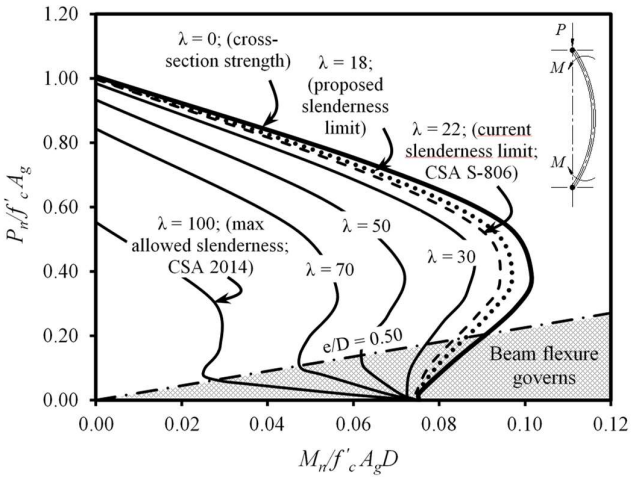

Figure 4.13– Comparison of the proposed and current slenderness lower limits.

Regarding the shape of the failure surface, all the GFRP-reinforced concrete columns had an inflection point at which the column bending moments and axial loads started to decrease

simultaneously. The same point is defined for steel-reinforced concrete columns as a balanced point that differentiates the tension (steel yielding) and the compression (concrete crushing) failure modes. A second inflection point occurred in the columns with slenderness ratios equal to 50 or higher. At this second inflection point, the failure path for all the columns tended to reach a similar bending capacity.

Figure (4.14) displays the effect of the applied eccentricity to the column axial capacity. Except for the columns with $\lambda > 70$ at an eccentricity level of less than 25% of the cross-section size, all the columns tended to abruptly lose their carrying capacity with an average decreasing rate approximately equal to 2.4% of the peak for each 1% increase in the e/D. Afterwards, this sharp reduction became nonlinear and smoother until reaching $e/D = 60\%$. Then, no further reduction in the column axial strength occurred. The vertical dash-dotted line at $e/D = 50\%$ represents the margin for the applicability of beam flexure theories according to Jawaheri Zadeh and Nanni (2017). This limit may be conservatively shifted to $e/D \geq 60\%$ based on current investigations.

Figure (4.15) shows the contribution of GFRP bars to the overall carrying capacity of the GFRP-reinforced concrete columns. The GFRP-bar contributions to the axial capacity $P_{n(FRP)}$ and the corresponding contribution to the bending moments $M_{n(FRP)}$ are defined as the column full strength less the concrete contribution. In the case of both the short $(\lambda \leq 18)$ and slender $(\lambda > 18)$ GFRP-reinforced concrete columns, FRP reinforcement effectively participated in the columns' ultimate strength for all the slenderness ratios tested. Up to an e/D close to 16%, where the cross section was under full compressive stresses, the FRP-bar contribution was identical for all the slenderness ratios and could be calculated as $A_{FRP} f_c'$, where A_{FRP} is the total nominal area of FRP bars (see Table 4.2). Once, the column cross section experienced tensile stresses, either due to direct loading or secondary moments, the FRP internal reinforcement contributed even more. The moment contribution of the FRP bars to the full moment capacity increased, on average, from 7% at $e/D = 25\%$ to 26% at $e/D = 60\%$ for columns with a slenderness ratio of $\lambda \leq 33$.

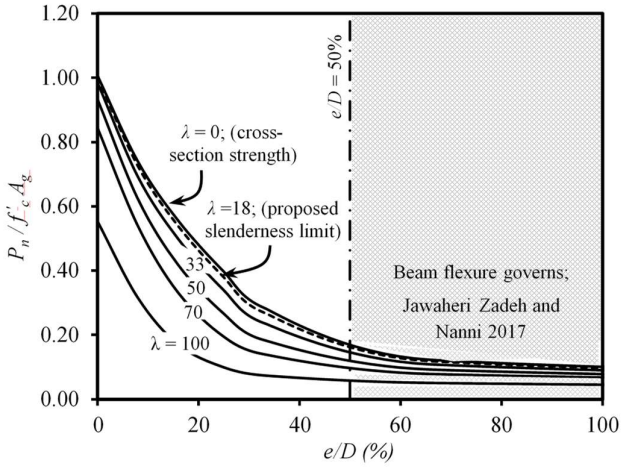

Figure 4.14– Normalized applied load versus the load eccentricity ratio.

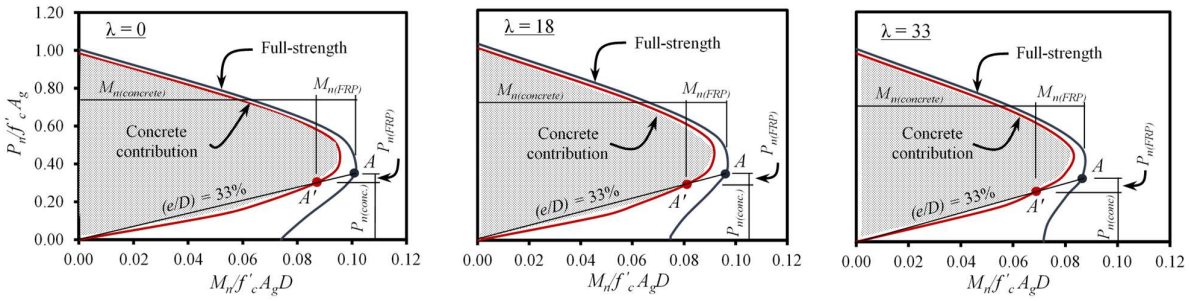

Figure 4.15– Concrete and GFRP reinforcing bars contribution to the ultimate capacity of the GFRP-RC columns with various slenderness ratios.

4.8 Conclusions

Based on the conducted experiments and the developed model, the following conclusions can be made.

1. Regardless of the slenderness ratio, the GFRP-reinforced concrete columns tested under concentric or low $(e/D = 16\%)$ or moderate $(e/D = 33\%)$ eccentric loads exhibited a material-type failure, specifically concrete-cover spalling at peak followed by a significant

drop in column carrying capacity. Beyond peak, the tensile rupture of GFRP spirals, compression rupture of GFRP bars, and buckling of steel bars were observed at ultimate stages.

2. The failure mode attributed to the slender GFRP-reinforced concrete columns tested under large eccentric loading $\left(e/D = 66\%\right)$ was controlled by exaggerated tensile cracks, accompanied by excessive lateral deformations triggering large support rotation. This was metaphorically termed as tension-based failure.
3. The slender GFRP-reinforced concrete columns exhibited the outmost decay in load-carrying capacity at $e/D = 33\%$ compared to their GFRP-reinforced concrete counterparts tested under concentric loads or eccentric loads with $e/D = 16\%$ or $e/D = 66\%$. For example, the GFRP-reinforced concrete columns with slenderness ratios of 23 and 33 lost 8.3% and 19.1%, respectively, of their peak loads compared to the columns with a slenderness ratio of 19.
4. The model for slender GFRP-reinforced concrete columns proposed to mirror the second-order effects was verified with test results for 42 specimens and yielded an appropriate precise estimation of the axial and flexural capacities of slender concrete columns reinforced with GFRP bars, taking into consideration both material and geometrical nonlinearities.
5. Based on the experimental results, the database from the literature, and the developed analytical second-order model for columns entirely reinforced with GFRP bars, a slenderness limit of 18 was proposed for short GFRP-reinforced concrete columns bent in a single curvature. This proposed limit replaces the current limit of 22 in CSA S806-12 (CSA 2012).

6. Applying ACI 318-19 (ACI 2019) recommendations to avoid stability failure in steel-reinforced concrete columns to GFRP-reinforced concrete columns provided rational limits for the slender upper limits, while CSA A23.3-14 (CSA 2014) provisions were found to be far from accurate. Consequently, a slenderness upper limit corresponding to a secondary-to-primary moment ratio of 1.4 was proposed for GFRP-reinforced concrete columns, like that for steel-reinforced concrete columns.
7. Both the experimental observations and analytical investigations revealed that the columns loaded under $e/D > 60\%$ had an overall performance similar to that of flexural members. This eccentricity limit is proposed to replace the value of $e/D > 50\%$ found in literature.

Lastly, based on this study of the experimental program conducted and the developed second-order model for GFRP-reinforced concrete columns, the GFRP longitudinal-bar contribution to the column capacity and its provision of adequate stability can be described as “significant” over the wide range of parameters tested. Therefore, we recommend that GFRP reinforcement can safely replace traditional steel bars in both short and long columns provided the proposed limitations herein are complied with.

CHAPTER 5

Effect of Critical Test Parameters on the Behavior of GFRP-RC Slender Columns under Eccentric Load

Effet des paramètres critiques d'essai sur le comportement de poteaux élancés en béton armé de prfv sous charge excentrique

Foreword

Authors and Affiliation:

- **Waseem Abdelazim** is a doctoral candidate in the Department of Civil Engineering at the University of Sherbrooke, Sherbrooke, QC, Canada, J1K 2R1.
- **Hamdy M. Mohamed** is a research associate and lecturer in the Department of Civil Engineering at the University of Sherbrooke, Sherbrooke, QC, Canada, J1K 2R1.
- **Brahim Benmokrane**, **FACI**, is a Professor in the Department of Civil Engineering, Université de Sherbrooke, Sherbrooke, Quebec, Canada, J1K 2R1.
- **Mohammad Z. Afifi** is a postdoctoral fellow in the Department of Civil Engineering at the University of Sherbrooke, Sherbrooke, QC, Canada, J1K 2R1.

Journal Title and Paper Status:

Published in *ACI Structural Journal*, V. 117, No. 4, July 2020. *DOI: 10.14359/51723507*

Contribution to the Thesis:

The study presented in the manuscript includes twenty-two full-scale slender GFRP-RC columns which were tested to assess the impact of utilizing GFRP-reinforcement on slender

RC columns. Four test parameters were included in the study: slenderness ratio, eccentricity level, longitudinal-reinforcement ratio, and confinement ratio. The experimental investigations were extended using an analytical second-order model accounting for material and geometrical nonlinearities. Moreover, a value for permissible tensile design strain of the GFRP-bars was proposed to avoid stability failure.

Abstract

This paper intends to experimentally and theoretically support the North American technical committees engaged in developing design provisions for slender glass-fiber-reinforced-polymer (GFRP) reinforced-concrete (RC) columns. Consequently, 22 full-scale slender GFRP-RC columns with slenderness ratios of 23 and 33 were produced and tested at four different initial eccentricities (0%, 16%, 33%, and 66% of the column diameter). Moreover, the levels of GFRP-longitudinal and transversal reinforcement were also observed and are presented. During all testing phases, the GFRP-reinforcement proved its capacity to maintain stability and resistance to the applied loads. An analytical second-order model accounting for material and geometrical nonlinearities was then developed to extend the parametric study and include additional parameters such as the longitudinal tensile modulus of the GFRP bars. A model for slender GFRP-RC columns was developed by discretizing the section into several integration layers. The ACI stability index corresponding to the ratio of the secondary to the primary moment of 1.4 is applied to GFRP-RC columns to define the permissible tensile design strains at which acceptable lateral deformations are expected. The derived model correlated substantially with the test results. Lastly, based on the experimental results and the developed model, the permissible tensile design strain of the GFRP-bars was proposed to be limited to 0.9% to avoid stability failure.

5.1 Introduction

The current rapid development of high-strength materials and improved erection techniques has resulted in the design of more slender structures and, in turn, more slender members such as slender RC columns. Slender RC columns can be defined as having a noticeable strength reduction due to their high susceptibility to second-order responses compared to stocky or short columns. Moreover, ACI 318-14 defines steel-reinforced concrete columns as short or long based on the so-called "slenderness limit (λ)" below which second-order effects can be ignored. Beyond that limit, ACI requires performing a second-order analysis to account for pronounced slenderness effects.

Designers are relying more on glass-fiber-reinforced-polymer (GFRP) bars as an alternative to traditional steel reinforcement, especially, in areas with harsh environments. Therefore, current editions of North American design codes include comprehensive sections dealing with the design of slabs and beam members reinforced with GFRP-bars. Yet current standards either do not recommend integrating FRP bars into compression members (ACI 440.1R-15) or conservatively ignore their contribution to the capacity of such members (AASHTO 2018a; CSA S806-12). Furthermore, CSA S806-12 stipulates that slender columns shall not be permitted to have FRP longitudinal reinforcement. Consequently, enormous efforts are being deployed to provide sections considering the design of GFRP-RC columns in upcoming editions of FRP design codes. This, in turn, requires a large experimental database to assess the behavior of short and long GFRP-RC columns and to propose rational design limits to the code technical committees.

As a valuable step on the right direction, various researchers have extensively investigated the behavior of short FRP-RC columns over a wide range of test parameters (De Luca et al. 2010; Tobbi et al. 2012; Afifi et al. 2014; Tobbi et al. 2014; Mohamed et al. 2014; Hadi et al. 2016). In addition, Hadhood et al. (2017a, b, and c) conducted a series of experimental and analytical studies on the performance of short circular GFRP-RC columns ($\lambda = 19$) loaded at various initial eccentricities. All the tested columns experienced a material-type failure with a slight effect of second-order response. Thus, Hadhood et al. (2017a, b, and c) discarded second-order effects from the analysis. Guérin et al. (2018a, and b) tested 16 square pin-ended GFRP-RC

columns ($\lambda = 16$) under eccentric loads ranging from 10% to 80% of the column size. Two different types of GFRP-bars with two moduli of elasticity (51.3 GPa (7440.55 ksi) – GFRP-bar Type A, and 48.2 GPa (6990.93 ksi) – GFRP-bar Type B) were implemented in this research. Guérin (2018b) concluded that the second-order effect was insignificant over all the tested parameters.

Unlike with short GFRP-RC columns, little experimental work has focused on the behavior of slender GFRP-RC columns. Hales et al. (2016) conducted an experimental study on the behavior of slender circular high-strength RC columns reinforced with GFRP-bars under eccentric and concentric loading. A stability failure was indicated by the authors for slender columns ($\lambda = 49$) loaded at an initial eccentricity of 33% of the column diameter. The behavior of slender columns with lower slenderness ratios ($22 < \lambda < 49$) was not investigated. Recently, Xue et al. (2018) conducted concentric and eccentric loading tests on slender rectangular GFRP-RC columns (λ varied from 20.8 to 41.6). They concluded that all the tested columns exhibited concrete-crushing failure with no rupture of the FRP bars. Clearly, the research database has a paucity of data on the performance of slender GFRP-RC columns. This emphasizes the critical need for more experimental investigations on the behavior of slender GFRP-RC columns.

5.2 Research Significance

Forthcoming editions of North American FRP design codes will include sections dealing with the design of FRP-RC columns. Consequently, this research program attempted to provide comprehensive tests and analytical investigations of slender GFRP-RC columns in order to support the work of the relevant technical committees. Four test parameters were used to cover most practical cases of slender GFRP-RC columns, specifically slenderness ratio, applied initial eccentricity, longitudinal-reinforcement ratio, and confinement level. Then, the research was extended with an analytical second-order model to incorporate a broad range of test parameters and to support design recommendations. Lastly, limitations on the GFRP-bar

tensile design strains were proposed based on the mechanical properties of GFRP-bars on the market.

5.3 Experimental Program

5.3.1 Materials

All the columns were entirely reinforced with sand-coated GFRP-bars and spirals manufactured according to a pultrusion process using continuous glass fibers impregnated in a thermosetting vinyl-ester resin. Two bar sizes were used to reinforce the columns in the longitudinal direction: No. 5 GFRP-bars with a nominal area of 198 mm^2 (0.31 in.^{2}) and No. 6 GFRP-bars with a nominal area of 284 mm^2 (0.44 in.^{2}). Both bar sizes had an average elastic tensile modulus (E_{frp}) of 61.75 GPa (8,956 ksi) (Grade III in accordance with CSA S807-10). Number 3 Grade II (CSA S807-10) sand-coated GFRP-spirals (E_{frp} = 51.1 GPa (7,411 ksi)) with a nominal area of 71 mm^2 (0.11 in.^{2}) were used to transversally confine all the GFRP-RC columns. The average ultimate longitudinal tensile properties of the GFRP-materials were provided by the manufacturer, as reported in Table 5.1.

A single batch of ready-mixed normal-strength concrete with 10 mm (0.394-in.) maximum aggregate size was used to cast all the column specimens in an upright position. Prior to casting, all cages were inserted in the form tubes and a sufficient number of spacers were used to keep the cages in place during casting. Nine 100 mm × 200 mm (3.94 in. × 7.88 in.) standard concrete cylinders were prepared during column casting and cured under the same conditions as the column specimens. Afterwards, the concrete cylinders were tested on the same day as the start of testing of the column specimens. The measured average concrete compressive strength used in the analysis was 46 MPa (6,672 psi).

Table 5.1 – Mechanical properties of the GFRP reinforcement

Bar Size	Diameter (mm)	Area [1] (mm^2)	Fiber Content [2] (%)	Elastic Tensile Modulus [3] (GPa)	Nominal Tensile Strength (MPa)	Tensile Strain (%)
No. 3	9.5	71	78.9	51.1	1281	2.51
No. 5	15.9	200	83.6	61.8	1449	2.35
No. 6	19	284	84.0	61.7	1411	2.29

[1] Nominal area.
[2] According to the test method described in ASTM D2584 (temp 650°C, sand coating discarded from results).
[3] Average tensile properties were provided by the manufacturer (test method in CSA S806 Annex C).
Notes: 1 mm = 0.0394 in.; 1 MPa = 145.04 psi; 1 GPa = 145.04 ksi.

5.3.2 Test Matrix and Specimen Details

The experimental program consisted of 22 full-scale slender GFRP-RC columns and was conducted to investigate the performance of such columns given a wide range of test parameters. The parameters targeted herein were the slenderness ratio $(\lambda = kl/r)$, longitudinal-reinforcement ratio (ρ_L), confinement level in terms of the transverse reinforcement ratio (ρ_T), and the applied initial eccentricity-to-diameter ratio (e/D), where k is the effective length factor equal to unity (case of an ideal pin-ended column); l is the unsupported length of the column; and r is the radius of gyration of its cross section. The column slenderness ratio was determined in terms of column length as all the tested columns were 305 mm (12 in.) in diameter (D) with a clear concrete cover of 25 mm (1 in.). Two different column lengths of 1,750 mm (68.95 in.) $(\lambda = 23)$ and 2,500 mm (98.5 in.) $(\lambda = 33)$ were selected to define the zone of slender columns according to ACI 318-14 and CSA A23.3-14 provisions. The design of the longitudinal reinforcement was established to eliminate test complexity and provide minimum bar-size requirements as per the limits specified in ACI 318-14 and CSA S806-12, respectively. Therefore, three configurations of longitudinal reinforcement were used: 8 No. 5, 12 No. 5, and 12 No. 6 bars (ρ_L = 2.19%, 3.28%, and 4.66%, respectively).

As for the horizontal reinforcement, GFRP-spirals were designed to provide thorough confinement so as to avoid buckling of the longitudinal reinforcing bars. All the columns were

reinforced in the transverse direction with No. 3 GFRP-spirals, where the impact of the confinement level was tested in terms of the spiral pitch. Hence, four columns were fabricated and transversally reinforced with GFRP-spirals at 40 mm (1.58 in.) center-to-center spacing (less than $1/6$ of the core diameter; CSA S806-12) along the whole column height. The remaining 18 columns had the minimum confinement level as per CSA S806-12 requirements. Each column was divided into two regions: a middle region with a spiral pitch of 80 mm (3.15 in.) and top- and bottom-end regions (each 250 mm (9.85 in.) in length) with a tighter spiral pitch of 50 mm (1.97 in.) to prevent any premature failure near stress concentration zones, as shown in Fig. 5.1.

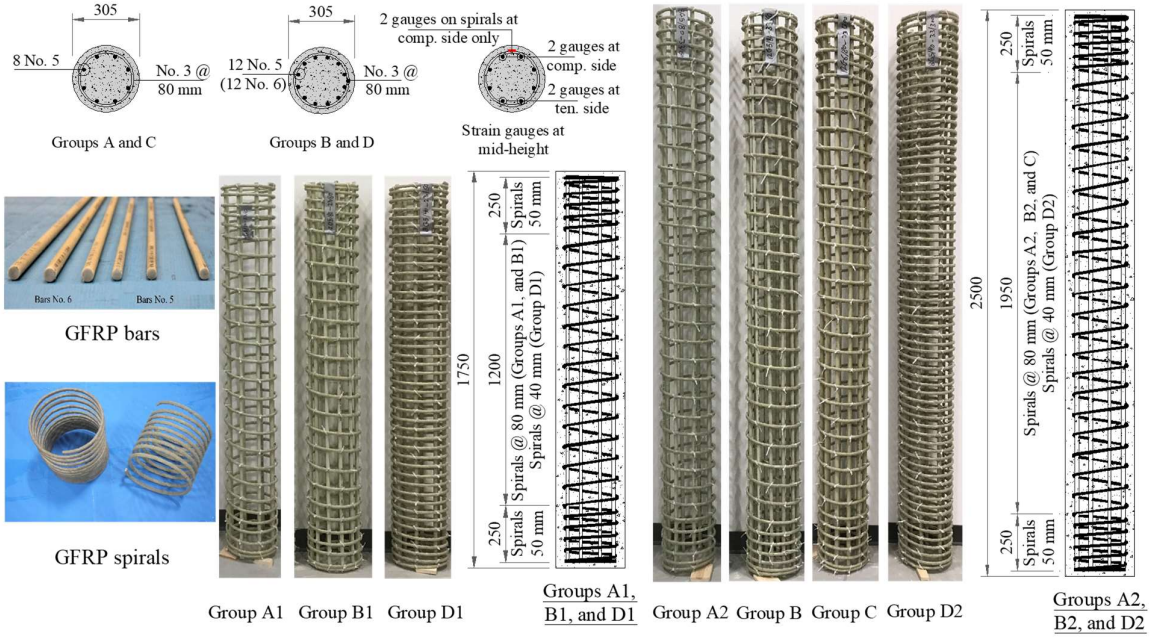

Figure 5.1– Geometry, reinforcement details, and internal instrumentation. (Note: Dimensions are in mm; 1 mm = 0.0394 in.).

All the columns were tested up to failure under monotonic static concentric and eccentric loading. In addition to the pure axial loading ($e = 0.0$), three levels of the applied eccentricity were predesigned and set to exhibit most of the expected failure modes as well as to define and develop an experimental interaction diagram for the tested slender GFRP-RC columns: $e/D = 16\%$ (low eccentricity), $e/D = 33\%$ (moderate eccentricity), and $e/D = 66\%$ (high eccentricity). All the column specimens were arranged as indicated in Table 5.2.

Table 5.2 – Test matrix and results

Group	Specimen ID	Geometry [1]		Longitudinal Reinforcement		Transverse Reinforcement			e (mm); e/D (%)	P_u $(kN)^2$	δ (mm)
		L (mm)	λ	Configuration	ρ_L (%)	Spiral size	Pitch	ρ_T (%)			
A1	GA-23-C	1750	23	8 No. 5	2.19	No. 3	80	1.17	C	3,453	0.8
	GA-23-16								50; 16	1,807	6.3
	GA-23-33								100; 33	891	12.2
	GA-23-66								200; 66	388	15.4
A2	GA-33-C	2500	33	8 No. 5	2.19	No. 3	80	1.17	C	3,331	2.9
	GA-33-16								50; 16	1,725	13.7
	GA-33-33								100; 33	786	22.2
	GA-33-66								200; 66	371	33.7
B1	GB-23-C	1750	23	12 No. 5	3.28	No. 3	80	1.17	C	3,463	0.6
	GB-23-16								50; 16	1,881	5.4
	GB-23-33								100; 33	1,029	9.7
	GB-23-66								200; 66	448	13.5
B2	GB-33-C	2500	33	12 No. 5	3.28	No. 3	80	1.17	C	3,360	2.6
	GB-33-16								50; 16	1,785	11.8
	GB-33-33								100; 33	898	21.2
	GB-33-66								200; 66	435	31.2
C	GC-33-C	2500	33	12 No. 6	4.66	No. 3	80	1.17	C	3,588	2.4
	GC-33-66								200; 66	489	29.3
D1	GD-23-C	1750	23	8 No. 5	2.19	No. 3	40	2.34	C	3,417	0.7
	GD-23-66								200; 66	420	18.2
D2	GD-33-C	2500	33	8 No. 5	2.19	No. 3	40	2.34	C	3,460	2.5
	GD-33-66								200; 66	374	34.6

[1] All columns measure 305 mm in diameter (D).[2] All listed test results are at the 1st peak load.
Notes: L is the column height, λ is the slenderness ratio; e is the initial load eccentricity; δ is the mid-height lateral displacement; P_u is the ultimate applied load. Notes: 1 mm = 0.0394 in.; 1 kN = 0.225 kpi

5.3.3 Instrumentation

Internal and external instrumentation was installed to monitor several column responses during the testing. Prior to installing the cage into form tubes, GFRP-bars and spirals were instrumented with strain gauges with a 6 mm gauge length to record the bar and spiral strains at column mid-height. As mentioned above, two loading patterns (concentric and eccentric)

were considered. Consequently, two different configurations for the location of the strain gauges on the longitudinal GFRP-bars and spirals were used conforming to each loading pattern (see Fig. 5.1). In addition to the strains in the longitudinal GFRP-bars and spirals, the concrete strains on the compression side were also monitored up to spalling of the concrete cover with 60 mm strain gauges attached at the column mid-height. Readings from the concrete strain gauges taken after concrete-cover spalling cannot be relied on. Therefore, two LPOTs were mounted vertically on two steel rods (300 mm apart) at the locations of the concrete strain gauges and embedded in the columns before casting the concrete to monitor the strains after the concrete cover spalled. The column buckling profile was defined at five levels along the whole column length as three linear potentiometers (LPOTs) were mounted horizontally at the mid- and quarter-heights, while the top and bottom column ends were restrained against lateral displacement by the machine head and the bottom rigid concrete floor, respectively. Lastly, the applied axial load and the machine-head axial displacement were measured with the machine's internal sensitive load cells and linear variable differential transformers (LVDTs), respectively.

5.3.4 Testing

Prior to testing, both ends of each column were capped with a thin layer of perfectly self-leveling high-strength cementitious grout to achieve uniform distribution of the applied loads. In order to avoid any undesired local failure in the loading regions, all the columns were confined with top and bottom rigid steel caps to enhance the confinement level at these stress-concentration zones. The steel caps were equipped with adjustable steel roller bearings to attain the pre-designated eccentricity as well as to replicate the case of a perfect pin-ended column: $k = 1$ (see Fig. 5.2). Then, the test specimen was placed into an 11,400 kN (2,565 kip) capacity MTS testing machine and aligned with the machine's loading axis. Afterwards, all internal and external instrumentation was connected to a data-acquisition system to record all readings during testing. Lastly, the testing started with a load-controlled technique at a rate of 2.5 kN/s (562.5 lb/s), up to 75% of the estimated specimen capacity. Then, the testing continued under displacement control at a displacement rate of 0.002 mm/s (7.87×10^{-5} in./s) up to failure.

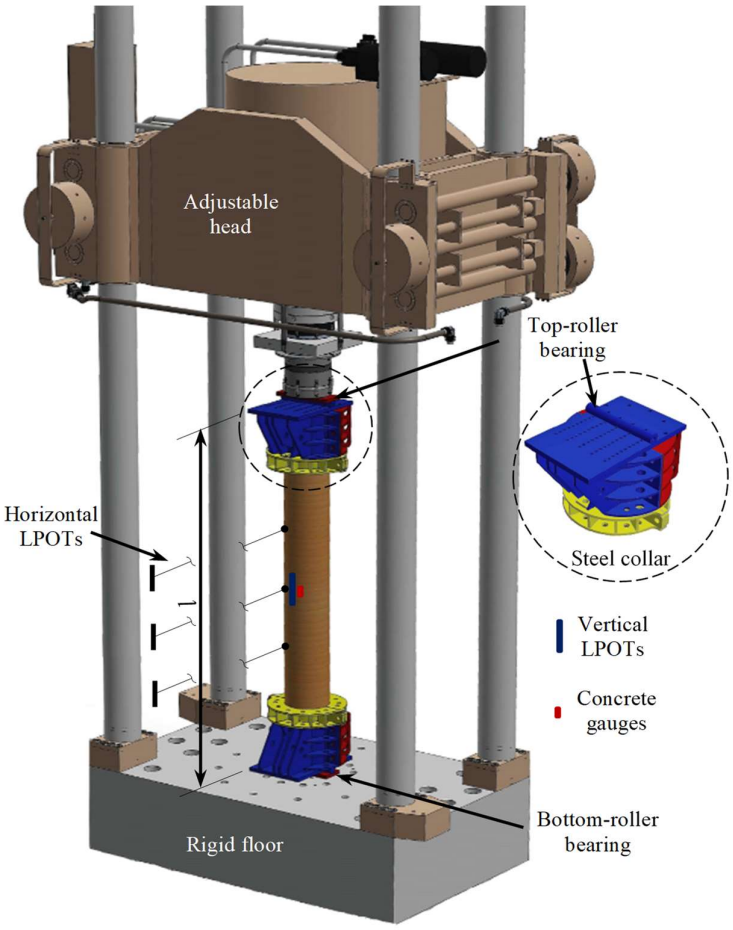

Figure 5.2– Test setup and testing machine.

5.4 General Observations and Failure Modes

Over the wide range of parameters tested, all the GFRP-RC columns adequately resisted the applied loads and provided sufficient stability during the various testing stages. In general, the failure mechanisms of the tested specimens were more influenced by the applied eccentricity than the other testing parameters. Figure 5.3 displays the different modes of failure observed for all the GFRP-RC columns. The following sections outline the test observations and the dominant failure experienced.

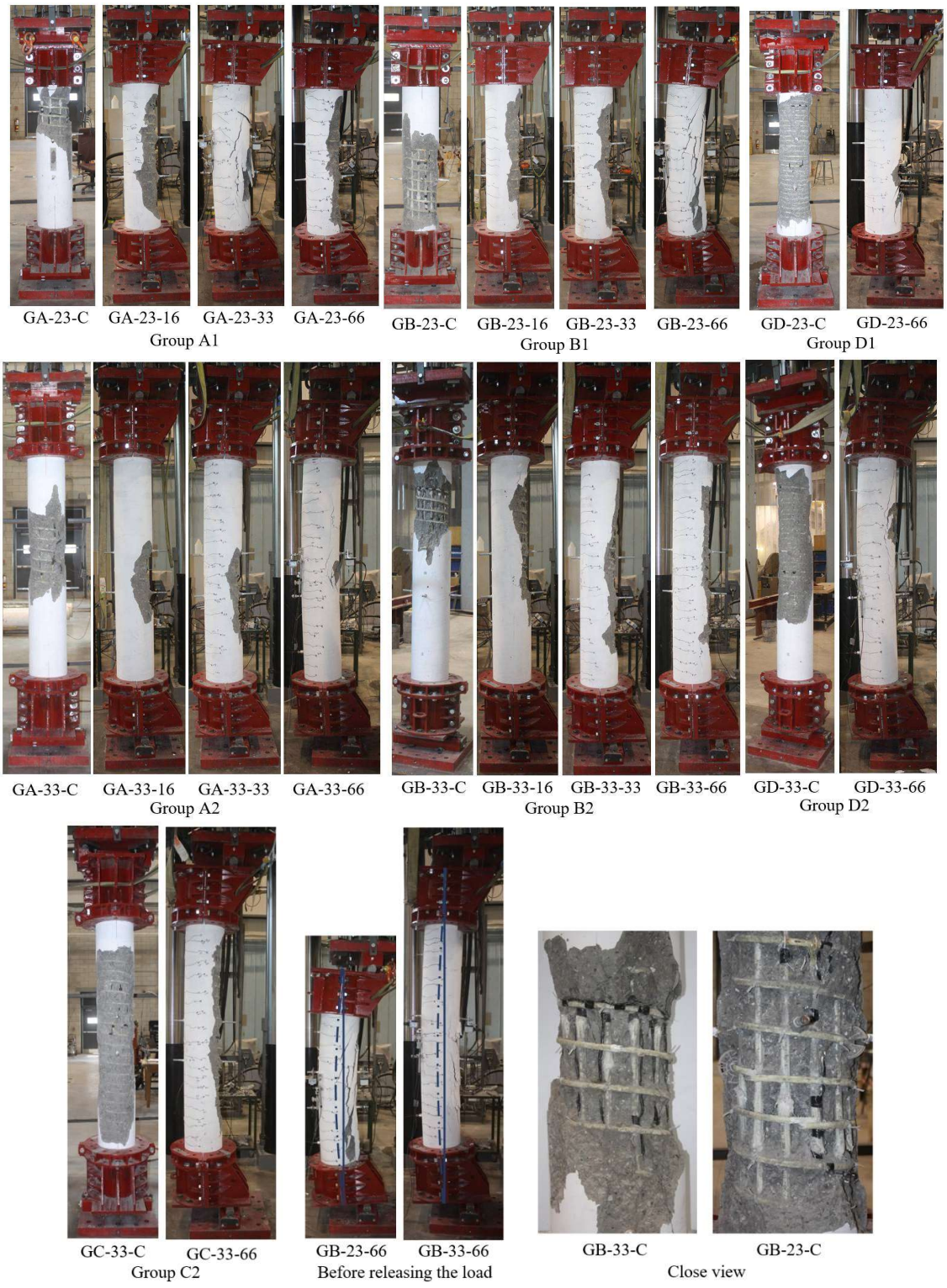

Figure 5.3– Failure modes.

5.4.1 Columns Loaded Axially and with Low Eccentricity

The GFRP-RC columns tested under concentric or low-eccentricity loading experienced a material-type failure with concrete crushing on the compression side initiated by gradual spalling of the concrete cover at peak, followed by a significant drop in column carrying capacity. As the load increased, the test specimens demonstrated elasticity up to approximately 75% of the maximum achieved peak load, regardless of the column slenderness ratio. None of the GFRP-RC columns had any visual cracks. Afterward, the specimens started to behave plastically up to and beyond peak. At almost 90 % of the peak load, limited vertical cracks started to initiate gradually until the concrete cover spalled and concrete compression failure occurred. Referring to Figure 5.4 (a), the average recorded compressive concrete strains at concrete crushing was of –2,700 $\mu\varepsilon$ ($1.23\varepsilon_o$) and –3,800 $\mu\varepsilon$ ($1.27\varepsilon_{cu-ACI}$) for the columns loaded concentrically and at low eccentricity, respectively, where ε_o is the concrete strain corresponding to the maximum concrete compressive strength and ranges from 1,900 to 2,500 $\mu\varepsilon$ for normal-strength concrete (Popovics 1973), and ε_{cu} is the ultimate strain in concrete in compression and specified as 3,000 $\mu\varepsilon$ and 3,500 $\mu\varepsilon$ in ACI and CSA provisions, respectively. Unlike in the axially loaded specimens and with respect to specimens with an initial eccentricity near the kernel $\left(e/D = 16\%\right)$, concrete tensile strains were observed when these specimens were loaded close to 50% of their ultimate capacity. Moreover, with respect to the columns loaded at low eccentricity, the average tensile strains in the GFRP bars were 550 $\mu\varepsilon$ and 620 $\mu\varepsilon$ at peak for $\lambda = 23$ and $\lambda = 33$, respectively, as illustrated in Fig. 5.4(c). Once the tensile strains reached the concrete rupture strains, limited horizontal tensile cracks were observed on the tension side of the specimens tested at low eccentricity $\left(e/D = 16\%\right)$. This was near to 95% of the maximum bearing capacity with tensile bar strains approximately equal to 410 $\mu\varepsilon$. The maximum peak load achieved occurred with the concentrically loaded specimens with an average value of 3,440 kN (774 kip) (see Table 5.2). At $e/D = 16\%$, the specimen carrying capacity dropped to around 52% (1,770 kN (398.25 kip)) compared to the axially loaded members. Up to peak point, the GFRP-reinforcing bars and spirals did not exhibit any compression failure. Beyond peak, the other testing parameters dominated the state

of the descending loading branch. At the end of testing, specimen failure was dominated by either GFRP-bar compressive rupture, spiral tensile rupture, or both, as depicted in Figure 5.3. At the ultimate stage, the GFRP-bars in specimens GA-23-16, GB-23-16, and GD-23-C were able to sustain compressive strains exceeding –13,000 $\mu\varepsilon$ (55% ε_{frpu}) before bar rupture occurred, if any. Similarly, the ultimate recorded compressive bar strains of the specimens with higher slenderness ratios ($\lambda = 33$) were, on average, –11,500 $\mu\varepsilon$ (49% ε_{frpu}).

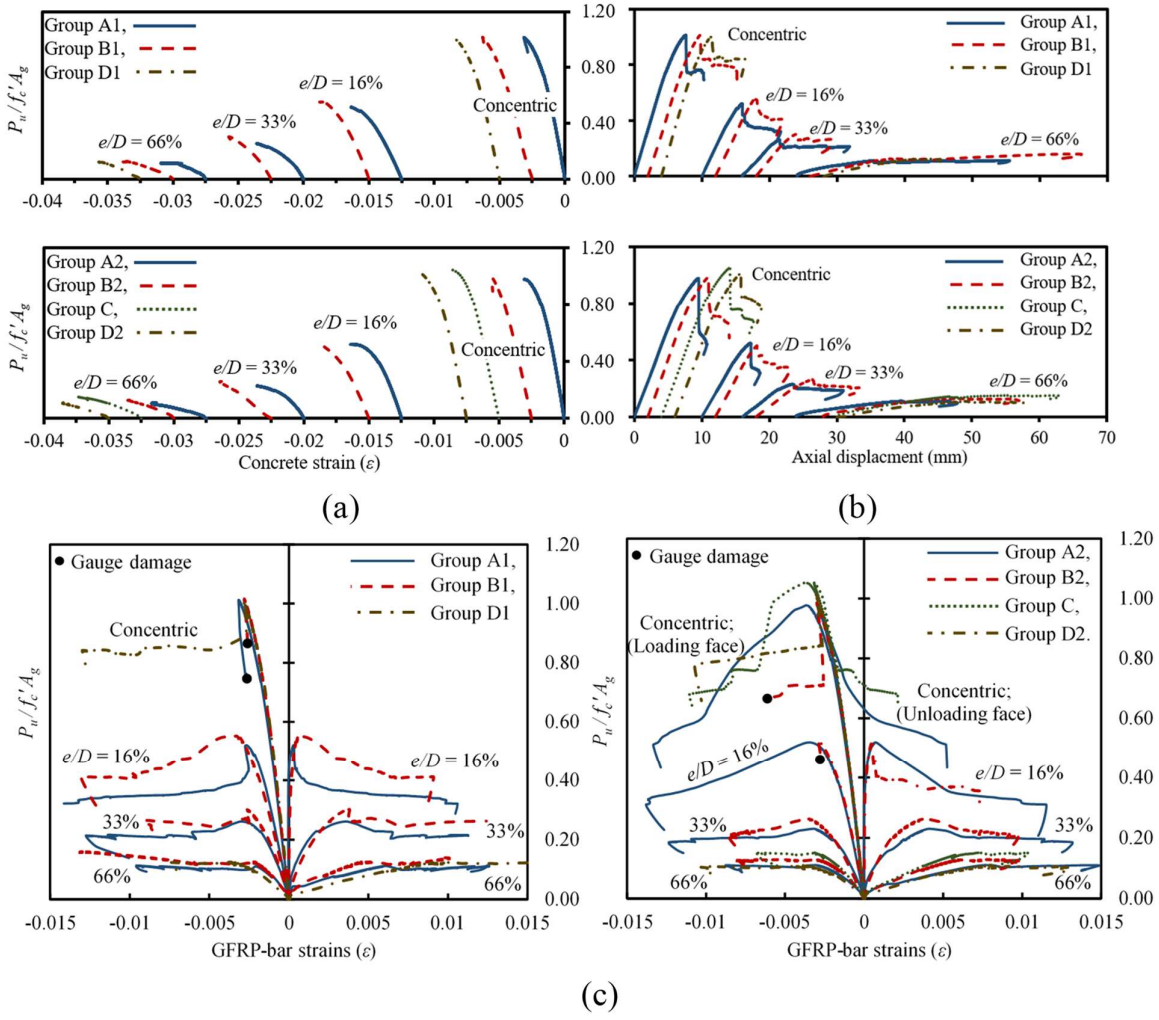

Figure 5.4– Normalized applied load versus: (a) concrete compression strain at mid-height; (b) axial-displacement response; and (c) longitudinal-bar strain. (Note: 1 mm = 0.0394 in.)

5.4.2 Specimens Loaded at Moderate Eccentricity

The GFRP-RC columns tested at an initial $e/D = 33\%$ exhibited concrete compression failure, preceded by early tensile concrete cracks (compared to specimens loaded at low e/D). Once the load was applied, mid-height tensile cracks initiated at around 400 kN (90 kip), representing 40% and 48% of the maximum load level at an average GFRP-bar tensile strain of 510 $\mu\varepsilon$ and 550 $\mu\varepsilon$ for the columns with slenderness ratios of 23 and 33, respectively. As the load continued, the cracks widened and propagated along the whole column height causing a noticeable degradation in the concrete compression block. Meanwhile, the column load–axial displacement response deviated from linearity at approximately 70% of the maximum attained strength. On average, the ultimate load of the columns loaded at moderate eccentricity was 26% of the axially loaded columns. Moreover, specimens GA-23-33, GA-33-33, GB-23-33, and GB-33-33 experienced concrete compression strains, at failure, of –4,440 $\mu\varepsilon$ ($1.48\varepsilon_{cu-ACI}$), –3,920 $\mu\varepsilon$ ($1.31\varepsilon_{cu-ACI}$), –3,770 $\mu\varepsilon$ ($1.26\varepsilon_{cu-ACI}$), and –3,680 $\mu\varepsilon$ ($1.23\varepsilon_{cu-ACI}$), respectively. In general, the axial stiffness of the test specimens was substantially influenced with the level of the applied eccentricity (see Figure 5.4(b)). For example, the specimens tested at $e/D = 33\%$ exhibited axial stiffness values 67% and 50% lower than the specimens tested with concentric and low eccentric loading, respectively. Lastly, the columns tested at moderate eccentricity experienced smooth failure and gradual concrete cover spalling with the GFRP-bars and spirals remaining intact until the end of testing.

5.4.3 Columns Tested at High Eccentricity

Seven GFRP-RC specimens were tested at an eccentricity of 200 mm (7.88 in.) ($e/D = 66\%$) located outside the column cross section. Accordingly, the impact of the eccentricity level was more pronounced, and all the tested columns behaved as flexural members regardless of column slenderness. Once this initial high eccentricity loading was applied, the columns experienced early formation of tensile cracks at a load level approximately equal to 24% (120 kN (27 kip), on average) of their ultimate bearing capacity. Soon after, cracks propagated along the column height and continued widening. These tensile cracks migrated inside the concrete

core towards the compression side, eliminating the concrete block under compression, causing a noticeable decrease in column axial and lateral resistance. Meanwhile, the compression side was free of any visual cracks up to 92% of the first peak load. At this high initial eccentricity, the columns' axial capacity abruptly declined to less than 12% (on average) of the axially loaded columns' strength.

After concrete-cover spalling at an average concrete strain of –4,000 $\mu\varepsilon$ ($1.33\varepsilon_{cu-ACI}$), a limited decay (7%, on average) in column strength was observed. The concrete compression failure did not, however, control the columns' ultimate capacity, and the GFRP-bars in the compression zone recovered lost strength and reached a second peak load with a slight average increase of 2% over the first peak. The tested specimen sustained exaggerated tensile cracks accompanied by excessive lateral deformations triggered by large support rotation. The test was halted for safety without any rupturing of the GFRP-reinforcement. At this stage, the GFRP-bars achieved an ultimate tensile strain greater than 15,000 $\mu\varepsilon$ (64% ε_{frpu}) without any tensile rupture. The compression face, however, recorded compressive-bar strains approaching –13,000 $\mu\varepsilon$ (55% ε_{frpu}), which clearly demonstrates that GFRP-bars can significantly contribute to column capacity without experiencing any compression failure.

ACI 318-14 classifies the failure of steel-RC members subjected to combined moment and axial force as compression- or tension-controlled failure if the strain in the extreme reinforcing bars is equal to 0.002 ($\varphi = 0.005/d$) or 0.005 ($\varphi = 0.008/d$), respectively. The latter curvature ($\varphi = 0.008/d$) is considered to give sufficient warning in terms of excessive deflections and exaggerated tensile cracks before complete failure occurred. Figure 5.5 provides the experimental strain gradient at peak load over the column cross-section at column mid-height. A linear strain distribution was assumed between the concrete compression surface and the extreme GFRP-bars on the tension side. The indicated experimental column curvature (φ) ranged from $0.010/d$ to $0.014/d$, from $0.007/d$ to $0.008/d$, and from $0.004/d$ to $0.005/d$ for $e/D = 66\%$, 33%, and 16%, respectively. Comparing ACI limitations with the test results and the observations discussed above, the failure of slender GFRP-RC columns tested at moderate eccentricity ($e/D = 33\%$) can be identified as a transition failure mechanism

between two extremes: compression-based ($e/D = 0$ and 16%) and tension-based failure ($e/D = 66\%$) governed by formation of excessive tensile cracks and large lateral deformations.

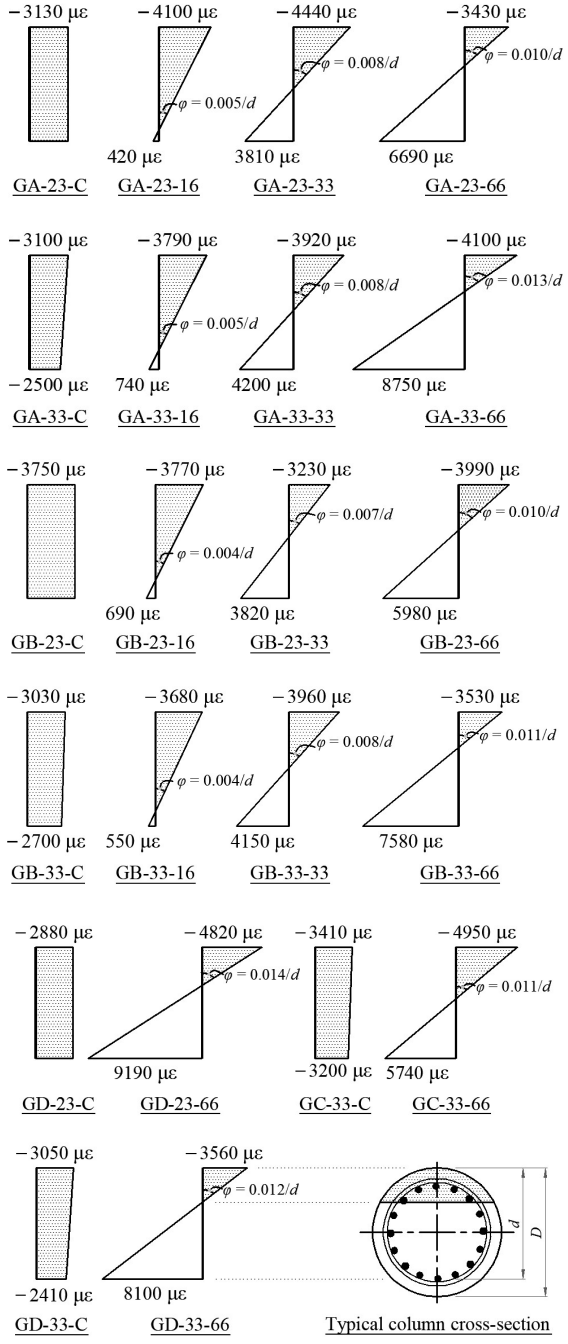

Figure 5.5– Mid-height linear-strain distribution over the column cross section at peak load.

Lastly, comparing the general failure mode of the tested slender GFRP-RC columns with the experimental research database of short GFRP-RC columns from literature (Afifi et al. 2014; Hadi et al. 2016; Hadhood et al. 2017a, b, and c; Guérin et al. 2018a, and b) would indicate that the slenderness ratio (λ) had limited and insignificant impact on the mode of failure when most of the tested specimens failed in a similar way to the short GFRP-RC columns found in literature. In other words, when the failure mechanisms were similar, the slender GFRP-RC columns had lower column capacity than the short GFRP-RC columns. This reduction in column capacity can be considered in design by applying a second-order analysis using the deformed geometry of the structure.

5.5 Effect of Test Parameters

5.5.1 Slenderness Ratio

Two slenderness ratios (23 and 33) were implemented to assess the behavior of the slender columns entirely reinforced with GFRP-bars. The effect of slenderness ratio on the axially loaded columns was insignificant up to a slenderness ratio of 23 at which point, the loading capacity of the GFRP-RC columns exceeded the cross-sectional strength ($1.01f_c'A_g$), where A_g is the column gross cross-sectional area. After that limit at $\lambda = 33$, and since the stress distribution was not perfectly uniform due to initial imperfections or an asymmetrical initiation of internal cracks, the column experienced buckling. At the start of buckling at 75% of P_{max}, the compressive strains on the concave (loading) face of the columns further increased, and the compressive strains on the convex (unloading) face decreased by a value of $\Delta\varepsilon$ (see Fig. 5.6). In the case of eccentric loading, the column experienced noticeable lateral deformations as the loading started and tensile cracks initiated (see Fig. 5.7). At the same eccentricity level, the slenderness ratio controlled the induced lateral deformations throughout all loading stages. Further, increasing λ from 23 to 33 approximately doubled the lateral deformations at peak load and, therefore, reduced column ultimate capacity due to the second-order effects arising. Moreover, the influence of slenderness ratio on the maximum column capacity was more

obvious at low $e/D = 16\%$ and moderate $e/D = 33\%$ levels of eccentricity than otherwise (see Table 5.2). This is consistent with the analytical results achieved by Mirmiran et al. (2001a).

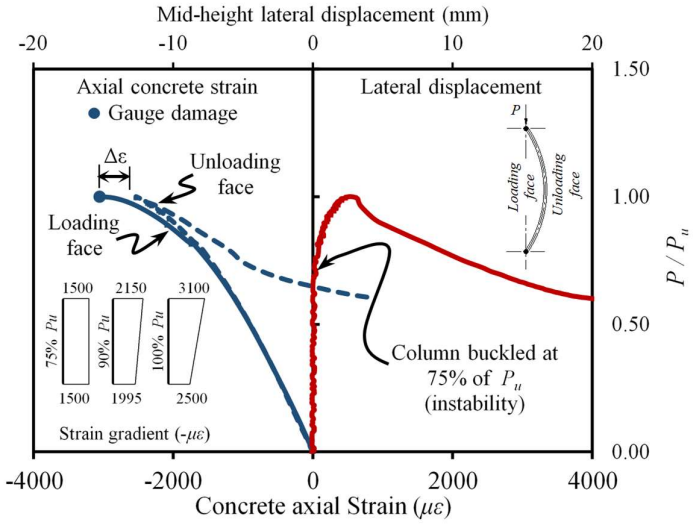

Figure 5.6– Axial-strain gradient and mid-height lateral displacement of specimen GA-33-C. (Note: 1 mm = 0.0394 in.).

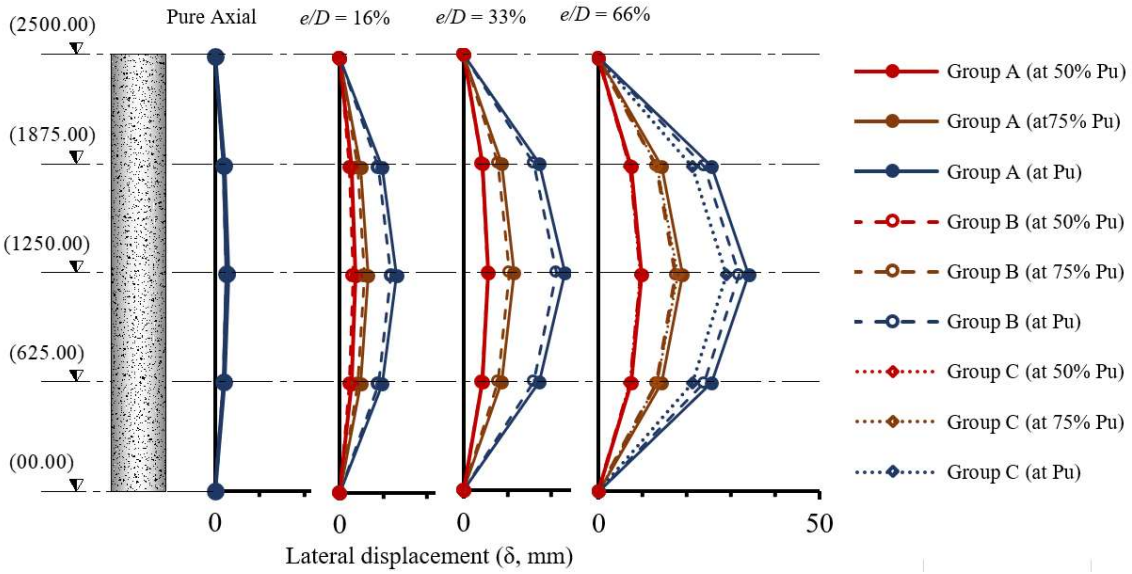

Figure 5.7– Effect of test parameters on the buckling profile for the GFRP-RC columns. (Note: levels are in mm; 1 mm = 0.0394 in.).

In addition, the specimens with higher slenderness ratios achieved lower load decreases beyond peak than the specimens with lower slenderness ratios (Fig. 5.4(b)). The columns loaded concentrically or at low eccentricity experienced drops in column capacity of 25% and 37% (on average) for the columns with $\lambda = 23$ and $\lambda = 33$, respectively. Finally, column slenderness had an insignificant effect on the measured concrete strains, as illustrated in Fig. 5.5.

5.5.2 Level of Applied Eccentricity

This section extends the above discussion on the effect of the eccentricity-to-diameter ratio on the slender GFRP-RC columns. As explained earlier, the more the tension cracks occurred early (when the cracked section properties governed overall specimen behavior), the more the column abruptly lost its axial capacity as well as axial and lateral stiffness. Consequently, for such cases ($e/D = 33\%$, and 66%), the exposure to higher lateral deformations were anticipated more at the early ages of loading, as indicated in Fig. 5.8(a), especially for the columns with lower slenderness ratios. Furthermore, Fig. 5.8(a) shows the effect of the test parameters—including applied eccentricity—on column axial strength. Among other things, the applied eccentricity had greater impact on column ultimate loads. Regardless of the column slenderness ratio or the amount of longitudinal reinforcement, the GFRP-RC columns retained only 52%, 26%, or 12% (on average) of their axial capacity when e/D of 16%, 33%, and 66% were applied, respectively. Moreover, it was obvious that the loss in the bearing capacity was more pronounced at high levels of e/D. The degradation in column capacity found at high levels is consistent with the test results reported by Hadhood et al. (2017a) and Guérin et al. (2018a).

5.5.3 Longitudinal-Reinforcement Ratio

This study investigated the effect of three reinforcement ratios: low (2.19%), moderate (3.28%), and high (4.66%). Given the same slenderness and applied eccentricity ratios (see Fig, 5), all the longitudinal GFRP-bars exhibited similar axial stiffness with a linear stress–strain distribution up to more than 80% of peak. In the axially loaded members (GA-23-C, GB-23-C, and GB-33-C), GFRP-bar failure occurred in a brittle explosive manner. In general, the

difference between the lower and higher reinforcement ratios was that the bars with the higher reinforcement ratios produced a longer descending loading branch. Under pure axial compression loading, the reinforcement ratio insignificantly affected column axial capacity. Increasing the reinforcement ratios improved concrete-core confinement and, thus, the post-peak behavior. CSA S806-12 determines the nominal unconfined axial-load capacity of GFRP-RC column based on the gross concrete column sectional area, minus the area of the GFRP-bars. Unlike CSA S806-12 approach, the experimental results herein showed that all the test specimens with a $\lambda \leq 23$ achieved capacity based on the total gross column area without deducting the area of the GFRP-bars. The latter observation is consistent with the recommendations provided by Zadeh and Nanni (2017), which limit the contribution of FRP bars in compression to the concrete compressive strength.

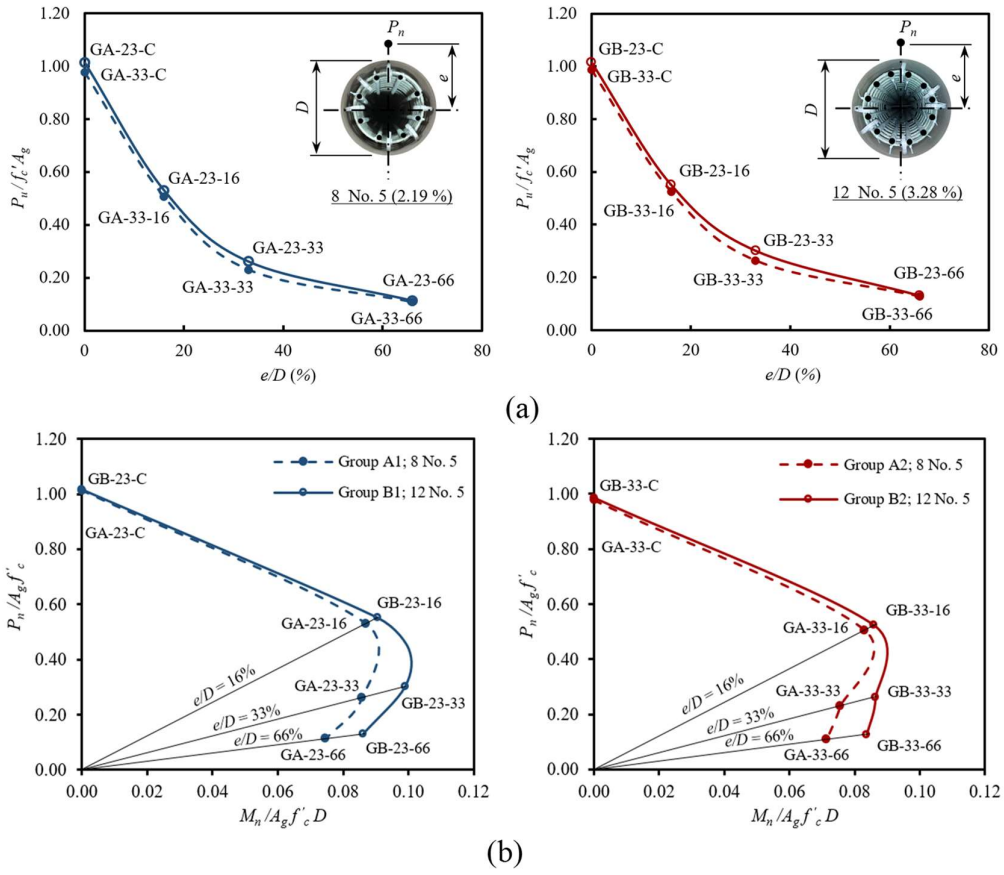

Figure 5.8– (a) Effect of the applied initial eccentricity on column ultimate bearing capacity; (b) experimental normalized load–normalized bending envelopes for slender GFRP-RC columns.

The GFRP-RC columns loaded under moderate (33%) to high eccentricity (66%) were more sensitive to the increase in longitudinal reinforcement ratios in terms of better resistance to the induced lateral deformations and enhanced flexural capacity. As shown in Fig. 5.8(b), increasing the reinforcement ratio from $\rho_L = 2.19\%$ to $\rho_L = 3.28\%$ enhanced the moment capacity of the slender GFRP-RC columns by 15.5% and 17.3% for $\lambda = 23$ and $\lambda = 33$, respectively. Furthermore, the measured mid-height lateral displacement at peak of columns GA-33-66, GB-33-66, and GC-33-66 was 33.7 (1.33), 31.2 (1.23), and 29.3 (1.15) mm (in.), respectively (see Fig. 5.7). This implies that GFRP-bar*s* can effectively improve the flexural stiffness of slender GFRP-RC columns and, as a result, can reduce the accompanied second-order effects. Lastly, the effect of the reinforcement ratio on bar tensile strains can be seen in Fig. 5.5. The maximum measured tensile strain at peak was recorded for specimen GD-23-66 and was approximately 9,190 $\mu\varepsilon$, which is less than 40% of the ultimate tensile strain (ε_{frpu}). In general, increasing the reinforcement ratio in terms of either number of bars or bar diameter significantly reduced the GFRP-bar tensile strains at peak loads, thereby amplifying the safety margins.

5.5.4 Confinement Level

Once the concrete cover spalled, the concrete core started to dilate, eliciting a passive confining pressure by the spirals. The GFRP-spirals confined the column concrete core in order to recover the load decrease due to the concrete cover spalling or to enhance the column's ability to experience higher lateral deformations, especially in the case of the concentrically loaded specimens. Until the test ended, the well-confined columns with tight spiral spacing or narrow bar spacing did not exhibit any crushing of the concrete-core components (transversal spirals, longitudinal bars, and concrete core).

Figure 5.9 explains the effect of the spiral-reinforcement ratios on spiral strains. At peak load, the GFRP-spirals had average tensile strains equal to 1,400 $\mu\varepsilon$ (5.6% ε_{su}) and 850 $\mu\varepsilon$ (3.4% ε_{su}) for light and heavy confinement, respectively, where ε_{su} is the ultimate tensile strain of the GFRP-spirals. The GFRP-spirals gained around 50% of the spiral strains at peak after reaching 90% of the maximum loading capacity, which made the spirals less effective along most of the

pre-peak loading path. At failure, the columns tested under concentric loads had average recorded GFRP-spiral strains of 7,000 $\mu\varepsilon$ (28% ε_{su}). In general, the slenderness ratio and applied initial eccentricity had limited effect on the spiral strains and could be described as insignificant. Regarding column capacity, the spiral volumetric ratio had a trivial effect on the ultimate strength and lateral displacement of the slender GFRP-RC columns. This was more evident for the columns loaded with initial high eccentricity (Fig. 5.7). Similar outcomes were reported by Martin et al. (1966) for eccentric slender steel-RC columns. Lastly, it is important to highlight that the spiral spacing of 40 mm (1.58 in.) yielded more gradual column failure than the wider spiral spacings.

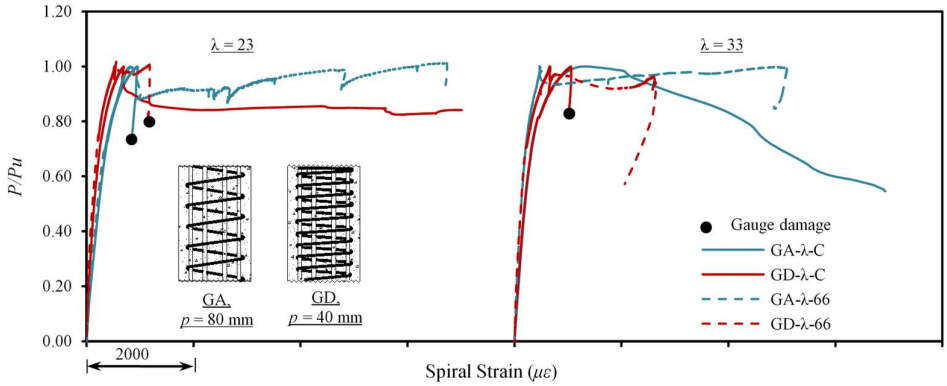

Figure 5.9– Effect of spiral pitch on the spiral-strain response for concentric and highly eccentric loading on slender GFRP-RC columns .

5.6 Inelastic Second-Order Modeling

Besides the force equilibrium and strain compatibility required for the analytical modeling of short columns, the modeling of slender and long columns requires the geometrical nonlinearities be integrated into the equilibrium equations when conducting a second-order analysis. Therefore, an analytical model for slender GFRP-RC columns was developed herein by discretizing the section into several integration layers. In addition to the fundamental assumptions of reinforced-concrete mechanics, additional assumptions were applied: (1) A column's deflected shape can be defined using a half-sine wave; (2) FRP bars have a linear

elastic stress–strain response up to failure; (3) The contribution of FRP bars in compression is limited to the concrete's compressive strength. This assumption has been adopted by many other researchers and proved its applicability to predict the compressive capacity of FRP-RC members (Zadeh and Nanni 2017; Hadhood et al. 2017a, b, c; Guérin et al. 2018a, b). (4) The confinement effect is limited by the strength of eccentric slender columns (Martin et al. 1966) and is therefore neglected in the analysis; and (5) The ACI 440.1R provisions for the ultimate concrete strain ε_{cu} are met (i.e., $\varepsilon_{cu} = 0.003$). In addition, the concrete compressive stress–strain distribution could be established by the unconfined three-parameter model proposed by Popovics (1973). The compressive stress (f_c) at the corresponding strain (ε_c) is expressed as

$$f_c = f_c'\left(\frac{n(\varepsilon_c/\varepsilon_o)}{n-1+(\varepsilon_c/\varepsilon_o)^n}\right) \tag{5.1}$$

where $\varepsilon_o = 0.002$ is the concrete strain at the compressive strength of concrete f_c' and *n* is a curve-fitting factor equal to $0.8 + f_c'/17$ in MPa.

Figure 5.10 considers the case of ideally hinged column bent in a single curvature. Then, the lateral deflection (y) at a distance *x* from the point of the mid-height deflection (y_o) can be expressed as

$$y = y_o \cos\left(\frac{\pi}{L}x\right) \tag{5.2}$$

where L is the total length of a half cosine wave. Therefore, the applied initial eccentricities at the column ends can be written in the form

$$e = y_o \cos\left(\frac{\pi}{L}\cdot\frac{l}{2}\right) \tag{5.3}$$

Solving for π/L yields

$$\frac{\pi}{L} = \frac{2}{l}\cdot\arccos\left(\frac{e}{y_o}\right) \tag{5.4}$$

Then, taking the derivative of π/L with respect to y_o and multiplying both sides by $y_o/(\pi/L)$ results in

$$\frac{y_o}{\left(\frac{\pi}{L}\right)}\cdot\frac{d\left(\frac{\pi}{L}\right)}{dy_o}=\frac{y_o}{\left(\frac{\pi}{L}\right)}\cdot\frac{2}{l\cdot y_o}\left(\frac{2e}{y_o\sqrt{1-\frac{e^2}{y_o^2}}}\right) \tag{5.5}$$

Substitute for e from Eq. (5.3) in Eq. (5.5) and rearranging the terms by applying the trigonometric function of $\cot\theta=\cos\theta/\sqrt{1-\cos^2\theta}$, Eq. (5) reduces to

$$\frac{y_o}{\left(\frac{\pi}{L}\right)}\cdot\frac{d\left(\frac{\pi}{L}\right)}{dy_o}=\left(\frac{\cot\left(\frac{\pi l}{2L}\right)}{\frac{\pi l}{2L}}\right) \tag{5.6}$$

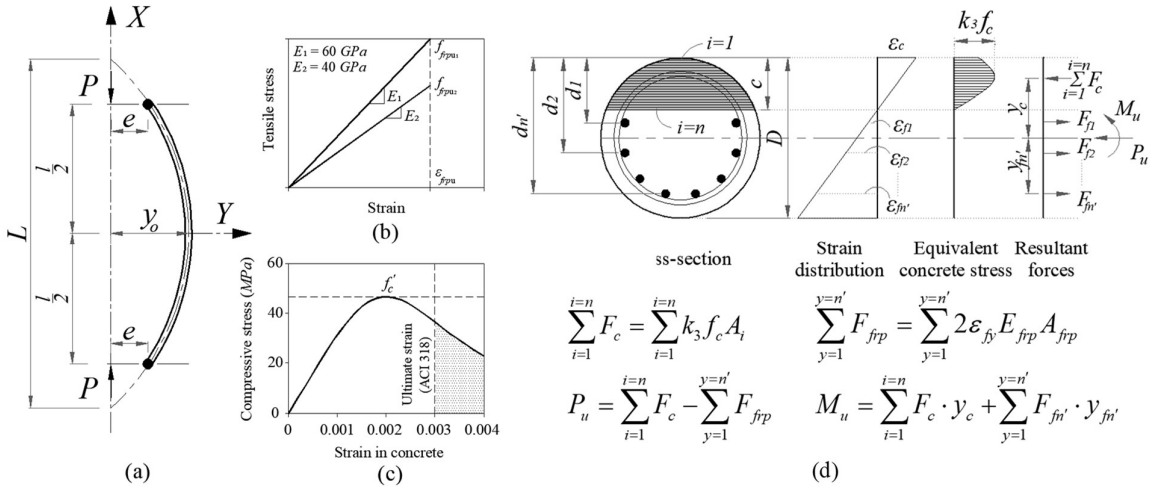

Figure 5.10– (a) Deflected shape for an ideally hinged column bent in a single curvature; (b) GFRP-linear stress–strain diagram; (c) concrete stress–strain model; (d) A strip-by-strip cross-sectional analysis.

This provides the second-order model for a column bent in a single curvature with equal end eccentricities. For other loading cases, refer to Mirmiran et al. (2001a). The left-hand side of

Eq. (5.6) can be represented considering the relation between the column curvature φ_o and the deflection y_o at column mid-height as

$$\varphi_o = y_o \left(\frac{\pi}{L}\right)^2 \tag{5.7}$$

Taking the derivative of φ_o and substituting with $y_o = M/P$, the left-hand side of Eq. (5.6) is written as

$$\frac{1}{2}\left(\frac{M/\varphi_o}{dM/d\varphi_o} - 1\right) \tag{5.8}$$

Then, the final form of the analytical model for slender GFRP-RC column can be

$$\frac{1}{2}\left(\frac{M/\varphi_o}{dM/d\varphi_o} - 1\right) = \frac{\cot\left(\frac{\pi l}{2L}\right)}{\frac{\pi l}{2L}} \tag{5.9}$$

An incremental-iterative process was performed to plot a series of $M-\varphi_o$ diagrams for various axial-load levels. At each load level, an incremental value for the concrete compressive strain was set and the corresponding curvature was assumed. Then, the common strip-by-strip sectional analysis (described in Fig. 5.10(d)) was applied and the equilibrium of the corresponding concrete and FRP internal forces (calculated using the stress–strain relations discussed above) were verified. After the equilibrium of internal forces was achieved, the previous steps were repeated using another strain increment up to failure being triggered either by concrete crushing or rupture of the FRP bars. Thereafter, the axial-load level was increased until the column failed in pure compression. The *P–M* interaction diagram of the short column was constructed using the maximum moments at each load level. In order to develop a moment–thrust interaction diagram for a slender column, for each load level, the corresponding moments were calculated as $P \cdot e$, where e is the initial load eccentricity determined from Eq. (5.3). The total length of a half cosine wave (L) in Eq. (5.3) can be calculated with Eq. (5.6) or Eq. (5.9), where the left-hand side of Eq. (5.9) is a function of the moment and curvature of the short column.

Figure 5.11 compares the failure envelope plotted with the analytical model to the test results from our study. The model developed for FRP-RC columns correlated closely with the experimental data. Then, the analytical model was employed to extend the experimental observations and thoroughly investigate the behavior of the slender GFRP-RC columns. The analytical investigations performed herein cover the effect of the column slenderness ratio, eccentricity-to-diameter ratio, longitudinal-reinforcement ratio, and elastic tensile modulus on the behavior of the slender GFRP-RC columns. Table 5.3 lists the values for the targeted parametric study.

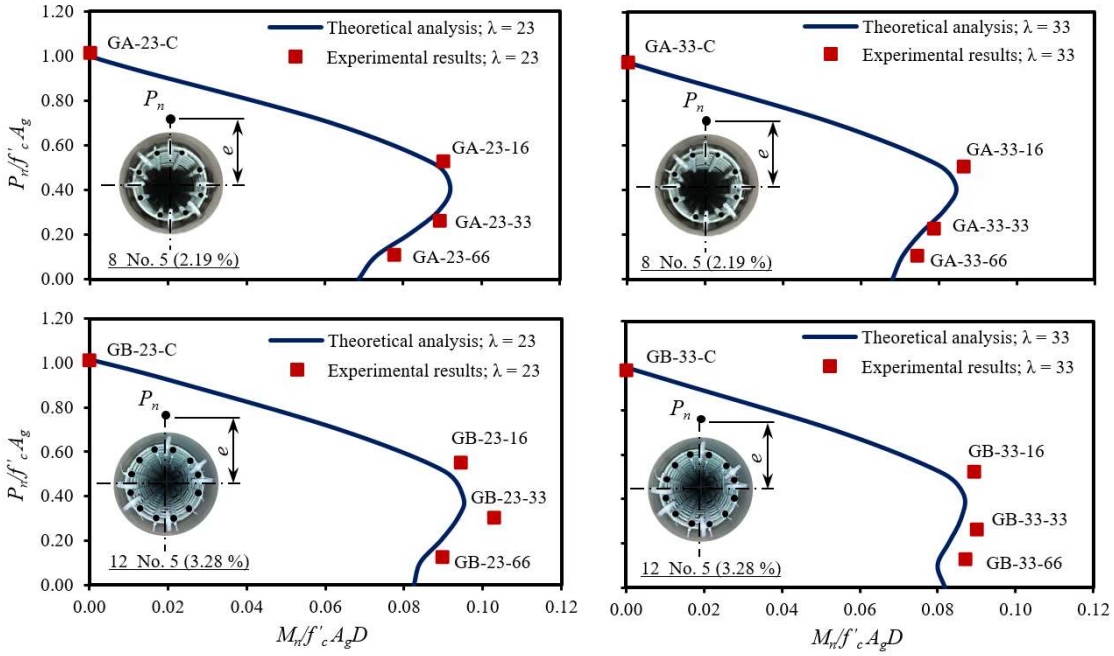

Figure 5.11– Verification of the analytical failure envelope with the experimental results.

Figure 5.12 examines the effect of selected parameters on the moment–thrust interaction considering the second-order effects, as derived earlier. The plotted interaction diagrams were found to be quite consistent with those based on the fiber-element model developed by Mirmiran (1998). Based on the experimental results, the slenderness ratio (up to $\lambda = 33$) had little impact on column capacity of both the perfectly axially loaded columns and the columns loaded with low axial-load levels. The proposed axial-load level at which GFRP-RC columns can be treated as flexural members is 10% of the column compressive strength $\left(0.1 f'_c A_g\right)$ based

on a longitudinal-reinforcement ratio of 1%. This limit approximately corresponds to $e/D > 0.6$. At this level of eccentricity, experimental observations showed that tested columns behaved as flexural members, as explained above. It is important to point out that ACI 318-14 tacitly classifies members subjected to axial loads less than $0.1f'_cA_g$ as beams (clause 9.3.3.1). Considering GFRP-RC columns have a $\lambda \geq 66$, the columns showed a dramatic decline in axial capacity due to premature stability failure. To eliminate this, ACI 318-14 requires revising the structure's system if the ratio of secondary to primary moments exceeds 1.4.

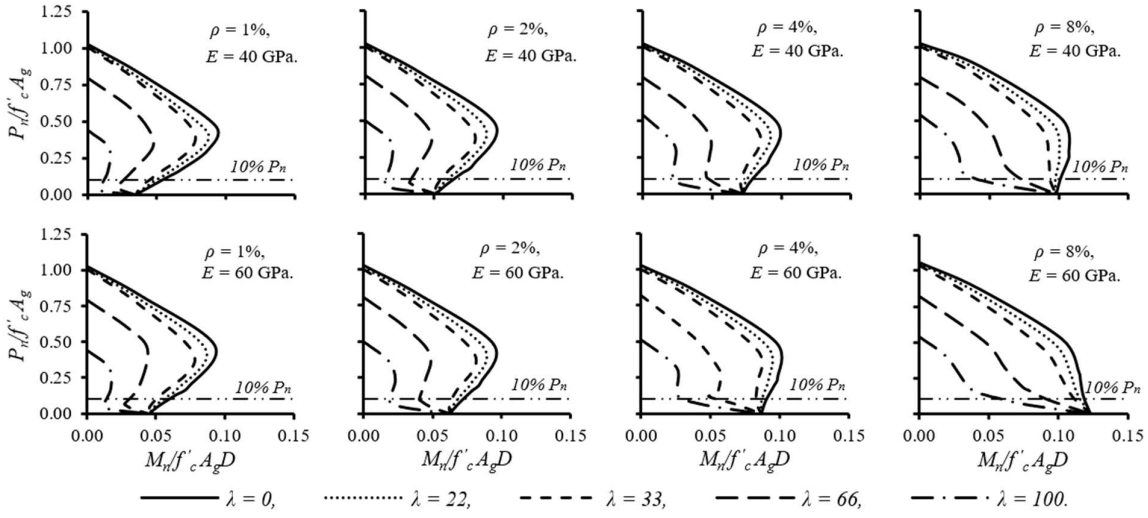

Figure 5.12– Impact of longitudinal-reinforcement ratio and Modulus of Elasticity of GFRP-bars on the P–M interaction diagram with various slenderness ratios. (Note: 1 GPa = 145.04 ksi).

The effect of the GFRP-reinforcing bars in terms of longitudinal-reinforcement ratio and tensile modulus of elasticity is more noticeable for eccentrically loaded columns for the entire range of reinforcement ratios tested ($1\% \leq \rho \leq 8\%$). As for the axially loaded columns, the GFRP-bar contribution was limited to the concrete strength (see Fig. 5.8(b) for the experimental *P–M* diagram). Lastly, none of the GFRP-bars at low levels of reinforcement ratios experienced any tensile rupture, even at extremely large eccentricities ($e/D \geq 100\%$) and large slenderness ratios ($\lambda = 100$). Therefore, the traditional minimum reinforcement ratio of 1% was found to be functional for slender GFRP-RC columns, just like for steel-RC columns.

Figure 5.13 plots a family of stability or strength curves in terms of normalized axial load and the corresponding slenderness ratios. As proposed earlier, at an axial-load level equal to 10% of the ultimate bearing capacity of the axially loaded members, the strength curves were almost linear with no considerable impact of the slenderness ratio on the GFRP-RC column strength. In addition, employing GFRP-bars with $E_{frp} = 60$ GPa (8,702 ksi) instead of $E_{frp} = 40$ GPa (5,802 ksi) had an insignificant influence on the performance of the slender GFRP-RC columns. The effect of the longitudinal-reinforcement ratio on column axial capacity was more effective for the columns loaded with $e/D = 40\%$. For example, at $\lambda = 22$, increasing the reinforcement ratio from 1% to 8% amplified the column's load-carrying capacity by 7% and 74% at $e/D = 5\%$ and $e/D = 40\%$, respectively.

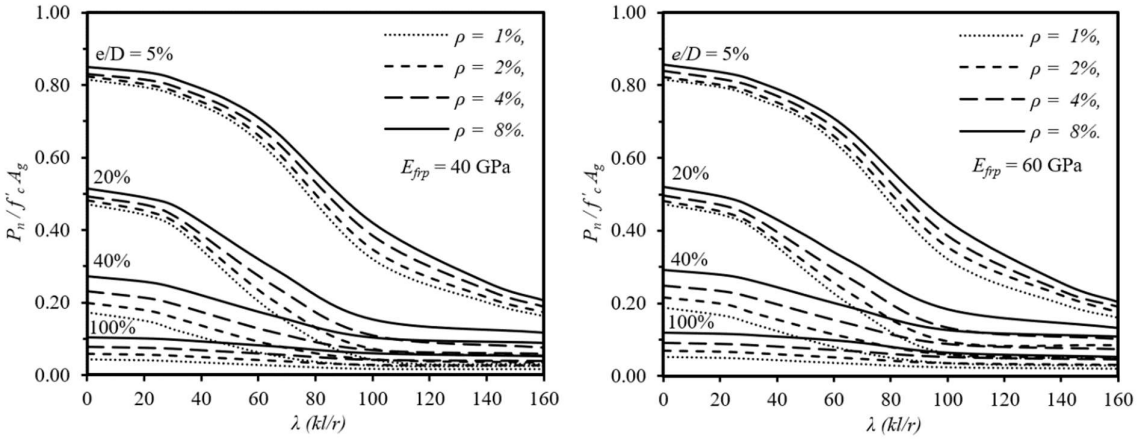

Figure 5.13– Analytical strength curves of GFRP-RC columns. (Note: 1 GPa = 145.04 ksi).

5.7 Permissible Tensile-Bar Strain

ACI 318-14 stipulates an upper limit of 1.4 for the secondary-to-primary moment ratio of slender steel-RC columns in order to achieve safe margins for column lateral deformations and, thus eliminate the probability of any undesired stability failure. In addition, ACI attributes the tension-controlled failure of steel-RC members subjected to combined moment and axial forces to a maximum tensile yielding strain in the extreme steel bars equal to 0.005. This tensile yielding strain is considered to give sufficient warning of complete failure in the form of

excessive deflections and exaggerated tensile cracks. Unlike steel bars, GFRP-bars do not yield. Considering the full GFRP-tensile-rupture strain results in large deformations that exceed the stability limit of 1.4 set by ACI. Consequently, the ACI stability limit of 1.4 was applied herein for the GFRP-RC columns to define the permissible tensile-design strains at which acceptable lateral deformations are expected.

Figure 5.14 shows the lateral displacement-to-initial eccentricity ratio (δ/e) versus the column slenderness ratio at a GFRP-longitudinal-reinforcement ratio of 1%. The horizontal dotted line represents the stability-failure limit for GFRP-RC-columns with $\delta_{limit}/e = 40\%$, which is equivalent to the ACI stability limit of 1.4. This line represents the unacceptable lateral deformation (δ_{limit}) at which it is supposed that GFRP-bars will exhibit the maximum permissible tensile strains. As the maximum tensile strains for any cross section is expected to reach its peak for columns with higher eccentricity and higher slenderness ratios, an $e/D = 100\%$ was chosen as the maximum limit above which the column should be treated as a flexural member. Therefore, two values of λ of 55.5 and 63.5 were chosen for $E = 40$ GPa (5,802 ksi) and $E = 60$ GPa (8,702 ksi), respectively, along with the $e/D = 100\%$ so as to represent the point at which the maximum permissible tensile strains is expected.

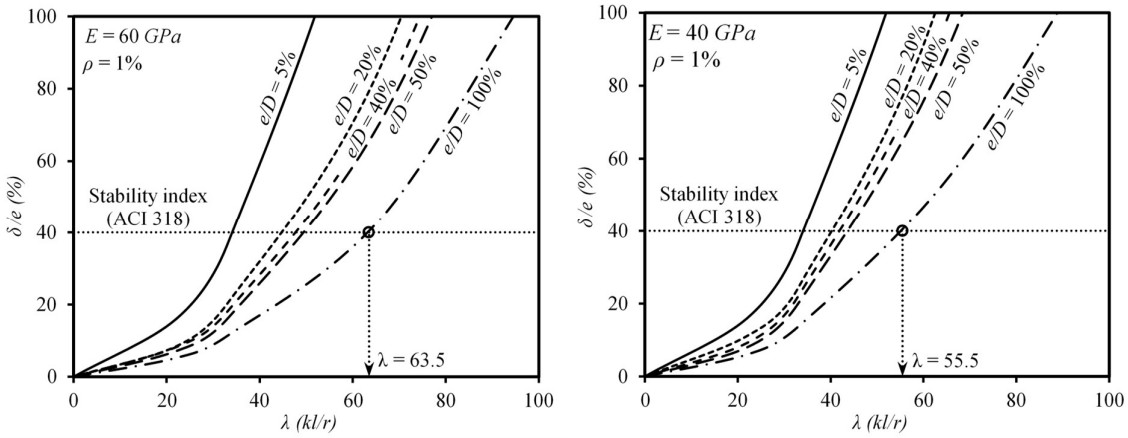

Figure 5.14– Lateral displacement-to-initial eccentricity ratio versus column slenderness ratio. (Note: 1 GPa = 145.04 ksi).

Figure 5.15 illustrates the effect of the test parameters on the tensile GFRP-bar strains at different eccentricities. The strain values from the analytical model were in good agreement with the experimental strain readings (see Fig. 5.5). The GFRP-bar strain values were greatly

influenced by increasing the longitudinal-reinforcement ratio (ρ_L) at low levels of reinforcement ratios. For example, the tensile strains decreased by approximately 50% when the ρ_L increased from 1% to 4%, while increasing the ρ_L from 4% to 8% reduced the tensile strain by only 20%. The horizontal line in Fig. 5.15 describes the maximum experienced tensile-bar strains at $e/D = 100\%$ and the two slenderness ratios discussed above. Therefore, the maximum tensile design strains at which GFRP-RC columns avoid stability failure with acceptable margins of lateral deformations range from 0.94% to 1.15%. This value is close to that proposed by Zadeh and Nanni (2013) to limit the maximum tensile strain in GFRP-bars to the minimum of 1% and ε_{frpu}. Conservatively and based on the derived analytical model and the tensile strain measurements of our experimental program, the permissible design tensile strain is proposed to be the lesser of 0.9% or ε_{frpu}.

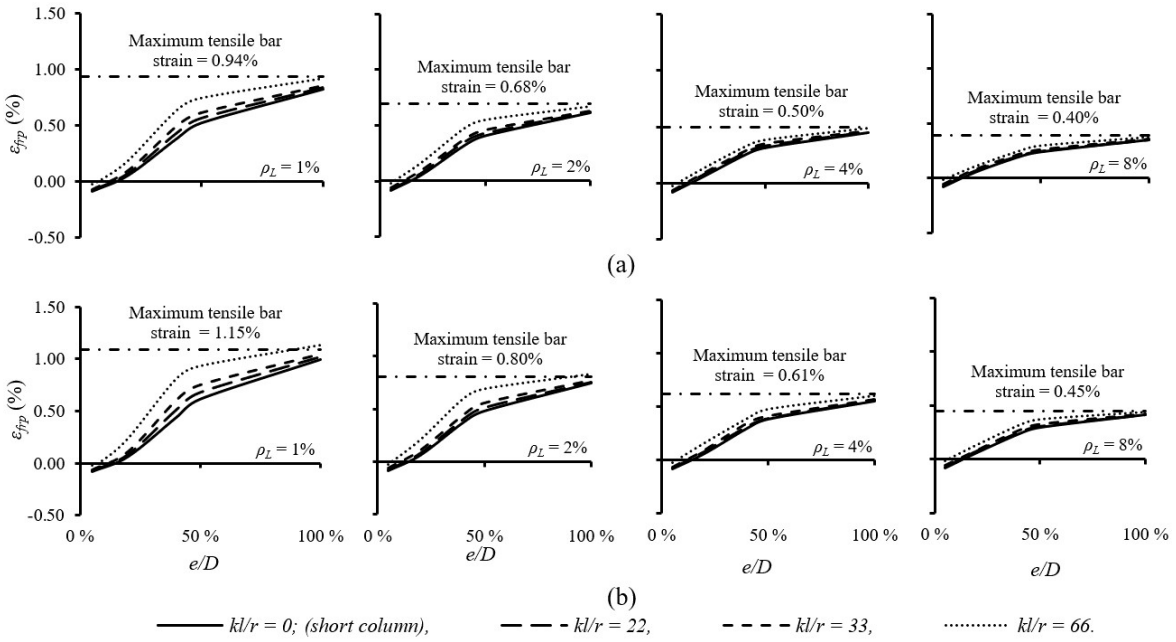

Figure 5.15– Lateral displacement-to-initial eccentricity ratio versus column slenderness ratio. (Note: 1 GPa = 145.04 ksi).

5.8 Conclusions

Twenty-two full-scale slender GFRP-RC columns were tested so as to assess the impact of utilizing GFRP-reinforcement on slender RC columns. The four test parameters were slenderness ratio, eccentricity level, longitudinal-reinforcement ratio, and confinement ratio. The experimental investigations were extended using an analytical second-order model accounting for material and geometrical nonlinearities. The developed model was in a good agreement with the test results. The following conclusions have been drawn:

1. Integrating GFRP-bars as internal reinforcement for slender RC columns proved to be adequate in resisting the applied loads and provided sufficient stability during the various testing stages.
2. The failure of slender GFRP-RC columns tested at moderate eccentricity ($e/D = 33\%$) can be termed a transition failure between two extremes: compression-based ($e/D = 0\%$ and 16%), in terms of concrete cover spalling at peak, and tension-based ($e/D = 66\%$), governed by the formation of excessive tensile cracks and large lateral deformations.
3. The GFRP-bars provided high resistance to both tensile and compressive strains prior to experiencing any bar rupture. On average, the ultimate measured tensile strains exceeded 15,000 με (64% ε_{frpu}), while the recorded compressive-bar strains approached –13,000 με (55% ε_{frpu}).
4. The slender GFRP-RC columns exhibited lower capacity with similar failure mechanisms compared to short GFRP-RC columns from literature. This reduction in column capacity

can be considered in design by applying second-order analysis that takes into account the structure's deformed geometry.

5. Of all the tested parameters, the applied eccentricity had the greatest influence on column ultimate loads. Regardless of the column slenderness ratio or the amount of longitudinal reinforcement, the slender GFRP-RC columns retained only 52%, 26%, and 12% (on average) of their axial capacity when an e/D of 16%, 33%, and 66% were applied, respectively.
6. The slender GFRP-RC columns loaded under moderate ($e/D = 33\%$) to high eccentricity ($e/D = 66\%$) were more sensitive to the increase in longitudinal-reinforcement ratios in terms of better resistance to the induced lateral deformations and enhanced flexural capacity.
7. An analytical model for slender GFRP-RC columns bent in a single curvature with equal end eccentricities was developed by discretizing the section into several integration layers. The model proved to correlate substantially with the experimental data.
8. Based on the experimental observations and the theoretical investigations, the axial-load level at which the columns should be treated as flexural members is 10% of the column ultimate strength with a longitudinal-reinforcement ratio of 1%.
9. The effect of the GFRP-reinforcing bars in terms of longitudinal-reinforcement ratio and tensile modulus of elasticity is more noticeable for eccentrically loaded columns for the entire range of reinforcement ratios tested ($1\% \le \rho \le 8\%$).

Based on the derived analytical model, along with the tensile-strain measurements in our experimental program, the permissible design tensile strain of GFRP-bars ($40\text{ GPa}\,(5{,}802\ ksi) < E < 60\text{ GPa}\,(8{,}702\ ksi)$) should be the lesser of 0.9% and ε_{frpu}. This allows for acceptable lateral deformations with an adequate warning prior to column failure.

CHAPTER 6

Strength of Bridge High-Strength Concrete Slender Compression Members Reinforced with GFRP Bars and Spirals: Experiments and Second-Order Analysis

Résistance de membrures élancées en compression de pont en béton à haute résistance armé de barres et de spirale en prfv: étude expérimentale et analyse de second ordre

Foreword

Authors and Affiliation:

- **Waseem Abdelazim** is a doctoral candidate in the Department of Civil Engineering at the University of Sherbrooke, Sherbrooke, QC, Canada, J1K 2R1.
- **Hamdy M. Mohamed** is a research associate and lecturer in the Department of Civil Engineering at the University of Sherbrooke, Sherbrooke, QC, Canada, J1K 2R1.
- **Brahim Benmokrane**, **FACI**, is a Professor in the Department of Civil Engineering, Université de Sherbrooke, Sherbrooke, Quebec, Canada, J1K 2R1.
- **Steven Nolan,** Bridge Engineer, Advanced Materials for Structural Durability & Resiliency, State Structures Design Office, Florida Department of Transportation (FDOT), 605 Suwannee St, Tallahassee, FL. 32399

Journal Title and Paper Status:

Accepted in *Journal of Bridge Engineering, ASCE* in April 22, 2020. *DOI: 10.1061/(ASCE)BE.1943-5592.0001601*

Contribution to the Thesis:

The reported study aimed at developing a valuable experimental database of slender GFRP-HSC members subjected to axial and flexural loads. Moreover, the research reported on herein targeted extending the applicability of AASHTO 2018a provisions to compression members with concrete compression strength exceeding 69 MPa. In order to broaden the research scope, the experimental program was followed up with second-order analytical modelling considering material and geometrical nonlinearities. Lastly, the design recommendations herein could support the work of North American technical committees engaged in developing standards and design provisions for slender GFRP-RC compression members.

Abstract

Design for slender high-strength concrete (HSC) bridge compression members (columns, piers, and piles) reinforced with glass fiber-reinforced polymer (GFRP) has yet to be addressed in the relevant American and Canadian codes and guidelines. Including such provisions undoubtedly requires a comprehensive assessment of the structural performance of such members, as well as a definition for the slenderness limit below which second-order responses can be discarded. Consequently, full-scale slender GFRP-HSC columns with a concrete compressive strength of 80 MPa and measuring 2,500 mm in height and 305 mm in diameter were prepared and tested at four eccentricity levels (0%, 16%, 33%, and 66% of the column size). The influence of HSC on the behavior of slender GFRP-HSC columns was also assessed with respect to reference normal-strength concrete (NSC) counterparts. Moreover, the effect of two different longitudinal GFRP-reinforcement ratios (3.28 % and 4.66 %) on the performance of the test specimens was investigated. The test results herein indicate the ability of HSC and GFRP reinforcement to improve column strength and to maintain stability at various loading stages. An analytical second-order model was then developed to extend the research program to include a wide range of parametric studies. The developed model was validated against the test results for 47 FRP-HSC columns selected from the current study and the literature. Lastly, the applicability of the current slenderness limit to HSC columns was verified and a modified slenderness limit was proposed to account for HSC columns with compressive strengths up to 125 MPa.

6.1 Introduction

Rapid innovations in the concrete industry have increasingly led to the use of high-strength materials such as high-strength concretes (HSC) in heavily loaded structures such as bridges and high-rise buildings. In addition to their superior durability and higher modulus of elasticity than normal-strength concretes (NSCs), HSC is predominantly used for their higher compressive strength that exceeds 55 MPa, as per ACI 318-19 (ACI 2019). This high compressive strength, along with reduced creep and shrinkage, has resulted in the design of more slender members, such as slender HSC columns. These slender columns are susceptible to buckling and stability problems, which is not normally a design consideration in conventional concrete. The use of HSC in columns has, however, been shown to be advantageous with regard to lateral stiffness and axial shortening (Colaco 1985). Reinforcing slender HSC columns with GFRP reinforcement extends the structure's life span and can eliminate the high repair and rehabilitation expenditures due to the inevitable corrosion of conventional steel. The US Federal Highway Administration (FHWA) reported that, in 2018, the estimated rehabilitation costs of structurally deficient (SD) national and nonnational highway system bridges due to steel corrosion exceeded $32.8 billion. Furthermore, the Canadian Construction Association (CCA) estimated that the investment required to rehabilitate public infrastructure overall hovers around C$900 billion (ISIS Canada 2007).

The most recent editions of the AASHTO LRFD *Bridge Design Guide Specifications for GFRP-Reinforced Concrete* (AASHTO 2018a) and the *Canadian Highway Bridge Design Code,* CAN/CSA S6-19 (CSA 2019) include valuable sections dealing with the design of GFRP-RC bridge columns and piers. CSA S806-12 (CSA 2012) classify GFRP-RC columns as short or long, relying on the slenderness limit (λ) for steel-RC columns stipulated in AASHTO LRFD *Bridge Design Specifications* for steel-RC members (AASHTO 2018b) and CSA A23.3-14 (CSA 2014), disregarding that FRP-RC members might resist buckling differently than steel-reinforced members, due to the lack of ductility in the constituents materials. Although AASHTO (2018a) and CSA (2012) allow the use of GFRP reinforcement in short columns only, it conservatively ignores the contribution of GFRP bars in compression. In addition, AASHTO (2018a) limits its applicability to members with concrete compressive strengths lower than 69 MPa. Lastly, many current provisions in AASHTO (2018a, b) were

developed based on experimental tests on NSC members with compressive strengths below 41 MPa. These provisions, therefore, might not be applicable to the design of HSC members and need to be reviewed, especially, for bridge pier and pile applications.

Recently, valuable experimental and analytical studies have been conducted to assess the performance of short FRP-HSC columns considering a wide range of parameters such as column cross section (square or circular), reinforcement type (glass, carbon, or basalt), longitudinal-reinforcement ratios, confinement levels and configurations (spirals or ties), concrete strength, loading type (concentric or eccentric) (Hadi et al. 2017; Hasan et al. 2017; Hadhood et al. 2017a ,b; Hadhood et al. 2018; Sheikh and Kharal 2018; Salah-Eldin et al. 2019a, b; Hasan et al. 2019). These studies have ascertained the feasibility of FRP reinforcement as a competitive replacement for traditional steel in short HSC columns.

Only a few studies provide experimental results involving HSC and FRP reinforcement in slender columns. Hales et al. (2016) conducted an experimental study on the behavior of short and slender circular HSC columns reinforced with GFRP bars under eccentric and concentric loading. Hales et al. (2016) observed that GFRP spirals and GFRP longitudinal bars are viable reinforcement for short or slender HSC columns. Moreover, a stability failure was indicated by the authors for slender columns with a slenderness ratio of 49 and loaded at an initial applied eccentricity of 33% of the column diameter. The behavior of slender columns with lower slenderness ratios ($22 < \lambda < 49$) was not, however, investigated. Recently, Xue et al. (2018) conducted concentric and eccentric loading tests on slender rectangular GFRP-RC columns with concrete compressive strengths varying from 29.1 to 55.2 MPa. The tested columns had various slenderness ratios ranging from 20.8 to 41.6. They concluded that all tested columns exhibited concrete-crushing failure with no rupture of the FRP bars. Jawaheri Zadeh and Nanni (2017) performed a theoretical derivation for the slenderness limits of FRP-RC columns with a rectangular cross section. They suggested slenderness limits of 14 and 19 for GFRP-NSC and CFRP-NSC columns bent in a single curvature, respectively. Moreover, Jawaheri Zadeh and Nanni (2017) reported that using HSC reduces the proposed slenderness limits of FRP-HSC columns. Clearly, the research database has a paucity of experimental data on the performance of slender FRP-RC columns, especially HSC ones. This emphasizes the critical need for more experimental investigations on the behavior of slender FRP-HSC columns.

6.2 Research Objectives

As stated above, the extensive use of HSCs in bridge components (e.g., columns, piers, and piles) drives many concerns over the applicability of the current design guidelines for the design and analysis of such members. Therefore, this study aimed at developing a valuable experimental database of slender GFRP-HSC members subjected to axial and flexural loads. Moreover, the research reported on herein targeted extending the applicability of AASHTO 2018a provisions to compression members with concrete compression strength exceeding 69 MPa. In order to broaden the research scope, the experimental program was followed up with second-order analytical modelling considering material and geometrical nonlinearities. Lastly, the design recommendations herein could support the work of North American technical committees engaged in developing standards and design provisions for slender GFRP-RC compression members: AASHTO 2018a, CAN/CSA S6-19 (CSA 2019), ACI 440.1R-15 (ACI 2015), and CSA S806-12 (CSA 2012).

6.3 Experimental Plan

The testing plan was conceived to assess the feasibility of GFRP bars and spirals as a primary reinforcement for slender HSC bridge columns, piers, and pile foundations. The sections below characterize the materials used and summarize the test-matrix design.

6.3.1 Test Specimens

All columns were 2,500 mm high and 305 mm in diameter, entirely reinforced with GFRP bars and spirals. Three groups of the test specimens were designed and tested under monotonic static loading to investigate the structural performance of slender GFRP-HSC columns. Group I consisted of four full-scale columns cast with normal-strength concrete (NSC) and served as the reference group. Groups II and III were cast with higher-strength concrete (HSC) to determine the effect of concrete compressive strength as a test parameter. Moreover, the experimental program investigated the effect of the longitudinal-reinforcement ratio in terms of bar diameter. Overall, the design of the internal reinforcement in all the column specimens

complied with AASHTO 2018a and CSA S806-12 provisions. Consequently, specimens in both Groups I and II were reinforced with 12 No. 5 GFRP bars, while those in Group III were reinforced with a higher longitudinal-reinforcement ratio (12 No. 6 GFRP bars). All specimens were laterally confined with No. 3 GFRP spirals with a center-to-center spiral pitch of 80 mm, giving the minimum spacing required to provide thorough confinement and to avoid buckling of the GFRP bars. The top and bottom end regions of the columns (250 mm each) were confined with a tighter spiral pitch of 50 mm to prevent any premature failure near the stress concentration zones, as shown in Fig. 6.1. The last test parameter considered the applied eccentricity level at four initial eccentricities (e) designed and applied to properly define the axial–flexural performance of the tested specimens, as well as to develop a reasonable experimental interaction envelope. The applied eccentricities (eccentricity-to-diameter ratios) were 0.0 (pure axial), 50 mm (16%), 100 mm (33%), and 200 mm (66%). Table 6.1 provides the test matrix and results. Each specimen was identified with three characters. The first letter stands for the type of concrete used; N for NSCs, and H for HSCs. The second letter denotes the bar diameter used; A for GFRP-bar No. 5, and B for GFRP-bar No. 6. Finally, the last number signifies applied eccentricity-to-diameter ratio (e/D).

6.3.2 Materials and Casting

Two batches of ready-mixed, normal-weight concrete with 10 mm maximum aggregate size were used to cast the column specimens: one was for NSC; the other HSC. Prior to casting, GFRP cages (Fig. 6.2-a) were inserted into the form tubes with enough spacers to keep the cages in place during the casting process. All columns were cast in an upright position with a high-pressure pump (Fig. 6.2-b) with the pump hose inserted down to the lowest level of the column specimen to prevent any undesired segregation during casting. In addition, all the columns were adequately consolidated to avoid any honeycombing or entrapped air. After testing, concrete cores (Fig. 6.2-d) were taken from the column top and bottom regions to visually inspect concrete consistency. The cores showed good consistency of the concrete paste throughout the column height. Moreover, during casting, a sufficient number of standard concrete cylinders 200 mm long 100 mm in diameter were prepared from each concrete batch to determine the concrete's compressive strength. All the cylinders were cured under the same

conditions as the column specimens so as to achieve the predicted strength gain. Table 6.2 reports the average concrete compressive strength at different ages.

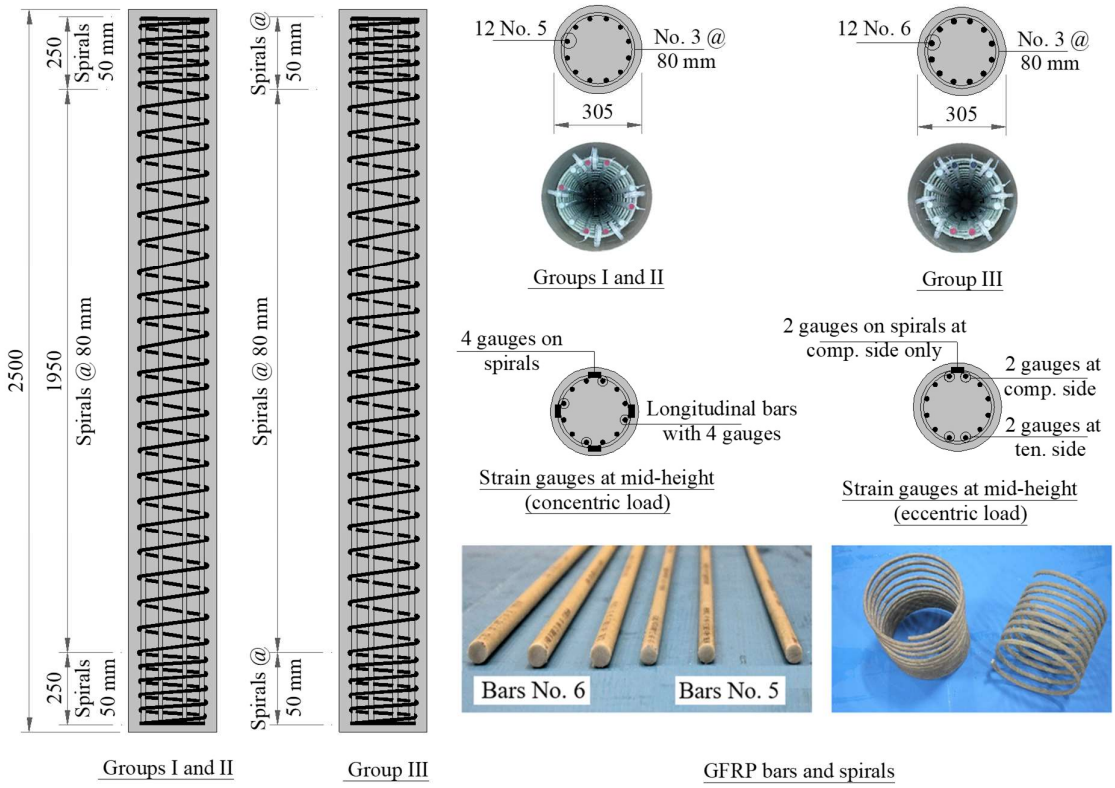

Figure 6.1– Specimen design, strain-gauge arrangement, and sand-coated GFRP bars and spirals.

Table 6.1 – Test matrix and results

Group	Column ID	f_c' (MPa)	Longitudinal Reinforcement		Transverse Reinforcement			e (*mm*); e/D (%)	P_u (*kN*) [2]	δ (*mm*)
			Configuration	ρ_L (%)	Spiral size	Pitch	ρ_T (%)			
I	NAC	46	12 No. 5	3.28	No. 3	80	1.17	C	3,360	2.6
	NA16							50; 16	1,785	11.8
	NA33							100; 33	898	21.2
	NA66							200; 66	435	31.2
II	HAC	80	12 No. 5	3.28	No. 3	80	1.17	C	4,620	1.2
	HA16							50; 16	2,396	11.6
	HA33							100; 33	1,178	21.3
	HA66							200; 66	545	33
III	HBC	80	12 No. 6	4.66	No. 3	80	1.17	C	4,671	0.8
	HB66							200; 66	564	28.8

[1] All columns measured 305 mm in diameter (D) and 2500 mm in length (L), [2] All test results are at the first peak load,
Notes: e is the initial load eccentricity; δ is the mid-height lateral displacement; and P_u is the axial applied load.

Table 6.2 – Concrete compressive strength [1]

Batch	f'_{c} (7-days)	f'_{c} (28-days)	f'_{c} (time of testing)
NSC	31.1 (4 cylinders)	40.8 (6 cylinders)	46 (154 days) (9 cylinders)
HSC	55.4 (4 cylinders)	72.9 (6 cylinders)	80 (90 days) (6 cylinders)

[1] Concrete compressive strength is determined based on the average value of the cylinders tested.

(a) (b) (c) (d)

Figure 6.2– (a) GFRP cages, (b) casting, (c) testing and test setup, (d) concrete cores.

All the columns were fully reinforced with sand-coated GFRP bars and spirals. Two GFRP-bar sizes with an average fiber content of 83.8% were used to longitudinally reinforce all the specimens: No. 5 GFRP bars (15.9 mm in diameter) and No. 6 GFRP bars (19 mm in diameter). The GFRP-reinforced specimens were confined with continuous sand-coated No. 3 GFRP spirals (9.5 mm in diameter). Longitudinal and transverse GFRP reinforcement was placed

without any lapped splices. Table 6.3 presents the average mechanical properties of the GFRP bars and spirals used, as provided by the manufacturer.

Table 6.3 – Mechanical properties of the GFRP reinforcement

Bar Size	Diameter (mm)	Nominal Area [1] (mm^2)	Immersion Area (mm^2)	Fiber Content [2] (%)	Elastic Tensile Modulus [3] (GPa)	Nominal Tensile Strength [4] (MPa)	Tensile Strain (%)
#3	9.5	71	89	78.9	51.1	1281	2.51
#5	15.9	200	225	83.6	61.8	1449	2.35
#6	19	284	318	84	61.7	1411	2.29

[1] The strength and modulus were calculated based on this area.
[2] According to the test method described in ASTM D2584 (temp 650°C, sand coating discarded from the results).
[3] Average ultimate longitudinal tensile properties as provided by the manufacturer; test method CSA S806 Annex C.

6.3.3 Instrumentation

Internal and external instrumentation was applied to each test specimen to record all targeted column responses during testing. Six-millimeter strain gauges with a gauge factor of 2.09% ± 1.0% were attached to the GFRP cages to measure the GFRP bar and spiral strain responses at column mid-height. The gauge arrangement varied according to loading type: concentric or eccentric (Fig. 6.1). Concrete compressive strains were recorded with 60 mm strain gauges with a gauge factor of 2.08% ± 1.0% located at column mid-height. Three linear potentiometers (LPOTs) were mounted horizontally at mid- and quarter-heights of the column specimens to monitor any exhibited lateral deformations and to experimentally define the column's lateral displacement profile. The applied axial load and machine-head axial displacement were measured, respectively, with the machine's sensitive internal load cells and linear variable differential transformers (LVDTs). The MTS testing machine and all instruments were connected to a data-acquisition system for continuous recording of results.

6.3.4 Testing and Test Setup

All the test specimens were tested at the Canada Foundation for Innovation (CFI) structural laboratory of the University of Sherbrooke (Sherbrooke, Québec, Canada). Prior to testing, all the columns were grouted with a thin layer of a self-levelling, high-strength grout. This thin layer of cementitious grout was used to level the top and bottom surfaces of the test specimens

to ensure uniform distribution of the applied load. Then two rigid steel collars were used to confine the columns at the top and bottom to prevent any tendency to premature failure at the stress concentration zones. The load was transferred from the machine's head to the column through adjustable steel roller bearings at the top and bottom attached to the steel collars. These steel rollers were used to attain the predesigned load eccentricity as well as to replicate the case of a pin-ended column: $k = 1$. All the columns were then placed in and aligned on an 11,400 kN capacity MTS testing machine. Figure 6.2-c provides the test setup, MTS testing machine, and data-acquisition system. As the column specimens were expected to behave linearly up to 75% of the estimated column capacity, the testing was initiated at a load-controlled rate of 2.5 kN/s. Then, the testing continued under displacement control at a displacement rate of 0.002 mm/s up to and beyond failure.

6.4 Results and Discussion

6.4.1 General Behavior and Failure Patterns

Figure 6.3 shows the failure modes dominating all the slender GFRP-RC columns tested. In general, the GFRP bars and spirals were able to sustain the applied loads and remained intact at failure occurring as either concrete-cover spalling (primary compression failure) or excessive tensile cracks (secondary tensile failure). The failure modes of tested specimens can be broken down into four groups based on the initial applied eccentricity: axially loaded members and specimens loaded at low, moderate, and high eccentricity, as discussed below.

Three slender GFRP-RC specimens were tested under monotonic pure axial loading: NAC, HAC, and HBC. All three exhibited a concrete-cover free of any visual cracks at approximately 90% of the attained load-carrying capacity. Through the uncracked stage, the specimens exhibited a linear-load–axial-deformation response up to approximately 85% of the peak load (Fig. 6.4-a). Once limited vertical cracks appeared, the column behaved plastically up to and beyond peak load. The failure of the axially loaded columns was classified as a material-type failure. It consisted of concrete crushing on the compression side initiated by a gradual spalling of the concrete cover at peak, followed by a significant drop in column carrying capacity.

Figure 6.3– Failure modes (after loads were released).

At peak load, specimens NAC, HAC, and HBC achieved concrete compressive strains of -3030 $\mu\varepsilon$, -2850 $\mu\varepsilon$, -3130 $\mu\varepsilon$, respectively, as shown in Figs. 6.4-b and 6.5. These strain values exceeded the theoretical values of ε_o, where ε_o is the concrete strain corresponding to the maximum concrete compressive strength. The measured GFRP-bar compressive strains at peak load were -2700 $\mu\varepsilon$, -2740 $\mu\varepsilon$, -3050 $\mu\varepsilon$ for specimens NAC, HAC, and HBC, respectively. The increase in concrete compressive strength had trivial impact on both the GFRP bars and concrete compressive strains. Early concrete cover spalling of the HSC columns was observed. Early cover spalling with HSC could be attributed to microcracks initiating between the concrete cover and column core because of the dissimilar levels of drying shrinkage. Further explanations of the factors resulting in premature spalling of concrete cover in HSC columns

can be found in Collins et al. (1993) and Cusson and Paultre (1994). This relatively early cover spalling prevented the HSC specimens from attaining experimental concrete compressive failure stresses similar to the average compressive strength determined from the standard concrete cylinders tested. For example, column NAC sustained an axial load of 3,360 kN with a column-to-cylinder compressive-strength ratio $\left(f_c'\right)_{column}/\left(f_c'\right)_{cylinder} \cong 1.0$, exceeding 0.85, which is commonly used in theoretical predictions of nominal cross-sectional axial strength at zero eccentricity, while columns HAC and HBC achieved a $\left(f_c'\right)_{column}/\left(f_c'\right)_{cylinder} \cong 0.8$ where $\left(f_c'\right)_{column} = P_u/A_g$. Furthermore, specimens HAC and NAC exhibited a comparable drop in load-carrying capacity as a result of cover spalling equals, on average, 28% of the peak load achieved. Thereafter, as the loading continued, the concrete core dilated laterally, and the GFRP spirals experienced higher tensile strains compared to the insignificant effect during the ascending loading branch, as depicted in Fig. 6.4-d. In addition, at peak load, specimen NAC had spiral tensile strains of 0.0011 $\mu\varepsilon$ compared to 0.0007 $\mu\varepsilon$, on average, for the HSC counterparts. The lower GFRP spiral's strains in HSC columns can be attributed to the relatively lower lateral expansion of the core of the HSC specimens compared to the NSC ones. Furthermore, an adequate confinement level was evidenced by no buckling of any GFRP bars. Lastly, the testing of specimen NAC terminated with tensile rupture of the GFRP spirals, followed by compressive crushing of the GFRP bars, while the GFRP reinforcement in the slender HSC specimens remained intact until the test was halted for safety reasons.

Slender GFRP-RC columns HA16 and NA16 were subjected to an initial low eccentricity of 50 mm (e/D = 16%). The failure mechanism of the low eccentrically loaded members can be defined as a material-type failure in terms of gradual concrete cover spalling on the compression side, preceded by limited horizontal tensile cracks on the concrete tension side. Before the concrete cover spalled off, the reinforced concrete columns behaved elastically up to approximately 75% of the maximum attained load-bearing capacity. Afterward, visual limited vertical cracks initiated on the compression side near 90% of the peak load. Unlike axially loaded specimens and once the tensile stresses on the tension side exceeded the maximum concrete tensile strength, HSC column HA16 exhibited horizontal tensile cracks on the concrete tension side close to 88% of the peak load compared to 96% of the peak load for

NSC specimen NA16. Then, the tensile cracks widened and propagated along the HSC column height until the concrete cover on the compression side crushed at a peak load value of 2,396 kN, which was approximately 52% of the bearing capacity of the axially loaded HSC specimens (HAC and HBC).

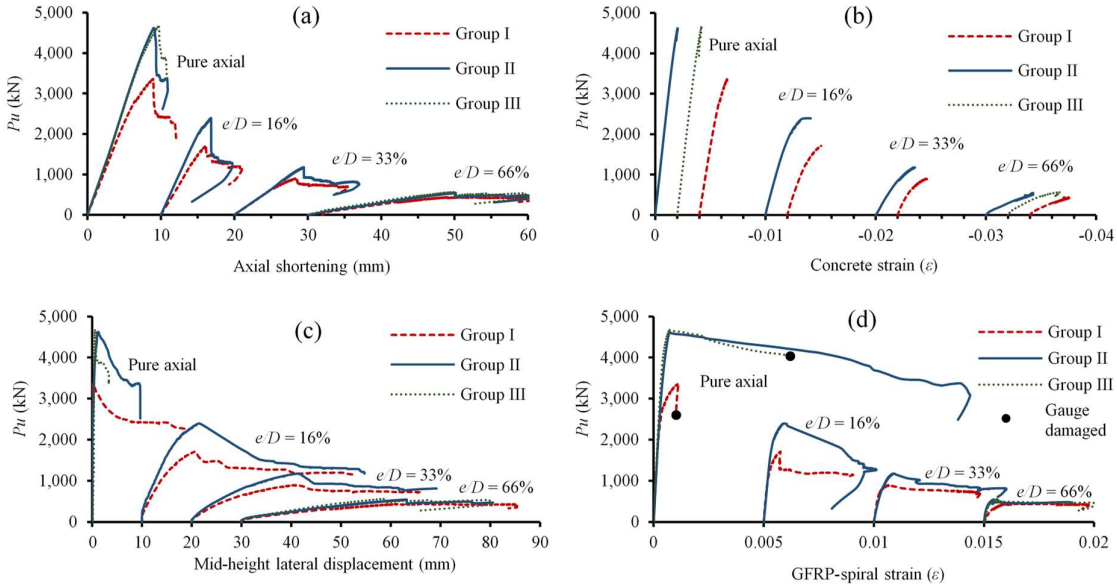

Figure 6.4– Applied load versus: (a) axial shortening, (b) concrete compression strain. (c) mid-height lateral displacement, (d) GFRP-spiral strain.

Both the NSC and HSC specimens achieved concrete compressive strains exceeding the ultimate design strains (ε_{cu} = 0.003) allowed by AASHTO (2018a, b). Specimens NA16 and HA16 recorded concrete compressive strains of -3680 $\mu\varepsilon$ and -3980 $\mu\varepsilon$ and tensile bar strains of 550 $\mu\varepsilon$ and 830 $\mu\varepsilon$, respectively. At failure (see Fig. 6.5), most of the slender columns' cross sections revealed compression stresses with $c/d_e = 0.87$ and 0.83 for NSC and HSC specimens (refer to Fig. 6.5 for the definition of c and d_e). This was in a good agreement with the test results of Hadhood et al. (2017e) and Salah-Eldin et al. (2019a). Low eccentrically loaded specimens HA16 and NA16 recorded a load drop of 33% and 21%, respectively, of the gained peak load as a result of the cross-section degradation due to concrete-cover spalling. Beyond the peak load, the GFRP bars and spirals did not exhibit any compression or tension failures and continued increasing strains up to test termination, as depicted in Figs. 6.4-d and 6.6.

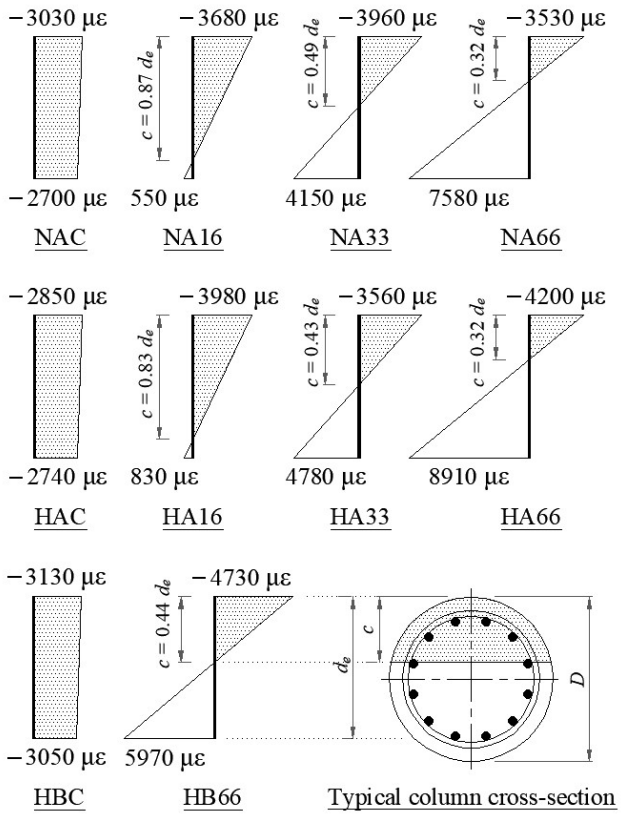

Figure 6.5– Strain gradient at first peak load.

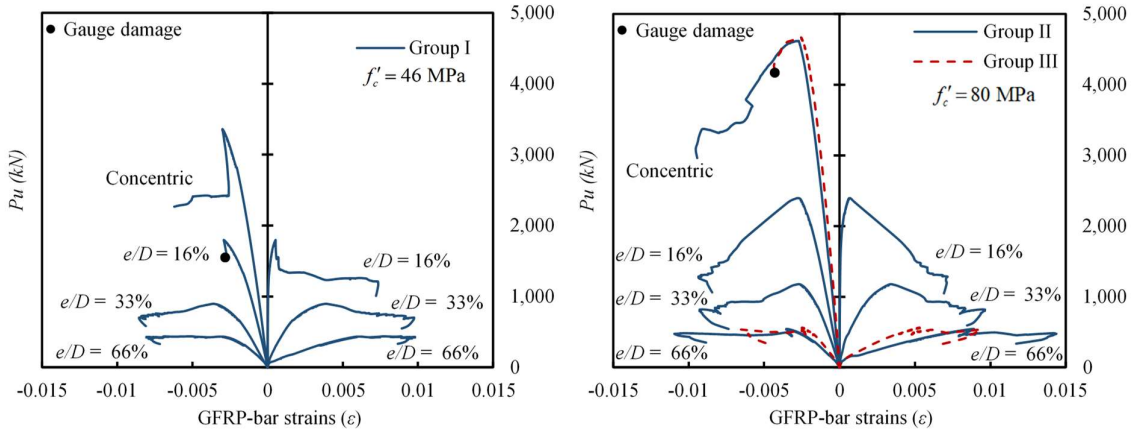

Figure 6.6– GFRP-bar strain response.

A moderate eccentricity of 100 mm (e/D = 0.33) was applied to specimens NA33 and HA33. This eccentricity level provided a transition failure zone between the low and high eccentrically

loaded columns. As the load increased, the test specimen exhibited a relatively rapid increase in lateral deformations compared to the low eccentrically loaded specimens (see Fig. 6.4-c). This caused early formation of horizontal tensile cracks in the concrete at an applied load approximately equal to 350 kN ($0.3P_u$) and 360 kN ($0.4P_u$) for the HSC and NSC specimens, respectively. The early formation of tensile cracks in specimen HA33 mirrored the less ductile nature of HSC columns. Soon after, the tensile cracks in column HA33 widened and propagated rapidly and extensively compared to the NSC benchmark. Early formed tensile cracks migrated into the column cross section with increasing load, approaching the column neutral axis with a compression concrete block depth (c) of $0.49d_e$ and $0.43d_e$ for specimens NA33 and HA33, respectively. In contrast, the concrete cover crushed at concrete compressive strains of -3960 $\mu\varepsilon$ and -3560 $\mu\varepsilon$ at an ultimate load-bearing capacity of 898 kN and 1,178 kN recorded for the NSC and HSC columns, respectively. A failure plane on compression side of the reinforced HSC columns crossed both the concrete paste and coarse aggregate, while, for the NSC columns, the compression failure was observed mostly in the concrete paste. After the concrete compression failure took place, the column strength dropped by approximately 22% and 16% for slender columns HA33 and NA33, respectively. At this stage, GFRP bars on the tension side experienced average tensile strains of 4150 $\mu\varepsilon$ and 4780 $\mu\varepsilon$ for the NSC and HSC columns, respectively. Beyond the load drop, load–axial deformation curves for the GFRP-RC columns exhibited a horizontal plateau until the test ended. The axial deformation at the end of the test was approximately twice that attained at the peak load for both types of concrete (see Fig. 6.4-a). This can be a good indication of greater column ductility. The term "ductility" herein describes the specimen's overall behavior (member level response) and is not intended to characterize the GFRP constituent reinforcing.

Three columns were tested under an initially applied large eccentricity of 200 mm located outside the column cross section (e/D = 66%). In general, at this eccentricity level, the columns behaved as flexural members. Once the load was applied, tensile cracks formed at a very low level of the applied loads (0.2 P_u) compared to low and moderate eccentrically loaded HSC columns. Then, the tensile cracks increasingly widened and propagated along the whole column height. In parallel, tensile cracks migrated through the concrete core, diminishing the concrete compression block (c) to approximately 0.32 d_e and 0.44 d_e for specimens HA66 and HB66, respectively. Accordingly, cracked cross-section properties governed the columns'

performance up to and after peak load had been attained, causing a noticeable decrease in column axial and lateral stiffnesses. With respect to the compression fiber, the concrete remained uncracked at around 92% of the peak load. The HSC specimens achieved a load-carrying capacity of 12% of the compressive strength of their axially loaded counterparts (see Table 6.1). After concrete-cover spalling occurred at concrete compressive strains exceeding -4200 $\mu\varepsilon$ and -3530 $\mu\varepsilon$ for the HSC and NSC columns, respectively, a limited average decay of 7% of the peak load was observed. Simultaneously, GFRP bars on the compression side retained the column capacity with a slight increase in the applied load until a second spalling of concrete cover occurred. Meanwhile, the tested specimen sustained exaggerated tensile cracks, accompanied by excessive lateral deformations triggered by large support rotation (see Figure 6.7). The test was terminated for safety reasons without any rupturing of the GFRP reinforcement. At the end of the test, GFRP bars sustained tensile and compressive strains exceeding 14,300 $\mu\varepsilon$ and -10,900 $\mu\varepsilon$, which represent 61% and 46%, respectively, of the ultimate tensile strains of the GFRP bars used (refer to Table 6.3). Lastly, after load had been released, all slender GFRP-RC columns dissipated most of the lateral deformations and returned to their undeformed pattern, as can be seen compared in Figs. 6.3 and 6.7.

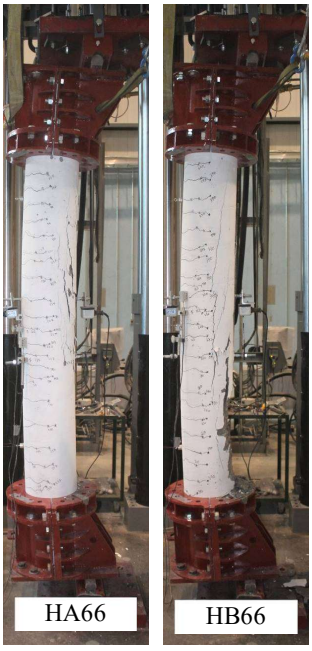

Figure 6.7– High eccentric loaded slender HSC columns before releasing the applied load.

In general, two types of failure dominate RC columns: material failure and stability failure. ACI 2019 states that the probability of stability failure arises at a secondary-to-primary moment ratio of 1.4. Primary moments result from multiplying the applied loads by the initial eccentricity, while secondary moments consider both second-order effects and the initial applied eccentricity. Applying this definition to the tested HSC slender columns, and in referencing the load-carrying capacity and lateral displacement values listed in Table 6.1, it can be seen that all the GFRP-RC columns experienced material failure with secondary-to-primary moment ratios ranging from 1.14 (e/D = 66%) to 1.24 (e/D = 16% and e/D = 33%). In other words, for the range of column slenderness tested, using GFRP as the main reinforcement in slender HSC columns maintained the column stability up to the column failure.

AASHTO (2018b) divides the material failure of steel-RC members subjected to combined axial and flexural loads into two main categories based on the yield strain limit in the extreme steel reinforcing bars: compression- (brittle) or tension-controlled failure. The compression-controlled strain limit has been defined as 0.002 ($c/d_e = 0.6$) for Grade 60 reinforcement, while tension failure is defined at a strain exceeding 0.005 ($c/d_e \leq 0.375$). The latter net tensile strain provides adequate warning of failure by excessive deflection and cracking. As GFRP bars do not yield, the failure modes of GFRP-RC slender columns have been categorized according to the c/d_e values at which failure occurs. Figure 6.5 provides the experimental strain gradient at peak load over the column cross section at column mid-height. A linear strain distribution has been assumed between the outermost concrete compression fiber and the extreme GFRP bars on the tension side. Accordingly, the failure mode observed for GFRP-RC columns NA66 and HA66 tested under the initial applied eccentricity $e/D \geq 0.66$ can be identified as tension-controlled failure in terms of excessive lateral deformations accompanied by exaggerated tensile cracks.

6.4.2 Second-Order Response

Experimentally, second-order effects were assessed by integrating the deformed geometry of the slender HSC columns during testing and the initial applied eccentricity. Figure 6.8 plots the experimental buckling profiles of all tested specimens for 25%, 50%, and 100% of the peak

loads. Overall, the curvature of the RC columns was found to be more affected by the applied eccentricity than the other parameters studied. At peak load, applying an initial $e/D=66\%$ magnified the lateral displacement by 52% and 174% compared to specimens tested under $e/D=33\%$ and $e/D=16\%$, respectively. As expected, the HSC columns revealed higher lateral stiffness to the applied eccentricities than the NSC columns, as shown in Fig. 6.4-c. Moreover, in the case of the GFRP-RC columns tested under $e/D=16\%$ or $e/D=33\%$, the induced buckling was more obvious beyond 50% of peak, while those tested under $e/D=66\%$ (tension-controlled failure) reached high levels of lateral buckling at earlier stages of loading due to early initiation of tensile cracks. Although the columns tested under high eccentricity revealed relatively high lateral deformations, compared to concentrically loaded and other reported column tests, this does not mean that the latter had lower second-order effects. As discussed above, the applied initial eccentricity reduced the increased load-carrying capacity, which might end with smaller secondary moments. Figure 6.9 shows the effect of load eccentricity on the second-order response. Furthermore, despite the noticeable increase in the loading capacity of the HSC columns, both of the HSC and NSC columns had quite similar secondary-to-primary moment ratios. The HSC columns were, however, more susceptible to secondary moments at e/D ranging from 0.16 to 0.33.

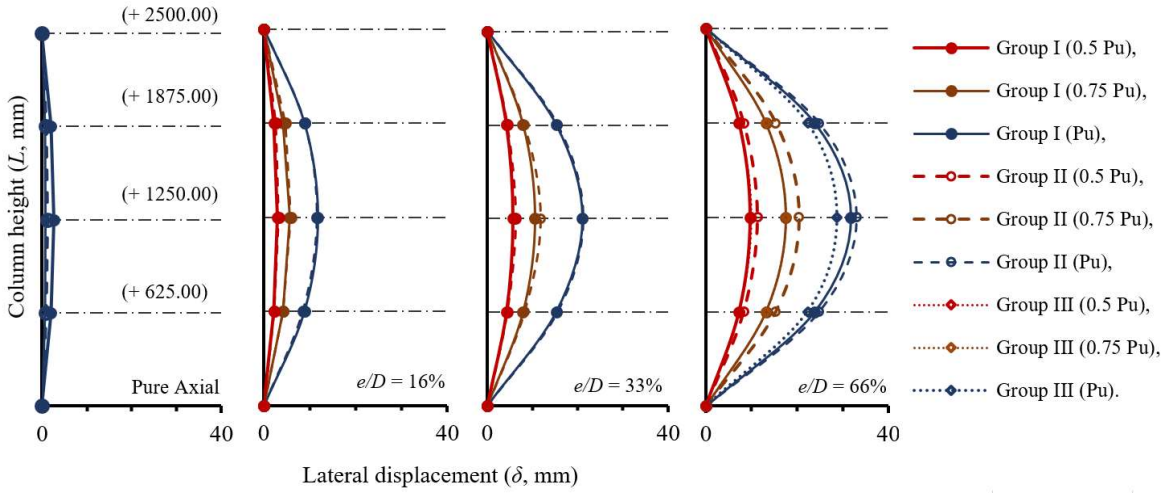

Figure 6.8– Experimental induced buckling profile.

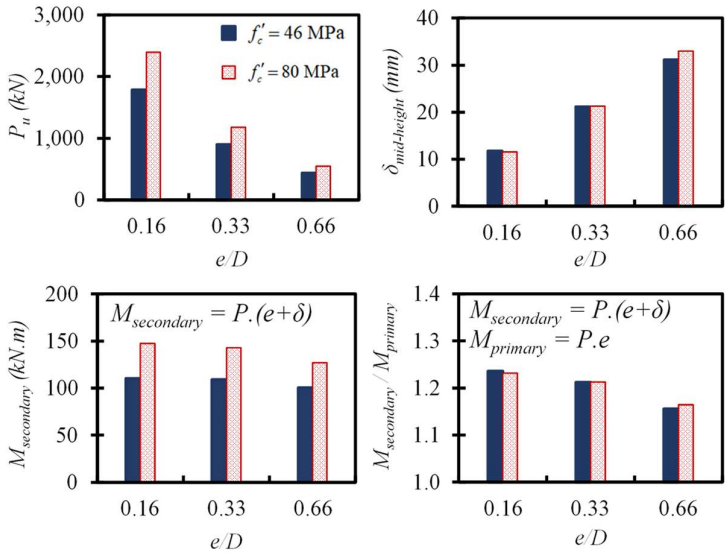

Figure 6.9– Effect of P–δ response on the induced second-order effects at different eccentricities.

Figure 6.10 compares the developed experimental *P–M* interaction diagram of the NSC and HSC columns. The axial load and corresponding flexure have been normalized to the gross area A_g and $A_g \cdot D$, respectively. The dashed and solid lines indicate the interaction envelopes for slender and short columns, respectively. Second-order effects were incorporated into the interaction curve by subtracting the second-order moments $P \cdot \delta$ from the nominal sustained moments at failure. Both slender GFRP-RC failure envelopes had similar shapes. Both diagrams had an inflection point similar to the common *P–M* interaction diagrams for steel-RC columns. The inflection points were developed at an e/D ranging from 0.16 to 0.33. These inflection points are usually used to indicate the transition regions of tension and compression failures of compression members subjected to eccentric loads. Further investigations related to *P–M* interaction diagrams are discussed below in the theoretical-analysis sections.

6.4.3 Effect of Test Parameters

Concrete Compressive Strength — Two groups of GFRP-RC columns were cast using concrete compressive strength of 80 MPa (>55 MPa) in order to assess the performance of slender GFRP-HSC columns. In addition, a reference group of GFRP-NSC columns (46 MPa) were prepared and tested to serve as a benchmark and to highlight the performance of HSC-column counterparts. As discussed earlier, impact of higher concrete compressive strength on

the failure modes of slender GFRP-RC columns could be described as having slightly less ductility and early concrete-cover spalling. The latter resulting in the HSC specimens having lower column-to-cylinder compressive-strength ratios $(f'_c)_{column}/(f'_c)_{cylinder}$.

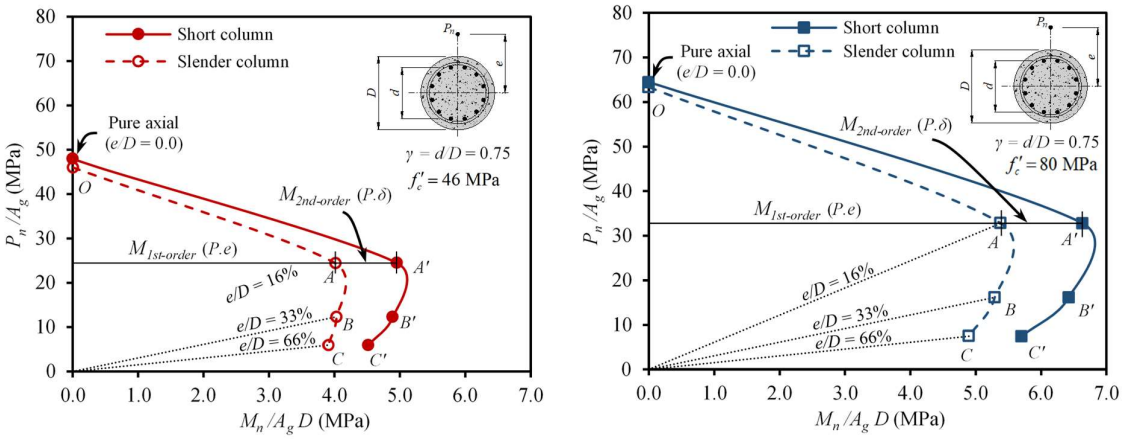

Figure 6.10– Experimental interaction envelopes for slender GFRP-RC columns.

In general, the effect of concrete compressive strength on column capacity was more pronounced under concentric and low eccentricity levels (Fig. 6.11). The HSC columns attained an increase in column axial capacity approximately equal to 38% (1,260 kN), 34% (611 kN), 31% (280 kN), and 25% (110 kN) at an initial applied eccentricity level of 0 %, 16%, 33%, and 66% compared to the NSC counterparts, respectively. Moreover, the GFRP-HSC specimens evidenced greater capacity in withstanding axial and lateral deformations compared to the GFRP-NSC columns due to the HSC having relatively higher elastic modulus than the NSC (see Fig. 6.4). In addition, both the slender NSC and HSC columns exhibited a certain ductility in developing axial and lateral deformations beyond peak loads. In fact, the tests of slender GFRP-RC columns under eccentric loading were halted due to excessive lateral deformations. The use of HSC had insignificant impact on concrete compressive strains. Concrete compressive strains varied from $-2850\mu\varepsilon$ (specimen HAC) up to more than $-4700\mu\varepsilon$ (specimen HB66). The latter strain values were close to those attained by the NSC columns (refer to Fig. 6.5). Lastly, with respect to the GFRP bars on the tension side, the GFRP

reinforcement in the HSC columns achieved higher tensile strains at peak loads (due to higher eccentric axial loads) than the GFRP-NSC columns.

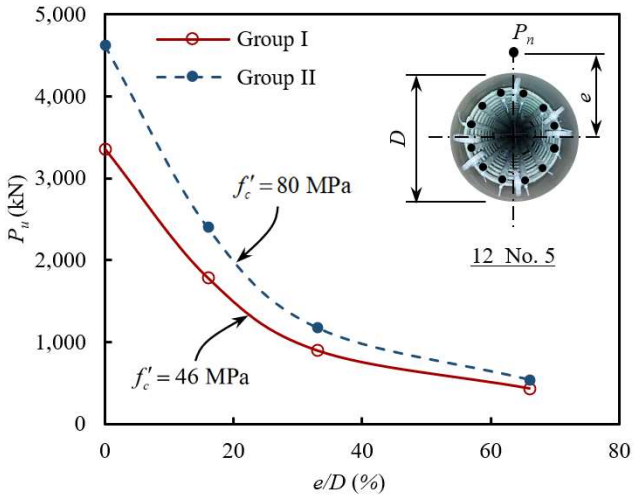

Figure 6.11– Effect of concrete strength on column strength at different eccentricity levels.

Eccentricity-to-Diameter Ratio — slender HSC columns herein were tested under four initial eccentricity levels: $e/D = 0.0$, $e/D = 0.16$, $e/D = 0.33$, and $e/D = 0.66$. Among all other parameters tested, eccentricity-to-diameter ratio had the greatest influence on the performance of slender columns. As depicted in Fig. 6.11, the loading capacity of the GFRP-HSC columns abruptly decreased with increased e/D ratio. For example, compared to concentrically loaded column HAC, the GFRP-HSC specimens retained only 51%, 25%, and 11% of their axial capacity when e/D of 16%, 33%, and 66%, were applied, respectively. These values were close to those recorded for the GFRP-NSC test specimens as GFRP-NSC columns (NA16, NA33, and NA66) retained 53%, 27%, and 13%, respectively, of the axial capacity of the concentrically loaded column NAC. The relatively higher reduction (2%) in the capacity of HSC specimens compared to their NSC counterparts can be attributed to the former experiencing rapid initiation and propagation of flexural cracks. Furthermore, as the initial applied eccentricity increased, the flexural cracks migrated into the column core, receding the concrete compression block. This, as a result, eliminated the column stiffness promising the axial shortening and the lateral displacement gained. For example, the HSC specimens achieved lateral mid-height displacements of 12 mm, 22 mm, and 33 mm at peak load,

compared to 45 mm, 55 mm, and 59 mm at an e/D of 16%, 33%, and 66%, respectively, before testing was stopped for safety reasons..

Longitudinal-Reinforcement Ratio —In this study, the longitudinal-reinforcement ratio was based on GFRP-bar diameter with two different diameters: No. 5 and No. 6. At the same applied eccentricity ratio (see Figure 6.5), all the longitudinal GFRP bars exhibited similar axial stiffness with a linear stress–strain distribution up to more than 80% of peak. In the axially loaded HSC columns, increasing the longitudinal-reinforcement ratio yielded an insignificant improvement in column axial capacity. AASHTO (2018a) determines the nominal unconfined axial-load capacity of GFRP-RC columns based on the gross concrete-column sectional area, minus the area of the GFRP bars. The experimental results herein, however, revealed that the axially loaded NSC columns achieved an axial capacity based on the total gross column area without deducting the area of the GFRP bars. That is consistent with recommendations found in the literature (Jawaheri Zadeh and Nanni 2017; Hadhood et al. 2017e, f; Salah-Eldin et al. 2019a, b). The GFRP-HSC columns tested under $e/D = 0.66$ were more sensitive to the increase in the longitudinal-reinforcement ratio. As shown in Table 6.1, increasing the reinforcement ratio from $\rho_L = 3.28\%$ to $\rho_L = 4.66\%$ slightly increased the load-carrying capacity by 4%, while it significantly decreased the mid-height lateral displacement at peak load by 13%. This implies that GFRP bars can effectively improve the flexural stiffness of slender GFRP-HSC columns and, as a result, can reduce the accompanying second-order effects. Lastly, the impact of increasing the longitudinal-reinforcement ratio was more pronounced regarding the induced GFRP-bar strains, where the measured tensile strains at peak load diminished by approximately 33% (from $+8910\mu\varepsilon$ to $+5970\mu\varepsilon$) when the GFRP-reinforcement ratio was increased by approximately 42%.

6.4.4 General Discussion

This section discusses the results of slender GFRP-HSC columns from the current study in comparison to the results for short HSC columns found in literature. Table 6.4 summarizes the main characteristics of the HSC columns in our study. The short FRP-HSC columns ($\lambda < 22$) in Table 6.4 experienced material failure similar to the slender HSC columns in our study. In

addition, the short FRP-HSC columns achieved an unconfined axial-load capacity based on the gross concrete-column sectional area without deducting the area of the FRP bars ($0.85 f_c' A_g$). The slender GFRP-HSC columns ($\lambda > 22$) examined in the current study, however, had reduced load-carrying capacity accompanying the second-order effects. This indicates that, for the range of slenderness ratios tested, the slenderness ratio had an insignificant effect on the mode of failure while it reduced the column axial capacity. This reduction in column capacity can be considered in design by applying a second-order analysis using the structure's deformed geometry. Short and slender columns herein are classified based on AASHTO (2018a) limits. Recent studies have, however, proposed lower values for slenderness limits (Mirmiran et al. 2001; Jawaheri Zadeh and Nanni 2017; Abdelazim et al. 2020).

6.5 Model for Slender GFRP-HSC Columns

Analysis of slender columns requires that the column's deformed geometry be included into the equilibrium equations. Consequently, the analysis models for slender columns should consider both the material and geometrical nonlinearities. Two models, therefore, were developed to account for the inevitable reductions in column strength due to second-order effects. The first model deals with concentrically loaded columns and conforms to the tangent (or incremental) modulus theory adopted by Bažant et al. (1991) for pin-ended steel-RC columns. The second model considers eccentrically loaded columns and was developed by discretizing the section into several integration layers. Both models for slender FRP-reinforced concrete columns follow the compatibility of the internal resultant forces and the external applied loads and deformations, as explained below.

Prior to establishing the second-order analytical models for slender FRP-HSC columns, the concrete compressive stress‑strain response should be clearly defined for high-strength concretes in terms of ascending and descending loading branches. Popovics (1973) proposed an unconfined three-parameter model expressing the compressive stress (f_c) at the corresponding compressive strain (ε_c) as

$$\frac{f_c}{f_c'}=\frac{\varepsilon_c}{\varepsilon_o}\cdot\frac{n}{n-1+\left(\varepsilon_c/\varepsilon_o\right)^n} \tag{6.1}$$

$$\varepsilon_o=\frac{f_c'}{E_c}\cdot\frac{n}{n-1} \tag{6.2}$$

where ε_o is the concrete strain at the compressive strength of concrete f_c'; n is a curve-fitting factor equal to $0.8+f_c'/17$ in MPa, as n becomes higher the ascending loading branch tends to be more linear; and E_c is the modulus of elasticity for concrete and can be calculated for normal-weight concrete as $4700\sqrt{f_c'}$ (ACI 2019). Thorenfeldt et al. (1987) reported that the model proposed by Popovics (1973) describes the ascending loading branch well. Popovics's expression for the stress–strain curve does not, however, descend fast enough beyond peak for high-strength concrete behavior. Therefore, Thorenfeldt et al. (1987) suggested a factor k to increase the post-peak decay (Figure 6.12). So, Eq. (6.1) becomes

$$\frac{f_c}{f_c'}=\frac{\varepsilon_c}{\varepsilon_o}\cdot\frac{n}{n-1+\left(\varepsilon_c/\varepsilon_o\right)^{nk}} \tag{6.3}$$

where k is calculated as

$$k=\begin{cases}1 & \varepsilon_c/\varepsilon_o\le 1\\ 0.67+\dfrac{f_c'}{62} & \varepsilon_c/\varepsilon_o>1\end{cases} \tag{6.4}$$

In 1993, Collins et al. concluded that when a realistic stress–strain curve is used to determine column capacity, the stress–strain model proposed by Thorenfeldt et al. (1987) overestimates the failure loads of HSC columns. Consequently, Collins et al. (1993) suggested reducing the stress–strain response by a factor k_3. Thus, k_3, as well as the reduced stress–strain model, can be redefined as

$$\frac{f_c}{f_c'}=\frac{\varepsilon_c}{\varepsilon_o}\cdot\frac{n}{n-1+\left(\varepsilon_c/\varepsilon_o\right)^{nk}}\cdot k_3 \tag{6.5}$$

$$k_3=0.6+\frac{10}{f_c'}\le 0.85 \tag{6.6}$$

Table 6.4 – Mechanical properties of the GFRP reinforcement

Ref.	Gr.	Column ID	Cross Section	λ	f'_c (MPa)	Longitudinal Reinforcement		Transverse Reinforcement		e (mm)	e/D (%)
						Material	No. & size	Material	Size & pitch		
Salah-Eldin et al. (2019a)	I	Ge80	Rectangular	17	71.2	GFRP	6 No. 6	GFRP stirrups	No. 3 @ 150	80	20
		Ge120								120	30
		Ge160								160	40
		Ge240								240	60
Salah-Eldin et al. (2019b)	I	Be80	Rectangular	17	71.2	BFRP	6 No. 6	BFRP stirrups	No. 4 @ 150	80	20
		Be120								120	30
		Be160								160	40
		Be240								240	60
Hadhood et al. (2018)	I	HHG0	Circular	19	70.2	GFRP	8 No. 5	GFRP hoops	No. 3 @ 80	0	C
		HHG1								25	8
		HHG2								50	16
		HHG3								100	33
		HHG4								200	66
	II	HVG0	Circular	19	70.2	GFRP	8 No. 5	GFRP spirals	No. 4 @ 80	0	C
		HVG1								25	8
		HVG2								50	16
		HVG3								100	33
		HVG4								200	66
Hadhood et al. (2017e)	I	HC-A0	Circular	19	70.2	GFRP	8 No. 5	GFRP spirals	No. 3 @ 80	0	C
		HC-A25								25	8
		HC-A50								50	16
		HC-A100								100	33
		HC-A200								200	66
	II	HC-B0	Circular	19	70.2	GFRP	12 No. 5	GFRP spirals	No. 3 @ 80	0	C
		HC-B25								25	8
		HC-B50								50	16
		HC-B100								100	33
		HC-B200								200	66
Hadhood et al. (2017f)	I	HC-e0	Circular	19	70.2	CFRP	8 No. 5	CFRP spirals	No. 3 @ 80	0	C
		HC-e25								25	8
		HC-e50								50	16
		HC-e100								100	33
		HC-e200								200	66
Hassan et al. (2017)	I	G60E0	Circular	15	85	GFRP	6 No. 4	GFRP spirals	No. 3 @ 60	0	C
		G60E25								25	12
		G60E50								50	24
Hadi et al. (2017)	I	G30E0	Circular	15	85	GFRP	6 No. 4	GFRP spirals	No. 3 @ 30	0	C
		G30E25								25	12
		G30E50								50	24
Hales et al. (2016)	I	#6T-SG1	Circular	49	90	GFRP	6 No. 5	GFRP spirals	No. 3 @ 76	25	8
		#9T-SG4								102	33

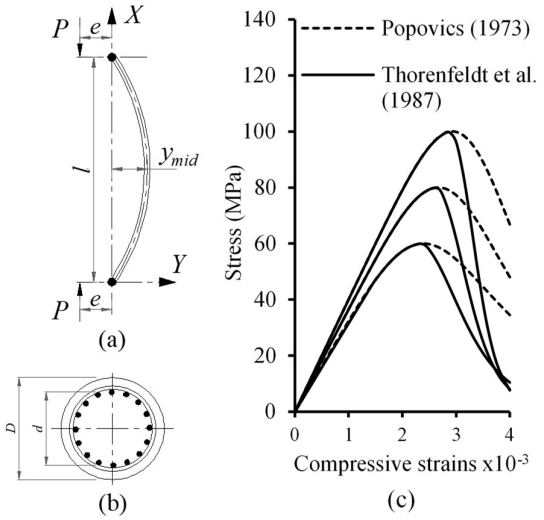

Figure 6.12– (a) Pin-ended column bent in a single curvature, (b) column cross section, (c) concrete stress–strain models.

Lastly, for consistency with AASHTO (2018b), two values of k_3 were verified against the test results: $k_3 = 0.85$ and the value obtained from Eq. (6.6).

6.5.1 Incremental Modulus Theory

The concept of incremental (or tangent) modulus was generalized by Shanley (1947). The tangent modulus theory requires that, when a perfectly undeformed column ($e = 0$) starts to buckle, the buckling load $P_{t(E)}$ must be equal to the axial-force resultant $P_{t(M)}$ relative to the stress–strain curve of the materials used. This could be developed by incorporating the tangent moduli of concrete and FRP materials at different strain increments into Euler's buckling load and comparing it to the material's cross-sectional strength at the same strain increment as follows.

$$P_{t(E)} = \frac{\pi^2}{L_e^2}\left(E_c^t I_c + E_f^t I_f\right) \tag{6.7}$$

$$P_{t(M)} = f_c A_g \tag{6.8}$$

where L_e is the effective buckling length of the column ($L_e = L$ for a pin-ended column), E_c^t and E_f^t are the tangential moduli of concrete and FRP, respectively; and I_c and I_f are the second moment of inertia of the concrete cross section and FRP bars about the centroidal axis, respectively. Herein, the contribution of FRP bars in compression is limited to the concrete's compressive strength (i.e., the FRP bars in compression are simply replaced by concrete, as shown in Eq. (6.8)). Many other researchers have adopted this assumption and proved its applicability in predicting the compressive capacity of FRP-RC members (Jawaheri Zadeh and Nanni 2017; Hadhood et al. 2017e, f; Salah-Eldin et al. 2019a). The tangent modulus of elasticity of concrete E_c^t is defined as the first derivative of the stress–strain model in Eq. (6.5) at each strain increment and could be calculated as

$$E_c^t = k_3 \cdot \frac{nf_c'}{\varepsilon_o}\left(\frac{(n-1)-(n-1)(\varepsilon_c/\varepsilon_o)^n}{\left((n-1)+(\varepsilon_c/\varepsilon_o)^n\right)^2}\right) \tag{9}$$

Unlike steel bars, FRP bars exhibit a linear elastic stress–strain relationship up to failure; i.e., $E_f^t = E_f$. Moreover, using the results from compression analytical and experimental studies, Hadhood et al. (2017e, f) implied that taking the compressive and tensile moduli of elasticity as being equal yielded a predicted capacity of FRP-RC columns similar to experimental results. Accordingly, the modulus of elasticity of the FRP bars in compression is assumed to be the same as their tensile modulus.

Equations 6.7 and 6.8 are two nonlinear equations with one unknown (ε) that can be solved with iterative analysis. For a given column geometry, the incremental strain is assumed and the convergence of the buckling load (Eq. 6.7) and the cross-sectional strength (Eq. 6.8) is checked. If that holds true, then the column axial capacity can be determined from either Eq. (6.7) or Eq. (6.8). Then, another parametric value defining the column's geometry, material properties, reinforcement ratio, and so on can be selected. The steps are repeated then to extend the experimental investigations over a wide range of test parameters.

6.5.2 Model for Eccentrically Loaded Columns

The proposed simple theoretical slender-column model for standard hinged steel-reinforced concrete columns externally confined with FRP developed by Jiang and Teng (2013) was adapted by the authors to RC columns internally reinforced with FRP bars. Given the fundamental assumptions of reinforced-concrete mechanics, five additional assumptions were applied: (1) a column's deflected shape can be defined using a half-sine wave; (2) the bars maintain perfect bond to the concrete; (3) FRP bars have a linear elastic stress–strain response up to failure; (4) the contribution of FRP bars in compression is limited to the concrete's compressive strength, as discussed above; (5) the confinement effect on the strength of eccentric slender columns is limited (Martin et al. 1966) and is, therefore, neglected in the analysis; and (6) ACI (2019) and AASHTO (2018a, b) provisions for ultimate concrete strain ε_{cu} are met (i.e., $\varepsilon_{cu} = 0.003$). The modeling of slender FRP-RC columns started by considering that a pin-ended column has a circular cross section and is exposed to equal end eccentricities, as shown in Figure 6.12. Applying the first assumption indicated above, the lateral deflection (y) can, therefore, be defined as

$$y = -y_{mid} \sin\left(\frac{\pi}{L}x\right) \tag{6.10}$$

where y_{mid} is the mid-height lateral deflection and x is the distance from the column base to the point at which the lateral deflection is calculated. Hence, the expression for the column curvature can be expressed by applying the second differentiation of the deflection as

$$y'' = y_{mid} \frac{\pi^2}{L^2} \sin\left(\frac{\pi}{L}x\right) \tag{6.11}$$

Substituting $x = l/2$ in Eq. (6.11) and solving for y_{mid} yields

$$y_{mid} = \frac{L^2}{\pi^2} y''_{mid} \tag{6.12}$$

Consequently, the mid-height bending moment (maximum expected value) considers the column's lateral deformation (i.e., the second-order effect) and can be determined based on Eq. (6.12) as

$$M_n = M_{1^{st}-order} + M_{2^{nd}-order} = P\left(e + y_{mid}\right) \tag{6.13}$$

The analysis initiated by assuming a lateral-displacement increment, so the corresponding curvature could be determined with Eq. (6.11) for $x = L/2$. Subsequently, the strip-by-strip section analysis described at Fig. 6.13 was applied by assuming a strain value in the cross section. Then, the equilibrium of the corresponding concrete and FRP internal forces was calculated and verified using the stress–strain relations discussed above. The iterative process terminates when the ultimate moment calculated from the section analysis converges with the secondary moments in Eq. (6.13). Then, another increment for the lateral displacement is set, and the process is repeated until the whole loading path up to failure has been plotted. Failure is defined either as the ultimate concrete predefined strain or when the FRP reaches a tensile-strain limit equal to the lesser of 0.01 or the FRP-rupture tensile strain (Jawaheri Zadeh and Nanni 2013). The load-carrying capacity developed from the past models was then verified with the test results from the current study as well as other test results from the literature. Table 6.4 lists all experimental database sources used for verification process.

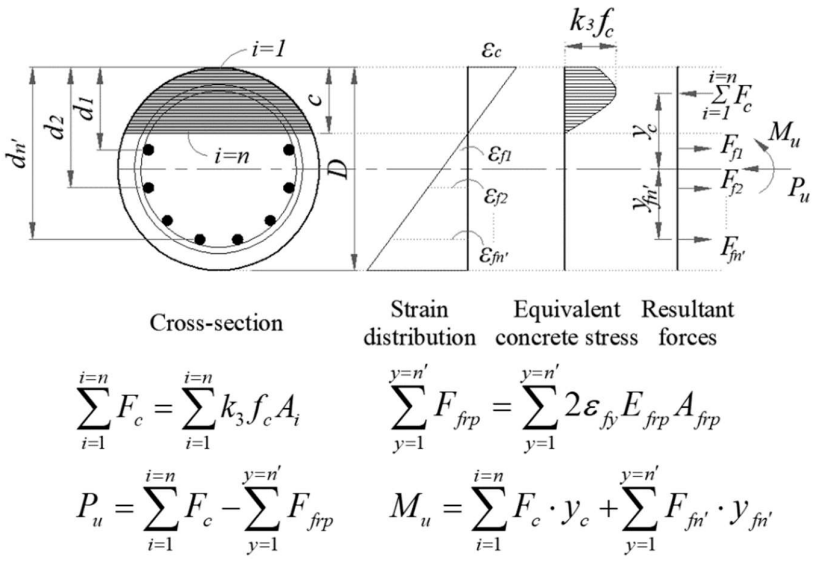

Figure 6.13– Strip-by-strip cross-sectional analysis.

Figure 6.14 compares the failure loads predicted analytically with the test results. The models developed for concentrically and eccentrically loaded FRP-RC columns conservatively predicted the column strength compared to the experimental data. Integrating the factor $k_3 = 0.85$ into concrete compressive stress-strain curves, however, yielded values closer to the test results. Then, the analytical model was used to extend the experimental observations and thoroughly investigate the behavior of the slender GFRP-HSC columns. The analytical investigations performed include the effect of the concrete compressive strength, column slenderness ratio, eccentricity-to-diameter ratio, and longitudinal-reinforcement ratio on the behavior of the slender GFRP-RC columns.

6.6 Proposed Slenderness Limit for GFRP-HSC Columns

Using HSCs in compression members improves the column axial capacity P_u more than the corresponding buckling loads P_{cr}, thereby magnifying the susceptibility to second-order effects. This is due to HSC columns being more sensitive to lateral deformations than NSC columns. As mentioned above, many design provisions (including slenderness limit) given in ACI (2019) and AASHTO (2018b) are based on tests of specimens with concrete compressive strengths of up to 41 MPa and, therefore, do not accurately reflect the behavior of HSC members (Logan et al. 2009). Thus, and due to the relatively rapid increase in the use of high-strength concretes, it is important to investigate the applicability of slenderness limits proposed for the GFRP-NSC columns to HSC columns. Recently, the authors conducted a series of experimental tests and proposed a slenderness limit of 18 for GFRP-NSC columns bent in a single curvature with equal end eccentricities (Abdelazim et al. 2020). The latter limit has been experimentally set at a 5% strength reduction with a normal-concrete compressive strength of 45 ± 1 MPa, a tensile modulus of GFRP bars of not less than 60 GPa ($E_{frp} \geq 60$ GPa), and a longitudinal-reinforcement ratio of 1%. This limit is referred to herein as $\lambda_{(f'_c \leq 55)}$.

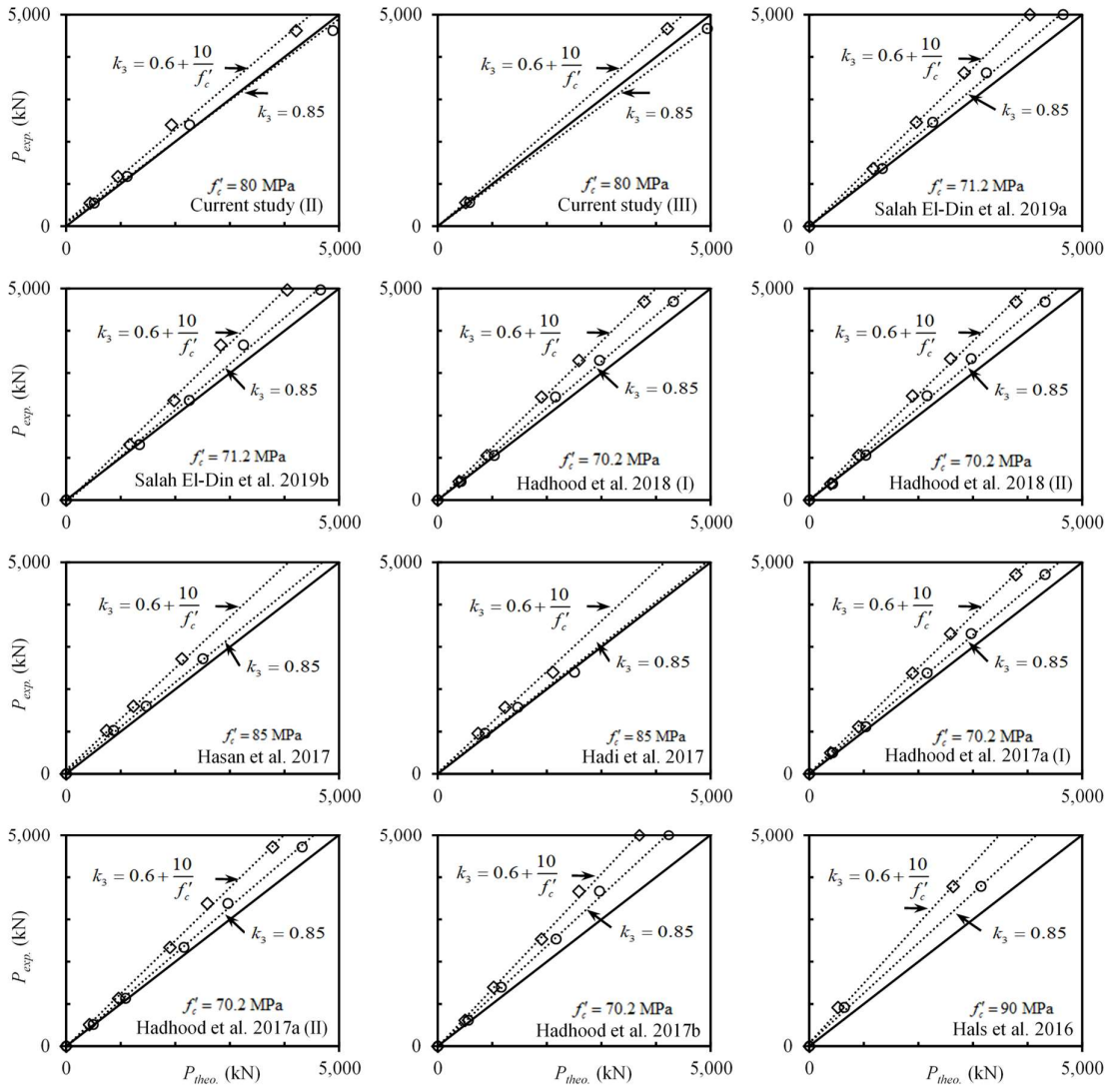

Figure 6.14– Verification of the theoretical peak load considering second-order effects with test results.

The stability or strength curves in Fig. 6.15 define the reduction in the ultimate capacity of slender GFRP-HSC columns with a reinforcement ratio of 1% in terms of normalized axial loads and slenderness ratios. In general, the GFRP-HSC columns evidenced a noticeable reduction in axial capacity at higher slenderness limits. This strength reduction increased at higher compressive concrete strengths. The dotted line in Fig. 6.15 represents the 5% reduction in column strength due to the slenderness effect. Macgregor et al. (1970) proposed this limit (5%) and AASHTO (2018b) includes it as a limit below which second-order effects can be

ignored and RC columns can be designed as short. The figure shows that the lower limits of slenderness are lowest when the applied eccentricity approaches 0.5. This is consistent with the outcomes of Mirmiran et al. (2001a) for FRP-NSC columns.

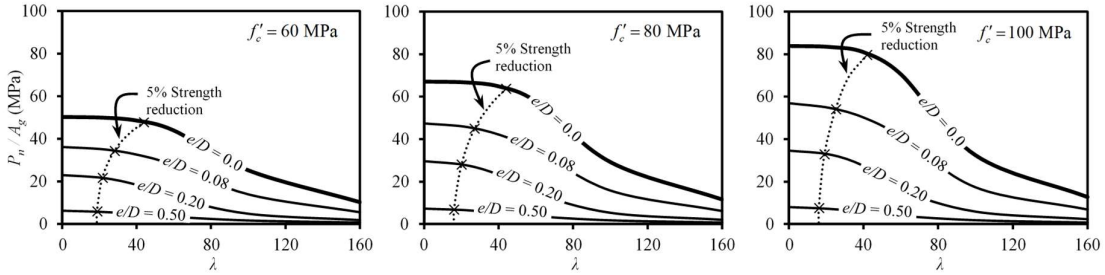

Figure 6.15– Effect of HSC and eccentricity ratio on column strength curves at $\rho_L = 1\%$.

Figure 6.16 represents the effect of using HSCs on the slenderness limit at a 5% strength reduction. Overall, there is a clear downward trend in the slenderness limit as the concrete compressive strength increases. It can also be inferred that concrete compressive strengths under 55 MPa (NSCs) have relatively little impact on the slenderness limit, while the slenderness limit drops sharply when the concrete compressive strength exceeds 55 MPa (HSCs). Lastly, the proposed slenderness limit for GFRP-HSC columns ($55 \le f'_c$ (MPa) ≤ 125) bent in a single curvature with equal end eccentricities, beyond which column design should consider second-order effects, can be written as

$$\lambda_{(f'_c>55)} = \lambda_{(f'_c\le 55)} - \frac{\left(f'_c - 55\right)^{1.44}}{100} \qquad 55 \le f'_c \text{ (MPa)} \le 125 \tag{6.14}$$

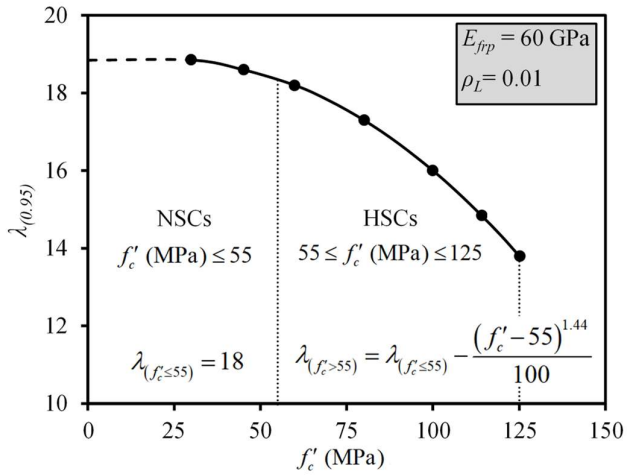

Figure 6.16– Effect of HSCs on the slenderness limit at 5% strength reduction.

6.7 Theoretical Investigations

Figure 6.17 plots a family of developed interaction diagrams for GFRP-HSC columns illustrating the effect of concrete compressive strength, slenderness ratio, and longitudinal-reinforcement ratio. As with the experimentally developed interaction envelope, all the GFRP-HSC columns had an inflection point below which the column bending moments and axial loads degraded simultaneously. Regardless of column geometry, the concrete strength, or the longitudinal-reinforcement ratio, the inflection point occurred at an eccentricity-to-diameter ratio close to 0.2, which is quite consistent with the experimental findings. At a loading level of $e/D < 0.2$, the column cross section was mostly in compression and the impact of using HSCs increased. Conversely, when the GFRP-bar compressive strength was limited to concrete compressive strength, the effect of the GFRP-reinforcement ratio was significant at $e/D > 0.2$ (i.e., when the column cross section experienced higher tensile stresses). Nevertheless, the increase in the GFRP-reinforcement ratio at $e/D < 0.2$ can improve the moment capacity, might enhance the confinement and the post-peak behavior of the columns, and would surely increase the margin of safety (Hadhood et al. 2019). In general, the effect of GFRP reinforcement was more pronounced in the HSC-RC columns with higher slenderness ratios, as can be seen in Fig. 6.18, especially at $e/D > 0.2$. Therefore, when the GFRP-reinforcement ratio was increased,

the columns with $\lambda = 60$ had higher loading capacities than those with lower slenderness ratios. Furthermore, GFRP reinforcement improved the stability of the slender GFRP-HSC columns in terms of eliminating the lateral deformations and, in turn, the induced second-order effects. For instance, at $e/D = 0.2$, $\lambda = 60$ and $f_c' = 80$ MPa, the reduction in column capacity due to the slenderness effect was 50.7%, 46.8%, and 40.7% compared to cross-sectional strength at a GFRP-reinforcement ratio of 1%, 2%, and 4%, respectively. In contrast, the influence of the column slenderness ratio was more pronounced at higher concrete compressive strengths. This is in good agreement with the experimental results and is also consistent with the downward trend of the curve in Fig. 6.16. For example, at an $e/D = 0.2$, $\rho_L = 1\%$ and $\lambda = 60$, the load-bearing capacity dropped by 45.5%, 50.7%, and 53.4% of the corresponding cross-sectional strength when concrete compressive strengths of 60 MPa, 80 MPa, and 100 MPa were considered, respectively.

Figure 6.18 depicts the impact of the eccentricity level on column compressive strength. At all slenderness for the GFRP-HSC columns levels and at $e/D < 0.5$, column axial capacity was more sensitive to the applied-load eccentricity at higher values of concrete compressive strengths. In other words, GFRP-HSC columns tended to abruptly lose their load carrying capacity as the applied initial eccentricity increased up to approximately $e/D = 0.5$. Thereafter, all columns were slightly affected by the increase in the applied eccentricity. At this limit, it is better to treat the column as a flexural member according to beam theories (Jawaheri Zadeh and Nanni 2017). Lastly, the remarks above about failure envelopes can also be demonstrated by and concluded from the constructed P_n-e/D diagrams.

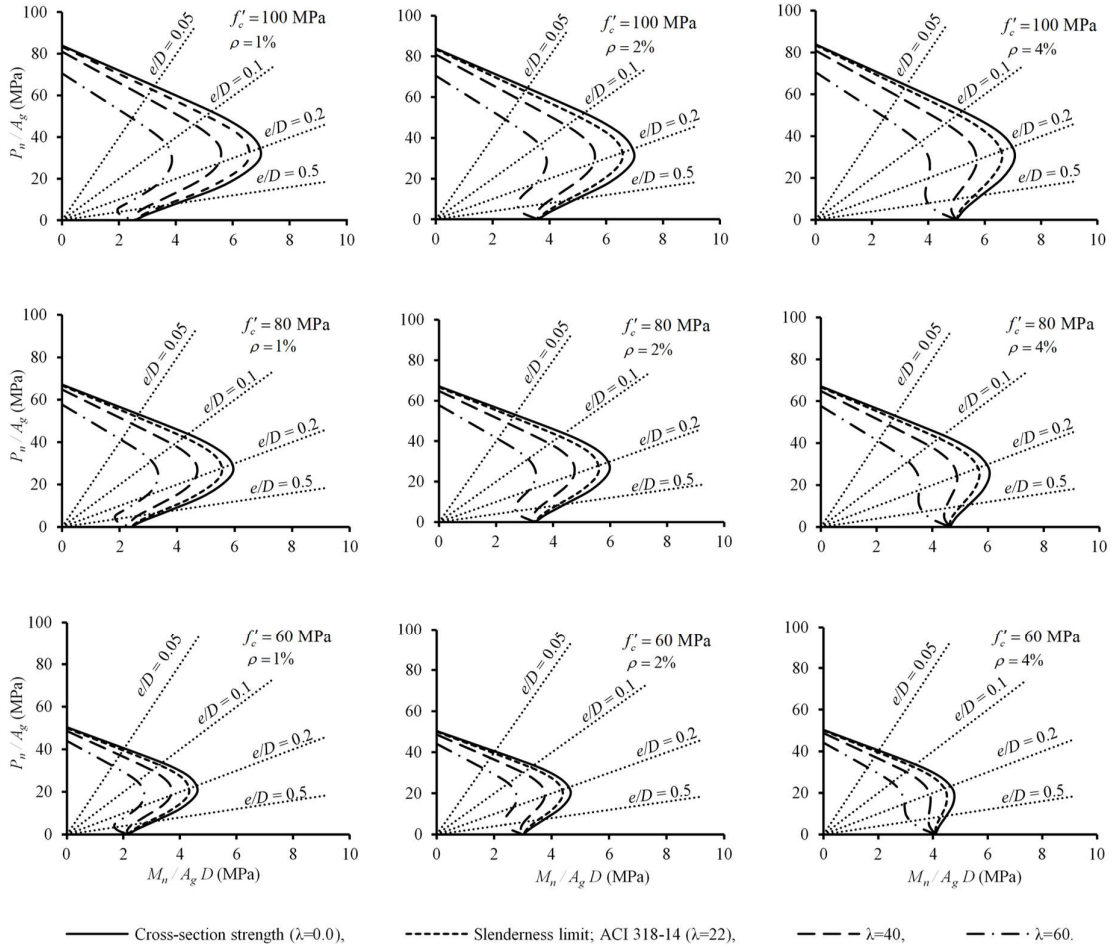

Figure 6.17– Effect of implementing HSC on the developed interaction diagrams at different slenderness ratios.

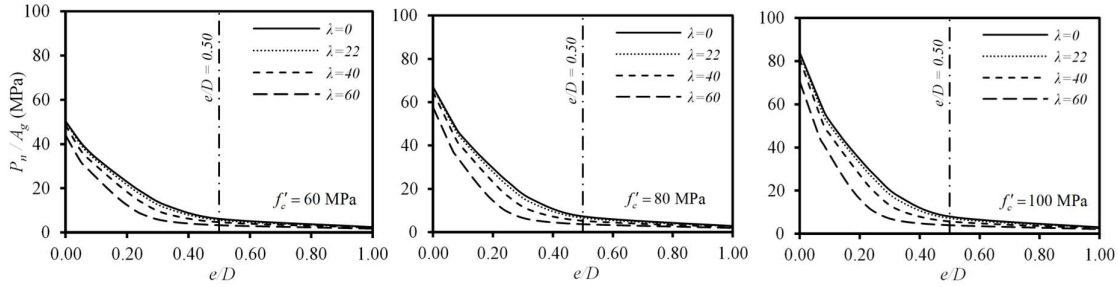

Figure 6.18– Normalized load versus eccentricity ratio of HSC columns at various slenderness ratios.

6.8 Conclusions

Based on the experimental tests extended by the theoretical second-order analysis, the following conclusions can be drawn.

1. Over the range of slenderness ratios and compressive strength of HSC tested, GFRP reinforcement proved its feasibility as a substantial replacement for conventional steel in slender HSC columns. Moreover, GFRP bars improved the capacity and lateral resistance of the slender HSC columns, while GFRP spirals provided thorough confinement levels.

2. Up to the slenderness limit tested ($\lambda = 33$), all slender GFRP-HSC columns experienced material failure and did not exhibit any stability failure. Stability failure is defined herein according to ACI provisions (2019), which set the stability index in terms of a secondary-to-primary moment ratio equal to 1.4.

3. The axially loaded slender GFRP-HSC columns experienced early concrete-cover spalling compared to the NSC columns. This caused that concentrically loaded HSC columns achieved a column-to-cylinder compressive-strength ratio $\left(f_c'\right)_{column} / \left(f_c'\right)_{cylinder} = 0.8$, while the slender GFRP-NSC columns had a ratio approaching 1.

4. Considering AASHTO (2018b) definition of the compression- and tension-controlled failures, the slender GFRP-RC columns tested under concentric or low eccentric ($e/D = 0.16$) loading experienced compression failure in terms of concrete-cover spalling, tensile rupture of GFRP spirals, and compressive crushing of GFRP bars. In contrast, the failure mode attributed to the slender GFRP-RC specimens loaded at an $e/D = 0.66$ exhibited tension failure that was controlled by exaggerated tensile cracks, accompanied by excessive lateral deformations triggering large support rotations. Lastly, the slender GFRP-RC columns tested under moderate eccentric ($e/D = 0.33$) loading experienced a transition failure between compressive and tensile failure mechanisms.

5. The slender GFRP-HSC columns was slightly more susceptible (2%) to the initial applied eccentricity compared to their NSC counterparts owing to the relatively early exposure to

flexural–tensile cracks attributed by the HSC specimens. For example, at e/D values equal to 16%, 33%, and 66%, the GFRP-HSC specimens lost, respectively, 49%, 75%, and 89% of their axial capacity, while the GFRP-NSC columns lost 47%, 73%, and 87% of their axial capacity, respectively.

6. The models developed for the axially and eccentrically loaded GFRP-HSC columns were verified against the results of the current experimental program as well as the experimental database from the literature. Both models considered the material and geometrical nonlinearities and yielded a substantial correlation with the test results.

7. A family of $P-M$ interaction diagrams were plotted over a wide range of test parameters, including slenderness ratio, concrete compressive strength, and GFRP-reinforcement ratio. The theoretically established interaction envelopes were found to be in good agreement with those developed experimentally. All developed $P-M$ interaction diagrams revealed an inflection point at e/D near to 0.2.

8. The impact of GFRP-reinforcement on the behavior of slender GFRP-HSC columns was more pronounced at higher slenderness ratios in terms of reducing the induced second-order effects. For example, at $e/D=0.2$, $\lambda=60$, and $f_c'=80$ MPa, axial column capacity dropped by 50.7%, 46.8%, and 40.7% compared to the concentrically loaded strength when the GFRP-reinforcement ratios were 1%, 2%, and 4%, respectively.

9. Based on the results of the conducted tests, experimental database from literature, and the analytical modeling performed, a slenderness limit for short HSC columns bent in a single curvature with equal end eccentricities considering the limited ductility of constituent materials was proposed as

$$\lambda_{(f_c'>55)}=\lambda_{(f_c'\le 55)}-\frac{\left(f_c'-55\right)^{1.44}}{100} \qquad 55\le f_c' \text{ (MPa)} \le 125$$

Finally, the experimental and analytical evidences from this study provide valuable data and design provisions that encourage implementation of GFRP reinforcement in slender HSC compression members. These provisions, therefore, support including sections dealing with the

design and use of non-prestressed slender compression members (columns, piles, and piers) entirely reinforced with GFRP bars into future editions of the AASHTO (2018a), ACI (2015), and CSA (2012 and 2019).

CHAPTER 7

Proposed Flexural Stiffness of Slender Concrete Columns Reinforced with GFRP-Bars

Proposition de la rigidité en flexion de poteaux élancés en béton armé de barres de PRFV

Foreword

Authors and Affiliation:

- **Waseem Abdelazim** is a doctoral candidate in the Department of Civil Engineering at the University of Sherbrooke, Sherbrooke, QC, Canada, J1K 2R1.
- **Hamdy M. Mohamed** is a research associate and lecturer in the Department of Civil Engineering at the University of Sherbrooke, Sherbrooke, QC, Canada, J1K 2R1.
- **Brahim Benmokrane**, **FACI**, is a Professor in the Department of Civil Engineering, Université de Sherbrooke, Sherbrooke, Quebec, Canada, J1K 2R1.

Journal Title and Paper Status:

Submitted to *ACI Structural Journal* in February 17, 2020.

Contribution to the Thesis:

The reported study introduces a multiple linear regression analysis of the simulated theoretical data of 9,500 RC columns in order to propose a simple and practical design equation for the effective flexural stiffness of slender GFRP-RC columns. This included a re-examination of the current moment magnification method in ACI 318 for the structural analysis of slender steel-RC columns to accommodate concrete columns reinforced with GFRP bars. Finally, the

stiffness reduction factor used to reduce the critical buckling load of a single isolated slender GFRP-RC column was recommended as 0.6 based on the one-percentile statistical analysis.

Abstract

The well-established moment magnifier approach specified in ACI 318 for the structural analysis of steel-reinforced concrete (RC) slender columns, was re-examined herein to accommodate glass fiber-reinforced polymer (GFRP)-RC columns. This undoubtedly encourages North American codes and guidelines (ACI 440.1R; CSA S806) to include detailed sections dealing with the design and analysis of RC columns entirely reinforced with FRP-bars. Consequently, a 2nd-order analytical model was derived to assess the structural performance of more than 9,500 GFRP-RC slender columns dominated a wide range of design parameters. The developed analytical model indicated a good correlation with the experimental data of 72 large-scale FRP-RC columns were assembled from the current study and the literature. The investigated parameters were the applied eccentricity ratio, the slenderness ratio, the longitudinal GFRP-reinforcement ratio, the elastic modulus of GFRP-bars, the concrete compressive strength, the column cross-section geometry, and GFRP-bars arrangement. Thereafter, a multiple linear regression analysis was conducted of the simulated theoretical data in order to propose a simple and practical design equation of the effective flexural stiffness of GFRP-RC slender columns. Lastly, the stiffness reduction factor used to reduce the critical buckling load of a single isolated GFRP-RC slender column was recommended as 0.6 based on the one-percentile statistical analysis.

7.1 Introduction

Design for reinforced concrete (RC) slender columns can be generally broken down into two main stages. The first stage is the analysis of the structure to calculate the moment and forces in each member, accounting for the reduction in the members' stiffness due to the concrete cracking. This structural analysis should allow in some way to consider the additional moments formed due to any initiated lateral deformations. Several factors stimulate these lateral deflections such as the exposure to eccentric or lateral loads, column slenderness, and structure sidesway. The second design phase is to properly specify the column cross-section geometry, material properties, and reinforcement details that is capable to sustain the straining actions determined from stage one. Phase two is well-addressed by many codes and guidelines for both steel-RC columns (ACI 318-19; CSA A23.3-14) and FRP-RC columns (CSA S806-12).

Again, precise analysis of any structure requires that the deformed geometry of the structural members and the initial applied forces be integrated into the equilibrium equations; this is called second-order analysis. The main challenge in the second-order analysis is that the structure deformations and the applied external loads are reciprocal, interdependent parameters that necessitate a convergence iterative process. This is a time-consuming process and, thus, is not suitable for repetitive office design. ACI building code (ACI 318-19), therefore, adopts the simple and satisfactory moment magnifier approach to replace the rigorous and extensive 2nd-order analysis of steel-RC slender columns. ACI approach uses the axial load (P_u) obtained from first-order analysis, while considers the slenderness effects through applying a magnification factor (δ) to the first-order factored moments. This magnification factor is a function of the critical buckling load (P_c) of the column and can be computed as

$$\delta = \frac{C_m}{1 - \dfrac{P_u}{\phi_K P_c}} \geq 1.0 \tag{7.1}$$

$$P_c = \frac{\pi^2 \, (EI)_{eff}}{(kl_u)^2} \tag{7.2}$$

where C_m is a correction factor relating the actual moment diagram to an equivalent uniform moment diagram, ϕ_K is a stiffness reduction factor, k is the effective length factor mirrors the column end conditions, and l_u is the column unsupported length. The main challenge to generalize the applicability of the moment magnifier approach to include FRP-RC slender columns is the properly choice of a flexural stiffness $(EI)_{eff}$ that is used to determine the critical buckling loads. The selected EI value should reasonably approximate the variations in the column stiffness due to cracking, creep, nonlinearity of the concrete stress-strain curves along with the FRP-bars compressive characteristics and the relatively lower flexural stiffness of FRP-bars compared to steel-bars.

In the last two decades, limited attempts have been conducted to assess and develop expressions for the effective flexural stiffness of FRP-RC columns (Mirmiran et al. 2001a; Jawaheri Zadeh and Nanni 2017; Xue et al. 2018; Hadhood et al. 2018b). Among each other, Xue et al. (2018) and Hadhood et al. (2018) supported their work with experimental evidences using test results of FRP-RC columns. A review of the proposed effective flexural stiffness of FRP-RC slender columns found in literature are comprehensively discussed below. However, the recommendations for the effective flexural stiffness of FRP-RC slender columns found in the literature have several discrepancies that should be reviewed. Moreover, the obvious scarcity of test data of FRP-reinforced slender columns accentuates the need for more experimental studies that investigate the performance of such members. Therefore, the major objectives of our experimental and theoretical program can be summarized as follows:

1. To experimentally assess the moment-curvature relationship of GFRP-RC slender columns, identifying the influence of the different test parameters on the column flexural stiffness.
2. To quantify the simulated theoretical flexural stiffness of approximately 9,500 FRP-RC slender columns, conducting a comparative study with the ACI 318-19 provisions of steel-RC slender columns.
3. To develop EI design equations for GFRP-RC slender columns that could support the work of the North American technical committees engaged in developing standards and design guidelines for GFRP-reinforced concrete columns.

4. To propose a stiffness reduction factor ϕ_K that is used to consider the probability of understrength of a single isolated GFRP-RC slender column.

7.2 A Review of the Flexural Stiffness

7.2.1 Steel-RC columns

ACI 318-19 permits using two simple and approximate expressions (Eq. 7.3 and Eq. 7.4) to calculate the effective flexural stiffness EI_{eff} used to define the critical buckling load P_c of steel-RC columns and, hence, to determine the corresponding moment magnification factor δ. For the case of no sustained loads, ACI EI is expressed as

$$EI_{ACI(a)} = 0.2E_cI_g + E_sI_s \tag{7.3}$$

$$EI_{ACI(b)} = 0.4E_cI_g \tag{7.4}$$

where E_c and E_s are the moduli of elasticity of concrete and steel, respectively; I_g and I_s are the moment of inertia of gross concrete cross-section and steel reinforcement about centroidal axis, respectively. The main concern about these two expressions that these equations were basically derived for slender columns fail in compression with small eccentricity-to-depth ratios (e/h) and high axial load ratios (P_u/P_o), and thus overestimates EI values for steel-RC slender columns have eccentricity ratios $e/h > 0.4$ (MacGregor et al. 1975). Moreover, Eq. (7.4) is more desirable for cases where the slenderness effects are not very substantial (MacGregor et al. 1970). However, ACI permits to use these two formulas for all range of axial loads, initial applied eccentricities, and slenderness ratios. Khuntia and Ghosh (2004) avoided the weaknesses of EI formulas in ACI and provided more refined values of the effective EI including the influence of reinforcement ratio ρ, e/h and P_u/P_o into the proposed equation (Eq. 7.5) of the effective flexural stiffness. Current edition of ACI 318-19 allows applying Khuntia and Ghosh's expression for $(EI)_{eff}$ of steel-RC columns.

$$EI_{ACI(c)} = E_c I_g (0.80 + 25\rho) \times (1 - e/h - 0.5\, P_u / P_o) \tag{7.5}$$

Eq. (7.5) is restricted to minimum and maximum boundaries of $0.35E_cI_g$ and $0.875E_cI_g$, respectively. ACI reports that the latter formula gives an improved accuracy for the effective EI value. Nevertheless, it provides EI values close to the twice of the effective EI computed using ACI expressions $EI_{ACI(a)}$ and $EI_{ACI(b)}$, especially for high levels of P_u/P_o and low levels of e/h.

Tikka and Mirza (2005) examined the applicability of ACI EI equations using over 11,000 isolated square steel-RC columns bent in a symmetrical single curvature. They showed that ACI EI values substantially deviate from the theoretically computed ones. These theoretical secant stiffness values were defined by the moment-curvature $(M-\varphi)$ relationships. Moreover, Tikka and Mirza inferred that the one-percentile stiffness ratios (EI_{th}/EI_{ACI}) were extremely low with significant variations over the specified studied parameters. The discrepancies in the ACI EI formulas were related to the constant coefficient value of 0.2 or 0.4 assigned to the contribution of concrete in the ACI stiffness equation (E_cI_g). In addition, ACI equation b (Eq. 7.4) ignores the influence of the reinforcement ratio to the computed effective flexural stiffness. Therefore, Tikka and Mirza (2005) proposed the following equation for the short-term EI_{eff}.

$$EI_{eff} = \left(0.47 - 3.5 e/h \left(\frac{1}{1 + \beta e/h} \right) + 0.003 \frac{k l_u}{h} \right) E_c I_g + 0.8 E_s I_s \tag{7.6}$$

in which $\beta = 7.0$ for $\rho \le 2\%$ and $\beta = 8.0$ for $\rho > 2\%$. The positive sign of the geometrical slenderness ratio factor is explained by Tikka and Mirza as the distance between successive cracks in longer columns is more than shorter ones, which results in a higher effective flexural stiffness for longer columns. In other words, this expression (Eq. 7.6) means that, at the same cross-section geometric, material, and loading conditions, longer columns effectively resist lateral buckling than short columns which needs to be revised.

7.2.2 FRP-RC columns

Limited endeavors have been driven to develop an EI_{eff} for slender columns entirely reinforced with FRP-bars. These attempts have been made as an inevitable result of the successful introduction of FRP-reinforcements in construction market owing to its great advantages over the traditional steel-bars. Consequently, Mirmiran et al. (2001a) conducted a detailed parametric study to adjust the ACI stiffness formulas to consider FRP-reinforcement. They kept the expression of $EI_{ACI(a)}$ was applied to FRP-RC columns with no changes needed. In addition, they performed some modifications to the ACI equation b (Eq. 7.4), considering the change in the applied eccentricity ratio up-to 1.0.

$$EI_{eff} = \begin{cases} 0.25E_cI_g \ \ (\text{for } e/h \le 0.4) \\ 0.10E_cI_g \ \ (\text{for } e/h \le 1.0) \end{cases} \tag{7.7}$$

Additionally, Mirmiran et al. (2001a) proposed a stiffness reduction factor ϕ_K ranges from 0.35 to 0.75 based on the applied eccentricity ratio and the FRP to concrete modular ratio. Alternatively, Jawaheri Zadeh and Nanni (2017) derived an expression for EI value based on a plane analysis of a rectangular cross-section. They employed the derived equations to modify the ACI formulas to accommodate FRP reinforcement as given below

$$EI_{eff(a)} = 0.2E_cI_g + 0.75E_{frp}I_{frp} \tag{7.8}$$

$$EI_{eff(b)} = 0.2E_cI_g + 0.2E_cI_g\,(E_{frp}/E_s) \tag{7.9}$$

in which the first and second terms denote the concrete and FRP contributions to the flexural stiffness, respectively; E_{frp} is the modulus of elasticity of FRP-bars; I_{frp} are the moment of inertia of the FRP-reinforcement about centroidal axis. Furthermore, Jawaheri Zadeh and Nanni (2017) applied a stiffness reduction factor $\phi_K = 0.75$ similar to ACI provisions for steel-RC columns. Hadhood et al. (2018) developed an analytical expression (Eq. 7.10) for EI_{eff} of FRP-RC columns similar to the $EI_{ACI(c)}$ formula which is originally proposed by Khuntia and Ghosh (2004) for steel-RC columns.

$$EI_{eff} = \begin{cases} E_c I_g (0.50 + 25\rho E_{frp}/E_s) \times (1 - e/h) & (\text{for } e/h < 0.5) \\ E_c I_g (0.15 + 25\rho_{ten} E_{frp}/E_s) & (\text{for } e/h \geq 0.5) \end{cases} \quad (7.10)$$

where ρ_{ten} is the FRP-reinforcement ratio on tension side only. The proposed expressions showed a good correlation with the results from test data of 25 FRP-RC circular columns have a mechanical slenderness ratio $kl_u/r = 19$, where r stands for the radius of gyration of the column cross-section. Recently, Xue et al. (2018) established a nonlinear finite element modelling to perform a parametric study of FRP-RC slender columns have a rectangular cross-section. The effective flexural stiffness of FRP-RC columns was expressed as

$$EI_{eff} = \max. \begin{cases} \left(0.45 - \left(1 + 0.01 kl_u/h\right) e/h + 0.008 kl_u/h\right) E_c I_g + E_f I_f \\ 0.055 E_c I_g + E_f I_f \end{cases} \quad (7.11)$$

which was subjected to the following limitations: $e/h \geq 0.1$; $kl_u/h \leq 30$; and $f_c' \leq 50$ MPa, where h is the column minimum dimension. The concerns regarding the positive sign of the factor of the geometrical slenderness ratio can be demonstrated as discussed earlier for the formula derived by Tikka and Mirza (2005). The stiffness reduction factor ϕ_K was proposed as 0.7. The above review of the EI design equations reveals an obvious scattering in the proposed EI values found in the literature. Thus, a detailed statistical analysis was validated with test results to verify the existing design provisions and to propose a new EI expression for FRP-RC slender columns. The conducted analytical program is introduced in the forthcoming sections.

7.3 Generating of the EI Theoretical Model

Timoshenko and Gere (1963) obtained the maximum secondary moments $M_{\max}$ at the middle of a pin-ended column bent in a single curvature and subjected to equal end eccentricities (Fig. 7.1) as

$$M_{\max} = -EI\left(\frac{d^2y}{dx^2}\right)_{x=l/2} = M_0 \sec u \quad (7.12)$$

in which $M_{\max} = P_u \cdot (e + y_{\max})$; $M_0 = P_u \cdot e$; and $u = (\pi/2)\sqrt{P_u/P_c}$. Substituting for u and P_c from Eq. (7.2) in Eq. (7.12), and solving for EI, one can write

$$EI_{th} = \frac{P_u l^2}{4\left[\sec^{-1}\left(\frac{M_{\max}}{M_0}\right)\right]^2} \tag{7.13}$$

Which provides the theoretical value of the flexural stiffness for slender columns. In Eq. (7.13), P_u and M_0 are the cross-section strength, while $M_{\max}$ is the column strength. Both the cross-section and column strength values can be represented by the typical $P-M$ interaction diagram shown in Fig. (7.2). Development of the simulating model used to calculate P_u, M_0, and $M_{\max}$ is outlined below. Prior to that, the axial load-moment-curvature $(P-M-\varphi)$ relationship was established to be used in the analytical derivation of the EI_{th}.

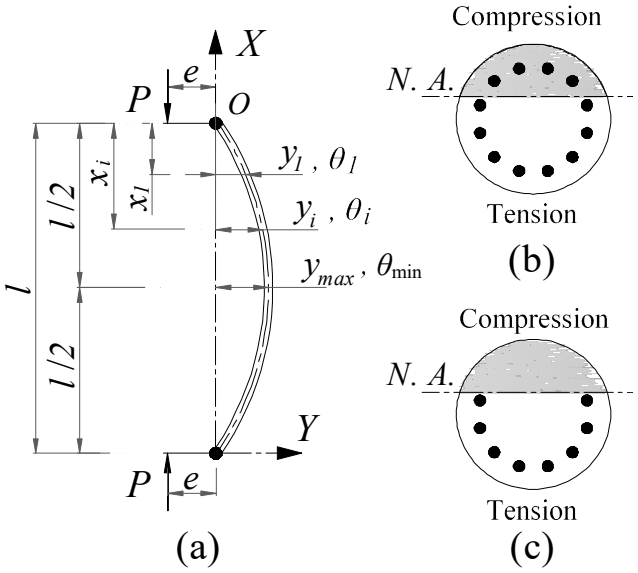

Figure 7.1– (a) Pin-ended column model; (b) Real cross-section; (c) Assumed equivalent cross-section

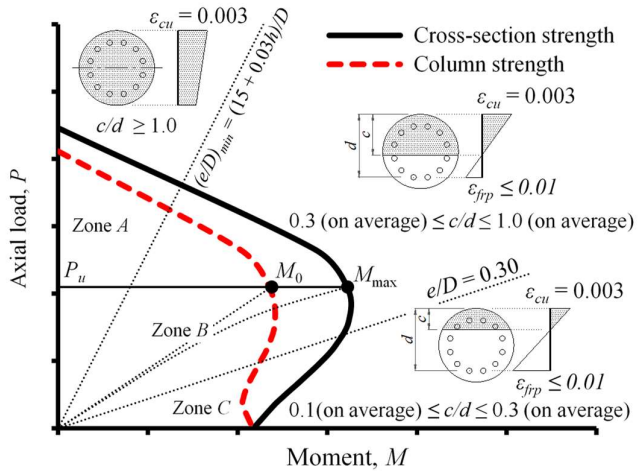

Figure 7.2– Typical P-M interaction diagrams of GFRP-RC cross-section and column analysis.

7.3.1 Load-moment-curvature relationship

A $P-M$ strength curve with a constant curvature which is, also, known as $P-M-\varphi$ diagram can be constructed using a cross-section analysis, accounting for material nonlinearities. Herein, a strip-by-strip approach, in which the cross-section is discretized into several integration layers, was used to compute the cross-section strength at a series of curvature (φ) increments. Given the fundamental assumptions of reinforced-concrete mechanics, additional assumptions were applied: (1) FRP-bars have a linear elastic stress–strain response up to failure. The ultimate tensile strain in FRP-bars was assumed to be the lesser of 0.01 or ε_{frpu} to avoid any excessive lateral deformations of FRP-RC columns (Jawaheri Zadeh and Nanni 2013, Hadhood et al. 2019), where ε_{frpu} is the ultimate tensile FRP-bar strain; (2) The contribution of FRP-bars in compression is limited to the concrete's compressive strength (see Fig. 7.1c). This assumption has been adopted by many other researchers and proved its applicability to predict the compressive capacity of FRP-RC members (Jawaheri Zadeh and Nanni 2017; Hadhood et al. 2018b; Guérin et al. 2018). (3) The confinement effect is limited by the strength of eccentric slender columns (Martin et al. 1966) and is, therefore, neglected in the analysis; and (4) The ACI 440.1R-15 provisions for the ultimate concrete strain ε_{cu} are met (i.e., $\varepsilon_{cu} = 0.003$). In addition, the concrete compressive stress–strain distribution could be

established by the unconfined three-parameter model reported by Thorenfeldt et al. (1987) which is originally proposed by Popovics (1973). The compressive stress (f_c) at the corresponding strain (ε_c) is expressed as

$$\frac{f_c}{f_c'}=\frac{\varepsilon_c}{\varepsilon_o}\cdot\frac{n}{n-1+\left(\varepsilon_c/\varepsilon_o\right)^{nk}} \tag{7.14}$$

$$\varepsilon_o=\frac{f_c'}{E_c}\cdot\frac{n}{n-1} \tag{7.15}$$

where ε_o is the concrete strain at the compressive strength of concrete f_c'; n is a curve-fitting factor equal to $0.8+f_c'/17$ in MPa; and E_c is the modulus of elasticity for concrete and can be calculated for normal-weight concrete as $4700\sqrt{f_c'}$ (ACI 318-19); k is a factor and can be calculated as

$$k=\begin{cases}1 & \varepsilon_c/\varepsilon_o\le 1\\ 0.67+f_c'/62 & \varepsilon_c/\varepsilon_o>1\end{cases} \tag{7.16}$$

At each value for the column curvature φ_j, an incremental value of the concrete strain ε_i was set and the neutral axis position c was located at $c=\varepsilon_i/\varphi_j$, where the subscripts $i=1,2,...,n$ and $j=1,2,...,m$ identify the step number. Applying a strip-by-strip cross-sectional analysis on the basis of force equilibrium and compatibility conditions, the resultant axial load P_{ji} and corresponding bending moment M_{ji} was determined. Then, the previous steps were repeated using another strain increment ε_{i+1} up to the failure was triggered either by the concrete crushing or the rupture of the FRP-bars. Finally, a $P-M$ strength curve with a constant curvature φ_j was plotted. Different values of curvatures up-to $\varphi_{j=m}$ were assumed in order to plot a complete family of the $P-M-\varphi$ curves for each predefined column cross-section parameters (Fig. 7.3). The boundary of the developed $P-M-\varphi$ curves (solid line in Fig. 7.3) defines the cross-section strength (i.e. $M_{\max}$).

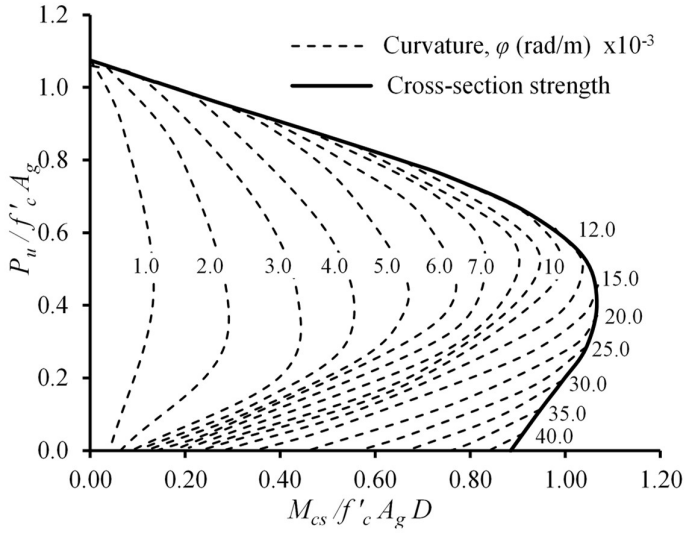

Figure 7.3– Typical P-M-φ curves.

7.3.2 Second-order analysis

Besides the force equilibrium and strain compatibility required for the analytical modeling of short columns (cross-sectional analysis), the modeling of slender and long columns requires the geometrical nonlinearities be integrated into the equilibrium equations, this is called as a second-order analysis. In computing the flexure stiffness of a slender column, it is desired to define an effective flexural stiffness value that expresses an average magnitude for both the cracked and uncracked regions along the column length and not relying upon the most cracked section. Therefore, the numerical integration scheme herein was performed by subdividing the column length into equal N segments as presented by Chen and Atsuta (1976). This approach considers the variation of the column curvature along the column height and does not require any assumptions for the column's deflected shape as being sine or cosine waves.

At each combination of P and e, column rotation θ_o at point O was assumed (see Fig. 7.1a). Then, the column deflection y_i and rotation θ_i at the column segment N_i was determined from the following expressions:

$$y_i = y_{i-1} + \theta_{i-1}(x_i - x_{i-1}) - \frac{1}{2}\varphi_{i-1}(x_i - x_{i-1})^2 \tag{7.17}$$

$$\theta_i = \theta_{i-1} - \varphi_i (x_i - x_{i-1}) \tag{7.18}$$

in which the curvature φ_i can be found from the developed $P-M-\varphi$ relationships using the initial value of P and a secondary moment $M_i = P(e + y_i)$. Then, y and θ values were successively calculated for each segment till the value of $y_{\max}$ was achieved at the column mid-height. At $y = y_{\max}$, corresponding rotation at mid-height $\theta_{\min}$ should equal or approach to zero, otherwise another value of θ_o was assumed and the calculations were repeated. Thereafter, at the same eccentricity, the axial load level was increased till the column failure achieved in one of the previously discussed mechanisms. Other points on the $P-M$ interaction diagram of the FRP-RC slender columns can be found by assuming various eccentricities and replicating the analysis. Finally, the magnitudes of M_0 and $M_{\max}$ to be used in the computation of the theoretical EI in Eq. (7.13) can be calculated as

$$M_0 = P_u \cdot e \tag{7.19}$$

$$M_{\max} = P_u \cdot (e + y_{\max}) \tag{7.20}$$

7.4 Experimental Program and Model Verification

7.4.1 Testing plan and failure modes

The experimental program herein was conducted to investigate the buckling behavior and moment-curvature relationships of GFRP-RC slender columns. The test program, therefore, was consisted of 28 pin-ended GFRP-RC columns have different slenderness ratios and were loaded at different eccentricity ratios. The relevant test matrix, column geometry and test parameters are summarized in Table 7.1. The design for internal reinforcement in all specimens complied with ACI 318-19 and CSA S806-12 provisions. No. 5 Grade III sand-coated GFRP-bars with an average fiber content of 83.8% and No. 3 Grade II sand-coated GFRP spirals with an average fiber content of 78.9% were used to fully reinforce all the GFRP-reinforced specimens. Table 7.2 reports the average ultimate longitudinal tensile properties of the GFRP

and steel materials, as provided by the manufacturers. The significance of the confinement level was quantified in terms of the spiral pitch distance (40 mm and 80 mm) as indicated in Table 7.1. A tighter spiral pitch of 50 mm was used in the top and bottom regions (each was 250 mm in length) to prevent any premature failure near the zones of stress concentration.

All columns were cast using a single batch of ready-mixed normal-strength, normal-weight concrete has a maximum aggregate size of 10 mm. At the same day of testing, the average concrete compressive strength was 46 MPa. All the specimens were instrumented to measure the axial and lateral deformations as well as the local strains in the longitudinal bars, spirals, and concrete surface. All the strain gauges were located at the mid-height of the columns, where the maximum strain values are expected. All the test specimens were tested at the Canada Foundation for Innovation (CFI) structural laboratory of the University of Sherbrooke (Sherbrooke, Quebec, Canada) using an 11,400 kN MTS testing machine. All columns were loaded up-to a level of 75% of the estimated capacity under loading control at a constantly increasing rate of 2.5 kN/s. Testing continued under displacement control at a displacement rate of 0.002 mm/s until the specimens could not withstand any additional increase in the applied axial force or the longitudinal GFRP-bars ruptured. Fig. 7.4 shows the test-setup and the typical failure modes.

All GFRP-RC columns exhibited a material-type failure with no tensile rupture of GFRP-bars was observed till the end of the test. The GFRP-reinforced concrete columns tested under concentric or low $(e/D = 16\%)$ or moderate $(e/D = 33\%)$ eccentric loads exhibited a compression-based failure in terms of concrete-cover spalling at peak accompanied with a significant drop in the column carrying capacity. Beyond peak, axially loaded columns (Fig. 7.5) experienced a tensile rupture of GFRP spirals followed by compression rupture of GFRP-bars at ultimate stages. The failure mode attributed to the slender GFRP-reinforced concrete columns tested under large eccentric loading $(e/D = 66\%)$ was controlled by exaggerated tensile cracks, accompanied by excessive lateral deformations triggering large support rotation. This was metaphorically termed as tension-based failure. Further details regarding the testing program and the failure mechanisms dominated the behavior of GFRP-RC slender columns can be found in Abdelazim et al. (2020).

Table 7.1 – Test matrix and results

Gr.	Column ID	Geometry		Longitudinal Reinforcement		Transverse Reinforcement		e (mm)	e/D (%)	P_n (kN)	δ (mm)	GFRP-bar strain ($\mu\varepsilon$)		Concrete strain ($\mu\varepsilon$)	EI_{exp} / E_cI_g
		L (mm)	λ	No. & size	ρ_L (%)	Size & pitch	ρ_T (%)					Comp.	Ten.		
1	G1-C	1000	14	8 No. 5	2.2	No. 3 @ 80	1.17	C	0	3,535	—	– 3,420	– 3,420	– 3,420	—
	G1-66							200	66	417	9.1	– 3,050	6,610	– 3,050	0.20
2	G2-C	1250	17	8 No. 5	2.2	No. 3 @ 80	1.17	C	0	3,490	—	– 3,130	– 3,130	– 3,130	—
	G2-66							200	66	403	12.1	– 2,830	6,400	– 3,080	0.20
3	G3-C	1750	23	8 No. 5	2.2	No. 3 @ 80	1.17	C	0	3,453	—	– 3,130	– 3,130	– 3,130	—
	G3-16							50	16	1,807	6.3	– 3,170	420	– 4,100	0.52
	G3-33							100	33	891	12.2	– 3,190	3,810	– 4,440	0.33
	G3-66							200	66	388	15.4	– 3,100	6,690	– 3,430	0.19
4	G4-C	1750	23	12 No. 5	3.3	No. 3 @ 80	1.17	C	0	3,463	—	– 3,520	– 3,520	– 3,750	—
	G4-16							50	16	1,881	5.4	– 3,440	690	– 3,770	0.58
	G4-33							100	33	1,029	9.7	– 2,850	3,820	– 3,230	0.34
	G4-66							200	66	448	13.5	– 3,200	5,980	– 3,990	0.22
5	G5-C	1750	23	8 No. 5	2.2	No. 3 @ 40	2.34	C	0	3,417	—	– 2,880	– 2,880	– 2,880	—
	G5-66							200	66	420	18.2	– 3,640	9,190	– 4,820	0.19
6	G6-C	2000	26	8 No. 5	2.2	No. 3 @ 80	1.17	C	0	3,359	—	– 3,370	– 3,370	– 3,370	—
	G6-66							200	66	382	37.6	– 3,070	8,280	– 3,070	0.18
7	G7-C	2500	33	8 No. 5	2.2	No. 3 @ 80	1.17	C	0	3,331	—	– 3,100	– 2,500	– 3,100	—
	G7-16							50	16	1,725	13.7	– 3,270	740	– 3,790	0.46
	G7-33							100	33	786	22.2	– 3,490	4,200	– 3,920	0.26
	G7-66							200	66	371	33.7	– 3,020	8,750	– 4,100	0.17
8	G8-C	2500	33	12 No. 5	3.3	No. 3 @ 80	1.17	C	0	3,360	—	– 3,030	– 2,700	– 3,030	—
	G8-16							50	16	1,785	11.8	– 2,920	550	– 3,680	0.56
	G8-33							100	33	898	21.2	– 3,560	4,150	– 3,960	0.31
	G8-66							200	66	435	31.2	– 2,950	7,580	– 3,530	0.23
9	G9-C	2500	33	8 No. 5	2.2	No. 3 @ 40	2.34	C	0	3,460	—	– 3,050	– 2,410	– 3,050	—
	G9-66							200	66	374	34.6	– 3,560	8,100	– 3,560	0.17
10	G10-C	2500	33	12 No. 6	4.7	No. 3 @ 80	1.17	25	0	3,588	—	– 3,410	– 3,200	– 3,410	—
	G10-66							200	66	489	29.3	– 2,770	5,740	– 4,950	0.27

Notes: All columns measure 305 mm in diameter (D); All listed test results are at the 1st peak loads; magnitudes of EI_{exp} was computed at a compressive concrete strain does not exceed 0.003; P_u is the axial applied load; δ is the mid-height lateral displacement.

Table 7.2 – Mechanical properties of the GFRP reinforcement

Bar Size	Diameter (mm)	Nominal area [1] (mm^2)	Immersion area (mm^2)	Fiber Content [2] (%)	Elastic Tensile Modulus [3] (GPa)	Nominal Tensile Strength (MPa)	Tensile Strain (%)
# 3	9.5	71	89	78.9	51.1	1281	2.51
# 5	15.9	200	225	83.6	61.8	1449	2.35
# 6	19	284	318	84	61.7	1411	2.29

[1] The strength and elastic modulus were calculated based on this area.
[2] According to the test method described in ASTM D2584 (temp 650°C, sand coating discarded from the results).
[3] Average ultimate longitudinal tensile properties as provided by the manufacturer; test method CSA S806 Annex C.

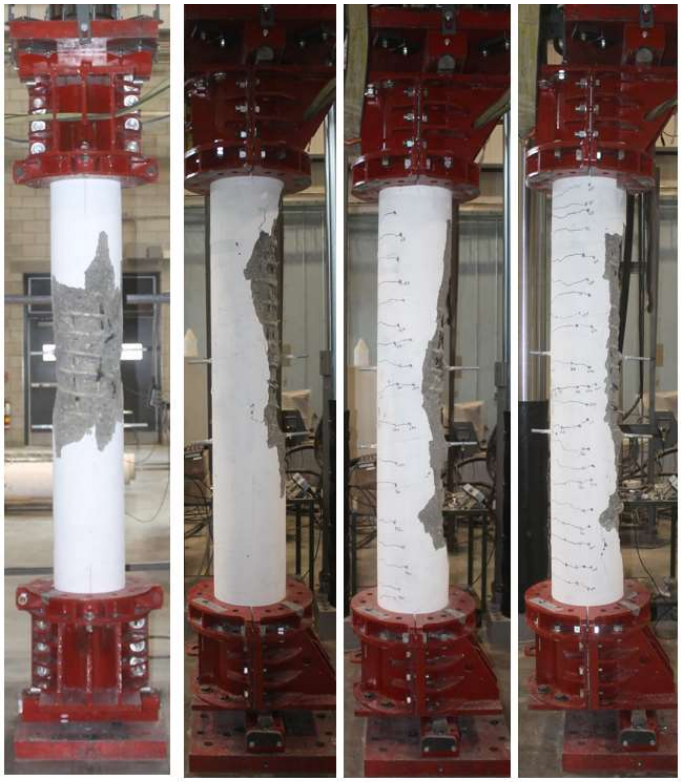

Figure 7.4– Typical failure modes and test setup.

Figure 7.5– Rupture of GFRP-bars and spirals.

7.4.2 Flexural stiffness of the tested specimens

In general, it is customary to define the experimental short-term secant flexural stiffness $(EI_{\exp})$ of GFRP-RC columns from the moment-curvature $(M-\varphi)$ relationship using the following expression:

$$EI_{\exp} = M_{\max}/\varphi \tag{7.21}$$

Consequently, the experimental $M-\varphi$ diagrams were plotted for all the tested column specimens as shown in Fig. 7.6. In general, the magnitude of the flexural stiffness of a steel-RC column can be computed up to the yielding of steel bars on tension side, as the value would drastically diminish after steel yielding and, thus, is of little importance for frame analysis (Khuntia and Ghosh 2004). As GFRP-bars do not yield, the flexural stiffness of GFRP-RC columns was computed up to either the first concrete-cover spalling at a concrete compressive strain of 0.003 as per ACI 440.1R-15, or at a tensile GFRP-bar strain reached 0.01. The latter GFRP-bar tensile strain (0.01) provides an enough warning of failure in terms of excessive deflection and cracking. It is substantial to emphasize that all tested specimens did not reveal GFRP-bar tensile strains exceeded the previous specified strain limit as indicated in Table 7.1.

Recalling Fig. 7.6, it can be revealed that, among each other test parameters, the impact of eccentricity ratio has the most influence on the magnitude of the flexural stiffness of the tested GFRP-RC slender columns as seen in Table 7.1. In addition to the applied eccentricity ratio as a test parameter, the column stiffness experienced a noticeable reduction by the increase in the column slenderness ratio. This reduction in the magnitude of $EI_{\exp}$ due to slenderness ratio attained its maximum at $e/D = 0.33$. The latter observation can be evidenced as the effect of slenderness ratio on the FRP-RC column strength is more significant at e/D near 0.4 (Mirmiran et al. 2001a). Moreover, limited and insignificant variation in the flexural stiffness was revealed when the slenderness ratio of the GFRP-RC columns was increased from 14 (G1-66) to 17 (G2-66). The influence of the longitudinal GFRP-reinforcement ratio on the stiffness value $EI_{\exp}$ was also assessed, as applying a reinforcement ratio $\rho = 3.3\%$ improved the lateral stiffness of the GFRP-RC slender columns on average by 10% (at $\lambda = 23$) and 24% (at $\lambda = 33$) compared to GFRP-RC columns have $\rho = 2.2\%$. This reveals the feasibility of employing the GFRP-bars as an internal reinforcement for RC short as well as slender columns. Finally, using a spiral spacing of 40 mm render the column failure in more ductile manner than those reinforced with larger spacing spirals. However, the confinement effect on the column flexural stiffness was not observed and further experiments are required.

7.4.3 Model verification

The flexural stiffness capacity developed from the theoretical model was verified with the test results from the current study as well as other test results gathered from the literature (Total of 72 specimens). The specimens specified for the verifications have different cross-section geometries (rectangular and circular), reinforcement types (GFRP and CFRP), reinforcement ratios (from 0.9% to 4.7%), slenderness ratios (from 14 to 42), concrete compressive strengths (ranging from 29.1 to 55.2 MPa), and applied eccentricity ratios range from 0.08 to 1.0. Figure 7.7 compares the flexural stiffness predicted analytically with the test results. The theoretical and experimental flexural stiffnesses were normalized to $E_c I_g$. The ratio of the $EI_{\exp}/EI_{th}$ of the 72 specimens ranged from 0.8 to 1.4 with a mean value of 1.02 and a coefficient of variation of 11.5 %. These values provide a reasonable and sensible level of accuracy of the developed

theoretical model for the strength of the FRP-RC slender columns. Hence, the analytical model was used to extend the experimental observations and thoroughly investigate the flexural stiffness behavior of the slender FRP-RC columns.

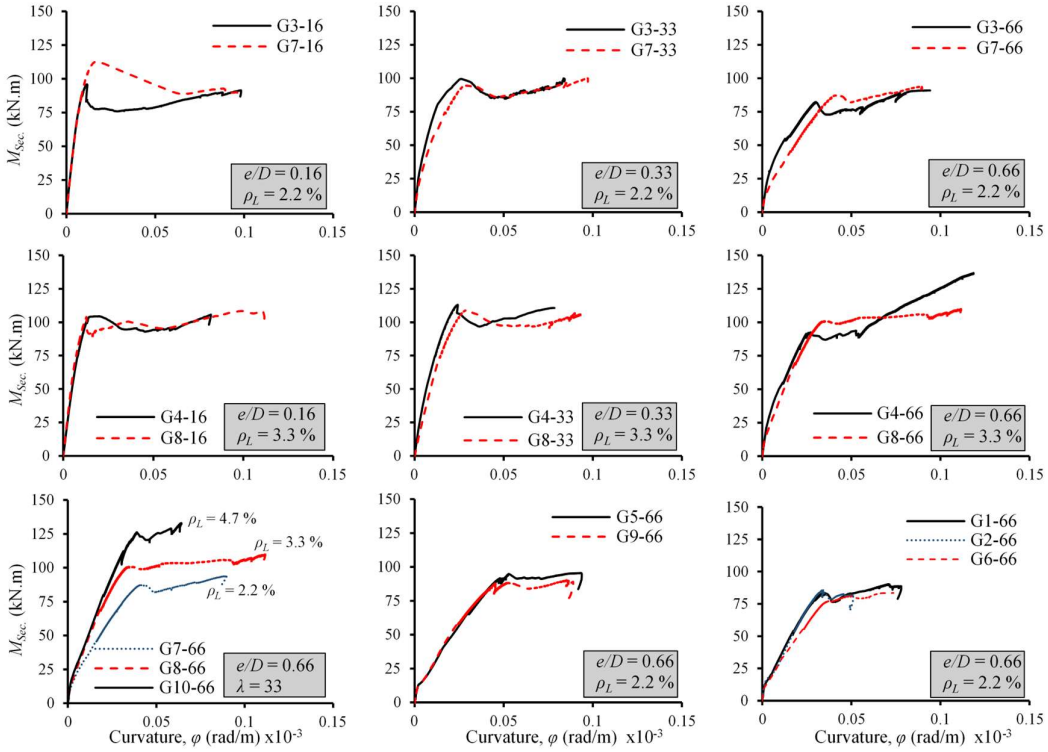

Figure 7.6– Moment-curvature behavior of the tested GFRP-RC columns.

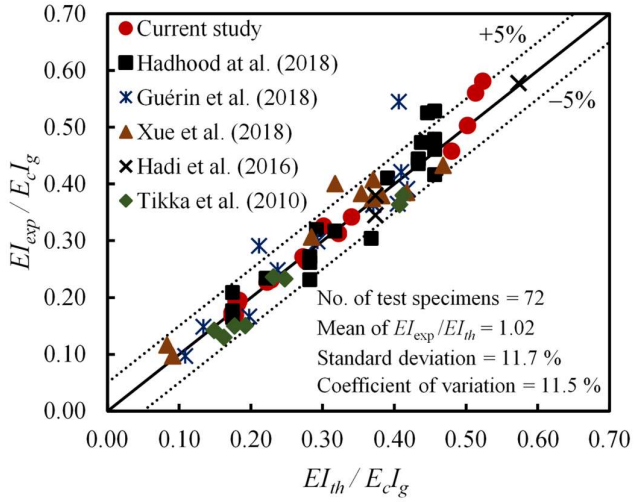

Figure 7.7– Verification of the analytical model with the test results.

7.5 Parametric Evaluation for EI Value

The column parameters and parametric values involved herein were specified to imitate most of the practical cases of normal-strength GFRP-RC slender columns. Table 7.3 and Fig. 7.8 provide the selected parameter values and column geometric properties considered. The associated modulus of elasticity of GFRP-bars E_{frp} for the parametric study was determined based on the usual range of mechanical properties of GFRP-bars on the market. CSA S806-12 limits the longitudinal GFRP-reinforcement ratio (ρ) in columns as ranges from 1% to 8% including splice regions. Therefore, ρ should usually not exceed 4% if the column bars are required to be lap spliced. The GFRP-reinforcement ratio herein was limited to 4%. Moreover, eleven eccentricity ratios ranged from 0.05 to 1.0 were employed in this study. It should be noted that the usual range of e/D (e/h) for practical RC columns in buildings varies from 0.1 to 0.8 (Khuntia and Ghosh 2005). Another study reported that for reinforced concrete buildings, e/h usually ranges from 0.1 to 0.65 (Mirza and MacGregor 1982). In addition, regarding columns have small factored bending moments, ACI 318-19 provisions require applying a minimum eccentricity $e_{\min} = 15 + 0.03h$ (h is in mm) for the design of slender columns. Finally, the parameters discussed earlier were integrated for the analysis of more than 9,500 GFRP-RC columns, with each column has different specified variables.

Table 7.3 – Studied parameters [1]

Properties	Selected values	Number of selected values
f'_c (MPa)	30; 40; 50; 60	4
E_{frp} (GPa)	40; 50; 60	3
$\lambda\,(kl_u/r)$	20; 30; 40; 50; 60; 70	6
ρ (%)	1; 2; 3; 4	4
e/D (e/h)	0.05; 0.10; 0.15; 0.20; 0.25; 0.30; 0.40; 0.50; 0.6; 0.8; 1.0	11
Cross-section geometry and GFRP-bars arrangement	See Fig. (7.8)	3

[1] Total number of studied columns equals ($4 \times 3 \times 6 \times 4 \times 11 \times 3$ =) 9504.

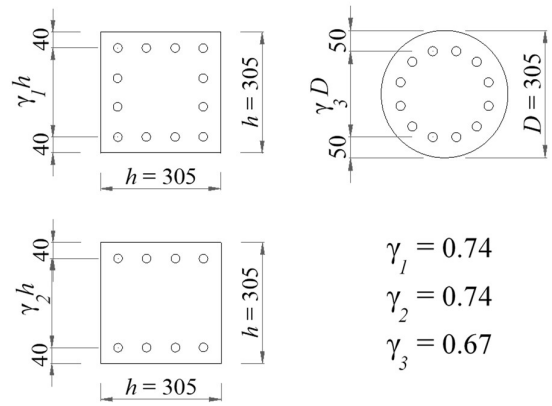

Figure 7.8– Typical cross-sections of GFRP-RC columns considered in the parametric study.

7.5.1 Evaluation of ACI provisions of EI

A comparative review was undertaken to examine the applicability of the ACI expressions (Eq. 7.3 and Eq. 7.4) to be considered as an effective flexural stiffness of GFRP-RC columns. Fig. 7.9 indicates a histogram analysis for the ratio of the derived theoretical flexural stiffness of GFRP-RC slender columns to the ACI effective stiffness formulas (EI_{th}/EI_{ACI}). It could be noticed that both ACI equations revealed unconservative stiffness values for GFRP-RC columns, especially at eccentricity ratios exceeded 0.30 (on average). Moreover, ACI expression 'a' exhibited a better correlation to the theoretical data in terms of the mean stiffness ratio as 1.11. However, the latter expression failed to achieve conservative values of the effective flexure stiffness for more than 50% of the tested columns. Figure 7.10 compares the theoretical flexural stiffness with the ACI equations at each test parameter. The theoretical flexural stiffness and ACI approach in Fig. 7.10 were normalized to the concrete flexural stiffness of the uncracked cross-section $(E_c I_g)$. As shown in Fig. 7.10, over the selected range of the test parameters, ACI expression 'a' defines the lower limit for the flexural stiffness if compared to ACI expression 'b', even at high longitudinal GFRP-reinforcement ratios. Finally, and except the influence of the longitudinal reinforcement ratio, other specified parameters have a trivial and insignificant effect on the normalized ACI EI.

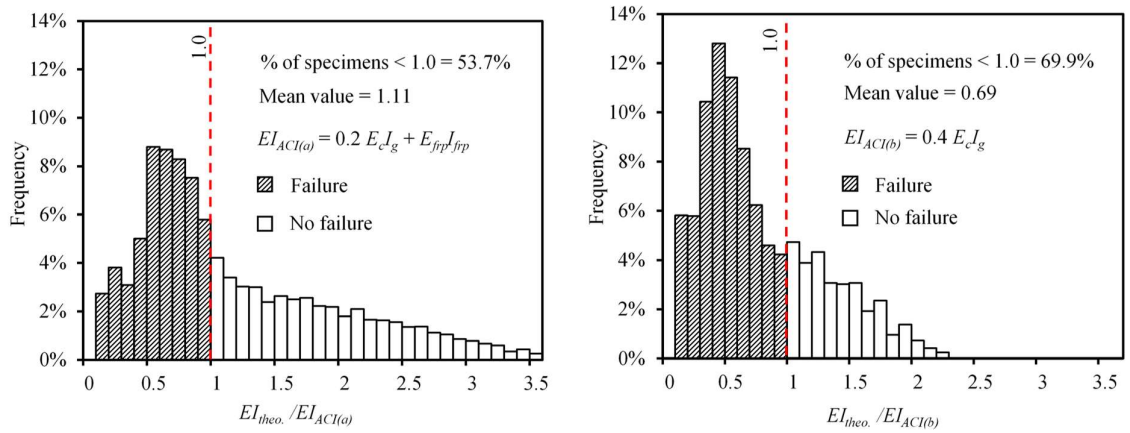

Figure 7.9– Comparison of theoretically-based flexure stiffness with ACI stiffness equations.

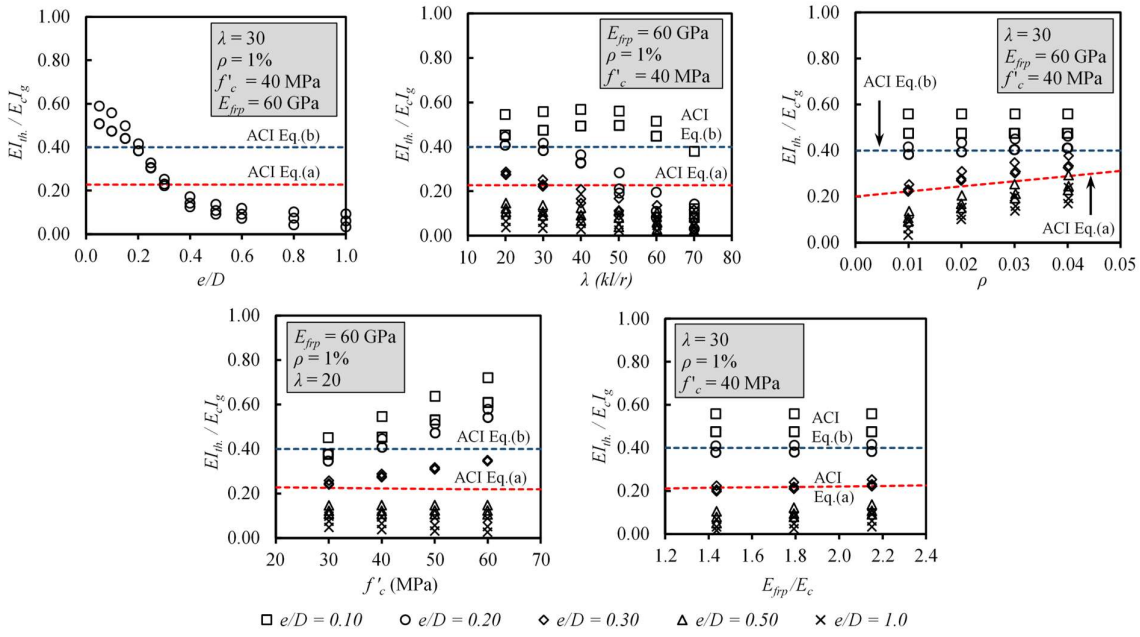

Figure 7.10– Effect of test parameters on the flexural stiffness of GFRP-RC columns.

7.5.2 Influence of the selected parameters on EI value

As discussed earlier, Fig. 7.10 identifies the effect of the various test parameters on the calculated EI_{th}. The applied eccentricity has the major impact on the computed EI_{th} magnitudes, as GFRP-RC columns subjected to high eccentricity ratio demonstrates larger tensile cracks, and thus leading to a relatively lower lateral stiffness. However, the impact of

the eccentricity ratio on the EI_{th} diminishes at an eccentricity ratio exceeds 0.8. The effect of slenderness ratio on EI_{th} is connected and interrelated to the applied eccentricity. In other words, the influence of the slenderness ratio, regarding EI values, was more pronounced at eccentricity ratios range from 0.2 to 0.3. This correlates the experimental results, as GFRP-RC columns have $\lambda = 33$ lost, respectively, 12% and 21% of its lateral stiffness at eccentricity ratios of 0.16 and 0.33 compared to columns have $\lambda = 23$ (see Table 7.1).

As explained before, the resistance of GFRP-bars in compression was limited to the concrete compressive strength. This hypothesis minimized the GFRP-bars compression contribution particularly at low levels of the applied eccentricities $(e/h \le 0.15)$, as at these levels most of the column cross-section suffers compressive stresses (refer to Fig. 7.2). Once the load eccentricity exceeds 0.2, the GFRP-bars contribution to the flexural stiffness of RC slender columns is more pronounced and effectively improved the column resistance to the induced lateral deformations. This, also, is consisted with the findings from experimental tests. As shown in Table 7.1, the normalized experimentally defined EI is always higher for higher longitudinal GFRP-reinforcement ratios of GFRP-RC slender columns tested at e/D ranged from 0.16 to 0.66. Additionally, the contribution of GFRP-reinforcement ratio to the lateral buckling resistance is more pronounced at higher slenderness ratios as well.

For a given e/h, employing a concrete has a higher compressive strength in GFRP-RC slender columns improves the column resistance to the applied loads and corresponding moments which is consistent with the numerical data developed by Hassan et al. (2019b). In addition, a trivial change in the neutral axis position was gained. Clearly, concrete has higher strength enhances the effective flexural stiffness of the GFRP-RC slender columns in terms of higher moment resistance at the same gained curvature compared to concrete columns have lower compressive strength. For example, at $e/h = 0.20$, the $EI_{th}/E_c I_g$ ratio increased from 0.35 to 0.60 when the concrete compressive strength increased from 30 MPa to 60 MPa. On the other hand, the effect of GFRP-bar modulus of elasticity was insignificant. This may be associated with the narrow range of the elastic modulus of GFRP-bars on markets.

In general, as the tensile stresses on the concrete tension side reach the concrete rupture strength, the column cross-section initiates concrete cracking. Soon after, and as the loading continues, the cracks migrate into column cross-section eliminating the compression-zone depth and thus, the effective flexural stiffness of the column descends. Figure 7.11 depicts the effect of test parameters on the cracked and uncracked depth ratio (c/d) as an indication for the column effective flexural stiffness. It can be inferred that the compression-zone depth is strongly affected by the change in the e/h ratio, as the column strength was declined within 70% (on average) at an applied $e/h = 0.3$ compared to the strength of axially-loaded GFRP-RC columns. Comparing to the experimental program, and for example, GFRP-RC slender column G3-33 loaded at $e/h = 0.33$ exhibited a strength reduction of 74% compared to column G3-C. After this eccentricity ratio $(e/h > 0.3)$, the decay in the c/d ratio had a less steep downward trend. As discussed earlier, the effect of longitudinal GFRP-reinforcement ratio was revealed beyond an $e/h = 0.15$. This, also, can be evidenced by the experimental results (refer to Table 7.1). Afterwards and at e/h approximately equaled 0.40, the ρ-effect was steady over the examined e/h ratios. The effect of column slenderness on the effective flexural stiffness achieved its maximum at $e/h < 0.30$ and was less pronounced at higher eccentricity ratios. Furthermore, GFRP-RC columns that have a square cross-section were exposed to higher variation in the column stiffness with the change in the column slenderness ratio compared to circular columns. Further, remarks related to Fig. 7.10 can be also drawn from Fig. 7.11.

Figure (7.12) defines the stability and material failure modes of the GFRP-reinforced concrete columns at a constant eccentricity and various slenderness ratios. In the case of the not overly slender columns $(\lambda \le 50)$, all GFRP-RC columns reached their maximum axial capacity (failed) at a point tangent to the envelope of the cross-sectional strength. This defines the case of the material failure. On the other hand, the failure (peak) for overly slender columns $(\lambda > 50)$ occurred early before the ultimate cross-section strength was achieved due to the significant second-order effects. This is called as stability failure. The latter limit $(\lambda > 50)$ specifies when GFRP-RC slender columns need rigorous and more accurate analysis and the approximate analysis methods—such as the expressions of effective flexural stiffness in ACI 318-19— may be far from the experimental results.

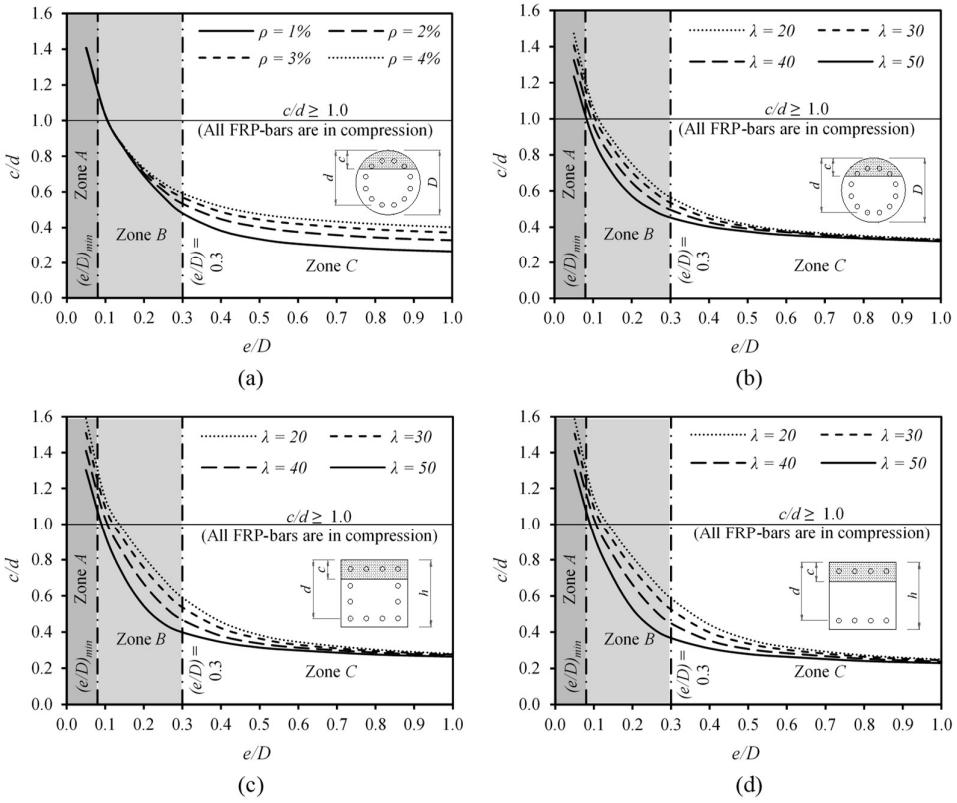

Figure 7.11– Effect of test parameters on the concrete compression-zone depth;(a) λ = 30, $f_c' = 40$ MPa , $E_{frp} = 60$ GPa ;(b, c, and d) ρ = 2%, $f_c' = 40$ MPa , $E_{frp} = 60$ GPa .

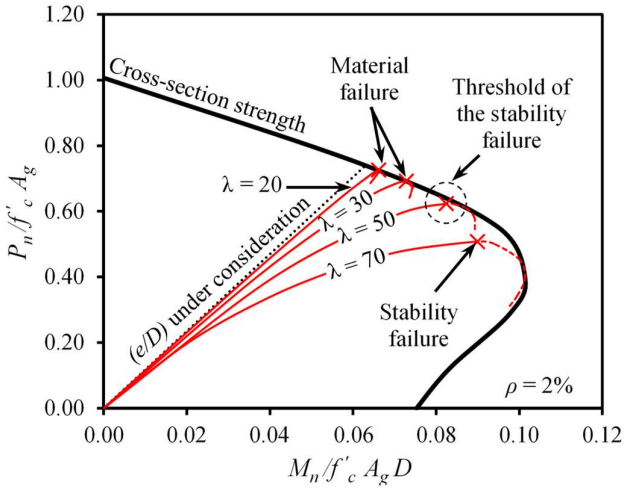

Figure 7.12– Definition of material and stability failure modes.

7.6 Development of EI Proposed Equation

In general, the proposed flexural stiffness herein can be broken down into two main terms which is like the ACI format (Eq. 7.3). The first term corresponds to the contribution of concrete effective cross-sectional area considering cracks propagation, while the second term expresses the GFRP-bars contribution to the effective flexural stiffness (see Eq. 7.22).

$$EI_{eff} = \alpha_c E_c I_g + \alpha_{frp} E_{frp} I_{frp} \tag{7.22}$$

The contribution of concrete cross-section and the GFRP-reinforcement were denoted by α_c and α_{frp}, respectively. MacGregor et al. (1975) suggested to include the effectiveness of reinforcement in terms of the longitudinal-reinforcement ratio. However, incorporating the contribution of FRP-reinforcement using the moment of inertia of FRP-bars mirrors the significance of FRP-bars arrangement into the effective flexure stiffness.

As explained earlier, the effective flexural stiffness of GFRP-RC slender columns is affected by many variables. Certainly, practical and feasible design equation of the effective flexural stiffness should accommodate, only, the most effective parameters. Among each other factors, previous studies (Mirza 1990; Tikka and Mirza 2005) showed that α_c was more influenced by the applied eccentricity ratio and the columns slenderness ratio. Therefore, Eq. (7.22) was reformulated as indicated in Eq. (7.23) based on the latter findings and, thus, was used in the conducted regression analysis.

$$EI_{eff} = (a + b \cdot \lambda + c \cdot e/h) E_c I_g + \alpha_{frp} E_{frp} I_{frp} \tag{7.23}$$

In Eq. (7.23), a is equivalent to the intercept of a simple linear equation, b and c are dimensionless regression coefficients that reflect the impact of the concerned parameters to the effective flexural stiffness. In addition, and as explained in Fig. 7.12, GFRP-RC slender columns have $\lambda > 50$ suffer a stability failure and require more accurate analysis. Therefore, the proposed expression of the effective flexural stiffness was limited to GFRP-RC columns have $\lambda \leq 50$. Moreover, the effective flexural stiffness (EI_{eff}) drops sharply when the eccentricity ratio is lower than 0.30, while the change in EI_{eff} is relatively steady beyond this

eccentricity limit. Consequently, it would be more efficient if two expressions were established to define the magnitude of the EI_{eff} before and beyond $e/h = 0.30$.

A multiple linear regression analysis was applied to the generated theoretical stiffness data in order to propose an effective flexural stiffness formula that best fit the results from the analytical model with an acceptable margin of accuracy. The proposed equation of the effective flexure stiffness $(EI_{proposed})$ respects two major concerns: (1) the mean stiffness ratio $(EI_{th}/EI_{proposed})$ should have an adequate level of conservatism not only similar to the current EI_{eff} formulas in ACI 318-19 for steel-RC slender columns but also justifies all examined range of e/h; (2) the frequency of the $EI_{th}/EI_{proposed}$ should overlay with the normal distribution curve (bell-shaped curve). The latter controls the diffusion and scattering of the $EI_{th}/EI_{proposed}$ values. Then, the proposed short-term effective flexural stiffness of GFRP-RC slender columns can be expressed as

$$EI_{proposed} = \alpha_c E_c I_g + 0.8 E_{frp} I_{frp} \le 0.35 E_c I_g \tag{7.24}$$

where

$$\alpha_c = \begin{cases} 0.44 - 0.0018\lambda - 0.9\, e/h & \left(e/h \le 0.3\right) \\ 0.1 - 0.09\, e/h & \left(0.3 < e/h \le 1.0\right) \end{cases} \tag{7.25}$$

The constant value of the $\alpha_{frp} = 0.8$ can be attributed to the linear behavior of GFRP-bars up-to failure. This coefficient is slightly lower than that for steel-bars $(\alpha_s = 1.0)$ which satisfies the assumed lower compressive contribution of GFRP-bars than steel. It can also be pointed out that both the e/h and λ adversely affect the contribution of concrete cross-section to the overall effective stiffness. Moreover, and regarding columns have an $e/h > 0.30$, the impact of slenderness ratio to the effective flexural stiffness was insignificant and, consequently, was excluded from the proposed EI formula. The distribution of the $EI_{th}/EI_{proposed}$ is indicated in Fig. (7.13). The mean value of the $EI_{th}/EI_{proposed}$ is 1.86 with 1.3% of the tested specimens have a stiffness ratio lower than unity.

Figure (7.14) compares the proposed equation of the effective flexural stiffness to the simulated theoretical results. In addition, the recent formula (Eq. 7.11) which was developed by Xue et al. (2018) was also verified. Both expressions appropriately demonstrate the downward trend of the flexural stiffness of the GFRP-RC slender columns. However, the formula developed by Xue et al. (2018) revealed unconservative values of effective flexural stiffness particularly at lower levels of e/h. On the other hand, the current proposed formula indicates a conservative margin of safety over the selected range of the tested parameters. Finally, in contrast to ACI 318-19 design equations, the proposed formula herein satisfies the variation in the effective flexural stiffness at all practical levels of the applied eccentricities. Note that for reinforced concrete buildings, e/h usually ranges from 0.1 to 0.65 (Mirza and MacGregor 1982). For columns have $e/h > 0.65$, the axial capacity of the column is normally less than $0.1 f'_c A_g$. For such cases, ACI 318-19 permits the design of the column as a flexure member ignoring the influence of the axial loads.

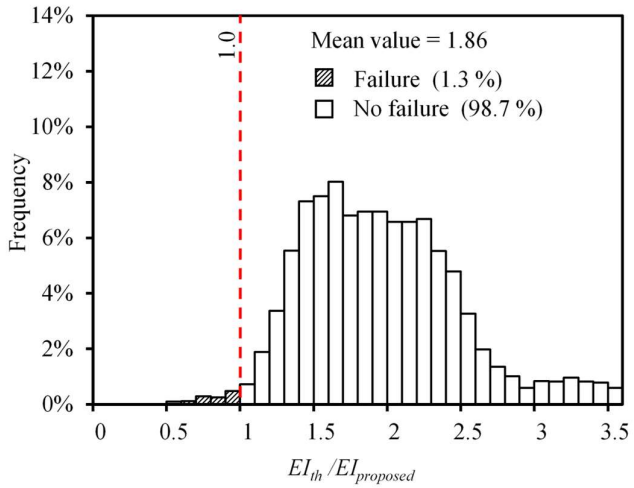

Figure 7.13– Comparison of the proposed flexural stiffness with the theoretical results.

7.7 Frames Subjected to Sustained Loads

FRP-RC columns in frames subjected to long-term or sustained loads suffer additional stresses due to creep effects. This kind of loads increase the induced lateral deflections and, thus, the 2nd-order effects in terms of the moment magnification factor. For steel-RC slender columns,

ACI 318-19 approximates such effects by dividing the short-term flexural-stiffness by $(1+\beta_{dns})$, in which the creep factor $\beta_{dns} \leq 1.0$ and is defined as the ratio of the sustained to ultimate loads. For simplicity, and whenever no accurate data are available, ACI 318-19 assumes $\beta_{dns} = 0.6$. According to ACI 318, creep transfer some of the loads to the longitudinal steel-reinforcement which may cause a premature yielding of steel-bars in case of lightly reinforced columns. Consequently, ACI 318 applied the creep factor β_{dns} to both concrete and longitudinal reinforcement terms in Eq. (7.3).

Similarly, the creep effects are considered for FRP-RC slender columns by reducing the proposed effective flexural stiffness using the creep factor β_{dns}. However, and as the compressive contribution of FRP-bars are negligible and was limited herein to the concrete compressive strength, only concrete term in the proposed EI equation is reduced for sustained load effects. Finally, the proposed effective flexural stiffness of FRP-RC slender columns, accounting for long-term loading is written as

$$EI_{eff} = \text{min.} \begin{cases} \dfrac{\alpha_c E_c I_g}{1+\beta_{dns}} + 0.8 E_{frp} I_{frp} \\ \dfrac{0.35 E_c I_g}{1+\beta_{dns}} \end{cases} \tag{7.26}$$

in which α_c is the concrete contribution to the EI_{eff} and can be determined from Eq. (7.25). Similarly, and complying with ACI 318 provisions, β_{dns} can be assumed as 0.6.

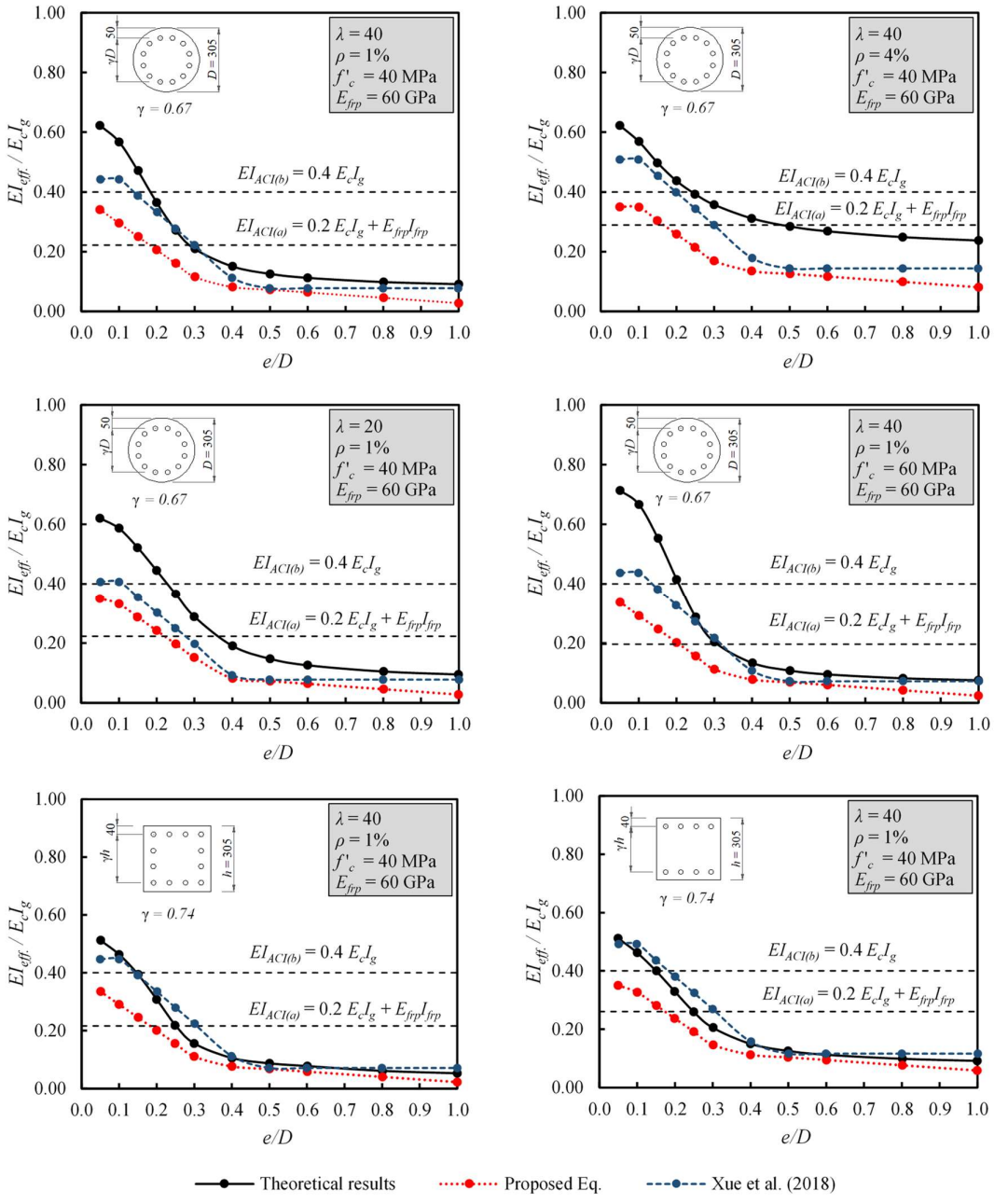

Figure 7.14– Verification of the proposed flexure stiffness equation with the theoretical results.

7.8 Proposed Stiffness Reduction Factor

ACI 318-19 introduces a reduction factor $\phi_K = 0.75$ for use when computing the critical buckling loads of steel-RC columns. This factor is based on the probability of under strength of a single isolated slender column. The stiffness reduction factor specified in ACI 318 is obtained using one-percentile statistical analysis as previously suggested by MacGregor (1976). However, Mirza (1990) reported that computing the ϕ_K factor requires complex analysis and the one-percentile stiffness ratio provides a crude estimation of ϕ_K value which is not statically justified.

Nevertheless, and in order to be consistent with ACI provisions, ϕ_K is estimated herein for a single understrength GFRP-RC slender column using the one-percentile analysis. Fig. 7.15 displays the effect of the eccentricity ratio as the most significant test parameter on the one-, five-percentiles, and average stiffness ratios $(EI_{th}/EI_{proposed})$. The proposed design equation provided an insignificant variation in the one-percentile stiffness ratio, especially over the usual range of the applied eccentricities in practical slender columns $(0.1 \le e/h \le 0.65)$. Moreover, the mean stiffness ratios calculated based on the proposed EI_{eff} for all examined GFRP-RC slender columns exceeded 1.0, while the five- and one-percentile stiffness ratios were at least 0.8 and 0.6, respectively. Therefore, the proposed stiffness reduction factor $\phi_K = 0.6$ is used to reduce the critical buckling load of a single GFRP-RC slender column as shown in Eq. (7.1).

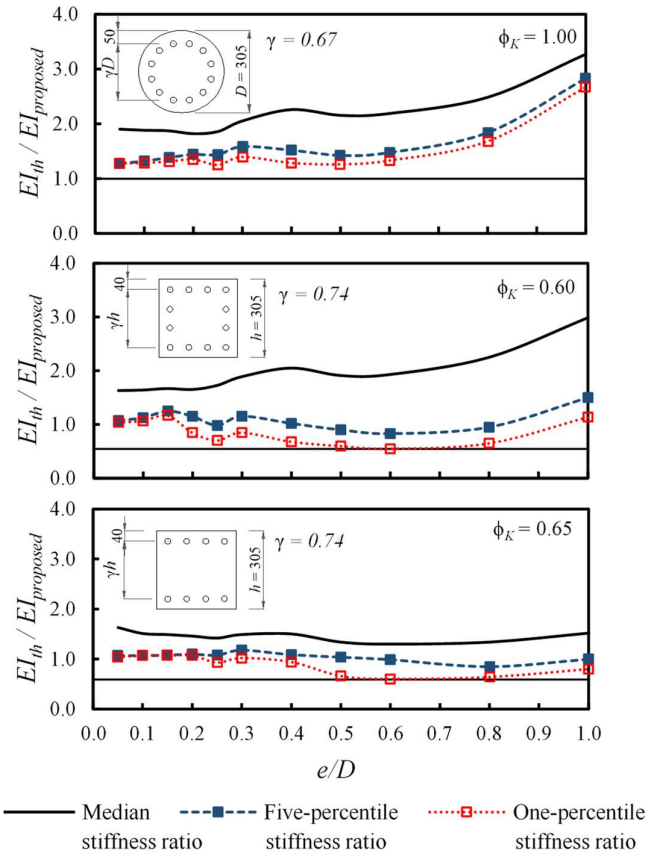

Figure 7.15– Effect of the cross-section geometry and GFRP-bars configuration on the stiffness reduction factor (ϕ_K).

7.9 Conclusions

An effective flexural stiffness of FRP-RC slender columns was presented based on a statistical assessment of more than 9,500 columns covering the practical range of the column design parameters. The developed second-order model was verified with 72 FRP-RC columns gathered from the current study and the literature. The proposed design EI equation accounts for the variation in stiffness due to both concrete and FRP-bar characteristics. Lastly, the following conclusions can be drawn.

1. The GFRP-RC columns tested under concentric or low ($e/D = 16\%$) or moderate ($e/D = 33\%$) eccentric loads exhibited compression-based failure, while the failure mode attributed to the specimens tested under large eccentric loading ($e/D = 66\%$) was controlled by exaggerated tensile cracks, accompanied by excessive lateral deformations triggering large support rotation.
2. Over the tested range of slenderness ratios ($14 \le \lambda \le 33$), all the GFRP-RC columns exhibited a material-type failure with no tensile rupture of GFRP bars observed until the end of the test. Moreover, all tested specimens revealed GFRP-bar tensile strains of less than 0.01 at the ultimate peak loads.
3. Of the investigated parameters, the flexural stiffness of the GFRP-RC columns was strongly affected by the applied eccentricity. The impact of the eccentricity ratio on the EI values diminished, however, when the eccentricity ratio exceeded 0.8.
4. Theoretical analysis supported with the experimental results demonstrate that the effect of the slenderness ratio on EI magnitude was more pronounced at eccentricity ratios ranging from 0.2 to 0.3. This correlated with the experimental results, as the GFRP-RC columns with $\lambda = 33$ lost approximately 12% and 21% of their lateral stiffness at eccentricity ratios of 0.16 and 0.33, respectively, compared to the GFRP-RC columns with $\lambda = 23$.
5. The feasibility of employing GFRP bars as an internal reinforcement in compression members was demonstrated experimentally and theoretically, particularly at $e/h \ge 0.2$. Experimentally, applying a reinforcement ratio of 3.3% improved the lateral stiffness of the slender GFRP-RC columns on average by 10% at $\lambda = 23$ and 24% at $\lambda = 33$, compared to the GFRP-RC columns with $\rho = 2.2\%$.

6. For a given e/h, concrete with higher compressive strength improved the effective flexural stiffness of the slender GFRP-RC columns in terms of higher moment resistance at the same curvature compared to the concrete columns of lower compressive strength. For example, at $e/h = 0.20$, the $EI_{eff}/E_c I_g$ ratio increased from 0.35 to 0.60 when the concrete compressive strength increased from 30 (4,350) to 60 (8,700) MPa (psi).
7. The simulated flexural stiffness data of more than 9,500 slender GFRP-RC columns were integrated into a multiple linear regression analysis in order to approximate the EI magnitudes of such members. The proposed effective flexural stiffness of slender GFRP-RC columns can be expressed as

$$EI_{eff} = \min. \begin{cases} \dfrac{\alpha_c E_c I_g}{1+\beta_{dns}} + 0.8 E_{frp} I_{frp} \\ \dfrac{0.35 E_c I_g}{1+\beta_{dns}} \end{cases} \tag{26}$$

where α_c is the concrete contribution to the EI_{eff} and can be determined from Eq. (25). Similarly, and conforming to ACI 318 provisions, the creep factor β_{dns} can be assumed to be 0.6. The proposed expression is limited to slender GFRP-RC columns with $\lambda \le 50$ and $f'_c \le 60\ (8,700)$ MPa (psi).

8. Consistent with the ACI approach, the stiffness reduction factor ϕ_K was recommended to be 0.6 based on one-percentile statistical analysis. This factor is used to reduce the critical buckling load of a single slender GFRP-RC column in calculating the magnification factor (δ).

CHAPTER 8

Summary and Conclusion

8.1 Summary

The research program entitled herein aimed at experimentally and analytically assessing the feasibility of integrating glass fiber-reinforced polymers- (GFRP-) bars and spirals as an internal reinforcement of slender reinforced-concrete (RC) columns. Consequently, thirty-four full-scale slender GFRP-RC columns were tested so as to assess the impact of various test parameters on such structural members. Additional four specimens were reinforced using traditional steel bars and tested at the same test conditions to serve as benchmarks. The column's slenderness ratio was achieved using different column's heights where all columns had the same diameter of 305-mm and similar boundary conditions. Therefore, the test parameters can be summarized as the reinforcement type (GFRP and steel), slenderness ratio (14, 17, 23, 26, and 33), load eccentricity level (0, 0.16, 0.33, and 0.66), longitudinal-reinforcement ratio (2.2, 3.3,and 4.7), confinement ratio (1.17 and 2.34), and concrete compressive strength (46 MPa and 80 MPa).

The experimental investigations were, then, extended using an analytical second-order model accounting for material and geometrical nonlinearities. The developed model was in a good agreement with the test results of the current study and literature database. Moreover, buckling-load analyses following the incremental (tangent) modulus and reduced modulus theories was conducted to predict the axial strength of concentrically-loaded FRP-RC columns considering second-order effects. Moreover, an effective flexural stiffness of FRP-RC slender columns is provided based on a statistical assessment of more than 9,500 columns which cover the practical range of the column design parameters. The proposed design EI equation accounted for the variation of stiffness due to both concrete and FRP-bars characteristics. Then, the

developed flexural stiffness was verified with 72 FRP-RC columns that were gathered from the current study and the literature.

8.2 Conclusion

The results and discussion of the conducted research program was introduced into five articles (chapters). Each article focused on a different topic using a specific number of the tested specimens. The major concluding remarks drawn from the experimental and analytical investigations can be listed as in the following context.

8.2.1 Strength, behavior, and failure Modes

1. Integrating GFRP-bars as internal reinforcement for slender RC columns proved to be adequate in resisting the applied loads and provided sufficient stability during the various testing stages.
2. The failure of both the short and slender GFRP-RC columns was dominated by a material-type failure in terms of gradual concrete cover spalling at the peak load. Beyond peak, tensile rupture of GFRP spirals, compression rupture of GFRP bars, and buckling of steel bars were observed at ultimate stages.
3. The slender GFRP-RC columns exhibited lower capacity with similar failure mechanisms compared to short GFRP-RC columns from literature. This reduction in column capacity can be considered in design by applying second-order analysis that takes into account the structure's deformed geometry.
4. The GFRP reinforcement significantly contributed to resisting the applied compression loads and yielded failure modes similar to the steel-reinforced-concrete columns at all slenderness ratios tested from $\lambda = 14$ to $\lambda = 33$. In comparison to the short-column control specimens $(\lambda = 14)$, the more slender columns at zero-eccentricity lost 1.3%, 2.3%, 5.2%, and 5.8% of their strength at slenderness ratios of $\lambda = 17$, $\lambda = 23$, $\lambda = 26$, and $\lambda = 33$, respectively.

5. The instability of concentrically loaded FRP-RC columns was experimentally investigated in terms of column lateral displacement and was observed at 75% of the column capacity with an ultimate lateral response measured 1% of the column size. The experimental second-order moments were limited and not significant over the range of slenderness ratios studied ($\lambda = 14$ to $\lambda = 23$).
6. Regardless of the slenderness ratio, the GFRP-reinforced concrete columns tested under low $\left(e / D = 16\%\right)$ or moderate $\left(e / D = 33\%\right)$ eccentric loads exhibited a material-type failure, specifically concrete-cover spalling at peak followed by a significant drop in column carrying capacity.
7. The failure mode attributed to the slender GFRP-reinforced concrete columns tested under large eccentric loading $\left(e / D = 66\%\right)$ was controlled by exaggerated tensile cracks, accompanied by excessive lateral deformations triggering large support rotation. This was metaphorically termed as tension-based failure.
8. The failure of slender GFRP-RC columns tested at moderate eccentricity ($e/D = 33\%$) can be termed a transition failure between two extremes: compression-based ($e/D = 0\%$ and 16%), in terms of concrete cover spalling at peak, and tension-based ($e/D = 66\%$), governed by the formation of excessive tensile cracks and large lateral deformations.
9. The slender GFRP-reinforced concrete columns exhibited the outmost decay in load-carrying capacity at $e / D = 33\%$ compared to their GFRP-reinforced concrete counterparts tested under concentric loads or eccentric loads with $e / D = 16\%$ or $e / D = 66\%$. For example, the GFRP-reinforced concrete columns with slenderness ratios of 23 and 33 lost 8.3% and 19.1%, respectively, of their peak loads compared to the columns with a slenderness ratio of 19.
10. Of all the tested parameters, the applied eccentricity had the greatest influence on column ultimate loads. Regardless of the column slenderness ratio or the amount of longitudinal reinforcement, the slender GFRP-RC columns retained only 52%, 26%, and 12% (on average) of their axial capacity when an e/D of 16%, 33%, and 66% were applied, respectively.

11. Over the tested range of slenderness ratio $(14 \le \lambda \le 33)$, All GFRP-RC columns reached the expected peak loads and the entire GFRP-bars remained intact. Moreover, all tested specimens revealed GFRP-bar tensile strains less than 0.01 at the ultimate peak loads.
12. The GFRP-bars provided high resistance to both tensile and compressive strains prior to experiencing any bar rupture. On average, the ultimate measured tensile strains exceeded 15,000 με (64% ε_{frpu}), while the recorded compressive-bar strains approached –13,000 με (55% ε_{frpu}).
13. The slender GFRP-RC columns loaded under moderate ($e/D = 33\%$) to high eccentricity ($e/D = 66\%$) were more sensitive to the increase in longitudinal-reinforcement ratios in terms of better resistance to the induced lateral deformations and enhanced flexural capacity.
14. The effect of the GFRP-reinforcing bars in terms of longitudinal-reinforcement ratio and tensile modulus of elasticity is more noticeable for eccentrically loaded columns for the entire range of reinforcement ratios tested ($1\% \le \rho \le 8\%$).
15. Over the range of slenderness ratios and HSCs tested, GFRP reinforcement proved its feasibility as a substantial replacement for conventional steel in slender HSC columns. Moreover, GFRP bars improved the capacity and lateral resistance of the slender HSC columns, while GFRP spirals provided thorough confinement levels.
16. Up to the slenderness limit tested ($\lambda = 33$), all the slender GFRP-HSC columns experienced material failure and did not exhibit any stability failure. Stability failure is defined herein according to ACI provisions (2019), which set the stability index in terms of a secondary-to-primary moment ratio equal to 1.4.
17. The axially loaded slender GFRP-HSC columns experienced early concrete-cover spalling compared to the NSC columns. This caused the concentrically loaded HSC columns to achieve a column-to-cylinder compressive-strength ratio $\left(f'_c\right)_{column} / \left(f'_c\right)_{cylinder} = 0.8$, while the slender GFRP-NSC columns had a ratio approaching 1.
18. Considering AASHTO (2018b) definition of the compression- and tension-controlled failures, the slender GFRP-HSC columns tested under concentric or low eccentric ($e/D = 0.16$) loading experienced compression failure in terms of concrete-cover

spalling, tensile rupture of GFRP spirals, and compressive crushing of GFRP bars. In contrast, the failure mode attributed to the slender GFRP-HSC specimens loaded with an initial applied high eccentricity ($e/D = 0.66$) exhibited tension failure that was controlled by exaggerated tensile cracks, accompanied by excessive lateral deformations triggering large support rotations. Lastly, the slender GFRP-HSC columns tested under moderate eccentric ($e/D = 0.33$) loading experienced a transition failure between compressive and tensile failure mechanisms.

19. The slender GFRP-HSC columns was slightly more susceptible (2%) to the initial applied eccentricity compared to their NSC counterparts owing to the relatively early exposure to flexural–tensile cracks attributed by the HSC specimens. For example, at e/D values equal to 16%, 33%, and 66%, the GFRP-HSC specimens lost, respectively, 49%, 75%, and 89% of their axial capacity, while the GFRP-NSC columns lost 47%, 73%, and 87% of their axial capacity, respectively.
20. The GFRP-reinforcement improved the stability of the slender GFRP-HSC columns in terms of reducing the induced second-order effects. For example, at $e/D = 0.2$, $\lambda = 60$, and $f'_c = 80$ MPa, axial column capacity dropped by 50.7%, 46.8%, and 40.7% compared to the concentrically loaded strength when the GFRP-reinforcement ratios were 1%, 2%, and 4%, respectively.

8.2.2 Buckling and second-order modeling

21. Euler–Johnson's proposed stability envelope yielded conservative values of column ultimate capacity against the test results over the range of the slenderness ratios tested. The method developed revealed the applicability limit of Euler's and Johnson's formulas for FRP-RC columns at $\lambda = 60$ for $\rho_L = 1\%$ and at $\lambda = 70$ and $\lambda = 75$ for $\rho_L = 8\%$, using the lateral stiffness provisions of Zadeh and Nanni (2017) and Mirmiran et al. (2001a), respectively.
22. When the test results were verified, the proposed tangent modulus model yielded a lower and acceptable limit for the buckling load of FRP-RC columns for the range of the slenderness ratios investigated. The double (reduced) modulus theory provided

rational limits for FRP-RC-column strength with slenderness ratios less than or equal 14.

23. The model for slender GFRP-RC columns bent in a single curvature with equal end eccentricities was proposed to mirror the second-order effects. The model was developed by discretizing the section into several integration layers and was verified with test results yielding an appropriate precise estimation of the axial and flexural capacities of slender concrete columns reinforced with GFRP bars, taking into consideration both material and geometrical nonlinearities.

24. The models developed for the axially and eccentrically loaded GFRP-HSC columns were verified against the results of the current experimental program as well as the experimental database from the literature. Both models considered the material and geometrical nonlinearities and yielded a substantial correlation with the test results.

25. A family of $P-M$ interaction diagrams were plotted over a wide range of test parameters, including slenderness ratio, compressive strength of the HSC, and GFRP-reinforcement ratio. The theoretically established interaction envelopes were found to be in good agreement with those developed experimentally. All the developed $P-M$ interaction diagrams revealed an inflection point at e/D near to 0.2.

8.2.3 Flexural stiffness

26. Among each other investigated parameters, the flexural stiffness of GFRP-RC columns was strongly affected by the applied eccentricity. However, the impact of the eccentricity ratio on the EI values diminishes at an eccentricity ratio exceeds 0.8.

27. Theoretical analysis supported by the experimental results demonstrated that the effect of slenderness ratio on EI magnitudes was more pronounced at eccentricity ratios range from 0.2 to 0.3. This correlated the experimental results, as GFRP-RC columns have $\lambda = 33$ lost approximately 12% and 21% of its lateral stiffness at eccentricity ratios of 0.16 and 0.33, respectively, compared to the GFRP-RC columns have $\lambda = 23$.

28. The feasibility of employing GFRP-bars as an internal reinforcement of compression members was experimentally and theoretically evidenced, particularly at $e/h \geq 0.2$.

Experimentally, applying a reinforcement ratio $\rho = 3.3\%$ improved the lateral stiffness of the GFRP-RC slender columns on average by 10% at $\lambda = 23$ and 24% at $\lambda = 33$ compared to GFRP-RC columns have $\rho = 2.2\%$.

29. For a given e/h, Using HSC improves the effective flexural stiffness of the GFRP-RC slender columns in terms of higher moment resistance at the same gained curvature compared to NSC columns. For example, at $e/h = 0.20$, the $EI_{eff}/E_c I_g$ ratio increased from 0.35 to 0.60 when the concrete compressive strength increased from 30 MPa to 60 MPa.

8.2.4 Design provisions

30. Both the experimental observations and analytical investigations revealed that the columns loaded under $e/D > 60\%$ had an overall performance similar to that of flexural members. This eccentricity limit is proposed to replace the value of $e/D > 50\%$ found in literature.
31. Based on the experimental observations and the theoretical investigations, the axial-load level at which the columns can be treated as flexural members is 10% of the column ultimate strength with a longitudinal-reinforcement ratio of 1%. Similarly, ACI 318-19 tacitly classifies members subjected to axial loads less than $0.1 f_c' A_g$ as beams.
32. The design provisions for FRP spirals in CSA S806-12 for short FRP-RC columns provided sufficient confining levels for the slender GFRP-RC columns tested with slenderness ratios up-to 33. Therefore, these design provisions for FRP spirals are recommended for slender FRP-RC columns.
33. Based on the derived analytical model, along with the tensile-strain measurements in our experimental program, the permissible design tensile strain of GFRP-bars ($40 \text{ GPa } (5{,}802 \text{ } ksi) < E < 60 \text{ GPa } (8{,}702 \text{ } ksi)$) should be the lesser of 0.9% and ε_{frpu}. This allows for acceptable lateral deformations with an adequate warning prior to column failure.

34. Based on the experimental results, the database from the literature, and the developed analytical buckling and second-order models for columns entirely reinforced with GFRP bars, a slenderness limit of 18 was proposed for short GFRP-reinforced concrete columns bent in a single curvature. This proposed limit replaces the current limit of 22 in CSA S806-12. This limit can be reformulated in a form similar to the limit in ACI 318-19 as $kl_u/r \le 30+12\left(M_1/M_2\right) \le 36$.

35. Applying ACI 318-19 recommendations to avoid stability failure in steel-reinforced concrete columns to GFRP-reinforced concrete columns provided rational limits for the slender upper limits, while CSA A23.3-14 provisions were found to be far from accurate. Consequently, a slenderness upper limit corresponding to a secondary-to-primary moment ratio of 1.4 was proposed for GFRP-reinforced concrete columns, like that for steel-reinforced concrete columns.

36. Based on the results of the conducted tests, experimental database from literature, and the analytical modeling performed, a slenderness limit for short HSC columns considering the limited ductility of constituent materials was proposed as

$$\lambda_{(f_c'>55)} = \lambda_{(f_c'\le 55)} - \frac{\left(f_c'-55\right)^{1.44}}{100} \qquad 55 \le f_c' \text{ (MPa)} \le 125$$

37. The simulated flexural stiffness data of more than 9,500 GFRP-RC slender columns were integrated into a multiple linear regression analysis in order to approximate the EI magnitudes of such members. The proposed effective flexural stiffness of GFRP-RC slender columns can be expressed as

$$EI_{eff} = \text{ min. } \begin{cases} \dfrac{\alpha_c E_c I_g}{1+\beta_{dns}} + 0.8E_{frp}I_{frp} \\ \dfrac{0.35E_c I_g}{1+\beta_{dns}} \end{cases}$$

in which α_c is the concrete contribution to the EI_{eff} and can be determined from Eq. (7.25). Similarly, and conforming to ACI 318 provisions, the creep factor β_{dns} can be assumed as 0.6. The proposed expression is limited to GFRP-RC slender columns have $\lambda \le 50$ and $f_c' \le 60$ MPa.

38. Complying with ACI approach, the stiffness reduction factor ϕ_K was recommended as 0.6 based on the one-percentile statistical analysis. This factor is used to reduce the critical buckling load of a single GFRP-RC slender column in the calculations of the magnification factor (δ)

8.3 Recommendations for future work

The established experimental and analytical database provided several valuable recommendations for the relevant design codes and guidelines. However, Additional efforts that address column design is still recommended based on the findings of the current study to cover the following points:

- Performance of FRP-RC slender columns at lateral cyclic loading is a debatable topic that need further investigations.
- Integrating different concrete types such as ultra high-performance concrete with FRP-RC slender columns could be promising for both materials.
- The study herein focused on the feasibility of GFRP-reinforcement as an alternative for traditional steel. However, the adequacy of utilizing different FRP-materials such as carbon or basalt may be observed.

The French version of this section is presented below:

8.4 Sommaire et Conclusions

8.4.1 Sommaire

Le programme expérimental développé pour cette recherche visait à évaluer expérimentalement et analytiquement la faisabilité d'intégrer des barres et des spirales en polymères renforcés de fibres de verre (PRFV) en tant qu'armature interne de colonnes élancées en béton armé (BA). Par conséquent, trente-quatre colonnes élancées grandeur nature

en BA-PRFV ont été testées afin d'évaluer l'impact de divers paramètres d'essai sur ces éléments structuraux. Quatre échantillons supplémentaires ont été renforcés à l'aide de barres d'acier traditionnelles et testés dans les mêmes conditions pour servir de référence. L'élancement de la colonne a été atteint en utilisant différentes hauteurs de colonne où toutes les colonnes avaient le même diamètre de 305 mm et des conditions limites similaires. Par conséquent, les paramètres d'essai peuvent être résumés comme le type d'armature (PRFV et acier), l'élancement (14, 17, 23, 26 et 33), l'excentricité de la charge (0, 0,16, 0,33 et 0,66), l'armature longitudinale (2,2, 3,3 et 4,7), le confinement (1,17 et 2,34) et la résistance à la compression du béton (46 MPa et 80 MPa).

Les recherches expérimentales ont ensuite été étendues à l'aide d'un modèle analytique de second ordre tenant compte des non-linéarités des matériaux et géométriques. Le modèle développé était en bon accord avec les résultats des essais de la base de données actuelle de l'étude et de la littérature. De plus, des analyses de charge de flambement ont suivi le module incrémentiel (tangent) et des théories de module réduit ont été menées pour prédire la résistance axiale des colonnes concentriques en BA-PRFV tenant compte des effets de second ordre. De plus, une rigidité à la flexion efficace des colonnes élancées en BA-PRFV est fournie sur la base d'une évaluation statistique de plus de 9 500 colonnes couvrant la plage pratique des paramètres de conception de la colonne. L'équation de conception EI proposée tenait compte de la variation de la rigidité due aux caractéristiques du béton et des barres en PRFV. Ensuite, la rigidité en flexion développée a été vérifiée avec 72 colonnes en BA-PRFV recueillies à partir de l'étude actuelle et de la littérature.

8.4.2 Conclusion

Les résultats et les discussions de ce programme de recherche mené ont été présentés dans cinq articles (chapitres). Chaque article portait sur un sujet différent en utilisant un nombre spécifique d'échantillons testés. Les principales conclusions tirées d'études expérimentales et analytiques peuvent être énumérées dans le contexte suivant :

8.4.2.1 Résistance, comportement and modes de rupture

1. L'intégration de barres en PRFV en tant qu'armatures internes pour les colonnes élancées en BA s'est avérée adéquate pour résister aux charges appliquées et a fourni une stabilité suffisante pendant les différentes étapes d'essais.
2. La rupture des colonnes courtes et élancées en BA-PRFV a été dominée par une rupture de type matériau par le délaminage progressif de l'enrobage du béton à la charge maximale. Au-delà du pic, une rupture en traction des spirales en PRFV, une rupture en compression des barres en PRFV et un flambement des barres en acier ont été observés aux stades ultimes.
3. Les colonnes élancées en BA-PRFV présentaient une capacité inférieure avec des mécanismes de rupture similaires par rapport aux colonnes courtes en BA-PRFV trouvées dans la littérature. Cette réduction de la capacité des colonnes peut être prise en compte dans la conception en appliquant une analyse de second ordre qui prend en compte la géométrie déformée de la structure.
4. L'armature en PRFV a contribué de manière significative à résister aux charges de compression appliquées et a donné des modes de rupture similaires aux colonnes en béton armé d'acier à tous les élancements testés de $\lambda = 14$ à $\lambda = 33$. Par rapport aux colonnes courtes pris comme échantillons témoins, $\lambda = 14$, les colonnes les plus élancées à zéro excentricité ont perdu 1.3%, 2.3%, 5.2% et 5.8% de leur résistance aux rapports d'élancement de $\lambda = 17$, $\lambda = 23$, $\lambda = 26$, et $\lambda = 33$ respectivement.
5. L'instabilité des colonnes BA-PRF chargées concentriquement a été étudiée expérimentalement en termes de déplacement latéral de la colonne et a été observée à 75% de la capacité de la colonne avec une réponse latérale ultime mesurée à 1% de la taille de la colonne. Les moments expérimentaux de second ordre étaient limités et non significatifs sur la plage d'élancements étudiés à ($\lambda = 14$ à $\lambda = 23$).
6. Quel que soit l'élancement, les colonnes en béton armé de PRFV testées sous des charges excentriques faibles (e/D = 16%) ou modérées (e/D = 33%) ont présenté une rupture de type matériau, en particulier le délaminage de l'enrobage au pic suivi d'une baisse significative de la capacité de charge des colonnes.

7. Le mode de rupture attribué aux poteaux élancés en béton armé de PRFV testés sous d'importantes charges excentriques (e/D = 66%) a été contrôlée par des fissures excessives de traction, accompagnées de déformations latérales importantes incitant une grande rotation des appuis. Ceci a été appelé rupture basée sur la tension.
8. La rupture de colonnes élancées en béton armé de PRFV testées à une excentricité modérée (e/D = 33%) peut être qualifiée de rupture de transition entre deux extrêmes : basée sur la compression (e/D = 0 and e/D = 16%), par l'écrasement du béton dominé par le délaminage de l'enrobage au pic, et basée sur la tension (e/D = 66%), régie par la formation de fissures excessives de traction et de grandes déformations latérales.
9. Les colonnes élancées en béton armé de PRFV présentaient la plus forte réduction de la capacité portante à e/D = 33% par rapport à leurs pareilles en béton armé de PRFV testées sous des charges concentriques ou excentriques avec e/D = 16% où e/D = 66%. Par exemple, les colonnes en béton armé de PRFV avec les élancements de 23 et 33 ont perdu respectivement 8,3% et 19,1% de leurs charges maximales par rapport aux colonnes avec l'élancement de 19.
10. De tous les paramètres testés, l'excentricité a eu la plus grande influence sur les charges ultimes des colonnes. Quel que soit l'élancement des colonnes ou la quantité des armatures longitudinales, les colonnes élancées en béton armé de PRFV ne conservaient que 52%, 26% et 12% (en moyenne) de leur capacité axiale lorsque *e/D* de 16%, 33% et 66% ont été appliqués, respectivement.
11. Sur la plage d'élancements testée $14 \leq \lambda \leq 33$, toutes les colonnes en BA de PRFV ont atteint les charges maximales attendues et toutes les barres en PRFV sont restées intactes. De plus, tous les échantillons testés ont montré des déformations en traction de barres en PRFV inférieures à 0,01 aux charges ultimes.
12. Les barres en PRFV ont fourni une résistance élevée aux contraintes de traction et de compression avant de subir une rupture de barre. En moyenne, les déformations de traction ultimes mesurées dépassaient 15 000 με (64% ε_{frpu}), tandis que les déformations de barre en compression enregistrées approchaient –13 000 με (55% ε_{frpu}).
13. Les colonnes élancées en BA en PRFV chargées sous une excentricité modérée (e/D = 33%) à celle élevée (e/D = 66%) étaient plus sensibles à l'augmentation des armatures

longitudinales en termes de meilleure résistance aux déformations latérales induites et de l'amélioration de la capacité de flexion.

14. L'effet des barres d'armature en PRFV en terme du taux d'armature longitudinale et de module d'élasticité en traction est plus sensible pour les colonnes chargées excentriquement pour toute la gamme des taux d'armatures testés ($1\% \leq \rho \leq 8\%$).
15. Sur la gamme d'élancements et de BHPs testés, le renforcement en PRFV a prouvé sa faisabilité en tant que remplacement substantiel de l'acier conventionnel dans des colonnes élancées en BHP. De plus, les barres en PRFV ont amélioré la capacité et la résistance latérale des colonnes élancées en BHP, tandis que les spirales en PRFV ont fourni des niveaux de confinement complets.
16. Jusqu'à la limite d'élancement testée ($\lambda = 33$), toutes les colonnes élancées BHP-PRFV ont connu une rupture de matériau et n'ont présenté aucune défaillance de stabilité. La défaillance de stabilité est définie ici conformément aux dispositions de l'ACI (2019), qui fixent l'indice de stabilité en termes de rapport de moment secondaire / primaire égal à 1,4.
17. Les colonnes élancées en BHP-PRFV chargées axialement ont connu un délaminage précoce de l'enrobage du béton par rapport aux colonnes de béton à résistance normale. Cela a amené les colonnes à béton à haute performance (BHP) chargées concentriquement à atteindre un rapport résistance à la compression colonne / cylindre de $(f'_c)_{column} / (f'_c)_{cylinder} = 0.8$, tandis que les colonnes élancées en béton normal de PRFV avaient un rapport approchant à 1.
18. Considering AASHTO (2018b) definition of the compression- and tension-controlled failures, the slender GFRP-HSC columns tested under concentric or low eccentric (e/D = 16%) loading experienced compression failure in terms of concrete-cover spalling, tensile rupture of GFRP spirals, and compressive crushing of GFRP bars. In contrast, the failure mode attributed to the slender GFRP-HSC specimens loaded with an initial applied high eccentricity (e/D = 66%) exhibited tension failure that was controlled by exaggerated tensile cracks, accompanied by excessive lateral deformations triggering large support rotations. Lastly, the slender GFRP-HSC columns tested under moderate

eccentric (e/D = 33%) loading experienced a transition failure between compressive and tensile failure mechanisms.

19. Compte tenu de la définition d'AASHTO (2018b) des ruptures en compression et en tension, les colonnes élancées BHP-PRFV testées sous un chargement concentrique ou à faible excentrique (e/D = 16%), ont subi une rupture en compression par le délaminage de l'enrobage du béton, de rupture en traction des spirales en PRFV et de compression par écrasement des barres en PRFV. En revanche, le mode de rupture attribué aux échantillons élancés de BHP-PRFV chargés avec une excentricité initiale élevée (e/D = 66%) a montré une rupture de tension qui était contrôlée par des fissures excessives de traction, accompagnées de déformations latérales déréglées déclenchant de grandes rotations de l'appui. Enfin, les colonnes élancées en BHP-PRFV testées sous une charge excentrique modérée (e/D = 33%) ont connu une rupture de transition entre les mécanismes de rupture en compression et en traction.
20. Les colonnes élancées en BHP-PRFV étaient légèrement plus sensibles (2%) à l'excentricité initiale appliquée par rapport à leurs semblables avec béton normal en raison des fissures précoces de flexion-traction attribuées aux échantillons en BHP. Par exemple, à des valeurs de *e/D* égales à 16%, 33% et 66%, les échantillons BHP-PRFV ont perdu, respectivement, 49%, 75% et 89% de leur capacité axiale, tandis que les colonnes en béton normal de PRFV ont perdu 47%, 73% et 87% de leur capacité axiale, respectivement.
21. Les armatures en PRFV ont amélioré la stabilité des colonnes élancées en BHP en termes de réduction des effets induits du second ordre. Par exemple, à e/D = 0.2, $\lambda = 60$ et $f_c' = 80$ MPa, la capacité de la colonne axiale a chuté de 50,7%, 46,8% et 40,7% par rapport à la résistance à la charge concentrique lorsque les taux d'armatures en PRFV étaient respectivement de 1%, 2% et 4%.

8.4.2.2 Flambement et modélisation de second ordre

22. L'enveloppe de stabilité proposée par Euler–Johnson a donné des valeurs conservatrices de la capacité ultime de la colonne par rapport aux résultats des essais sur la plage d'élancements testés. La méthode développée a montré la limite d'applicabilité des formules d'Euler et Johnson pour les colonnes BA-PRFV à $\lambda = 60$ pour $\rho = 1\%$ et à λ

= 70 et λ = 75 pour ρ = 8%, en utilisant les données de rigidité latérale de Zadeh et Nanni (2017) et Mirmiran et al. (2001a), respectivement.

23. Lorsque les résultats des essais ont été vérifiés, le modèle de module tangent proposé a donné une limite inférieure et acceptable pour la charge de flambement des colonnes en BA-PRFV pour la plage d'élancements étudiés. La théorie du module double (réduit) a fourni des limites rationnelles pour la résistance de la colonne en BA-PRFV avec les élancement inférieurs ou égaux à 14.
24. Le modèle des colonnes élancées en BA-PRFV à simple courbure avec des excentricités d'extrémité égales a été proposé pour refléter les effets du second ordre. Le modèle a été développé en discrétisant la section en plusieurs couches d'intégration et a été vérifié avec des résultats de l'essai donnant une estimation précise et appropriée des capacités axiales et de flexion de colonnes élancées en béton renforcées avec des barres en PRFV, en prenant en compte les non-linéarités des matériaux et géométriques.
25. Les modèles développés pour les colonnes en BHP-PRFV chargées axialement et excentriquement ont été vérifiés contre les résultats du programme expérimental ici présent ainsi qu'à la base de données expérimentales de la littérature. Les deux modèles ont pris en compte les non-linéarités des matériaux et géométriques et ont produit une considérable corrélation avec les résultats des essais.
26. Une famille de diagrammes d'interaction $P-M$ a été tracée sur une large gamme de paramètres d'essai, y compris l'élancement, la résistance à la compression du BHP et le taux d'armature PRFV. Les enveloppes d'interaction établies théoriquement étaient en bon accord avec celles expérimentalement développées. Tous les diagrammes d'interaction $P-M$ développés ont révélé un point d'inflexion à *e/D* proche de 0.2.

8.4.2.3 Rigidité en flexion

27. Parmi les autres paramètres étudiés, la rigidité en flexion des colonnes en BA-PRFV a été fortement affectée par l'excentricité appliquée. Cependant, l'impact du rapport d'excentricité sur les valeurs EI diminue à l'excentricité supérieur à 0.8.

28. L'analyse théorique soutenue par les résultats expérimentaux a démontré que l'effet d'élancement sur les valeurs EI était plus prononcé à des valeurs d'excentricité de 0,2 à 0,3. Cela a corrélé les résultats expérimentaux, car les colonnes en BA-PRFV avec λ = 33 ont perdu environ 12% et 21% de leur rigidité latérale à d'excentricité de 0,16 et 0,33, respectivement, par rapport aux colonnes BA-PRFV avec λ = 23.

29. L'utilisation de barres de PRFV comme renforcement interne des éléments en compression a été mise en évidence expérimentalement et théoriquement, en particulier à $e/h \geq 0.2$. Expérimentalement, l'application d'un taux d'armature de ρ = 3.3% a amélioré la rigidité latérale des colonnes élancées en BA-PRFV en moyenne de 10% à λ = 23 et 24% à λ = 33 par rapport aux colonnes avec ρ = 2.2%.

30. Pour une donnée, le béton avec une résistance à la compression plus élevée améliore la rigidité à la flexion effective des colonnes élancées en BA-PRFV en termes de résistance au moment plus élevée avec la même courbure par rapport aux colonnes en béton avec une résistance à la compression plus faible. Par exemple, à e/h = 0.2, le ratio $EI_{eff} / E_c I_g$ est passé de 0,35 à 0,60 lorsque la résistance à la compression du béton est passée de 30 MPa à 60 MPa.

8.4.2.4 Dispositions de conception

31. Les observations expérimentales et les analyses analytiques ont révélé que les colonnes chargées sous $e / D > 60\%$ avaient une performance globale similaire à celle des éléments en flexion. Cette limite d'excentricité est proposée pour remplacer la valeur de $e / D > 50\%$ trouvée dans la littérature.

32. Sur la base des observations expérimentales et des investigations théoriques, le niveau de charge axiale auquel les colonnes peuvent être traitées comme des éléments de flexion est de 10% de la résistance ultime de la colonne avec un taux de renforcement longitudinal de 1%. De même, ACI 318-19 classe implicitement les éléments soumis à des charges axiales moins que $0.1 f_c' A_g$ comme des poutres.

33. Les dispositions de conception pour les spirales en PRFV dans la norme CSA S806-12 pour les colonnes courtes en BA-PRFV ont fourni des niveaux de confinement

suffisants pour les colonnes élancées en BA-PRFV testées aux élancements jusqu'à 33. Par conséquent, ces dispositions de conception pour les spirales en PRF sont recommandées pour les colonnes élancées en BA-PRF.

34. Sur la base du modèle analytique dérivé, ainsi que des mesures de déformation en traction dans notre programme expérimental, la déformation de traction de conception admissible des barres de PRFV (40 GPa (5,802 *ksi*) < *E* < 60 GPa (8,702 *ksi*)) devrait être la moindre de 0,9% et ε_{frpu}. Cela permet des déformations latérales admissibles avec un avertissement adéquat avant l'écrasement de la colonne.
35. Sur la base des résultats expérimentaux, de la base de données de la littérature et des modèles analytiques de flambement et de second ordre développés pour les colonnes entièrement renforcées avec des barres en PRFV, une limite d'élancement de 18 a été proposée pour les colonnes courtes en béton armé de PRFV à simple courbure. Cette limite proposée remplace la limite actuelle de 22 dans la norme CSA S806-12. Cette limite peut être reformulée sous une forme similaire à la limite de l'ACI 318-19 comme $kl_u/r \le 30 + 12\left(M_1/M_2\right) \le 36$
36. L'application des recommandations ACI 318-19 pour éviter les ruptures par stabilité des colonnes en béton armé d'acier aux colonnes en béton armé de PRFV a fourni des limites rationnelles pour les limites supérieures d'élancement, tandis que les dispositions de la CSA A23.3-14 se sont avérées loin d'être exactes. Par conséquent, une limite supérieure d'élancement correspondant à un rapport de moment secondaire / primaire de 1,4 a été proposée pour les colonnes en béton armé de PRFV, comme celle pour les colonnes en béton armé d'acier.
37. Sur la base des résultats des essais effectués, de la base de données expérimentales issues de la littérature et de la modélisation analytique effectuée, une limite d'élancement pour les colonnes courtes à BHP, compte tenu de la ductilité limitée des matériaux constitutifs, a été proposée comme suit :

$$\lambda_{(f'_c>55)} = \lambda_{(f'_c\le 55)} - \frac{\left(f'_c - 55\right)^{1.44}}{100} \qquad 55 \le f'_c \text{ (MPa)} \le 125$$

38. Les données simulées de rigidité en flexion de plus de 9 500 colonnes élancées en BA-PRFV ont été intégrées dans une analyse de régression linéaire multiple afin d'approximer les valeurs de EI de ces éléments. La rigidité à la flexion effective proposée des colonnes élancées BA-PRFV peut être exprimée comme :

$$EI_{eff} = \min. \begin{cases} \dfrac{\alpha_c E_c I_g}{1+\beta_{dns}} + 0.8 E_{frp} I_{frp} \\ \dfrac{0.35 E_c I_g}{1+\beta_{dns}} \end{cases}$$

Avec α_c contribution du béton EI_{eff} et peut être calculé avec l'équation (7.25). De même, et conformément aux dispositions de l'ACI 318, le facteur de fluage β_{dns} peut être supposé égal à 0,6. L'expression proposée est limitée aux colonnes élancées en BA-PRFV avec $\lambda \leq 50$ et $f'_c \leq 60$ MPa.

39. Conformément à l'approche de l'ACI, le facteur de réduction de la rigidité ϕ_K a été recommandé à 0,6 sur la base de l'analyse statistique. Ce facteur est utilisé pour réduire la charge critique de flambement d'une seule colonne élancée en BA-PRFV dans les calculs du facteur d'amplification (δ)

8.4.3 Recommandations pour les travaux futurs

La base de données expérimentale et analytique établie a fourni plusieurs recommandations précieuses pour les codes et les guides de conception. Cependant, des efforts supplémentaires concernant la conception des colonnes sont toujours recommandés sur la base des résultats de la présente étude pour couvrir les points suivants :

- La performance des colonnes élancées en BA-PRFV à chargement cyclique latéral est un sujet incertain qui nécessite des investigations supplémentaires.
- L'intégration de différents types de béton tels que le béton ultra haute performance (BUHP) avec des colonnes élancées renforcés de PRFV pourrait être prometteuse pour les deux matériaux.

- Cette étude s'est concentrée sur la l’armature de PRFV comme alternative à l'acier traditionnel. Cependant, l'adoption de différents matériaux en PRF tels que le carbone ou le basalte peut être étudiée.

REFERENCES

AASHTO. (2018a). AASHTO LRFD Bridge Design Guide Specifications for GFRP–Reinforced Concrete. 2nd ed. Washington. DC: AASHTO.

AASHTO. (2018b). AASHTO LRFD Bridge Design Specifications. 8th ed. Washington. DC: AASHTO.

Abdelazim, W.; Mohamed, H. M.; Afifi, M. Z.; and Benmokrane, B. (2019). "Proposed Slenderness Limit for GFRP-RC Columns Based on Experiments and Buckling Analysis." *ACI Structural Journal*, V. 117, No. 1, January 2020.

ACI (American Concrete Institute). (2019) "Building Code Requirements for Structural Concrete." ACI 318-19. Farmington Hills. MI. 2019.

ACI Committee 318, 2014, "Building Code Requirements for Structural Concrete (ACI 318-14) and Commentary (318R-14)," American Concrete Institute, Farmington Hills, MI, 519 pp.

ACI Committee 440, 2015, "Guide for the Design and Construction of Structural Concrete Reinforced with FRP Bars (ACI 440.1R-15)," American Concrete Institute, Farmington Hills, MI, 88 pp.

Afifi, M. Z.; Mohamed, H. M.; and Benmokrane, B, 2014, "Axial capacity of circular concrete columns reinforced with GFRP-bars and spirals," *Journal of Composites for Construction*, ASCE, V. 18, No. 1, Feb., p. 04013017.

ASTM Standard C39/C39M-17b, 2017, "Standard Test Method for Compressive Strength of Cylindrical Concrete Specimens," ASTM International, West Conshohocken, PA, 8 pp.

ASTM Standard D2584, 2008, "Standard test method for ignition loss of cured reinforced resins," ASTM International, West Conshohocken, PA, 3 pp.

Bažant, Z. P.; Cedolin, L.; & Tabbara, M. R., 1991, "New method of analysis for slender columns," *ACI Structural Journal*, V. 88, No. 4, July-Aug., pp. 391-401.

Canadian Standards Association (CSA), 2010, "Specifications for Fiber-Reinforced Polymer," CSA S807-10, Rexdale, ON, Canada, 34 pp.

Canadian Standards Association (CSA), 2012, “Design and construction of building components with fiber reinforced polymers,” CAN/CSAS806-12, Mississauga, Ontario, Canada, 198 pp.

Canadian Standards Association (CSA), 2014, “Design of concrete structures,” CSA A23.3-14, Rexdale, ON, Canada, 298 pp.

Choo. C. C. Harik. I. E. and Gesund. H. (2006). “Strength of rectangular concrete columns reinforced with fiber-reinforced polymer bars.” ACI Struct. J. 103(3). 452–459.

Chovichien V., Gutzwiller M. J., and Lee R. H. (1973). “Analysis of Reinforced Concrete Columns Under Sustained Load.” *ACI Structural Journal.* V. 70. No. 10. Jan. pp. 692-700.

Collins, M. P., Mitchell, D., and MacGregor, J. G. (1993). “Structural Design Considerations for High-Strength Concrete.” *Concrete International: Design and Construction.* V15. No. 5. May 1993.

CSA (Canadian Standards Association). 2019. Canadian highway bridge design code. CAN/CSA S6-19. Rexdale, ON, Canada: CSA.

Cusson, D., and Paultre, P. (1994). “High-Strength Concrete Columns Confined by Rectangular Ties.” *Journal of Structural Engineering.* ASCE. V. 120. No.3. March 1994.

De Luca, A.; Matta, F.; and Nanni, A., 2010, “Behavior of Full-Scale Glass Fiber-Reinforced Polymer Reinforced Concrete Columns under Axial Load,” *ACI Structural Journal*, V. 107, No. 5, Sept.-Oct., pp. 589-596.

Engesser, F. (1889), "Uber die Knickfestigkeit gerader Stabe," *Zeitschrift fur Architektur und lngenieurwesen, Vol. 35 (Sec. 8.1).*

Guérin, M.; Mohamed, H. M.; Benmokrane, B.; Nanni, A.; and Shield, C. K., 2018b, “Eccentric behavior of full-scale reinforced concrete columns with glass fiber-reinforced polymer bars and ties,” *ACI Structural Journal*, V. 115, No. 2, March, pp. 489–500.

Guérin, M.; Mohamed, H. M.; Benmokrane, B.; Shield, C. K.; and Nanni, A., 2018a, “Effect of Glass Fiber-Reinforced Polymer Reinforcement Ratio on Axial-Flexural Strength of Reinforced Concrete Columns,” *ACI Structural Journal*, V. 115, No. 4, July, pp. 1049-1061.

Hadhood, A.; Mohamed, H. M.; and Benmokrane, B., 2017a, "Axial load-moment interaction diagram of circular concrete columns reinforced with CFRP bars and spirals: Experimental and theoretical investigations," *Journal of Composites for Construction*, ASCE, V. 21, No. 2, Jan., p. 04016092.

Hadhood, A.; Mohamed, H. M.; Ghrib, F.; and Benmokrane, B., 2017b, "Efficiency of glass-fiber reinforced-polymer (GFRP) discrete hoops and bars in concrete columns under combined axial and flexural loads," *Composites Part B: Engineering*, V. 114, No. 6, pp. 223–236.

Hadhood, A.; Mohamed, H. M.; and Benmokrane, B., 2017c, "Failure envelope of circular concrete columns reinforced with GFRP-bars and spirals." ACI Struct. J. 114 (6): 1417–1428.

Hadhood, A.; Mohamed, H. M.; and Benmokrane, B., 2017d, "Strength of Circular HSC Columns Reinforced Internally with Carbon-Fiber-Reinforced Polymer Bars under Axial and Eccentric Loads," *Construction and Building Materials*, V. 141, pp. 366-378.

Hadhood. A., Mohamed. H. M., and Benmokrane. B. 2017e. "Experimental study of circular high-strength concrete columns reinforced with GFRP bars and spirals under concentric and eccentric loading." *Journal of Composites for Construction*. ASCE. V. 21. No. 2. Jan. p. 04016078.

Hadhood. A., Mohamed. H. M., and Benmokrane. B. 2018a. "Assessing Stress-Block Parameters in Designing Circular High-Strength Concrete Members Reinforced with FRP Bars." *Journal of Structural Engineering.* ASCE. V. 144. No. 10. July 2018.

Hadhood. A., Mohamed. H. M., and Benmokrane. B. 2018b. "Flexural Stiffness of GFRP- and CFRP-RC circular Members under Eccentric Loads Based on Experimental and Curvature Analysis." *ACI Structural Journal*. V. 115. No. 4. July. 2018.

Hadhood, A.; Mohamed, H. M.; and Benmokrane, B., Nanni, A., Shield C. K., 2019, "Assessment of Design Guidelines of Concrete Columns Reinforced with Glass Fiber-Reinforced Polymer Bars," *ACI Structural Journal*, V. 116, No. 4, July, pp. 193-207.

Hadi, M. N.; Karim, H.; and Sheikh, M. N., 2016, "Experimental Investigations on Circular Concrete Columns Reinforced with GFRP-bars and Helices under Different Loading Conditions," *Journal of Composites for Construction*, ASCE, V. 20, No. 4, 04016009.

Hadi. M. N. S., Hassan. H. A., and Sheikh. M. N. (2017). "Experimental Investigation of Circular High-Strength Concrete Columns Reinforced with Glass Fiber-Reinforced Polymer Bars and Helices under Different Loading Conditions." *Journal of Composites for Construction*. ASCE. V. 21. No. 4. 04017005.

Hales, T. A.; Pantelides, C. P.; and Reaveley, L. D., 2016, "Experimental evaluation of slender high-strength concrete columns with GFRP and hybrid reinforcement," *Journal of Composites for Construction*, ASCE, V. 20, No. 6, Dec., p. 04016050.

Hassan. H. A., Sheikh. M. N., and Hadi. M. N. (2017). "Performance evaluation of high strength concrete and steel fibre high strength concrete columns reinforced with GFRP bars and helices." *Construction and Building Materials*. V. 134. pp. 297–310.

Hassan. H. A., Karim. H., Sheikh. M. N. and Hadi. M. N. S. (2019a). "Behavior of Full-Scale Glass Fiber-Reinforced Polymer Reinforced Concrete Columns under Axial Load." *ACI Structural Journal*. V. 107. No. 5. Sept.-Oct. 2019.

Hassan. H. A., Karim. H., Sheikh. M. N. and Hadi. M. N. S. (2019b). "Moment-Curvature Behavior of Glass Fiber-Reinforced Polymer Bar-Reinforced Normal-Strength Concrete and High-Strength Concrete Columns." *ACI Structural Journal*. V. 116. No. 4. July. 2019.

ISIS (Intelligent Sensing for Innovative Structures) Canada. (2007). Reinforcing Concrete Structures with Fibre-Reinforced Polymers. ISIS Canada research network. Winnipeg. Manitoba. Canada.

Jawaheri Zadeh H., and Nanni. A. (2013). "Design of RC Columns Using Glass FRP Reinforcement." *Journal of Composites for Construction.* ASCE. V. 17. No. 3. June. pp. 294-304.

Jawaheri Zadeh H., and Nanni. A. (2017). "Flexural Stiffness and Second-Order Effects in Fiber-Reinforced Polymer-Reinforced Concrete Frames." *ACI Structural Journal*. V. 114. No. 2. Mar.-Apr. pp. 533-544.

Jiang. T. Teng. J. G. (2013). "Behavior and design of slender FRP-confined circular RC columns." *Journal of Composites for Construction*. ASCE. V. 17. No. 4. August 2013.

Karim. H., Sheikh. M. N. and Hadi. M. N. S. (2016). "Load and Moment Interaction Diagram for Circular Concrete Columns Reinforced with GFRP Bars and GFRP Helices." *Journal of Composites for Construction.* ASCE. V. 21. No. 1. July 2016.

Logan, A.; Choi, W.; Mirmiran, A.; Rizkalla, S., Zia, P., 2009, "Short-Term Mechanical Properties of High-Strength Concrete," *ACI Structural Journal*, V. 106, No. 5, Sep.-Oct. 2009.

MacGregor, J. G., 1976, "Safety and Limit States Design for Reinforced Concrete," *Canadian Journal of Civil Engineering*, V. 3, No. 4, pp. 484-513.

MacGregor, J. G.; Breen, J. E.; and Pfrang, E. O., 1970, "Design of Slender Concrete Columns," *ACI Journal Proceedings*, V. 67, No. 1, Jan., pp. 6-28.

MacGregor, J. G.; Oelhafen, U. H.; and Hage, S. E., 1975, "A Re-Examination of the EI Value for Slender Columns," Reinforced Concrete Columns, SP-50, American Concrete Institute (ACI), Farmington Hills, Mich., pp. 1-40.

MacGregor. J. G., and Hage. S. E., (1977). "Stability Analysis and Design of Concrete Frames." *Proceedings*. ASCE. V. 103. No. ST10. Oct. pp. 1953-1970.

Manuel R. F., MacGregor J. G. (1967). "Analysis of Restrained Reinforced Concrete Columns Under Sustained Load." *ACI Structural Journal.* V. 64. No. 1. Jan. pp. 12-24.

Maranan, G. B.; Manalo, A. C.; Benmokrane, B.; Karunasena, W.; and Mendis, P., 2016, "Behavior of Concentrically Loaded Geopolymer-Concrete Circular Columns Reinforced Longitudinally and Transversely with GFRP Bars," *Engineering Structures*, V. 117, No. 15, June, pp. 422-436.

Martin, I.; MacGregor, J. G.; Pfrang, E. O.; and Breen, J. E., 1966, "A Critical Review of the Design of Reinforced Concrete Columns," *Symposium on Reinforced Concrete Columns,* SP-13, American Concrete Institute (ACI), Detroit, pp. 13-53.

Mirmiran, A., 1998, "Length Effects on FRP-Reinforced Concrete Columns," *Proceedings of the 2nd International Conference on Composites in Infrastructure*, Tucson, Ariz., pp. 518-532.

Mirmiran, A.; Shahawy, M.; and Beitleman, T., 2001b, "Slenderness Limit for Hybrid FRP Concrete Columns," *Journal of Composites for Construction*, ASCE, V. 5, No. 1, Feb., pp. 26-34.

Mirmiran, A.; Yuan, W.; and Chen, X., 2001a, "Design for Slenderness in Concrete Columns Internally Reinforced with Fiber-Reinforced Polymer Bars," *ACI Structural Journal*, V. 98, No. 1, Jan.-Feb., pp. 116-125.

Mirza, S. A., 1990. "Flexural Stiffness of Rectangular Reinforced Concrete Columns." *ACI Structural Journal*, V. 87, No. 4, July-Aug. 1990.

Mirza, S. A., and MacGregor, J. G., 1982. "Probabilistic Study of Strength of Reinforced Concrete Members." *Canadian Journal of Civil Engineering*. V. 9. No. 3. 1982.

Mohamed, H. M.; Afifi, M. Z.; and Benmokrane, B., 2014, "Performance evaluation of concrete columns reinforced longitudinally with FRP bars and confined with FRP hoops and spirals under axial load," *Journal of Bridge Engineering*, Vol. 19, No. 7, June, p. 04014020.

Mohamed, H.M.; Abdel-Baky, H.; and Masmoudi, R., 2010, "Nonlinear stability analysis of concrete filled fiber-reinforced polymer-tube columns: experimental and theoretical investigation," *ACI Structural Journal*, V. 107, No. 6, Nov.-Dec., pp. 699–708.

Pantelides, C. P.; Gibbons, M. E.; and Reaveley, L. D., 2013, "Axial load behavior of concrete columns confined with GFRP spirals," *Journal of Composites for Construction*, ASCE, V. 17, No. 3, June, pp. 305–313.

Popovics, S., 1973, "A Numerical Approach to the Complete Stress-Strain Curve of Concrete," *Cement and Concrete Research*, V. 3, No. 5, Sep., pp. 583-599.

Salah-Eldin. A., Mohamed. H. M., and Benmokrane. B. (2019a). "Axial–Flexural Performance of High-Strength-Concrete Bridge Compression Members Reinforced with Basalt-FRP Bars and Ties: Experimental and Theoretical Investigation." *Journal of Bridge Engineering.* ASCE. V. 24. No. 7. Oct. p. 04019069.

Salah-Eldin. A., Mohamed. H. M., and Benmokrane. B. (2019b). "Structural performance of high-strength-concrete columns reinforced with GFRP bars and ties subjected to eccentric loads." *Engineering Structures.* V. 185. April 2019. p. 286-300.

Shanley, F.R. (1947). "Inelastic column theory." Journal of the aeronautical sciences. Vol. 14. No. 5. May 1947.

Sheikh, S.A.; Kharal, Z., 2018, "Replacement of Steel with GFRP for Sustainable Reinforced Concrete," *Construction and Building Materials*, V. 160, pp. 767-774.

Thorenfeldt, E., A. Tomaszewicz, and J. J. Jensen. 1987. "Mechanical properties of high strength concrete and application to design." In Proc., Symp., on Utilization of High-Strength Concrete, 149–159. Trondheim, Norway: Tapir.

Tikka, T. K., Mirza, S. A., 2005. "Nonlinear EI Equation for Slender Reinforced Concrete Columns." *ACI Structural Journal*. V. 102. No. 6. Nov.-Dec. 2005

Tikka. T. K., Francis. M., and Teng. B. (2010). “Strength of Concrete Beam Columns Reinforced with GFRP Bars.” *2nd International Structures Specialty Conference*. Winnipeg. MB. Canada. pp. 1194-1203.

Timoshenko, S. P., Gere, J. M. (1963). “Theory of Elastic Stability.” Second Edition. McGraw-Hill Book Co. New York. 1963.

Tobbi, H., Farghaly, A., and Benmokrane, B. (2012). "Concrete Columns Reinforced Longitudinally and Transversally by GFRP-bars." *ACI Structural Journal*, Vol. 109, No. 4, pp. 551-558.

Tobbi, H., Farghaly, A.S., and Benmokrane, B. (2014). "Behaviour of FRP-RC Columns with Varying Reinforcement Types and Ratios." *ACI Structural Journal*, Vol. 111, No. 2, 375-385.

U.S. Federal Highway Administration (FHWA). (2019). “Bridge Replacement Unit Costs 2018.” 〈https://www.fhwa.dot.gov/bridge/nbi/sd2018.cfm〉 (Oct. 09, 2019).

Xue, W.; Peng, F.; and Fang, Z, 2018, "Behavior and Design of Slender Rectangular Concrete Columns Longitudinally Reinforced with Fiber-Reinforced Polymer Bars," *ACI Structural Journal*, Vol. 115, No, 2, Mar., pp. 311-322.

Youssef. J., Hadi. M.N. (2017). “Axial Load-Bending Moment Diagrams of GFRP Reinforced Columns and GFRP Encased Square Columns.” *Construction and Building Materials*. V. 135. pp. 550-564.